

# **Upscaling of Nonlinear Reactive Transport: from Pore to Core**

Promotoren :      prof. dr. ir. S. E. A. T. M. van der Zee  
                              persoonlijk hoogleraar bij de leerstoelgroep Bodemscheikunde en  
                              Chemische Bodemkwaliteit,  
                              Wageningen Universiteit.  
                              prof. dr. ir. A. Leijnse  
                              hoogleraar grondwaterkwaliteit,  
                              Wageningen Universiteit.

Samenstelling promotiecommissie:

dr. ir. M.I.J. van Dijke, Heriot-Watt University, UK

prof. dr. ir. S.M. Hassanizadeh, Universiteit Utrecht

prof. dr. ir. C.P.J.W. van Kruijsdijk, Technische Universiteit Delft

prof. dr. ir. J. Grasman, Wageningen Universiteit

Ram Chandra Acharya

**Upscaling of Nonlinear Reactive Transport:  
from Pore to Core**

proefschrift  
ter verkrijging van de graad van doctor  
op gezag van de rector magnificus  
van Wageningen Universiteit,  
prof. dr. ir. L. Speelman,  
in het openbaar te verdedigen  
op dinsdag 21 december 2004  
des namiddags te 13:30 uur in de Aula.

Acharya, R. C.

Upscaling of Nonlinear Reactive Transport:  
from Pore to Core.

PhD Thesis, Wageningen University, Wageningen 2004.

ISBN 90-8504-130-9

**Keywords:** porosity; permeability; dispersion; reactive transport; nonlinear isotherm;  
pore-network modeling.

Copyright © Ram C. Acharya, 2004.

## Abstract

Acharya, R. C., 2004, Upscaling of Nonlinear Reactive Transport: from Pore to Core. PhD Thesis, Wageningen University, The Netherlands. ISBN 90-8504-130-9, 137 pages.

The major objective of this research is to gain a better understanding of the heterogeneous interactions between reactive solutes and the solid phase at the pore scale, to scale up to the core scale and compare with the results of experimental observations and analytical equations. In this research we develop a new technique for discretization of continuum space into a hydraulic pore-network (HYPON). With this model the microscopic geometric properties are realistically taken into account. With HYPON we study *diagenesis*, explore non-unique porosity-permeability relations, and gain an insight how the flow field should be handled while simulating gradual temporal changes in porosity. Additionally, the representative size of a 3D pore-network is determined. The longitudinal dispersion coefficient is derived by upscaling the Brownian motion and advective displacements at the pore scale for which a Brownian Particle Tracking Model (BPTM) is developed. With BPTM we reproduce the classical laboratory experiments of single tubes and then extend the model for the pore-network. The dispersion function is explored for different characteristic Peclet number ( $Pe_\ell$ ) regimes and for different pore-scale heterogeneities. A new method is introduced for calculating moments of First-arrival Times Distribution (FTD) and the method is verified by comparing with the moments of Spatial Positions Distribution (SPD). In addition, it is found that the account of molecular diffusion at the intersections of pores is crucial, especially for low  $Pe_\ell$  regimes. In general, we conclude that the presented network model with particle tracking is a robust tool for calculating the macroscopic longitudinal dispersion coefficient. Dispersion is studied also with a Mixing Cell Model (MCM) on HYPON for which the representative size of the network is also determined. Then we study the dispersion relation as a function of pore-size heterogeneity. Further, the results of MCM and BPTM are compared for the same porous medium with the same flow conditions. We consider a non-linearly adsorbing solute and simulate its transport with MCM. We determine the representative size of the pore-network and simulate transport for this size but with different pore-size heterogeneity. Our numerical experiments based on  $301 \times 61 \times 61$  sized network reveal that non-linearly adsorbing transport fronts in homogeneous media approach traveling waves, which indeed is theoretically expected. With the growth of heterogeneity the disagreement between the predicted and numerical concentration distributions becomes noticeable and can be better assessed with the method of moments. The simulations also reveal that the growth rate of second central moments is a quadratic function of the standard deviation of pore-sizes and therefore, it can systematically be estimated. The results of modeling of non-linearly adsorbing solutes transport in physically and chemically coupled but uncorrelated heterogeneous media reveal that with the growth of either physical or chemical heterogeneity the analytical predictions and the numerical results sharply disagree. The effect of chemical heterogeneity on a physically homogeneous medium is more dramatic

than that on the physically heterogeneous medium. With the increase of chemical heterogeneity in a physically homogeneous medium the difference compared with the traveling wave increases. Typical of this behavior is that it is neither according to a traveling wave nor is it perfectly Fickian. Consequently, no analytical solutions are yet available, which implies that it is disputable to describe non-linear transport using a convection-dispersion equation with a non-linear sorption term.

**Additional index words:** diagenesis; dispersion; dispersivity; network modeling; scale; up-scaling; reactive transport; permeability; porosity; Hagen-Poiseuille flow; Freundlich isotherm; Brownian particle tracking; mixing cell model; method of moments.

To my beloved **Mahendra Secondary School** (Kaski) that  
endowed me with the ability to be where I am now.

To the **ones** I dare and care about



# Acknowledgments

It was almost five years ago, I entered the Soil Quality building of the Wageningen University with a single *spirit*, deluded with a crazy passion, “the modeling”, which perhaps emerged during my student-years in Moscow. My *heart* was long seized by my first training on civil engineering that sowed a deep adoration for structures. The second training on hydrology preempted my *mind* leaving a humble fascination for hydrological extremes such as taming wild-rivers, channeling the torrential floods, rescuing dam-breaks and fighting terrific droughts. The theme “upscaling from pore to core” was simply daunting to me. I was neither aware of the importance of this scale, nor had I any experience with a “pore” nor with a “core”. This was the scale which I used only to specify the galvanized coating thickness or denominate the welding seams. Naturally, great worries started to germinate. Especially the two worries about “what can I learn?” and “what and how can I contribute to?” agitated my nerves. Had I been embraced by isolation, I do not know if I would have ever seen the completion of this thesis. Surprisingly, things went otherwise and now the thesis is on your hands. This is the result of enormous affection and special support from so many people who cared about my worries since their inception. I would like to use this opportunity to flashback in time, recall their deeds and express my earnest gratitude to these people.

Allow me to start with expressions of gratitude to my promoters and supervisors Prof. Sjoerd van der Zee and Prof. Toon Leijnse for their scientific as well as social and personal support. Because of their proper guidance I could conduct the research with pleasure and confidence. Just in a couple of meetings, they had remedy for my first worry. They directed me to learn and to enjoy. Each day brought me a new thing which I could attempt to conquer and a new joy to cherish. That was simply great. Sjoerd, I am deeply impressed and amazed by your frankness, and direct but kind dealing, your sharp insight into the subject, the “cut-the-crap”-style correction to my writing and financial arrangement for the completion of this thesis and much more. Apparently, I did not even notice how time lurched and how the years of my PhD-tenure slipped out. And now I have to say good-bye to you. But believe me, it will not be an easy task for me. Toon, I wish I could always be your assistant, just to mine your experience in applied matters and attempt to learn a bit of your diagnostic expertise and your openness. I would never forget how you amazed me by diagnosing my code. You always remained helpful and provided an easy access for communication. I have never seen a scientist who can act so earnestly and selflessly, as you do just to ease others to reach you.

All along I enjoyed working with you two. I should admit that I neither can reflect my admiration and impression about both of you nor do the words convey my gratefulness to you two. For sure, there remains a memory to cherish the retrospect, which stretches back to our meeting on October 22, 1999, when you two interviewed me for the first time. In this regard, my sincere thoughts also go to Henriëtte Keijzer, who, by introducing me to you two, has played a very special role in my scientific career. Henriëtte, without you, perhaps, I would have never thought of doing a PhD. I am proud to have you as more than just a “friend”. I always

remain grateful to you. My sincere appreciation is also due to Perry's moral support.

The other milestones of my scientific career are Prof. Ken Sorbie and Dr. Rink van Dijke from the Heriot-Watt University, UK. These are the people with a sharp sense of physics behind phenomena and with a meticulously pin-pointing reasoning ability. Working with these people means gathering a marvelous memory for future. Ken, without you my desire of understanding "dispersion" would have never come true. I am grateful to your interest, the time you spent in the work we did together and the support you arranged for my visits to Edinburgh. Rink, you showed not only your interest in the area where I wanted to work but also involved Ken who actually led us to the correct direction. In a sense you got "dispersed" and left me a room for "mixing in". This delivered a nice story, I truly cherish and adore. Apart from work, you two and your families did so much in order to make my stay in Edinburgh a memorable experience. Thank you so much.

There is a cause to every cause that delivers effect. The major cause to bring me to Rink's knowledge is Louise Wipfler. Louise, thanks for your kind effort for introducing me to Rink. I also cherish your company during the CiTG courses in Delft, at Gordon and obviously in Wageningen.

I would also like to thank Pore-to-Core project group, especially Prof. Majid Hassanizadeh, Prof. Hans van Duijn, Dr. Ruud Schotting, Dr. Hans Bruining, Dr. Sorin Pop, Ainhua Gorriti and Twan Gielen for helpful discussions. Majid, by introducing me to Prof. Al Valocchi you have paved my Pore-to-Core road to the University of Illinois at Urbana-Champaign. Thank you so much.

I always cherish the memory of sharing the office together with Maria Postma-Blaauw. Maria, you were always understanding and cheerful, sharing all the ups and downs all along our tenure. I enjoyed celebrating your wedding with Jouke who always supported me with his enthusiasm for my work. I thank you both for your cordial friendship and earnest support. Among others, I also thank Rasoul Rahnemaie, Nicole Wrage, Petra van Vliet, Debby Los, Walter Schenkeveld, Gijs Janssen, Ellen Fest, Odair Alberton, Erwin Kalis, Bert van der Stelt, Monika Stachowicz and Franciska de Vries, without whose computers the third chapter would have hardly come into light. My sincere thank goes to Thomas Schröder for his continuous support and for the pains he took to manage the printing of this thesis. I also like to thank Chris van Uffelen and Marc Hoffmann for their assistance in computing matters. I should be privileged to send my appreciation to "upstairs", especially to Bert Janssen, Claire Boddington, Christien Ettema, Ellis Hofland, Erwin Temminghoff, Liping Weng, Meindert Keizer, Ron de Goede, Theo Lexmond, Thom Kuyper, Tjisse Hiemstra and Wim Didden for useful discussions during our lunch or coffee breaks. I would also like to include all my colleagues from the Soil Quality Section, especially from the cellar, for their support and their active role in organizing social events such as sailing trips, section day-outs, social drinks, pan-cake parties, pea-soup evenings, and good-bye choirs. Especially the vocalists and the organizers like Jacqueline Postma, Laura van Schöll, Anke Wolthoorn, Renske Landeweert, Leonard Osté, Jeroen Filius, Bart Verschoor, Piet van Asten, Irena Cardoso, Simône Radersma and Annemieke Marsman will always be remembered. I also thank Johan Vermeulen and his team for integrating me into the PhD students' union (WIMEK) for a whole year.

My genuine thanks also go to the Heriot-Watt University, especially to Prof. Adrian Todd for his warm hospitality and to the fellow PhDs (Andrew, Giovanni, Igor, Jasper, Michał, Renata, Wah Khim and many others) for their friendship and enthusiasm. My cordial appreciation is also due to my Nepali colleagues Bishnu Upreti, Navin Devkota, Narayani Tiwari and many others for reminding me Nepal by organizing social events and occasional gatherings.

I am more than indebted to the management team of the Soil Quality Section without whose support my thesis would have been in a limbo. My last six months were supported by the departmental resources, for which I would especially like to thank Prof. Willem van Riemsdijk, Prof. Lijbert Brussaard, and Winnie van Vark. Winnie, thank you so much for your efforts in creating a good working atmosphere and in providing me good computers, without which I would have never been able to accomplish my computations. I would also like to express my gratitude to the IT-group, especially to Raymond Haagen and Ger van Dalum, who remained throughout helpful for recovering my tempo. There are many others to name and thank, but may be it is wiser not to forget them.

Last but not least I would like to thank Els. Without her love I do not know whether I would have ever thought of coming to Wageningen.

Some research has been carried out, the thesis is being defended and my first worry is alleviated, but over these years my second worry has started gripping me. I am leaving but not alone. I have been armored by the cooperation, knowledge and understanding gained in Wageningen. Thank you all for preparing and tempering me into a researcher in *heart*, in *mind* and in *spirit*.

**Hartstikke bedankt en tot ziens!**

December 21, 2004  
Wageningen, The Netherlands.



acharya\_ram@hotmail.com



# Contents

<b>1</b>	<b>General introduction</b>	<b>1</b>
1.1	Background . . . . .	1
1.2	Research objectives . . . . .	3
1.3	Outline of the thesis . . . . .	3
<b>2</b>	<b>Porosity-permeability properties</b>	<b>6</b>
2.1	Introduction . . . . .	9
2.2	Development of model . . . . .	10
2.3	Numerical experiment and results . . . . .	16
2.4	Discussion and conclusions . . . . .	20
	Appendix: Geometric and hydraulic calculations . . . . .	23
2.A	Geometry of HYPON . . . . .	23
2.B	Hydraulic calculation . . . . .	25
2.C	Geometric characteristics of HYPON model . . . . .	27
<b>3</b>	<b>Quantification of dispersion</b>	<b>31</b>
3.1	Introduction . . . . .	33
3.2	The upscaling problem . . . . .	34
3.3	Model . . . . .	37
3.4	Simulations . . . . .	42
3.5	Summary and conclusions . . . . .	52
<b>4</b>	<b>Comparison of two approaches of pore-network modeling</b>	<b>55</b>
4.1	Introduction . . . . .	55

4.2	Mathematical formulation of problem . . . . .	58
4.3	Models . . . . .	60
4.4	Results . . . . .	65
4.5	Summary and discussion . . . . .	70
<b>5</b>	<b>Transport modeling of nonlinearly adsorbing solutes I</b>	<b>72</b>
5.1	Introduction . . . . .	73
5.2	Mathematical formulation . . . . .	76
5.3	Numerical procedure . . . . .	82
5.4	Simulation cases . . . . .	84
5.5	Results . . . . .	86
5.6	Conclusions . . . . .	91
<b>6</b>	<b>Transport modeling of nonlinearly adsorbing solutes II</b>	<b>93</b>
6.1	Introduction . . . . .	93
6.2	The model . . . . .	95
6.3	Numerical experiments . . . . .	100
6.4	Simulation cases . . . . .	102
6.5	Results . . . . .	103
6.6	Discussion and conclusions . . . . .	109
<b>7</b>	<b>General conclusions</b>	<b>113</b>
7.1	Upscaling permeability . . . . .	113
7.2	Upscaling dispersion . . . . .	113
7.3	Upscaling reactive transport . . . . .	114
	References . . . . .	117
	Summary. . . . .	127
	Samenvatting. . . . .	131
	Biography . . . . .	137

# Chapter 1

## General introduction

### 1.1 Background

The study of flow in porous media is not restricted to a single discipline as this term applies for the movement of fluid in a solid-phase medium, such as movement of groundwater in aquifers, flow in lungs, wind blowing through a canopy and many others. Transport is a term that is commonly used for movement of a secondary parcel that is carried along by the fluid as its companion, and therefore, flow and transport are dealt together. The study of flow and transport in porous media is considered in many fields of science and technology ranging from mathematics [Harding and Kendall 1974] through solid state physics and materials science to applications in geology, hydrology, geophysics, environmental technology, petroleum engineering, medicine, or separation technology [Hoffmann 2003]. The essence of these phenomena is extensively discussed in recent reviews [Sahimi 1993] and therefore, it is not repeated here. Many studies of flow and transport in porous media were motivated by one central question, namely, *how does microscopic geometric structure of the medium influence the effective macroscopic transport parameters* ([http://www.ica1.uni-stuttgart.de/Recent\\_publications/Papers/acp/node3.html](http://www.ica1.uni-stuttgart.de/Recent_publications/Papers/acp/node3.html))? Without a good insight into such influence, sound remediation techniques and good forecasting models cannot be developed. To understand this influence it is necessary to understand flow and transport processes at microscopic (pore) scale and to describe their manifestation at the macroscopic (core) scale and field scale. Furthermore, while modeling at the field scale, it is usually not feasible to take all small scale heterogeneities into account. Without inclusion of the effects of such heterogeneities in field-scale descriptions, neither the techniques nor can their predictions about their reliability gain credibility. Capturing these heterogeneities is the intention of the central question and therefore, the question in this thesis accentuates on three components: (i) defining or conceptualizing *microscopic geometry*, (ii) composing and solving the equations of physics at the microscopic scale and (iii) defining and validating the macroscopic limits, or *upscaling*. According to the International Workshop of Approaches for Upscaling Processes Affecting Transport, June 18, 1999, Albuquerque, NM, USA (<http://www.nwmp.sandia.gov/wlp/upscaling/summary.htm>), *upscaling is the means by which appropriate parameter values, processes and conceptual models are assigned to the larger scale of performance assessment or process-level models*. The study proposed here is motivated by the same central question and aims to capture effects of these heterogeneities at the core scale. Hence, we elaborate these three components further, with emphasis on the scales considered in this thesis.

The first and second components are easy to distinguish from each other and are essentially

important. Geometric properties of porous media are determined exclusively by the complex system of internal boundaries which defines the microstructure. These properties can be calculated from a complete specification of the microstructure alone. Physical flow and transport properties on the other hand require in addition exact or approximate equations of motion. Often this involves steady or unsteady state transport of physical quantities such as mass, energy, charge or momentum. The connection of the flow physics between the pore- and the continuum-scale can be understood by *upscaling*, i.e. the third component of the central question. This is equivalent to the derivation of average (or effective/equivalent) flow and transport properties on a larger scale based on physical rules at smaller scales [Whitaker 1969; Hassanizadeh and Gray 1979a; b; Whitaker 1986]. In other words, upscaling focuses on the controlled transition from microscopic to macroscopic length scales or determines the macroscopic limits. Unfortunately, the macroscopic limit, i.e. the ratio of microscopic length scale to macroscopic length scale, differs from process to process. For example, macroscopic limit for permeability may not be the same as for dispersion. In addition, this limit depends on heterogeneity of microscopic geometry, physics or chemistry. Hence, each phenomenon in a particular medium has its own limit. This limit can be seen only through modeling. A very useful tool in this regard is a pore-scale network model, an aggregate of many pores.

Since Fatt [Fatt 1956a; b; c], pore-scale network models have become an elementary tool for combining all three components in one platform. With these models, a considerable work was carried out for several studies such as permeability [Payatakes et al. 1973; Blunt and King 1991], dispersion [Mohanty and Salter 1982; Sorbie and Clifford 1991], wettability, drainage, multiphase-flow dynamics [Celia et al. 1995] and many others [Van Brakel 1975]. However, for obtaining trust-worthy macroscopic parameters, a representative size (or the macroscopic limit) of the pore-network should be known *a priori*. We are aware of few works which were focused on finding the macroscopic limits. For example, for finding a asymptotic value of permeability for a 2D network, Koplik [Koplik 1982] determined the required size. However, a representative size of a 3D pore-network has not yet been determined. A considerable research was carried out for determining the dispersion coefficient with particle tracking [Sahimi et al. 1986; Verlaan 2001]. However, a representative size of a 3D pore-network with a mixing cell model of non-reactive tracer has not yet been carried out. Although some works on reactive transport were carried out through pore-network modeling [Suchomel et al. 1998a; b], the representative size of such a network has not yet been determined. Without knowing this size the conclusions about the macroscopic parameters or processes are poorly based.

There are also some more subtle issues. For example, although *heterogeneity* has been one of the best spoken issues in the study of flow and transport of porous media, no step has been made to evaluate its impact on the macroscopic parameters (such as the degree of spreading of the front of a single phase transport) on the basis of pore-to-core upscaling. Early studies on non-reactive transport showed that heterogeneity plays a role, namely, due to heterogeneity, the distribution of contaminant at the intersections of pores is proportional to the discharges through the intersecting pores [De Josselin de Jong 1958]. Recent studies showed that distribution of contaminants at the intersections of pores generally depends on the diffusion-advection regimes [Sorbie and Clifford 1991; Damion et al. 2000]. However, no upscaling step has been made to evaluate these findings. Likewise, no step has been taken to evaluate the macroscopic equations of non-linearly reactive transport on the basis of pore-to-core scale upscaling. Hence, it is not justified whether the extensions of the convection-dispersion equation with sorption terms are valid for non-linearly reactive solute transport. As the solute sorption obeys non-linear isotherms [Bolt 1982], the understanding of non-linearly reactive solute transport



is crucial. It is established that both physical (geometric) and chemical heterogeneities affect the concentration front-behavior [Dagan 1989]. However, it is not clear when and how these two sources of heterogeneity prevail in determining the fate of the contaminant-plume in porous media. The difficulty in understanding these heterogeneities can be understood from the fact that practically employed experimental methods for observing the pore space geometry often involve observations of macroscopic flow and transport phenomena from which the microscopic geometry is inferred by inversion techniques [Dias and Payatakes 1986]. Generally, such an inferred microscopic geometry is either over-simplified for numerical reasons or is very ambitious in the way they are directly related with experimental measurements, yet almost impossible to solve with currently available hardware, except for supercomputing facilities, in sufficiently large domains. That means a rigorous upscaling step is difficult to undertake. In addition, the interaction of different phases and the values of the relevant physical/chemical parameters are in general based on laboratory experiments. However, the processes in these experiments differ from the solute transport processes in porous media.

## 1.2 Research objectives

This research aims to identify and describe the physical/chemical processes that govern the interaction of reactive solutes with the solid phase at the pore scale and average (*upscale*) these to the core scale. We define the *microscopic geometry* with a pore-unit (or pore) and establish and solve the exact flow and transport equations for each pore-unit. By aggregating these pore-units into a representative pore network, we average (*upscale*) relevant parameters such as permeability, dispersion coefficient and the measure of plume spreading. Additionally, we apply different approaches and assumptions of physical and chemical processes and attempt to understand the behavior of the contamination front both qualitatively and quantitatively.

The major objective of this research is to gain a better understanding of the heterogeneous interactions between reactive solutes and the solid phase at the pore scale, to scale up to the core scale and compare with the results of experimental observations and analytical equations. With this understanding we can evaluate the limitations and sufficiency of the available analytical equations for prediction of transport behavior of reactive solutes.

## 1.3 Outline of the thesis

This study is aimed at describing steady state Newtonian fluid flow and contaminant transport in a rigid porous medium through pore-network modeling. To meet our objective we focus mainly on physical heterogeneity (differently sized pores) and chemical heterogeneity (variedly distributed chemical-affinity of pores). Hence, we focus on realizing a realistic microscopic geometry, applying exact equations of microscopic physics and chemistry and perform rigorous *upscaling*. This thesis contains five major themes and hence, each chapter is an independently-readable article. In Chapter 2, we develop a new approach for the construction of a comparatively realistic HYdraulic POre-Network model (HYPON). According to this technique, the continuum domain is discretized into a network of pore-units with converging-diverging architecture. The morphological characteristics of such a network are compared with those of physically based pore-networks [Øren et al. 1998]. Further, efforts are made to upscale the porosity-permeability relations of this network. Steady-state conditions are imposed on the network and the Kirchhoff problem is solved numerically by using preconditioned conjugate gradients

[Hestenes 1980]. The solution provides an intrinsic permeability of the network. For an asymptotic value of intrinsic permeability a representative size of pore network is deduced by using Monte Carlo technique and this size is verified with the effective medium theory [Woodside and Messmer 1961; Torquato and Hyun 2001]. Additionally, the results are verified also with the Carman-Kozeny theory. With several realizations of porebody sizes we derive permeability for all realistic porosities reported in the literature. The non-unique porosity-permeability relations are explored assuming diagenesis either in the porebodies or in the converging-diverging bonds. This provides insight whether it is necessary to periodically update the pressure field of simulating reactive solute transport, which causes clogging or mineral dissolution.

Chapter 3 and 4 deal with the quantification of local displacements due to Brownian motion caused by molecular diffusion ( $D_m$ ) and advection of non-reactive tracer particles and focus on upscaling such pore-scale displacements to a macroscopic parameter known as longitudinal dispersion coefficient ( $D_L$ ) for the entire network. For this purpose we develop two models: the Brownian Particle Tracking Model (BPTM) [Chandrasekhar 1943; Sahimi et al. 1983b; Sorbie and Clifford 1991; Damion et al. 2000; Acharya et al. 2004b] and the Mixing Cell Model (MCM) [Gunn and Pryce 1969; Appelo and Postma 1993; Sun 1996]. Chapter 3 describes the procedure of BPTM development and extensively elucidates the results from this model. We start with developing BPTM for a Taylor's capillary tube and verify it by reproducing the Taylor's laboratory experiments [Taylor 1953]. Then the model is extended to the network scale. The results obtained from BPTM for the network are compared with the theoretical model of Saffman [Saffman 1959; 1960] and with the experimental data compiled by earlier researchers [Perkins and Johnston 1963; Legatski and Katz 1966; Han et al. 1985]. Different intra-pore velocity profiles are considered. Different types of jump conditions at the intersections of pores and different regimes with respect to characteristic Peclet number ( $Pe_\ell = v\ell/D_m$ , where  $\ell$  denotes lattice constant, *mean pore length*, and  $v$  denotes the intrinsic velocity in the mean flow direction) [Brenner 1980] are considered. Also the impact of physical heterogeneity of the pore sizes on longitudinal dispersion is analyzed numerically. The method of moments is used for processing the BPTM data. The data are generated with two approaches: at designated time intervals the positions of the particles are scanned to obtain a Spatial Positions Distribution (SPD) [Chandrasekhar 1943] or the particles are injected from the inlet of the network and produced at the outlet to obtain a First-arrival Times Distribution (FTD) [Mohanty and Salter 1982; Sahimi et al. 1986]. Also a new method for computing dispersion coefficient from FTD data is introduced and elucidated.

In Chapter 4 we develop a MCM and use it to obtain  $D_L$  for HYPON. The starting point is the determination of the representative size of the pore-network that can produce an asymptotic value of *dispersivity* ( $\alpha_L \sim D_L/v$ ). Then the functional relationship of  $\alpha_L$  and the pore-size heterogeneity is explored. Also, the attention is paid on how these relations respond to the value of the iteration time  $\Delta t$ . Finally, these relations are verified in large pore-networks and thus, asymptotic values of  $\alpha_L$  are ascertained. In the next-step, we verify whether MCM is applicable for quantifying dispersivity. For that purpose five big networks with gradually varying pore-size heterogeneity are considered and the dispersivity with BPTM was computed to compare with MCM results.

The upscaling problem of non-linearly reactive transport is dealt with in Chapters 5 and 6. In Chapter 5 numerical simulations are aimed at whether in physically heterogeneous porous media (differently sized pores) traveling wave behavior develops. For this purpose, the starting point is again the determination of a representative size of pore-network. Then several cases with different pore-size variance are designed and the transport of solutes that obey the Fre-

undlich isotherm is simulated. The network of equal sized pores with homogeneous chemical properties is a special case of interest because in such a network theoretically a traveling wave behavior should develop [Van der Zee 1990; 1991; Bosma and Van der Zee 1992]. This case is also a reference bench mark for other cases. In addition to the direct comparison of numerical and theoretical (analytical) fronts, the agreement of the two is judged with the method of moments (up to fourth order). Finally, the functional relations of the moment growth rates to the pore-size statistics are derived.

Chapter 6 elucidates on non-linearly adsorbing solutes transport in porous media of combined heterogeneities: physical (pore size variance  $\geq 0$ ) as well as chemical (chemical property of each pore different). We examine how the growth rates of second central spatial moments respond to the chemical and physical heterogeneities. Efforts are aimed at understanding the competition of chemical and physical heterogeneities. Attention is given to exploring whether one of the heterogeneity sources prevails in determining the fate of displacement. Chapter 7 summarizes and generalizes the conclusions of these five chapters.



## Chapter 2

# Porosity-permeability properties generated with a new 2-parameter 3D hydraulic pore network model for consolidated and unconsolidated porous media<sup>\*</sup>

### Abstract

A new method is presented to construct a simple and general site bond correlated 3D HYdraulic POre Network model (HYPON) of hydraulic behavior of porous media for a wide range of permeability and porosity. Pore scale microstructure in this model is captured through simple power functions of Beti's influence lines that fix both the location and the size of throat (the narrowest section of bond) by relating the important elements of microstructure such as coordination number, porebody sizes and pore wall curvature. The new element in pore-network architecture is thus, the location of throat, which is important for smooth hydraulic transitions during steady state flow conditions. Despite the reduced number of parameters in comparison with other pore-network models, the morphological characteristics of HYPON compare well to those of the process-based predictive models in literature, and these characteristics are sensitive to the variance of porebody sizes rather than to the used type of the porebody size distributions. Processes such as diagenesis and dissolution are captured implicitly through the pore wall curvature parameter. Different combinations of porosity and permeability relations are obtained if the bond curvature and porebody sizes are varied. These relations reveal that effects of diagenesis and dissolution on the permeability may be ignored as they are secondary to effects on porosity.

**Keywords:** Biconical bond; throat; pore size; pore curvature; effective medium.

---

<sup>\*</sup>by Ram C Acharya, Sjoerd EATM van der Zee and Anton Leijnse, published in *Adv Water Res*, 2004;**27**:707-723.

*List of symbols and notations*

$\beta$ 3D coordination number [-]	$\tilde{\sigma}_{\tilde{R}}$ Standard deviation of porebody sizes [-]
$\chi$ Dimensionless resistance [-]	$\tau$ Tortuosity ( $\geq 1$ )
$\varepsilon$ Connected porosity [-]	$\xi$ Scaled abscissa [-]
$\kappa$ Intrinsic permeability [-]	$\xi_F$ Inlet of the BACON bond [-]
$\nu$ Kinematic viscosity [ $L^2T^{-1}$ ]	$\xi_t$ Throat position [-]
$\rho$ Water density [ $ML^{-3}$ ]	$\xi_G$ Outlet of the BACON bond [-]
$a_s$ Hydraulic shape factor [-]	$\zeta$ 2D coordination number [-]
$a_x$ Geometric shape factor [-]	$r(\xi_t)$ Throat size [-]
$c$ Conductance [-]	$R, \tilde{R}$ Porebody size [L], [-]
$g$ Magnitude of acceleration [ $LT^{-2}$ ]	due to gravity
$h$ Hydraulic head [L]	$Re$ Reynolds number [-]
$\Delta H$ Macroscopic head difference [L]	$s$ Specific surface area [ $L^{-1}$ ]
$K_D$ Darcy permeability [ $LT^{-1}$ ]	$S$ Surface area exposed to fluid phase [ $L^2$ ]
$L_N, \ell$ Network/lattice length [L]	$v$ Macroscopic (pore water) velocity [ $LT^{-1}$ ]
$\ell_b$ BACON bond length [L]	$V$ Volumes [ $L^3$ ] as specified in the text
$N$ Number of units or nodes [-]	$W_b, W_h$ Width and height of the network [L]
$n$ Curvature parameter [-]	$X, x$ Global and local mean flow direction
$q$ Microscopic flow [ $L^3T^{-1}$ ]	$Y$ Axis $\perp$ to the mean flow direction
$Q$ Macroscopic flow [ $L^3T^{-1}$ ]	$Z$ Axis $\perp$ to the mean flow direction
$\langle R \rangle$ Ensemble average of porebody sizes [-]	

*Subscripts*

$BB$ BACON Bond	$N$ Network
$BL$ Left cone of BACON Bond	$PB$ Porebody
$BR$ Right cone of BACON bond	$PU$ Pore unit
$D$ Darcy	$t$ Throat, throat position
$f$ Fluid phase	$X$ Along $X$
$el$ Elementary cube	$Y$ Along $Y$
$i, j$ Index of nodes	$XY$ plane
PDF Probability Density Function	$Z$ Along $Z$

*Acronyms*

BACON Biconical abscissa-Asymmetric CONcentric (bond)	
BD random Beta Distribution	ND random Normal Distribution
CDF Cumulative Distribution Function	PM Porous Medium
CT Computer-aided Tomography	PU Pore Unit
GD random Gamma Distribution	RD random Rayleigh Distribution
HYPON HYdraulic POre Network	REV Representative Elementary Volume
LN random Log Normal distribution	WD random Weibull Distribution
MRI Magnetic Resonance Index	UD random Uniform Distribution

## 2.1 Introduction

Physical properties that are related to fluid-flow and chemical transport such as permeability, dispersivity, and electrical conductivity of a porous medium depend on the texture and structure of the solid phase. One approach to understand and represent these dependencies well at the continuum model scale is to study processes for an ensemble of pores: the pore-network. This way the pore-scale micro-geometry can be related to hydraulic and transport behavior of porous media. Hilfer [Hilfer 2002] calls them geometric models and distinguishes several types: capillary tube and slit models [Muallem 1976; Dullien 1992; Wise 1992], grain models [Stoyan et al. 1995], percolation models [Chatzis and Dullien 1977; Sahimi 1993], fractal models [Katz and Thompson 1986], stochastic reconstruction models [Quiblier 1984], diagenetic models and (pore) network models [Fatt 1956a; b; c]. The growing interest in pore-scale network models is understandable due to the wide range of phenomena that can be studied with these models, such as wettability, multiphase flow dynamics, hysteresis, single-phase or multiphase mass transfer, and dispersion [Sahimi et al. 1986; Gielen et al. 2002; Van Dijke and Sorbie 2002]. Blunt [Blunt 2001] suggested that as the complex pore geometry can be adequately represented, pore-scale models can develop into predictive models [Blunt et al. 2002]. Network theory has been shown to be an accurate tool to study transport, for instance in Fontainebleau Sandstone [David et al. 1990; Øren et al. 1998; Blunt 2001].

After Fatt [Fatt 1956a; b; c], who first provided a capillary 2D network model to study relative permeability of porous media, other simple and complicated (pore) network models have been developed and reviewed [Van Brakel 1975; Dullien 1992; Celia et al. 1995; Hilfer 1996; Reeves and Celia 1996; Blunt 2001; Blunt et al. 2002; Hilfer 2002]. With pore-scale information such as porosity and pore size distribution data, it became possible to develop more realistic network models [Payatakes et al. 1973; Dias and Payatakes 1986]. Porosimetry was used to determine the porosity and pore size distribution of randomly packed beds [Mayer and Stowe 1966; Katz and Thompson 1987]. Additionally, pore networks were based on direct measurements of randomly packed beds [Finney 1970] and on mathematical models of spatial tessellation [Okabe et al. 1992]. For example, using Delaunay tessellation (subdivision of space by non-overlapping tetrahedra, at the vertices of which non-overlapping spheres are placed), Mason [Mason 1971] mathematically generated a random pack of uniform spheres similar to that constructed by Finney [Finney 1968; 1970]. Pore-networks were constructed by capturing the complementary pore-region (i.e. Voronoi tessellation [Okabe et al. 1992]) either implicitly or explicitly through one random distribution related to the porebody sizes, and another related to the bond sizes [Payatakes et al. 1973; Chatzis and Dullien 1977; Koplik 1982; Lernormand et al. 1983; Dias and Payatakes 1986; Jerauld and Salter 1990; Nowicki et al. 1992; Bryant et al. 1993a; Bryant et al. 1993b; Steele and Nieber 1994b; a; Toledo et al. 1994; Reeves and Celia 1996; Rajaram et al. 1997; Mogensen and Stenby 1998; Suchomel et al. 1998a; Dahle and Celia 1999; Held and Celia 2001; Verlaan 2001]. Porebodies represent the large voids and the bonds represent the connecting capillaries of smaller radii of the porous medium that is being modeled. Recently, based on observations with 2D-microtomography (e.g. the magnetic resonance index (MRI) and computer aided tomography (CT)), it became possible to derive pore-networks [David et al. 1990; Øren et al. 1998; Liang et al. 2000; Blunt et al. 2002; Hidajat et al. 2002].

Pore-network models can be either conceptual (e.g. [Reeves and Celia 1996]) or process-based (e.g. [Øren et al. 1998]). Porebodies and bonds of network models may have different shapes. For example, sinusoidal unit cells (“bow-tie” type) in the model of Dias and Payatakes

[Dias and Payatakes 1986] were constructed from randomly sized circular bonds and functionally correlated porebodies. The profile of these unit cells was derived using several constant parameters. The pore-networks of Koplik [Koplik 1982], and Nieber and co-workers [Steele and Nieber 1994b; a] are ensembles of randomly sized spherical porebodies and randomly sized straight tubes, whereas the pore-network of Ioannidis and Chatzis [Ioannidis and Chatzis 1993] has angular porebodies and correlated angular bonds, where the sizes are determined through three aspect ratios. Celia and co-workers [Reeves and Celia 1996; Reeves 1997; Held and Celia 2001] represented their pore-network with a realistic system of spherical porebodies and converging-diverging circular bonds, sizes of which were generated with two different random distribution functions. Bryant et al. [Bryant et al. 1993a] constructed their pore-network of converging-diverging tubes (of circular cross section) that could mimic the Finney's random packing of uniform spheres [Finney 1968; 1970]. They showed that through such a construction the need for empirical parameters of microstructure could be reduced.

Many of the pore-network models were focused on a particular porosity and permeability, such as a uniform sphere-packed bed [Bryant et al. 1993b; Thompson and Fogler 1997] or uniform sand [Payatakes et al. 1973; Reeves and Celia 1996; Held and Celia 2001] and sandstones [Øren et al. 1998]. Though these beds are porous media (not necessarily natural porous media [Mualem 1992; Scheidegger et al. 1993]) and provide insight into processes, more flexibility is needed to cover a wider range of porous media. Hence, the purpose of this study was to develop a conceptual porebody-bond correlated pore-network model that is rather general, flexible, and simple and that can represent microstructures of porous-media with a wide range of porosities and permeabilities. Main objective of this approach is to reduce the number of parameters which are unknown *a priori*, to avoid the irrational hydraulic transitions of the bond, and to eliminate the requirement of two separate distributions for porebodies and bonds. As the name “HYdraulic POre Network model (HYPON)” indicates, the intention of this model is to capture at least hydraulic properties for a broad range of porous media. We analyze predictions made with HYPON to assess its ability to mimic hydraulic properties of porous media.

## 2.2 Development of model

We assume that the soil pore space consists of porebodies and bonds that connect these porebodies [Scheidegger 1960; Payatakes et al. 1973]. The bonds have converging and diverging shapes [Reeves and Celia 1996] with a narrowest section (called the throat) between the transitions (conical cylinders). These conical cylinders are smoothly conjugated with the porebodies that are located at the two ends of the bonds. We require that the construction is as simple as possible, which implies that a pore bond should be constructed with a simple power function in a local (pore) coordinate system. We furthermore require that this function reflects the relation of distances between porebodies and their sizes and thus, produces a simple converging-diverging structure. By assembling these structures, there results a pore-network.

### 2.2.1 Geometric construction

We study a porous medium (PM) in which we distinguish a pore domain and a solid domain. The pore domain is assumed to consist of a discrete pore-network. This network consists of randomly sized porebodies (of size  $R$ ) that are equally spaced in 3D space at a distance equal to the lattice constant ( $\ell$ ). The lattice constant is assumed to be much smaller than the pore-



network size, i.e.  $\ell \ll L_N$ ,  $\ell \ll W_b$ , and  $\ell \ll W_h$ . The symbols  $L_N$ ,  $W_b$ , and  $W_h$  respectively denote the length, width and the height of the pore-network. The porebodies are connected by converging-diverging functionally derived bonds, to be described below. Concept of such a bond is not new but our approach will be shown to differ from previous researchers (e.g. Tsakiroglou and Payatakes [Tsakiroglou and Payatakes 1991], where the effect of correlation of pores was investigated, Celia and coworkers [Reeves and Celia 1996; Reeves 1997; Held and Celia 2001] where quasi-static regimes were investigated). We scale  $R$  by  $\ell$  to obtain dimensionless porebody size ( $\tilde{R}$ ), given by

$$\tilde{R} = \frac{R}{\ell}, 0 < \tilde{R} \leq 0.5, \quad (2.1)$$

where the porebody size  $R$  is not allowed to exceed  $\ell/2$ . We introduce  $x$  as the distance measured from a porebody center towards the adjacent pore. It is convenient to scale  $x$  by  $\ell$  to get  $\xi$  given by

$$\xi = \frac{x}{\ell} \text{ for } 0 \leq x \leq \ell \quad (2.2)$$

and hence,  $\xi$  varies from zero to one. For illustration, two porebodies are shown in Figure 2.1. The figure presents the concept of the new bond used in HYPON that is derived from the analogy of Beti's influence lines, widely used in structural engineering [French 1995]. As shown in Figure 2.1a, the influence lines used in this work are simple power functions that originate from the adjacent porebodies, e.g. from porebody  $i$  and porebody  $j$ . These functions represent the bond walls (as shown in Figure 2.1b) that guide the fluid from one porebody to another in the interval  $\xi_F$  and  $\xi_G$ , which are respectively the inlet and the outlet of the bond. The location on  $\xi$  where these functions intersect we denote with  $\xi_t$  and call the throat location. The subscript  $t$  indicates throat. Hence, the dimensionless bond-size function  $r(\xi)$  along the central axis ( $\xi$ ) of the bond can be given by:

$$r(\xi) = \begin{cases} T_i(1 - \xi)^n & \text{for } \xi_F \leq \xi \leq \xi_t \\ T_j(\xi)^n & \text{for } \xi_t \leq \xi \leq \xi_G. \end{cases} \quad (2.3)$$

In Eq (2.3), the exponent  $n$  is the curvature parameter that determines the longitudinal shape and the size of the bond. Equation (2.3) reveals that the bond-size function  $r(\xi)$  is continuous and at the point E the throat is located. This is a new detail in the pore-network architecture. The first derivative of  $r(\xi)$  [i.e.  $r'(\xi) = dr(\xi)/d\xi$ ] is discontinuous unless  $n$  is zero. Both  $T_i$  and  $T_j$  are the values of  $r(\xi)$  at the corresponding porebody centers and can be calculated by:

$$T_i = \frac{\tilde{R}_i \sin(\pi/\zeta)}{[1 - \tilde{R}_i \cos(\pi/\zeta)]^n}, n \geq 0, \quad (2.4)$$

where  $\zeta$  is the coordination number on the 2D plane, and  $\pi/\zeta$  is the angle BAF, i.e. the angle under the bisector AF for the porebody  $i$ , and the angle GBA under the bisector BG for the porebody  $j$ . By inserting  $\tilde{R}_j$  in Eq (2.4) we obtain the corresponding value of  $T_j$ . For illustration,  $T_i$  and  $T_j$  are shown in the figure. We require that

$$\xi_F = \tilde{R}_i \cos(\pi/\zeta) \quad (2.5)$$

and

$$\xi_G = 1 - \tilde{R}_j \cos(\pi/\zeta) \quad (2.6)$$

The third location  $\xi_t$  is given by:

$$\xi_t = \begin{cases} T_i^{1/n}(T_i^{1/n} + T_j^{1/n})^{-1} & \text{for } n > 0 \\ \tilde{R}_i(\tilde{R}_i + \tilde{R}_j)^{-1} & \text{for } n = 0, \end{cases} \quad (2.7)$$

where  $\xi_t$  can be as small as  $\tilde{R}_i$  and as large as  $(1-\tilde{R}_j)$ , i.e.  $\tilde{R}_i \leq \xi_t \leq (1-\tilde{R}_j)$ . In the case, where  $n$  is zero, the location  $\xi_t$  is fixed at a distance proportional to the porebody sizes  $\tilde{R}_i$  and  $\tilde{R}_j$ . Hence, by using two simple power functions in the appropriate intervals a smooth Biconical asymmetric CONcentric (BACON) bond can be obtained which is schematically shown in Figure 2.1b. The revolution of  $r(\xi)$  obtained from Eq (2.3) for the interval  $\xi_F$  and  $\xi_t$  yields a conical cylinder. Similarly, the revolution of  $r(\xi)$  obtained from Eq (2.3) for the interval  $\xi_t$  and  $\xi_G$  yields another conical cylinder. The union of these two conical cylinders gives a BACON bond of length  $\ell_b$ . The dimensionless bond length ( $\ell_b/\ell$ ) equals to the distance between  $\xi_F$  and  $\xi_G$ . The longitudinal shape of these cylinders depends on the curvature parameter  $n$ , as depending on  $n$ , the BACON bond represents an assemblage of two dissimilar hyperbolic, parabolic, or straight conical cylinders, which share a common plane (the throat) at section E. The bond is smoothly united with the porebodies. A 3D impression of a typical BACON bond is shown in Figure 2.2a. To provide a 3D impression of the new model, an elementary lattice with the circular BACON bonds and spherical porebodies is shown in Figure 2.2b. From the figure it is seen that the union of elements is smooth and rational. The size of the narrowest section of the bond  $r(\xi_t)$  is determined by

$$r(\xi_t) = T_i T_j (T_i^{1/n} + T_j^{1/n})^{-n}, n > 0. \quad (2.8)$$

Equation (2.8) cannot be used for the case with  $n$  equal to zero and unequal sized porebodies, because values of  $r(\xi_t)$  for the left side and the right side are different. Although a porebody may be connected to a number of adjacent ones (literature on pore-networks [Van Brakel 1975; Yanuka et al. 1986; Jerauld and Salter 1990; Bakke and Øren 1996] suggests coordination numbers ranging from 3 to 10), in this paper we assume the 2D-coordination number ( $\zeta$ ) to be four and the total coordination number ( $\beta$ ) to be six.

The reasonable values of the curvature parameter ( $n$ ) can be expected to fall between  $n_R$  and  $n_{thres}$ . The lower bound  $n_R$  can be determined based on the minimum and maximum porebody sizes, whereas  $n_{thres}$  may be estimated on the basis of the information on threshold porosity [Du Plessis 1999]. It is possible to assign a specific  $n$ -value to each bond (based on the porebody sizes the bond connects) or to assign a specific  $n$ -value to each specific principle direction. However, in this paper we use a single  $n$ -value for the entire network. The equation for computing  $n_R$  is derived in Appendix 2.A. For a network of equal sized porebodies  $n$  can be as small as zero (which gives straight tubes). The higher values of  $n$  produce squeezed bonds.

We consider a pore unit (PU) with a coordination number  $\beta$  equal to six. Hence, the pore unit is a union of six conical cylinders and one porebody at the center. For illustration, a pore unit is shown in Figure 2.3 with the BACON bonds emanating from a pore unit towards the adjacent ones (Figure 2.3a). In Figure 2.3b and Figure 2.3c pore units with different cross-section shapes of bond and porebody are shown. The lengths of cones that constitute bonds differ because they depend on the size of the porebodies they are connected with.

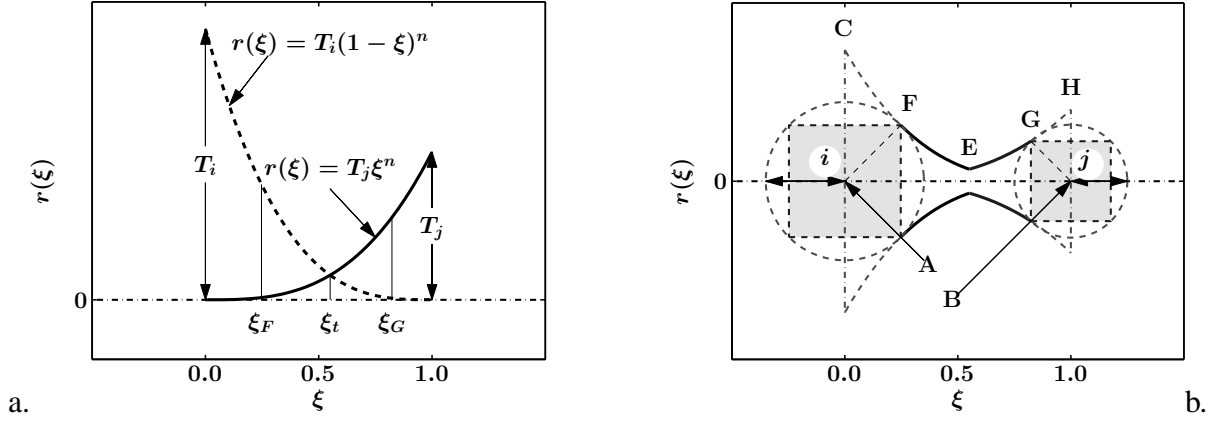


Figure 2.1: The construction of the BACON bond. a. The influence lines as a function of  $\xi$ . The locations of the inlet ( $\xi_F$ ), throat ( $\xi_t$ ), and the outlet ( $\xi_G$ ) are indicated. b. The outline of the bond connecting two pore bodies: porebody  $i$  with radius  $\tilde{R}_i$  and the center  $A$  at  $\xi = 0$ , and porebody  $j$  with radius  $\tilde{R}_j$  and the center  $B$  at  $\xi = 1$ . The bond walls (e.g. FEG) are thick solid lines and bisectors (AF and BG) are thin dashed lines.

If these pore units are assembled in a 3D space a pore-network arises. A typical pore-network is shown in Figure 2.4a. Although porous media usually consist of a mixture of shapes, we build our network with only one pure set of porebodies (either cubes or spheres) and bonds (of either circular or square cross section) such that the equations of flow and transport remain simple to handle. Of the different cross-section shapes of bonds shown in Figure 2.4b, all other cross sections of the same bond size can be inscribed within the square one. This indicates that with the square shape the largest porosities can be obtained [Torquato and Hyun 2001]. The geometric calculations for the microscopic as well as the macroscopic scales are included in Appendix 2.A.

### 2.2.2 Fundamental flow equations at pore-scale

In this section, the flow equations at the pore level (microscopic scale) are formulated [Bear and Bachmat 1990]. The pore-level flow equations are the Navier-Stokes equations for saturated steady state Newtonian viscous flow, which are also known as the Hagen-Poiseuille flow equations. Bear and Bachmat [Bear and Bachmat 1990] suggested that for the validity of these equations in a non-deformable porous medium, the Reynolds number should be less than 10, i.e. flow is laminar. All pore units are water filled.

The (average) flow rates in each bond of the network are calculated from the nodal pressures, which are induced by a (global) pressure difference between inlet and outlet faces. For convenience we use hydraulic heads instead of pressure, where pressure equals to the product of hydraulic head ( $h$ ), water density ( $\rho$ ) and the magnitude of acceleration due to gravity ( $g$ ).

Assuming that flow occurs from porebody  $i$  to porebody  $j$ , the discharge ( $q_{i,j}$ ) through the BACON bond in the local coordinate system follows from the Hagen-Poiseuille's equation [Shames 1992],

$$q_{i,j} = \frac{g}{\nu} \ell^3 c_{i,j} (h_i - h_j), \quad (2.9)$$

where  $q_{i,j}$  is the volumetric bond discharge of fluid [ $L^3T^{-1}$ ] from node  $i$  to  $j$ ,  $h_i$  and  $h_j$  are

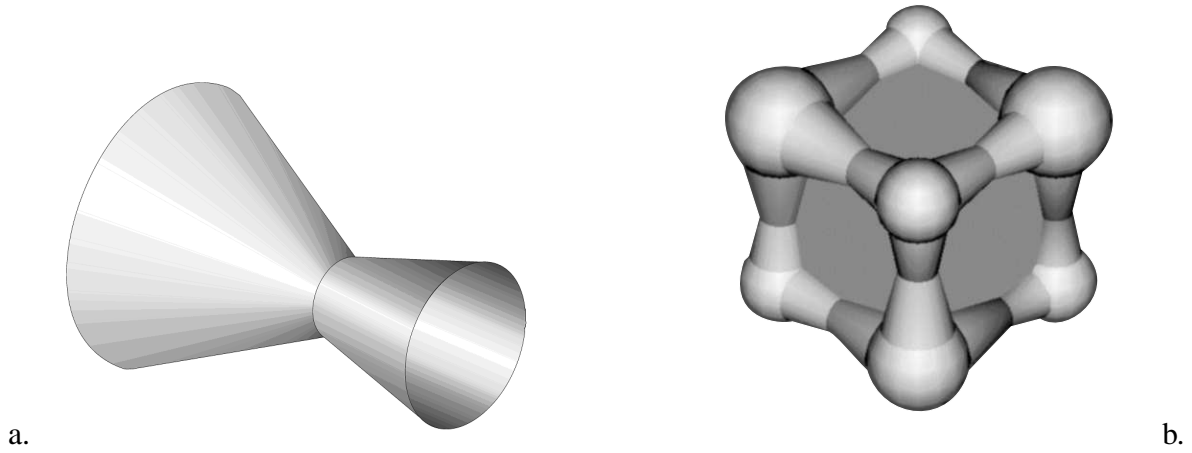


Figure 2.2: A 3D view of a typical shape of a BACON bond and an elementary lattice; a. Differently sized porebodies produce bond of differing lengths, causing different lengths of the left and the right side conical cylinders of the bond, b. The porebodies and the BACON bonds of an elementary lattice are shown. The inside of the lattice is filled with solid phase (that does not necessarily indicate to a grain).

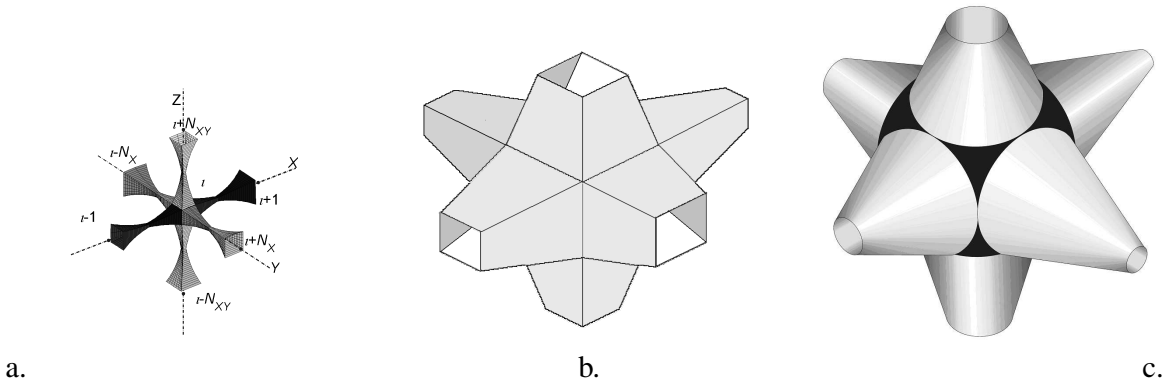


Figure 2.3: Illustration of a pore unit with 3D-coordination number  $\beta$  equal to six. a. A porebody with connecting BACON bonds (full length shown), b. A cube shaped porebody with bonds (of square shaped cross section) cutoff at throats, and c. A spherical porebody with circular bonds cutoff at throats, i.e. only the converging parts of the BACON bond with porebody are shown.  $N_X$  and  $N_{XY}$  are the number of nodes along the mean flow axis and in the  $XY$  plane respectively.

the hydraulic heads at the corresponding pore centers, and  $\nu$  is the kinematic viscosity of fluid [ $L^2T^{-1}$ ]. In Eq (2.9),  $c_{i,j}$  is the dimensionless conductance of the BACON bond, derivation of which is given in Appendix 2.B. For each pore unit we have also continuity condition, leading to a system of algebraic equations as discussed in literature [Suchomel et al. 1998a]. Thus,

$$\sum_j^{\beta} q_{i,j} = 0, j = 1, 2, \dots, \beta, \quad (2.10)$$

where  $j$  is the index of the porebodies that are connected to porebody  $i$ . Equation (2.10) is solved for the hydraulic heads at the pore-unit centers which are then used to compute the

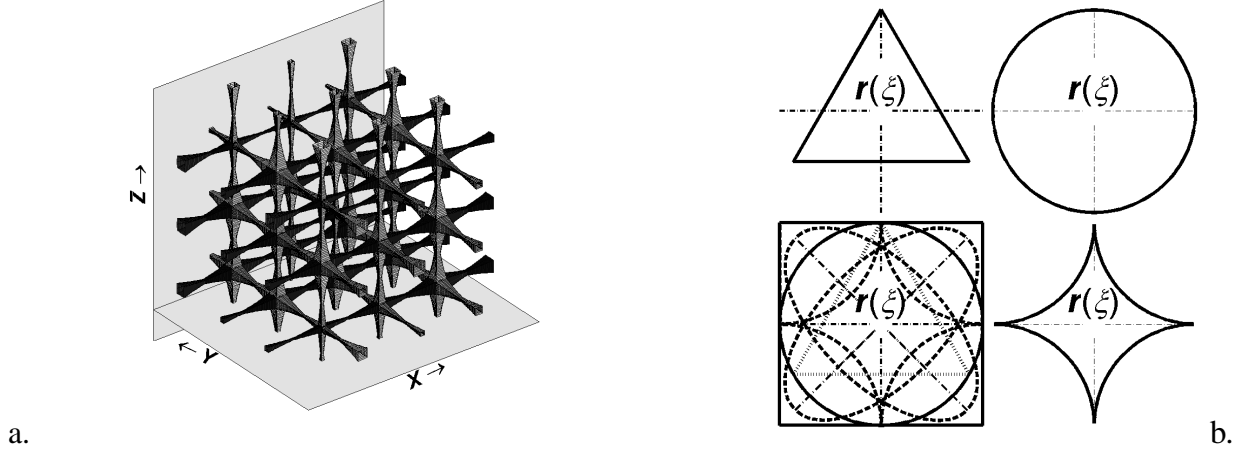


Figure 2.4: Schematic representation of a cubic lattice of HYPON. a. A 3D view, where  $X$ ,  $Y$  and  $Z$  are the global coordinates. b. Cross-section shapes of the BACON bond at position  $\xi$  (in the interval  $\xi_F \leq \xi \leq \xi_G$ ) and the characteristic size  $r(\xi)$ .

discharges from (or into) the pore units.

### 2.2.3 Macroscopic flow equations for the pore-network

On the macroscopic scale the permeability of the network is of interest, which can be derived numerically as well as analytically, for which many theories exist [Scheidegger 1960; Bear 1972]. We consider within three theories, i.e. Darcy's equation, the effective medium approximation and the Carman-Kozeny equation. The outermost lateral boundaries of the network are no-flow boundaries. The macroscopic head difference ( $\Delta H$ ) between inlet and outlet faces of the network would drive a constant discharge ( $Q$ ) through the network. From  $Q$  and the fluid phase volume of the network ( $V_f$ ), the macroscopic pore water velocity ( $v$ ) in the network can be computed with the Dupuit-Forcheimer equation,

$$v = \frac{QL_N}{V_f}, \quad (2.11)$$

where  $L_N$  is the distance between the inlet and outlet faces of the network (along  $X$  axis). The subscript  $F$  indicates fluid phase.  $Q$  is computed numerically by summing up the discharges from the bonds at the outlet face of the network. Because Darcy velocity ( $v_D$ ) is equal to the product of porosity ( $\varepsilon$ ) and  $v$ , the Darcy permeability ( $K_D$ ) [ $LT^{-1}$ ] can be computed with

$$K_D = \frac{\varepsilon v L_N}{\Delta H}, \quad (2.12)$$

where  $\Delta H > 0$ . The porosity is calculated as a ratio of  $V_f$  to the total volume ( $V = L_N \times W_b \times W_h$ ) occupied by the network. Calculations for  $\varepsilon$  are shown in Appendix 2.A. Scaling  $K_D$  by  $\ell^2$  and multiplying with  $\nu/g$  yields the dimensionless intrinsic permeability ( $\kappa$ ), i.e.

$$\kappa = \frac{\nu K_D}{g \ell^2}, \quad (2.13)$$

which is also called the effective (bond) conductance.

With other theories such as effective medium approximation [Brinkman 1947; Choy 1999] and Carman-Kozeny equation [Scheidegger 1960; Zhuang et al. 2000], intrinsic permeability

can be calculated without solving the pressure field. For example, the general effective medium approximation equation for calculating  $\kappa$  (by taking the ensemble average equal to zero), i.e.

$$\left\langle \frac{\kappa - c_{i,j}}{\kappa + \omega c_{i,j}} \right\rangle = 0, \quad (2.14)$$

contains only the individual conductance term ( $c_{i,j}$ ) and the coordination number information ( $\omega$ ). The dimensionless permeability  $\kappa$  (also called effective conductance) is optimized through averaging the differences between  $\kappa$  and the individual conductance of bonds ( $c_{i,j}$ ) [Brinkman 1947; Koplik 1982] or computed explicitly by using rigorous bounds recommended by Torquato and coworkers [Hashin 1983; Rubinstein and Torquato 1989; Torquato and Hyun 2001].

The third approach to calculate  $\kappa$  is the Carman-Kozeny equation. The dimensionless intrinsic permeability ( $\kappa$ ) in this case depends on the specific surface area ( $s$ ) [ $\text{L}^{-1}$ ], the porosity, and tortuosity ( $\tau \geq 1$ ):

$$\kappa = \frac{\varepsilon^3}{\tau^2 s^2 (1 - \varepsilon)^2 \ell^2}. \quad (2.15)$$

The specific surface area is defined as the ratio of total interfacial area of the fluid phase to the total volume of the solid phase [Scheidegger 1960]. Calculations for  $s$  in a pore-network are shown in Appendix 2.A. For the tortuosity, we assumed that  $\tau^2 = 5$  [Van Brakel 1975]. The lattice constant ( $\ell$ ) is used to make the intrinsic permeability dimensionless.

## 2.3 Numerical experiment and results

Numerical experiments were aimed at four aspects: 1. analysis of the morphological characteristics of the architecture made with HYPON in comparison to process-based models; 2. simulation of macroscopic porosity and permeability relations for porous media through Hagen-Poiseuille and Darcy equations; and 3. comparison (wherever applicable) of obtained permeabilities with predictions by other approaches (e.g. Carman-Kozeny equation).

### 2.3.1 Geometric characteristics of HYPON model

The geometric characteristics produced by HYPON were results of a pore-network of 223109 porebodies in a  $101 \times 47 \times 47$  cubic network. Networks were constructed from a single value of curvature parameter ( $n = 1$ ), cube shaped porebodies and bonds of square shaped cross-section. Seven types of random distributions of porebody sizes were considered, which are commonly used in the literature [Reeves and Celia 1996; Keller 1997; Lindquist and Venkatarangan 1999; Or and Tuller 1999; Sok et al. 2002]. An overview of statistics of all pore-networks is presented in Table 2.1. For comparison, we have looked at different aspects such as porebody to throat size  $r(\xi_t)$  relation, bond length ( $\ell_b/\ell$ ) to  $r(\xi_t)$  relation, probability density functions (PDFs) of porebodies,  $r(\xi_t)$  and ( $\ell_b/\ell$ ) due to different types of porebody-size distributions, cumulative density functions (CDFs) of throat sizes  $r(\xi_t)$ , microscopic heterogeneity (on the basis of discharges) and distributions of microporosity. In detail the computed data are shown in Appendix 2.C.

We observe that the variation of throat sizes depends on the variance of porebody sizes. For example, a narrow distribution of porebody sizes yields a narrow distribution of  $r(\xi_t)$ . Throat

Table 2.1: Statistics and the type of distributions of porebody sizes for pore-networks

Type of distributions	Ensemble mean ( $\langle \tilde{R} \rangle$ )	Standard deviation ( $\tilde{\sigma}_{\tilde{R}}$ )	Minimum size ( $\tilde{R}_{min}$ )	Maximum size ( $\tilde{R}_{max}$ )
Random uniform (UD)	0.268	0.134	0.035	0.500
Random Beta (BD)	0.240	0.120	0.010	0.500
Random Gamma (GD)	0.249	0.098	0.035	0.500
Random lognormal (LN)	0.248	0.093	0.037	0.500
Random normal (ND)	0.268	0.103	0.035	0.500
Random Rayleigh (RD)	0.232	0.111	0.108	0.500
Random Weibull (WD)	0.216	0.110	0.035	0.500

$\langle \tilde{R} \rangle$  and  $\tilde{\sigma}_{\tilde{R}}$  are respectively the ensemble mean and standard deviation of dimensionless porebody sizes.

sizes were found inversely related to the bond lengths ( $\ell_b/\ell$ ), the variation of which depends on the variance of porebody sizes and the magnitude of the curvature parameter ( $n$ ). The type of porebody size distributions has some influence on bond length PDFs and on the variance of the PDFs of the throat sizes. From the graphs of the CDFs of throat sizes computed with HYPON, it appears that the shape of the throat size distribution is quite insensitive to the used type of porebody size distributions. Almost all CDFs of  $r(\xi_t)$  can be fitted well with a Gamma-type distribution but in some cases, e.g. for random Rayleigh distribution (RD), random Beta distribution (BD) and random uniform distribution (UD), an equally good fitting is found with the Rayleigh distribution (not shown). Based on empirical studies, Keller [Keller 1997], Tuller et al. [Tuller et al. 1999] and Yanuka et al. [Yanuka et al. 1986] reported a lognormal, a Gamma or a Rayleigh distribution of throat sizes. Additionally, we analyzed the distributions of micro-porosity, i.e. the porosity within an elementary lattice, and also we looked at the distributions of transversal discharges in a cubic network (which may serve as a measure of microscopic heterogeneity). In all these experiments, we found that geometrical relations are sensitive to the variance of the porebody sizes rather than to the used type of porebody size distributions. Hence, we can conclude that a random uniform distribution can be used in HYPON, which has the advantage of simplicity and computational efficiency. However, for modeling a particular porous medium, a realistic porebody size distribution as obtained from micro-tomography may be more appropriate.

### 2.3.2 The scaled-up porosity-permeability relation

The first simulations were focused on finding a consistent size of the network, i.e. the representative elementary volume (REV). The consistent size is the threshold size of the pore-network for which the permeability (or effective conductance) is asymptotic [Koplik 1982], i.e. macroscopic characteristics of pore-network do not change considerably due to translation of positions [Bear 1972; Hilfer 2002]. Such a size can be found with Monte Carlo simulations for a prescribed pressure field. If permeabilities are equal for two different realizations of equal-sized networks with the same mean and variance of porebody sizes, the hypothesis of consistency is accepted. Since the consistent size depends on the variance of the porebody sizes as a smaller variance leads to a smaller consistent size, we considered ensembles of porebodies

with the highest possible variance (UD of Table 2.1) to assess consistency. This approach indicated that the size of a consistent network is  $25 \times 15 \times 15$ . Alternatively, the effective medium approximation approach with unknown pressure field requires that the upper bound of the effective site-conductance given by Woodside and Messmer [Woodside and Messmer 1961] or the symmetric rigorous bounds given by Torquato and Hyun [Torquato and Hyun 2001] become asymptotic. We applied the upper bound of effective site-conductance according to Woodside and Messmer [Woodside and Messmer 1961] and obtained  $20 \times 20 \times 20$  pore-network as the consistent size (see Figure 2.5), which is more conservative compared to  $25 \times 15 \times 15$  sized network.

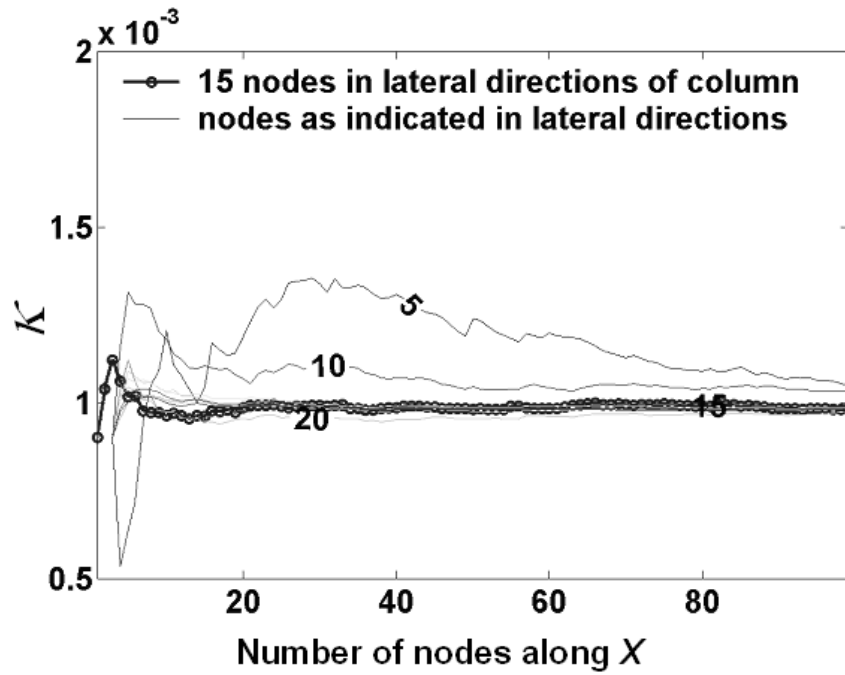


Figure 2.5: The upper bound of the dimensionless effective site-conductance ( $\kappa$ ) according to Woodside and Messmer [67] as a function of node number ( $N_X = 3, \dots, 101$ ) in the mean direction of flow ( $X$ ) in a network with UD (Table 2.1). The numbers at curves indicate maximum lateral size of pore-network in  $Y$  and  $Z$  directions in terms of node numbers.

We considered macroscopic porosity and Darcy permeability relations obtained for networks consisting of  $33 \times 23 \times 23$  pores, which size is sufficiently larger than the consistent size. For calculating the macroscopic porosities and permeabilities, a random uniform distribution of porebodies, with cube shaped porebodies and square shaped bonds were used, because that combination covers the largest range of porosity and permeability. We generated 99 cubic pore-networks, with a wide range ( $0.1 \leq \bar{R} \leq 0.50$ ) of mean porebody sizes. Either the minimum porebody size or the maximum porebody size was varied with increments of 0.01 for the random uniform distribution. Each network was solved for seven different values of curvature parameter (i.e.  $n = 0, 1, 2, 3, 4, 5$  and 6), which leads to a total of 693 networks. For  $n$  equal to zero, HYPON yields a classical 3D capillary network with straight tubes. Hence, for this  $n$ -value, a single porebody size was used because otherwise the bond size function  $r(\xi)$  has abrupt jump at the throat location ( $\xi_t$ ). We expect that such abruptly changing  $r(\xi)$  is not a physically realistic transition and also would profoundly complicate the hydraulic calculations.



The system of Hagen-Poiseuille flow equations for the entire network was solved numerically for each of the 693 pore-networks with the pre-conditioned conjugate gradient [Hestenes 1980]. The imposed head difference between inlet and outlet faces ( $\Delta H$ ) was fixed at 0.07 m. The procedure of computing Darcy scale porosity-permeability relations is as follows. We choose a minimum porebody size and a maximum porebody size and let the simulator produce a random uniform distribution, from which the network is constructed. This pore-network is solved for each of the six different values of  $n > 0$ . Then, we generate a network with equal sized porebodies with the same size as the mean size used for other values of  $n$  and solve the flow field for  $n$  equal to zero. This procedure is continued by fixing  $\tilde{R}_{min}$  at 0.01 and incrementing  $\tilde{R}_{max}$  (with an increment of 0.01) from 0.01 to 0.50. Then we fix  $\tilde{R}_{max}$  at 0.50 and increment  $\tilde{R}_{min}$  (with an interval of 0.01) from 0.01 to 0.50. Thus for the entire range of porebody sizes, porosity and permeability pairs are obtained that are plotted to produce isolines of curvatures ( $n$ ) and the isolines of mean porebody sizes. In Figure 2.6, the dimensionless intrinsic permeabilities ( $\kappa$ ) of all 693 pore-networks obtained with the Darcy equation (2.13) are shown as a function of porosities ( $\varepsilon$ ). Shown are the isolines of mean pore sizes, which are the lines that connect the porosity and permeability combinations of all pore-networks that have the same mean porebody size. Also, we show the isolines of curvature, which are the lines that connect the porosity and permeability combinations of all networks that have the same value of the curvature parameter ( $n$ ). A thick solid line, labeled with “0” is the special case where the pore-network is made of equal sized porebodies and bonds, and  $n$  equals to zero. This is the envelope curve, which appeared in good agreement with the Carman-Kozeny relation (2.15) and is also shown separately in Figure 2.7.

Figure 2.6 reveals a non-unique porosity-permeability relationship that is bounded at the top and at the left by an envelope curve (which is also an isoline of curvature), and at the right, by an isoline of mean pore sizes ( $\langle \tilde{R} \rangle = 0.5$ ). Moving along an isoline of pore sizes to larger  $n$ -values mimics consolidation or diagenesis processes in time. Consolidated media are more interesting than unconsolidated ones because of their non-unique relation between porosity and permeability. A number of such relations have been reported [Happel and Brenner 1965; Dullien 1992], and the new techniques are revealing the explanations behind such observed facts. Recent advances in micro-tomography (e.g. [Lindquist and Venkatarangan 1999]) show that neither are the particles spherical nor are the pore spaces of definite shape, size or orientation [Scheidegger et al. 1993]. Over time, both the pore spaces and particles change. For example, a loosely packed gravel may turn into completely cemented conglomerate [Press and Siever 1986], water filters used at our homes and sand beds in water treatment plants become clogged [Ives 1975]. This indicates that the porosity-permeability relation is dynamic in time and space. To mimic this, porebody size was kept unchanged but bonds were squeezed by changing  $n$ . The effect is that the capillary space becomes reduced due to either deposition of fine particles [Tien and Payatakes 1979], and colloids [Van de Weerd et al. 1998], adherence of biological substances [Keijzer et al. 1999], cementation [Panda and Lake 1994], or lining and filling [Panda and Lake 1994; Øren et al. 1998]. On the other hand, if porebodies are gradually filled such that  $n$  does not change (i.e. moving along the isoline of curvature) the change in porosity is relatively faster than in the previous case, whereas the change in permeability is slower than in the first case.

We observe that the rate of change of the curvature parameter (moving along an isoline of pore size) has a larger effect on the permeability than a change of the porebody size (i.e. moving along an isoline of curvature parameter). The trend of the isolines of mean pore sizes shows that due to the large  $n$  (i.e. squeezing of pore bonds of porous media), the permeability

will be reduced, but the porous medium may still possess high porosity. The porosity, where such a situation occurs (i.e. no occurrence of seepage), is known as the threshold-porosity. Looking at the isolines of curvatures, we can conclude that a gradual filling of porebodies only slowly decreases permeability. The practical implication is that, by ignoring the changes in permeability due to diagenesis in the porebodies, errors may not be dramatic. This assessment simplifies the numerical effort for modeling such processes profoundly, as we need not solve the flow field after each time interval to account for the new micro-structural conditions.

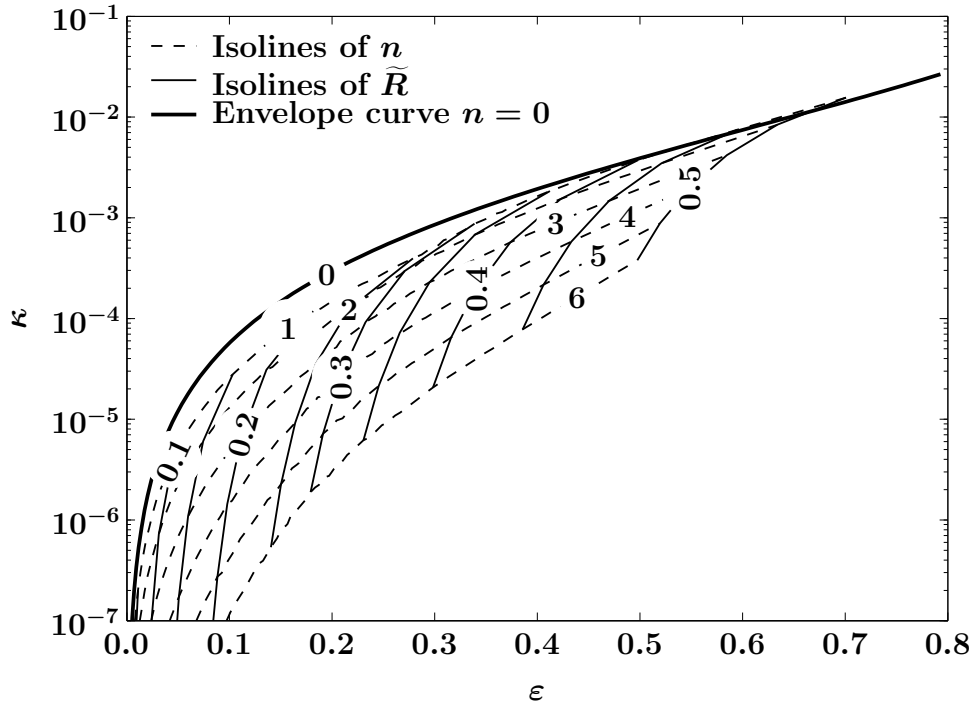


Figure 2.6: Dimensionless intrinsic permeability as a function of porosity. The isolines of mean pore body sizes are plotted with the thin solid lines and labeled with numbers 0.1 to 0.5 and the isolines of curvatures are plotted with the dashed lines and labeled with numbers 1 to 6. The thick solid line with label “0” is the envelope curve as well as curvature isocline.

In Figure 2.7 the dimensionless intrinsic permeabilities ( $\kappa$ ) predicted by the Carman-Kozeny equation (2.15) and the Darcy equation (2.13) are plotted as a function of porosity, for the case of equal porebody sizes and  $n$  equal to zero. The evident agreement of the two indicates that the Carman-Kozeny approximation and the rigorous numerical solution of Navier-Stokes equation agree for this combination. For very high porosities (say higher than 0.5) the Carman-Kozeny prediction only slightly deviates as is anticipated [Scheidegger 1960; Happel and Brenner 1965]. Such a good agreement is not expected if porebody sizes vary and  $n$  is unequal to zero.

## 2.4 Discussion and conclusions

HYPON is a simple model with few parameters that idealizes porous space with two different components: randomly distributed porebody sizes and the analytically derived BACON bonds.

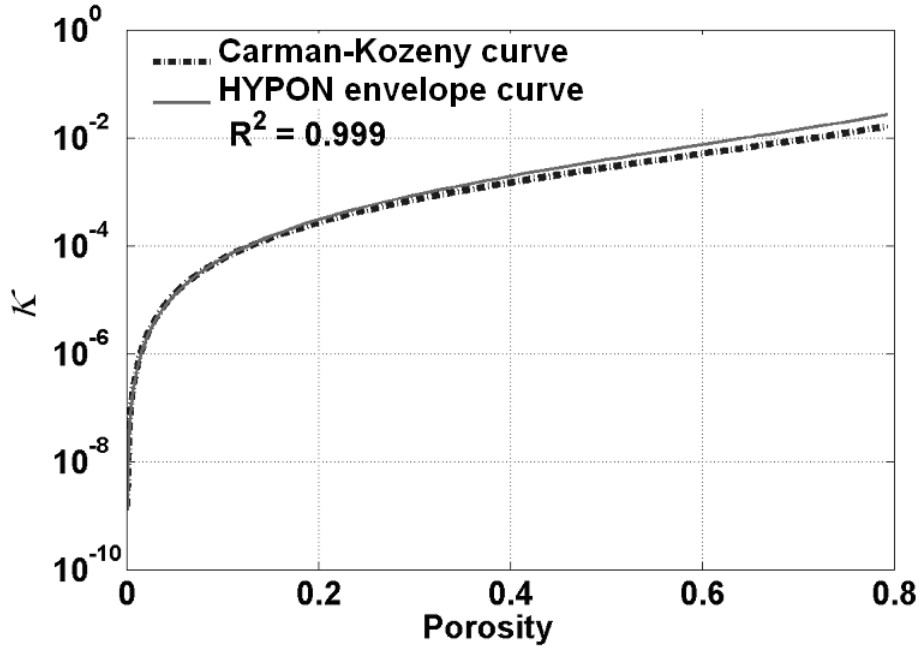


Figure 2.7: Comparison of the Carman-Kozeny predictions with the HYPON envelope curve produced by the exact solution of Hagen-Poiseuille and Darcy equations. Plotted are the dimensionless intrinsic permeabilities ( $\kappa$ ) as a function of porosity ( $\varepsilon$ ) for the case with  $n = 0$  and equal sized porebodies.

The sizes of bond throats are dictated by the adjacent porebody sizes ( $R$ ) and a curvature parameter ( $n$ ). Instead of two separate distributions for porebody and throat sizes, only a distribution of porebody sizes and a curvature parameter ( $n$ ) are needed.

The model is flexible in a hydraulic sense because it captures a broad and realistic range of porosities and permeabilities. HYPON can be adjusted (if required) to match the porosity and permeability characteristics [Mogensen and Stenby 1998] of a particular porous medium, if an isoline of curvature and an isoline of mean pore sizes are known. The pore-to-pore spacing ( $\ell$ ), which serves as the characteristic length, should be known *a priori*. Unfortunately, for a real porous medium, this pore-to-pore spacing is not easy to determine. Whitaker [Whitaker 1972] suggested the characteristic length to be six times larger than the hydraulic radius (which was recommended for uniform spheres). However, Roychoudhary [Roychoudhury 2001] indicated that it should exceed six hydraulic radii, whereas Bryant et al. [Bryant et al. 1993a] suggested that it should be larger than one grain size. An approach for inferring the characteristic length can be to combine micro-tomography, mercury-porosimetry and permeability measurements with simulations using a model such as HYPON. Such combination would be aimed at quantifying quite different effects e.g. throat size distribution, porosity and permeability, and making them all compatible with Figure 2.6 for different choices of  $\ell$ .

HYPON clearly demonstrates the existence of non-unique porosity-permeability relations [Scheidegger 1960] and their bounds. It extends the understanding of existing models. For example, intrinsic permeabilities of HYPON can be estimated by the effective medium approximation of Torquato and Hyun [Torquato and Hyun 2001], whereas the upper bound (envelope

curve) of the HYPON generated permeability-porosity relation agrees with the Carman-Kozeny prediction for the case with equal sized pores and  $n$  equal to zero. This is an indication of the validity of both the Carman-Kozeny and the Navier-Stokes equations for this simplified situation. For other combinations such as unequal porebody sizes and for  $n$  unequal to zero, solutions of the Carman-Kozeny equation may differ from HYPON simulations because it is a simplified relation. Additionally, the relation depends on tortuosity, which is a poorly-understood parameter [Scheidegger et al. 1993].

This paper showed that a simple model can mimic complex pore geometry, while maintaining considerable agreement between morphological characteristics derived with HYPON modeling and those from process-based models. The new BACON bond of HYPON eliminates the conjugation problems [Dias and Payatakes 1986; Bryant et al. 1993a; Ioannidis et al. 1993; Thompson and Fogler 1997], problems related to irrational hydraulic transitions [Nowicki et al. 1992; Toledo et al. 1994; Reeves and Celia 1996], and reduces the number of parameters [Dias and Payatakes 1986; Ioannidis et al. 1993]. Furthermore, literature showed that converging-diverging pores are helpful to account for static interface positions during quasi-static regimes [Nowicki et al. 1992; Toledo et al. 1994; Reeves and Celia 1996; Held and Celia 2001], and are good for smooth hydraulic transitions during steady-state conditions [Happel and Brenner 1965]. The simulations with HYPON showed that properties such as porosity and permeability are more sensitive to the variance of porebody sizes than to the used type of porebody size distributions, as shown by the sensitivity of shape of throat-size and bond-length distributions. Also, the effect of changing curvature appeared to be larger than the effect of changing porebody size. The practical implication of this is that the volumetric changes in porebody sizes have less effect on permeability than the change in the bond sizes. In such a case, by ignoring the permeability dynamics during transport computations error would not be dramatic. Thus, this simplifies the numerical efforts as the frequent updating of pressure field is computationally costly. In this paper we did not vary the coordination number or considered longer-range correlations of porebody sizes. We anticipate that changing these properties affects the magnitude of some effects that were illustrated, but does not influence the primary results, provided that the requirements for ergodic conditions are met.

For an improved understanding of processes such as single-phase or multiphase transport, and dispersion, HYPON may serve as a general scenario simulator. However, for those purposes HYPON should be adjusted to account for more fluid phases and particle transport. With the present paper, we showed that HYPON simulation results are hydraulically compatible with the literature. This observation supports that it is appropriate to extend HYPON to address multiphase and chemical transport problems.

## Acknowledgements

This study is performed under the research program “Upscaling Flow and Transport Processes in Porous Media: From Pore to Core” funded by the Dutch NWO/ALW project no. 809.62.010. The paper has benefited profoundly from the comments of the peer reviewers and the editor Professor D.A. Barry.

## Appendix: Geometric and hydraulic calculations

### 2.A Geometry of HYPON

In this appendix we consider the geometric relationships used in HYPON. The longitudinal shape as well as the bond size function  $r(\xi)$  depends on the value of the curvature parameter ( $n$ ). We introduce a minimum curvature parameter ( $n \geq n_R$ ) and determine it on the basis of porebody sizes the bond is connecting. For a bond that connects porebodies with sizes  $\tilde{R}_{max}$  and  $\tilde{R}_{min}$ ,  $n_R$  is calculated with Eq (2.7) by replacing  $\xi_t$  with  $(1 - \tilde{R}_{min})$ ,  $\tilde{R}_j$  with  $\tilde{R}_{min}$ , and  $\tilde{R}_i$  with  $\tilde{R}_{max}$ , i.e.

$$n_R = \frac{\ln \tilde{R}_{min} - \ln \tilde{R}_{max}}{\ln \tilde{R}_{min} - \ln(1 - \tilde{R}_{min}) + \ln[1 - \tilde{R}_{min} \cos(\pi/\zeta)] - \ln[1 - \tilde{R}_{max} \cos(\pi/\zeta)]}, \quad (2.A.1)$$

where  $\tilde{R}_{min} < \tilde{R}_{max}$ . Equation (2.A.1) shows that there exists a particular  $n_R$  for each bond that connects two porebodies, and it is deterministic. In this paper, we assume one  $n$ -value for the entire network, and  $n$  should be larger or equal to  $n_R$ . For  $n < 1$  we obtain parabolic bonds, whereas  $n > 1$  produces hyperbolic bonds. For  $n = 1$ , it produces simple biconical bonds similar to the ones proposed by earlier researchers [Nowicki et al. 1992; Toledo et al. 1994; Reeves and Celia 1996], although the throat is not fixed at the middle of  $\ell$  but is dictated by the adjacent porebody sizes. Equation (2.7) reveals that the throat is located closer to the smaller porebody and farther from the larger one. In the case of networks with equal sized porebodies,  $n$  must be zero or larger.

A pore unit (PU), as is shown in Figure 2.3b and Figure 2.3c, consists of the porebody at the center and the converging cones that emanate from that porebody. The volume of such a pore unit is equal to the sum of the porebody volume and the sum of volumes of  $\beta$  (the coordination number) number of converging parts (conical cylinders of the BACON bonds), i.e.

$$V_{PU} = V_{PB} + \sum_{j=1}^{\beta} (V_{BL})_j, \quad (2.A.2)$$

where subscripts  $PU$ ,  $PB$  and  $BL$  indicate respectively pore unit, porebody and left part of the BACON bond (see Figure 2.1b).  $V_{PU}$  is the volume of the pore unit,  $V_{PB}$  is the volume of the porebody, and  $(V_{BL})_j$  is the volume of the converging part of the bond which is connected to the porebody under consideration and the adjacent porebody  $j$ , i.e. the subscript  $j$  is the index of the adjacent porebodies. Bonds control the permeability, whereas the porebodies contribute most to the porosity and eventually regulate the macroscopic constitutive relations between permeabilities and porosities (and/or saturations). Only spherical and the cubic porebodies are considered here. In an orthogonal 3D lattice, the volume of a porebody equals

$$V_{PB} = \begin{cases} \frac{\pi \tilde{R}^3 \ell^3}{3} \{4 - \beta[2 - 3 \cos(\pi/\zeta) + \cos^3(\pi/\zeta)]\} & \text{for spherical PB} \\ 8 \tilde{R}^3 \ell^3 \sin^3(\pi/\zeta) & \text{for cubic PB.} \end{cases} \quad (2.A.3)$$

The volume of the converging (left) part ( $V_{BL}$ ) of a BACON bond is given by

$$V_{BL} = a_x \ell^3 \int_{\xi_F}^{\xi_t} T_i^2 (1 - \xi)^{2n} d\xi, \quad (2.A.4)$$

where  $a_x$  is the geometric shape factor. For a bond with circular cross section  $a_x = \pi$  and for a square cross section  $a_x = 4$ . We introduce the volume of the BACON bond ( $V_{BB}$ ), i.e. the volume of the both parts of the BACON bond: the converging (left) and the diverging (right), as shown in Figure 2.1b. The volume of the diverging part in the right hand side of  $\xi_t$  is denoted with  $V_{BR}$ . Hence, the total volume of the BACON bond is given by

$$V_{BB} = V_{BL} + V_{BR}, \quad (2.A.5)$$

where subscripts  $BB$  and  $BR$  indicate respectively the whole BACON bond and the diverging (right) part of it.  $V_{BL}$  is computed with Eq (2.A.4) and  $V_{BR}$  is computed with

$$V_{BR} = a_x \ell^3 \int_{\xi_t}^{\xi_G} T_j^2 \xi^{2n} d\xi. \quad (2.A.6)$$

The integrals of Eqs. (2.A.4) and (2.A.6) are evaluated analytically and the result can be written as

$$V_{BL} = \frac{a_x \ell^3}{(2n+1)} \frac{[\tilde{R}_i \sin(\pi/\zeta)]^2 \{ [1 - \tilde{R}_i \cos(\pi/\zeta)]^{2n+1} - (1 - \xi_t)^{2n+1} \}}{[1 - \tilde{R}_i \cos(\pi/\zeta)]^{2n}} \quad (2.A.7)$$

and

$$V_{BR} = \frac{a_x \ell^3}{(2n+1)} \frac{[\tilde{R}_j \sin(\pi/\zeta)]^2 \{ [1 - \tilde{R}_j \cos(\pi/\zeta)]^{2n+1} - \xi_t^{2n+1} \}}{[1 - \tilde{R}_j \cos(\pi/\zeta)]^{2n}}, \quad (2.A.8)$$

where  $\xi_F$ ,  $\xi_G$ ,  $T_i$  and  $T_j$  are replaced with their corresponding values. The pore volume ( $V_{el}$ ) of an elementary cube of volume  $\ell^3$  (as is shown in Figure 2.2b) is the sum of 1/8 volume of each porebody that is located at the vertex and 1/4 volume of each BACON bond that is aligned along the edge of the elementary cube. Hence,  $V_{el}$  is given by

$$V_{el} = \frac{1}{8} \sum_{j=1}^8 (V_{PB})_j + \frac{1}{4} \sum_{m=1}^{12} (V_{BB})_m, \quad (2.A.9)$$

where  $m$  is the index of bonds along the edges of the elementary cube and the subscript  $j$  is the index of the porebodies that belong to the elementary cube under consideration. The subscript  $el$  indicates the elementary cube. The number 8 is the total number of porebodies connected with the cube, whereas the number 12 is the number of edges along which the bonds are aligned. Hence, the total fluid-phase volume ( $V_f$ ) is equal to the sum of the pore unit volumes, i.e. Eq (2.A.2) as well as to the sum of the elementary pore volumes, i.e. Eq (2.A.9).  $V_f$  is given by

$$V_f = \sum_{i=1}^{N_{PU}} (V_{PU})_i = \sum_{k=1}^{N_{el}} (V_{el})_k, \quad (2.A.10)$$

where  $k$  is the index of the elementary cubes.  $N_{PU}$  and  $N_{el}$  are respectively the number of pore units and elementary cubes enclosed in  $V$ . The effective porosity of a mutually connected porous system is obtained by dividing  $V_f$  with the total volume  $V (= L_N \times W_b \times W_h)$ , i.e.

$$\varepsilon = V_f / V. \quad (2.A.11)$$

The difference between  $V$  and the fluid phase volume ( $V_f$ ) is the volume of the solid matrix ( $V_s$ ), i.e.

$$V_s = V(1 - \varepsilon), \quad (2.A.12)$$

where subscript  $s$  indicates the solid matrix. The surface area of walls of a single pore unit  $S_{PU}$  is the sum of the wall surfaces of the porebody ( $S_{PB}$ ) and the converging parts of the BACON bonds ( $S_{BL}$ ), and can be written as

$$S_{PU} = S_{PB} + \sum_{j=1}^{\beta} (S_{BL})_j. \quad (2.A.13)$$

For a network with the coordination number  $\beta$  and  $a_x = 4$ , the surface area of the walls of the cube-shaped porebody  $S_{PB} = 0$ , whereas for a spherical porebody and  $a_x = \pi$ , the surface area is calculated with

$$S_{PB} = 2\pi\ell^2\tilde{R}^2\{2 - \beta[1 - \cos(\pi/\zeta)]\}. \quad (2.A.14)$$

The surface areas of the converging parts is computed with

$$S_{BL} = 2\ell^2 a_x \int_{\xi_F}^{\xi_t} r(\xi) \sqrt{1 + [r'(\xi)]^2} d\xi, \quad (2.A.15)$$

where  $r'(\xi)$  is the first derivative of  $r(\xi)$  with respect to  $\xi$  and is continuous in the interval from  $\xi_F$  to  $\xi_t$ . For large or fractional values of  $n$ , Eq (2.A.15) is evaluated numerically. Thus, total surface area ( $S_F$ ) of the network exposed to the fluid phase becomes

$$S_F = \sum_{i=1}^{N_{PU}} (S_{PU})_i. \quad (2.A.16)$$

The specific surface area ( $s$ ) for Carman-Kozeny relation (2.15) is given by

$$s = S_F/V_s. \quad (2.A.17)$$

## 2.B Hydraulic calculation

In this appendix we compute the hydraulic conductance of a bond. To determine the conductance ( $c_{i,j}$ ) of a bond that is shown in Figure 2.1b, we follow the Hagen-Poiseuille equation given by

$$q_{i,j} = -a_s \frac{g}{\nu} [r(\xi)]^4 \ell^4 \frac{dh}{\ell d\xi}, \quad (2.B.1)$$

where  $dh/(\ell d\xi)$  is the hydraulic head gradient [ $LL^{-1}$ ].  $a_s$  is the hydraulic shape factor of the bond. For a circular bond  $a_s$  is equal to  $\pi/8$ . We can express the same equation for the left and the right conical cylinders of the bond in terms of bond function  $r(\xi)$ , yielding:

$$q = \begin{cases} q_{i,t} = -a_s(g/\nu)T_i^4(1-\xi)^{4n}\ell^3(dh/\ell d\xi) & \text{for } \xi_F \leq \xi \leq \xi_t \\ q_{t,j} = -a_s(g/\nu)T_j^4\xi^{4n}\ell^3(dh/\ell d\xi) & \text{for } \xi_t \leq \xi \leq \xi_G \end{cases} \quad (2.B.2)$$

where subscript  $i, t$  and  $t, j$  denote respectively from  $i$ -to-throat, and throat-to- $j$ . For the meaning of other symbols see the list of symbols and notations. Then, rearranging Eq (2.B.2) and integrating

$$\int_{\xi_F}^{\xi_t} \frac{d\xi}{a_s T_i^4 (1-\xi)^{4n}} = - \int_{h_i}^{h_t} \frac{g}{q_{i,t} \nu} \ell^3 dh \quad (2.B.3)$$

and

$$\int_{\xi_t}^{\xi_G} \frac{d\xi}{a_s T_j^4 \xi^{4n}} = - \int_{h_t}^{h_j} \frac{g}{q_{t,j} \nu} \ell^3 dh. \quad (2.B.4)$$

If we take the sum of the terms in the left hand sides of Eqs. (2.B.3) and (2.B.4) we obtain an expression for the total dimensionless resistance ( $\chi_{i,j}$ ) of the bond. Because of the continuity of discharge (i.e.  $q_{i,t} = q_{t,j}$ ) the right hand side is easily simplified and integrated with respect to the hydraulic head ( $h$ ), i.e.

$$\int_{\xi_F}^{\xi_t} \frac{d\xi}{a_s T_i^4 (1 - \xi)^{4n}} + \int_{\xi_t}^{\xi_G} \frac{d\xi}{a_s T_j^4 \xi^{4n}} = \frac{g}{q_{i,t} \nu} \ell^3 (h_i - h_j). \quad (2.B.5)$$

Hence,

$$\chi_{i,j} = \int_{\xi_F}^{\xi_t} \frac{d\xi}{a_s T_i^4 (1 - \xi)^{4n}} + \int_{\xi_t}^{\xi_G} \frac{d\xi}{a_s T_j^4 \xi^{4n}}, \quad (2.B.6)$$

i.e. the resistances of the two conical cylinders are summed up. For computing site-conductance according to Woodside and Messmer [Woodside and Messmer 1961], we consider only the first term of Eq (2.B.6) for each conical cylinder connected with the porebody under consideration, and the same is done for each pore unit. With  $\chi_{i,t}$  and  $\chi_{t,j}$  we denote respectively the first and second terms of Eq (2.B.6), and write the result of integration:

$$\chi_{i,t} = \frac{[1 - \tilde{R}_i \cos(\pi/\zeta)]^{4n}}{(4n - 1) a_s [\tilde{R}_i \sin(\pi/\zeta)]^4} \left\{ \frac{[1 - \tilde{R}_i \cos(\pi/\zeta)]^{4n-1} - (1 - \xi_t)^{4n-1}}{\left\{ [1 - \tilde{R}_i \cos(\pi/\zeta)] (1 - \xi_t) \right\}^{4n-1}} \right\}, \quad (2.B.7)$$

$$\chi_{t,j} = \frac{[1 - \tilde{R}_j \cos(\pi/\zeta)]^{4n}}{(4n - 1) a_s [\tilde{R}_j \sin(\pi/\zeta)]^4} \left\{ \frac{[1 - \tilde{R}_j \cos(\pi/\zeta)]^{4n-1} - (\xi_t)^{4n-1}}{\left\{ [1 - \tilde{R}_j \cos(\pi/\zeta)] (\xi_t) \right\}^{4n-1}} \right\}, \quad (2.B.8)$$

where  $\xi_F$ ,  $\xi_G$ ,  $T_i$  and  $T_j$  are replaced with their corresponding values. For other geometries than circular, the hydraulic shape factor ( $a_s$ ) can be derived by assuming that the Reynolds number ( $Re$ ) is the same for both cases. Then, the two cases are hydraulically equivalent. Because the characteristic size  $r(\xi)$  and the bond lengths in both cases are also the same, the equality of  $Re$  reduces to the equality of velocities, i.e.

$$\frac{q_1}{a_{x1} r^2} = \frac{q_2}{a_{x2} r^2}, \quad (2.B.9)$$

where subscripts 1 and 2 denote two cases. Hence, writing Eq (2.B.9) explicitly for  $q_2$ , we obtain

$$q_2 = \frac{a_{x2}}{a_{x1}} q_1 \quad (2.B.10)$$

and inserting the Hagen-Poiseuille equation (2.B.1) for  $q_1$  and assuming case 1 to be circular (i.e.,  $a_{x1} = \pi$  and  $a_{a1} = \pi/8$ )

$$q_2 = \frac{a_{x2} \pi g}{\pi 8 \nu} [r(\xi)]^4 \ell^3 \frac{dh}{d\xi}. \quad (2.B.11)$$

Therefore,  $a_{s2} = a_{x2}/8$ . For example, for a bond of square cross section shape  $a_s$  becomes 0.5 (because  $a_x = 4$ ). This assumption is valid for  $Re < 10$  [Bear 1972] and for similar sizes [Turian 1973]. Now  $c_{i,j}$  is given by

$$c_{i,j} = \frac{1}{\chi_{i,j}}, i \neq j. \quad (2.B.12)$$



## 2.C Geometric characteristics of HYPON model

In this appendix we analyze different geometric characteristics of HYPON, e.g. throat sizes  $r(\xi_t)$ , bond lengths ( $\ell_b/\ell$ ), flow field heterogeneity indicators and microporosity. Porebody and throat sizes are functionally related by HYPON but are not perfectly correlated. The narrower the range of porebody-sizes, the stronger is the correlation between throat size and porebody size, which agrees with the evidence presented in the literature [David et al. 1990; Øren et al. 1998; Blunt et al. 2002]. In Figure 2.8, throat sizes produced by the random UD (see Table 2.1) are shown as a function of size of porebodies. The cloud of data is distributed over the trapezoid formed by the minimum and maximum sizes of porebodies and throats, the spread of which clearly depends on the range ( $\tilde{R}_{min}$  and  $\tilde{R}_{max}$ ) of porebodies. For a homogeneous case, the trapezoid becomes a point and a perfect correlation results, as shown by the dashed line (for  $n = 0$ ) on that plot.

In Figure 2.8, throat sizes are plotted as a function of bond length for the same case. The inverse relation of throat-to-bond length is in agreement with experimental and theoretical results in the literature [David et al. 1990; Blunt et al. 2002; Øren and Bakke 2002]. An ensemble of porebodies of any random distribution can be used as input. The PDFs of porebody sizes include commonly used random distributions [Sahimi et al. 1986; Yanuka et al. 1986; Tsakiroglou and Payatakes 1991; Bakke and Øren 1996; Øren et al. 1998; Lindquist and Venkatarangan 1999; Tuller et al. 1999; Sok et al. 2002] such as Beta (BD), Gamma (BD), lognormal (LN), normal (ND), Rayleigh (RD), Weibull (WD) and uniform (UD). These PDFs are also shown in the corresponding subplots.

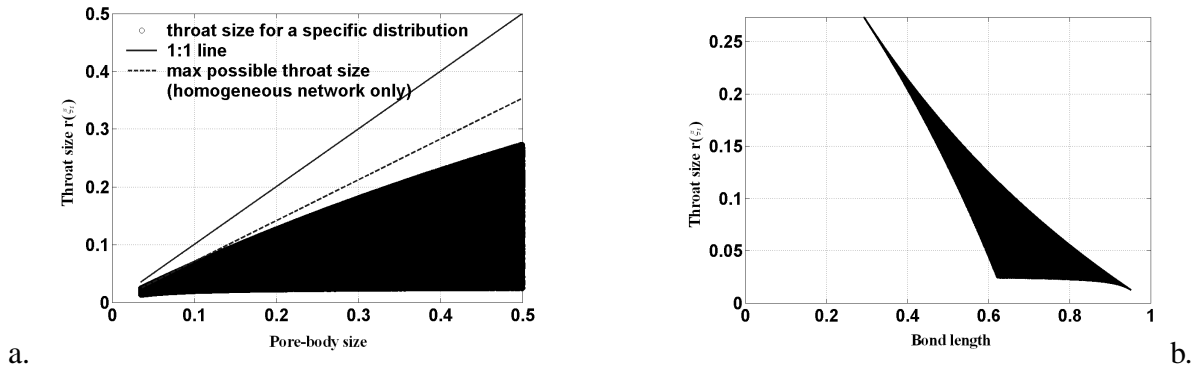


Figure 2.8: Scatter plots of throat sizes produced by HYPON with UD (see Table 2.1) ; a. throat sizes  $r(\xi_t)$  as a function of porebody sizes.; b. throat sizes as a function of bond lengths ( $\ell_b/\ell$ ).

Based on that ensemble which is distributed in 3D space, the throat sizes are computed with HYPON. In Figure 2.9 the PDFs of throat sizes  $r(\xi_t)$  and bond lengths ( $\ell_b/\ell$ ) obtained from the seven different PDFs of porebody sizes of Table 2.1 are shown. It is seen from the figure that irrespective of the input PDFs of porebody sizes, the shape of the PDFs of throat sizes looks similar in almost all cases. However, in the case of UD it is more skewed than in other cases. The cumulative distribution function (CDF) of throat sizes can quickly be compared with the ones from the literature. Throat size data obtained from four different distributions of porebody sizes i.e. GD, WD, ND and UD, are shown in Figure 2.10 and are fitted with the Gamma cumulative distribution function. In all subplots of Figure 2.10, a good agreement between the throat size  $r(\xi_t)$  data and the Gamma cumulative distribution function can be observed. However, the goodness of fitting differs. We observe that the fitting is best for the distribution GD and

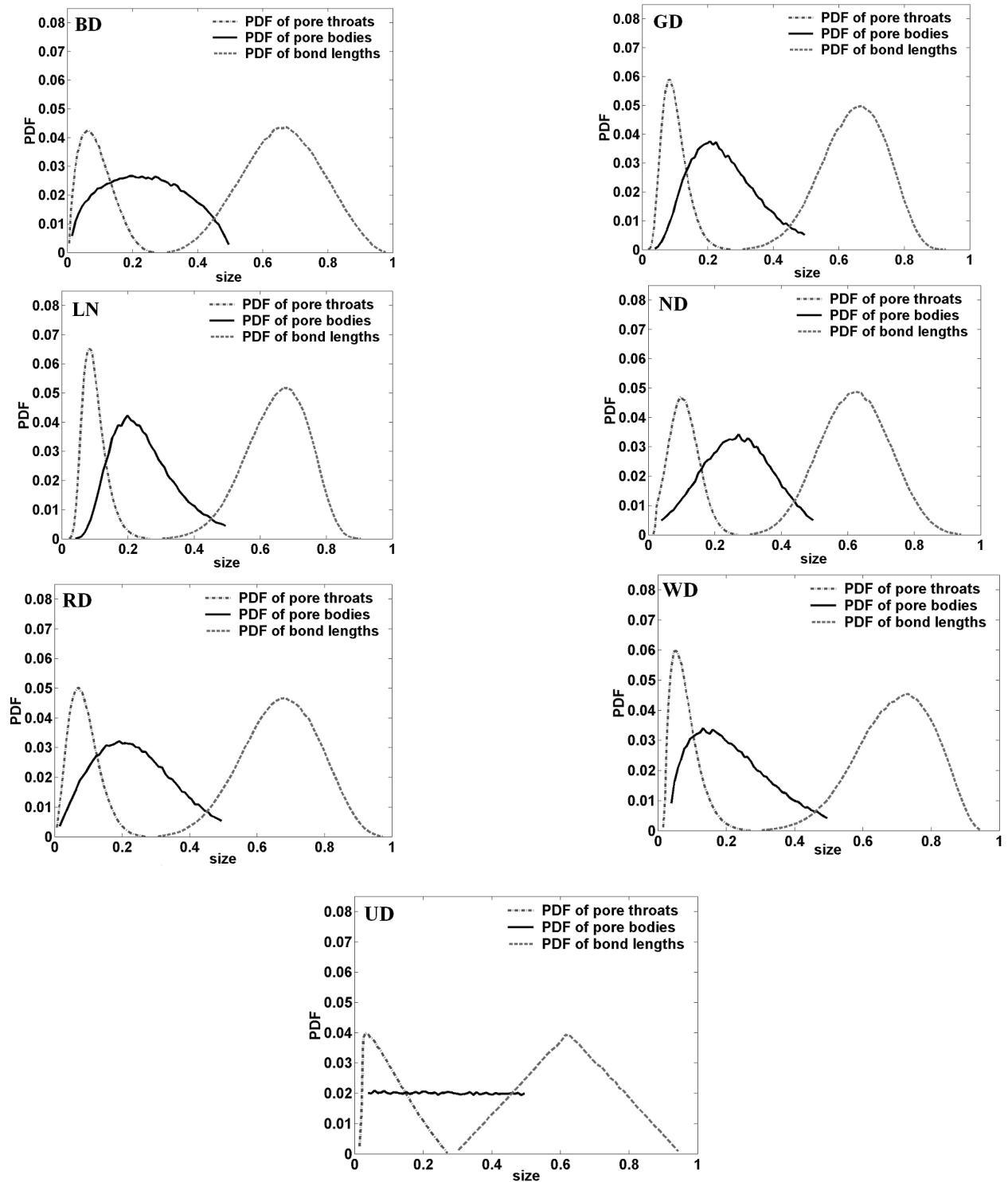


Figure 2.9: The PDFs of porebody sizes ( $\tilde{R}$ ) with solid lines, throat sizes  $r(\xi_t)$  with dashed-dotted lines and the bond lengths ( $\ell_b/\ell$ ) with dashed lines. Names of sub-plots are identified in Table 2.1.

becomes less for WD, ND, and UD respectively. An impression of inherent heterogeneity of

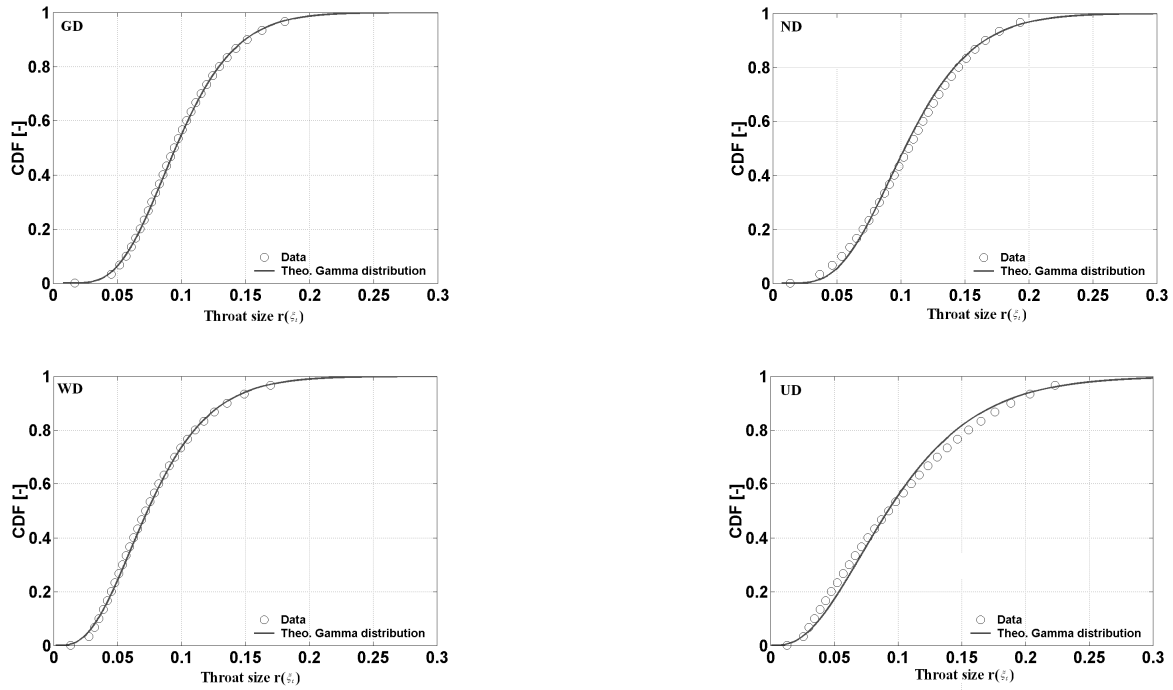


Figure 2.10: HYPON-generated throat size  $r(\xi_t)$  data (open circles) fitted with Gamma cumulative distribution function (solid lines). Cases GD, WD, ND, and UD are identified in Table 2.1.

a pore-network model may be developed from routing flow or transport (e.g. tracer particles), as a simple flow field simulation may furnish considerable information about micro-structural properties of the modeled porous medium. In Figure 2.11, absolute (dimensionless) transversal bond-discharges ( $q_Y$  and  $q_Z$  along global positive  $Y$  and  $Z$  axes respectively) at nodes are plotted as a function of the discharges ( $q_X$ ) at the same nodes in the mean flow direction (positive  $X$  axis). Two distributions, i.e. the random Rayleigh (RD) and the random uniform (UD) taken from Table 2.1, were considered and Eq (2.10) was solved numerically for pressure and flow fields.

In Figure 2.11, we observe that in both cases transversal bonds contribute considerably to the node discharges. In a regular grid, the most important factor to make the lateral bonds contribute is the variance of the porebody sizes. The higher the variance, the larger becomes the contribution from the transversal bonds. The variation is slightly larger for UD (transversal mean discharge is 32% of  $q_X$ ), but also the variation in mean porebody size is slightly larger. Hence, no significant role of the type of random distribution can be detected.

Finally, we compare microporosity distributions that result from two different distributions of porebody sizes. In Figure 2.12, microporosity distributions for two different distributions (ND and UD) of porebody sizes are shown. The microporosities are computed for each elementary cube as shown in Figure 2.2b in terms of bond-microporosity (volume of the bonds only), porebody-microporosity (volume of porebodies only) and total microporosity. Usually, microporosities are computed [Øren et al. 1998; Valvatne 2002] for a much larger block (i.e. a group of elementary cells). Here, the purpose is different, as we intend to show the effect of the type of random distributions of porebody sizes on the microporosity distribution. For a

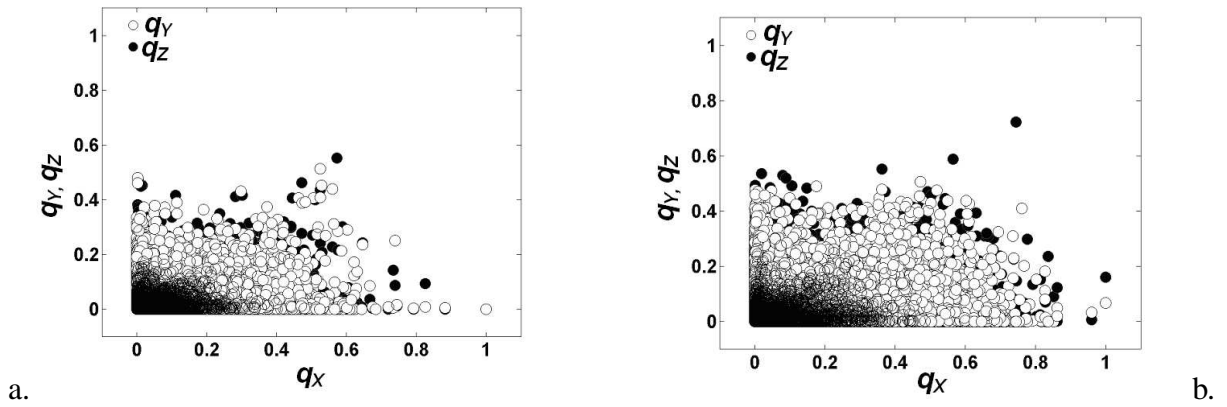


Figure 2.11: Absolute node-discharges in transversal directions (from a pore center) plotted as a function of the node-discharges along the mean flow direction in a  $101 \times 47 \times 47$  pore-network with RD. b. Discharges in network created with UD. The solid circles and the open circles indicate the discharges respectively along positive  $Y$  and  $Z$  axes.

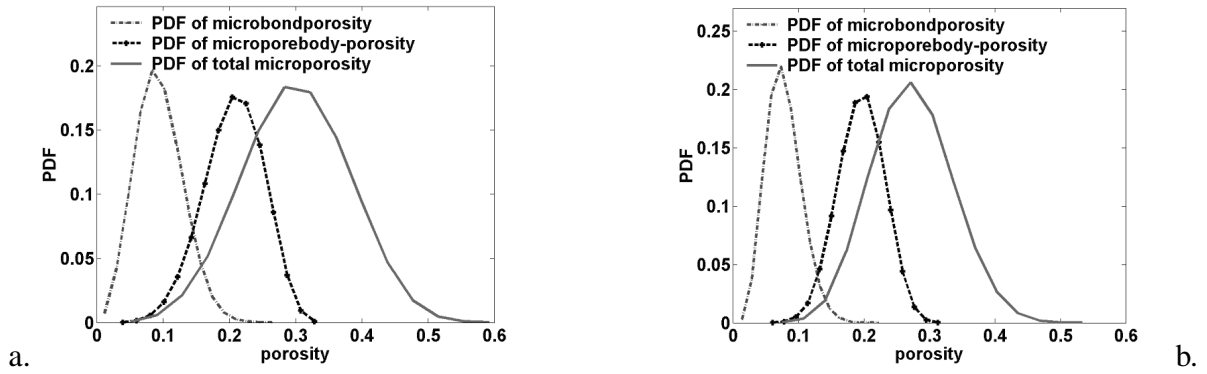


Figure 2.12: Microporosity of a pore-network with two different distributions of porebodies a. due to the random uniform distribution (UD) and b. due to the random normal distribution (ND) of porebody sizes. These cases are identified in Table 2.1.

homogeneous network, microporosity has a single value which is equal to the global porosity. The variation of porosity increases with the increase in variance of porebody sizes.

From Figure 2.12, it can be concluded that the shape of microporosity distribution is quite insensitive to the type of distribution of porebody sizes but has a shape reminiscent of a normal distribution. On the other hand, Blunt, Lindquist and their co-workers [Lindquist and Venkatarangan 1999; Blunt et al. 2002] showed a long tail in the microporosity distribution in reservoir sandstones. The reason for this disagreement may be either the difference in the method of computation or the larger heterogeneity in their samples, which is reflected in the permeability tensor in the recent work by Øren [Øren et al. 1998]. The microporosity shown in Figure 2.12 is in agreement with Lindquist [Lindquist et al. 1996] who reported a normal distribution for uniform beads.

## Chapter 3

# Quantification of dispersion by upscaling Brownian motion of tracer displacement in a 3D pore-scale network model\*

### Abstract

We present a 3D network model with particle tracking to upscale 3D Brownian motion of non-reactive tracer particles subjected to a velocity field in the network bonds, representing both local diffusion and convection. At the intersections of the bonds (nodes) various jump conditions are implemented. Within the bonds, two different velocity profiles are used. At the network scale the longitudinal dispersion of the particles is quantified through the coefficient  $D_L$ , for which we evaluate a number of methods already known in the literature. Additionally, we introduce a new method for derivation of  $D_L$  based on the First-arrival Time Distribution (FTD). To validate our particle tracking method, we simulate Taylor's classical experiments in a single tube. Subsequently, we carry out network simulations for a wide range of the characteristic Peclet number  $Pe_\ell$  to assess the various methods for obtaining  $D_L$ . Using the new method, additional simulations have been carried out to evaluate the choice of nodal jump conditions and velocity profile, in combination with varying network heterogeneity. In general, we conclude that the presented network model with particle tracking is a robust tool to obtain the macroscopic longitudinal dispersion coefficient. The new method to determine  $D_L$  from the FTD statistics works for the full range of  $Pe_\ell$ , provided that for large  $Pe_\ell$  a sufficiently large number of particles is used. Nodal jump conditions should include molecular diffusion and allow jumps in the upstream direction, and a parabolic velocity profile in the tubes must be implemented. Then, good agreement with experimental evidence is found for the full range of  $Pe_\ell$ , including increased  $D_L$  for increased porous medium heterogeneity.

**Keywords:** dispersion; transport; pore network; Brownian motion; particle tracking; nodal jump condition; moment methods.

---

\*by R. C. Acharya, MIJ van Dijke, K Sorbie, SEATM van der Zee and A Leijnse, submitted to *Adv Water Res*, 2004.

*List of symbols and notations*

$\langle . \rangle$	Ensemble average quantity
$C, \tilde{C}$	Concentration [ $\text{ML}^{-3}$ ] and dimensionless concentration
$D, D_L, D_T$	Dispersion coefficients: any effective, Longitudinal, and Taylor [ $\text{L}^2\text{T}^{-1}$ ]
$D_m, D_h$	Molecular diffusion coefficient and mechanical dispersion [ $\text{L}^2\text{T}^{-1}$ ]
$f_{i,j}$	Advection-diffusion fraction factor of Sorbie-Clifford formulation
$f(\lambda)$	Intra-pore velocity function
$H$	Heaviside integral
$i, j$	The indices of nodes and bonds
$k_{ax}$	Taylor's coefficient for cross-section shape (e.g. $1/48$ )
$L, \ell$	Length of the porenetwork and bond length [L]
$Pe_L$	Pore network (Column) Peclet number $vL/D_L$
$p(i, j)$	Transition probability density function
$Pe_b, Pe_T$	Bond Peclet and Taylor's Peclet numbers [-]
$Pe_{ref}$	A reference (conditional) threshold Bond Peclet number [-]
$Pe_\ell$	Characteristic Peclet number $v\ell/D_m$ [-]
$q_{i,j}, Q$	Discharge respectively through bonds and porenetwork [ $\text{L}^3\text{T}^{-1}$ ]
$R, \tilde{R}$	Radius [L] and aspect ratio ( $R/\ell$ ) of bonds (Taylor's tubes)
$\Delta\mathbf{r}$	Radius vector of Brownian sphere [L]
$t, \Delta t$	Time and time step of iteration [T]
$\tilde{T}$	Dimensionless time on network scale ( $vt/L$ )
$u$	Mean velocity in the Taylor's tubes [ $\text{LT}^{-1}$ ]
$v$	Mean intrinsic velocity along the principle flow direction in the pore network [ $\text{LT}^{-1}$ ]
$x, y$	Local reference system, $x \in [0, \ell]$ along the axial direction of fluid flow [L]
$X, Y, Z$	Global (network scale) reference system [L]
$\beta$	an exponent parameter
$\phi(\Delta\mathbf{r})$	Green's probability function for Markov's processes
$\mu$	Ensemble average as specified with subscript (e.g. $\mu_t$ and $\mu_X$ )
$\sigma^2$	Second central spatial moment(variance) of positions of particles with respect to a chosen direction (e.g. $\sigma_X^2$ ) [ $\text{L}^2$ ]
$\tau$	Dimensionless time on pore-scale ( $ut/\ell$ )
$\xi$	Local axis ( $x/\ell$ ) along flow in a capillary [-]
$\varpi$	A factor in Sorbie-Clifford formulation $(\pi R^2)/\ell$ [L]
$\varphi$	Polar angle of radius vector in Brownian spherical coordinate system $[0, \pi]$
$\psi$	Deviate of the Green's function [-]
$\zeta$	tortuosity [-]
$\theta$	Azimuthal angle of radius vector in Brownian spherical coordinate system $[0, 2\pi]$
$T, m, L, b$	Subscripts indicate Taylor, molecular, Longitudinal and bond
CDE	Convection-Dispersion Equation
(C)FTD	(Cumulative) First-arrival Times Distribution
SPD	Spatial Positions Distribution

## 3.1 Introduction

Dispersion in porous media is of interest in many fields, such as chemical, petroleum, civil and environmental engineering [Whitaker 1967]. It plays an important role in the accuracy of predictions during reactive and non-reactive transport in groundwater systems (porous media). In porous media, dispersion is caused by two processes: Brownian motion of solute molecules, or *molecular diffusion* and the velocity differences among solute-carrying solvent-streamlines, which is referred to as *mechanical* dispersion. The interplay of these two phenomena leads to the *hydrodynamic* dispersion [Koch and Brady 1985].

Because of its key role in the theory of mass transport, the dispersion process has been studied for a considerable time [Taylor 1953; Aris 1956; De Josselin de Jong 1958; Brenner 1980]. In general, two methodologies (models) have been devised to describe dispersion viz the deterministic (e.g. [Bear 1972]), and probabilistic or statistical approaches (e.g. [Sahimi et al. 1986; Dagan 1988; Sorbie and Clifford 1991; Damion et al. 2000]). The mixing cell model is an example of the first, whereas the particle tracking approach in combination with the method of moments serves as an example of the second approach. Dispersion is a scale dependent-phenomenon. At the continuum scale, Bear [Bear 1972] showed that dispersion takes the form of a second order tensor that depends not only on local variations of velocity field but also on large-scale characteristics of the medium [Bear 1972; Dagan 1988]. This tensor is used in the convection-dispersion equation (CDE). Alongside theoretical developments in dispersion theory, experimental and numerical works have emerged to determine the dispersion tensor [Freyberg 1986; Verlaan 2001]. Historical reviews of dispersion research can be found in [Perkins and Johnston 1963; Bear 1972; Van Brakel 1975; Freeze and Cherry 1979; Sahimi et al. 1983a; Han et al. 1985; Gelhar et al. 1992; Appelo and Postma 1993; Jiao 2001; Verlaan 2001].

As mentioned above, dispersion originates from variation of velocity at the pore scale (Taylor scale), i.e. within a pore cross-section, as well as from geometrical variation of the length scale of the distribution of pores within a porous medium. A first attempt to average these variations at the pore scale to an effective property at the continuum scale was made by Saffman [Saffman 1960]. Following Fatt [Fatt 1956a], Saffman used a pore network model as a tool to include the pore-scale physical phenomena. Since the work of Saffman, 2D network models, in combination with random-walker particle tracking, have often been employed to upscale the pore-scale dispersion coefficient to a network-scale quantity [Mohanty and Salter 1982; Sorbie and Clifford 1991; Damion et al. 2000; Park et al. 2001; Verlaan 2001]. However, a rigorous upscaling of multi-directional Brownian walker (3D motion of material points) from the Brownian sphere to the 3D pore network has not yet been presented.

One of the main reasons that has prevented such rigorous upscaling lies in the uncertainty of the mixing conditions and transition probabilities at the intersection of pores (nodes) in a network model [LaBolle et al. 1998; Bruderer and Bernabé 2001; Park et al. 2001]. The simplest assumption is to take the transition probability at a node proportional to the flow rates in the neighboring bonds [De Josselin de Jong 1958]. However, this method excludes the effect of molecular diffusion at the nodes. A more sophisticated approach consists of constructing a pattern of streamlines from inflowing to outflowing bonds at a node, such that the intra-pore particle tracking can be continued from pore to pore [Sahimi et al. 1986; Bruderer and Bernabé 2001]. The drawback of this method is that, so far, it has only been constructed for 2D networks. Sorbie and Clifford [Sorbie and Clifford 1991] have introduced a transition probability based on the arrival time statistics for particles in a single pore. Although some additional assumptions

must also be made in this method, it does include the effect of molecular diffusion and it can be employed in three dimensions.

An additional obstacle to rigorous upscaling is the difficulty of obtaining the dispersion coefficient from particle statistics, specially from the Spatial Position Distribution (SPD) and the First-arrival Times Distribution (FTD) of the tracer particles. In Section 3.2 we evaluate how these distributions are commonly used to obtain the dispersion coefficient and propose a new method that may overcome the various drawbacks of those currently used.

The purpose of this study is to quantify the longitudinal dispersion coefficient ( $D_L$ ) at the network scale by upscaling 3D Brownian motion of non-reactive tracer particles subjected to a velocity profile in capillary bonds of a 3D pore network. Using network model with particle tracking, the effects of different intra-pore velocity profiles are investigated in combination with different choices of the node transition probabilities for a wide range of flow velocities. Furthermore, various methods to determine  $D_L$  from the particle statistics are tested.

Flow simulations have previously been carried out in our 3D pore network model for three-phase immiscible flow [Van Dijke and Sorbie 2002]. However, since this paper focuses on single-phase miscible tracer transport, this model has been employed single phase mode to calculate the global velocity field. The velocities are then used in our network model in combination with the random walk model of Brownian particles. In contrast to Sorbie and Clifford [Sorbie and Clifford 1991], who approximated the intra-tube residence times of particles from single-tube random walk simulations, we carry out a full random walk throughout the network.

In Section 3.3.1 we describe the particle tracking algorithm for a single tube. In Section 3.3.2 the network implementation of the algorithm is described, with emphasis on the various nodal jump conditions. In Section 3.4.1 single tube simulations are presented to validate the particle tracking algorithm and we make a first assessment of the different methods for obtaining the corresponding dispersion coefficient. In Section 3.4.2.1 we present network simulations for a wide range of the characteristic Peclet number  $Pe_\ell$  to assess the various methods for obtaining  $D_L$ . Using a suitable method, in Section 3.4.2.2 additional simulation results are presented, which evaluate the choice of nodal jump conditions and velocity profile, in combination with varying network heterogeneity. The latter is achieved by changing the range of pore sizes.

Finally, we acknowledge that the issue of porous medium heterogeneity is very important and that the present study underemphasizes this aspect. However, to investigate heterogeneity fully, a large sensitivity study should be carried out with respect to pore size distribution, coordination number and pore orientation relative to the main flow direction for the velocity field calculations [Legatski and Katz 1967; Han et al. 1985; Bruderer and Bernabé 2001]. Additionally, more sophisticated pore geometry may affect the results, although we believe that this is not a major problem, as long as an intra-tube profile with varying velocities is applied. However, these issues are not the main focus of this paper and we show that even with the present simple model, we are able to draw sound conclusions which agree well with experimental observations and other theoretical results where these are available.

## 3.2 The upscaling problem

Models describing transport of particles on the continuum scale usually employ the convection-dispersion equation (CDE) [Bear 1972; Hassanizadeh 1996]. Assuming an elongated homogeneous and isotropic porous medium at the macroscopic level, the 1D formulation of the CDE



for the concentration  $C$

$$\frac{\partial C}{\partial t} + v \frac{\partial C}{\partial X} = D_L \frac{\partial^2 C}{\partial X^2} \quad (3.1)$$

can be used, which involves the longitudinal macroscopic dispersion coefficient  $D_L$  and the mean flow velocity  $v$ . In dimensionless form  $D_L$  is expressed through the macroscopic Peclet number

$$Pe_L = \frac{vL}{D_L} \quad (3.2)$$

as indicated in the *list of symbols and notations* and  $L$  is the length of the system. Traditionally,  $D_L$  has been expressed as empirical relations such as

$$D_L = D_m/\zeta + D_h, \quad (3.3)$$

where  $\zeta$  denotes tortuosity, while  $D_m$  and  $D_h$  denote molecular diffusion and mechanical dispersion, respectively [Bear 1972]. In this paper we aim to find the macroscopic dispersion coefficient  $D_L$  directly by tracking the paths of particles in the flow field in a 3D pore network. Note that, although the macroscopic porous medium can be assumed homogeneous and 1D, we use a 3D network to include microscale heterogeneities by randomly distributing the pore sizes. The resulting (longitudinal) dispersion coefficient in the mean flow direction of the network is identified with the macroscopic  $D_L$  and the length of the network with  $L$ .  $D_L$  (or  $Pe_L$ ) is determined as a function of the characteristic Peclet number  $Pe_\ell$

$$Pe_\ell = \frac{v\ell}{D_m}, \quad (3.4)$$

where  $\ell$  denotes the mean pore length.

In a particle tracking model the effective longitudinal dispersion  $D_L$  can be quantified by two methods. The first method is based on the statistics of the Spatial Position Distribution (SPD) of the Brownian particles, which follows from Einstein's relation [Chandrasekhar 1943]:

$$\sigma_X^2 = 2D_L t. \quad (3.5)$$

In Eq (3.5)  $\sigma_X^2$  is the variance of the X-coordinates of the ensemble of Brownian particles. Equation (3.5) can be used in two ways [Bruderer and Bernabé 2001]. In the secant method, the evolution of  $\sigma_X^2/2t$  is determined, assuming that the particles have been released in space at time  $t = 0$ . After sufficient time  $\sigma_X^2/2t$  should approach an asymptotic value, which is then identified with  $D_L$ . In the tangent method, the rate of change of the variance,  $\frac{1}{2}(\partial\sigma_X^2/\partial t)$  is evaluated as it approaches an asymptotic value that is identified as  $D_L$ . The tangent method is believed to be more accurate for determination of the transverse dispersion coefficient, but both methods give similar results for determination of the longitudinal dispersion coefficient [Bruderer and Bernabé 2001]. In Section 3.4.1 we show that the latter is indeed the case, but that the tangent method is very sensitive to local variations of the derivative  $\partial\sigma_X^2/\partial t$ .

Obtaining SPD statistics is relatively easy in a very long capillary, but it is computationally costly in a pore network. To determine  $D_L$  using the SPD approach, the positions of all particles must be scanned at regular time intervals until any of the above mentioned methods (secant or tangent) indicate that the asymptotic value of  $D_L$  is reached. That means that during the entire

simulation even the fastest moving particle should not leave the network, which is particularly stringent for large flow velocities, as it requires a very large network.

Since quantifying  $D_L$  through the SPD statistics is so expensive, we may alternatively use statistics of the First-arrival Times Distribution (FTD). In this case for each particle the time needed to travel from inlet to outlet of the network is recorded. The quantity  $D_L$  may be derived from the FTD approach in various ways.

Firstly, we may fit the Cumulative First-arrival Time Distribution (CFTD) directly to an analytical solution of the CDE (3.1) in a semi-infinite network or core [Van Genuchten and Alves 1982] for the dimensionless concentration  $\tilde{C}$  at the outlet, as is often done experimentally. The approximate analytical solution is given by

$$\tilde{C}(\tilde{X}, \tilde{T}) = \frac{1}{2} \left\{ \operatorname{erfc} \left[ (\tilde{X} - \tilde{T}) \sqrt{\frac{Pe_L}{4\tilde{T}}} \right] + \exp(Pe_L \tilde{X}) \operatorname{erfc} \left[ (\tilde{X} + \tilde{T}) \sqrt{\frac{Pe_L}{4\tilde{T}}} \right] \right\}, \quad (3.6)$$

where  $\tilde{X} = X/L$  and  $\tilde{T} = vt/L$  are dimensionless distance and time respectively. The CFTD is fitted against  $\tilde{C}(1, \tilde{T})$  to obtain the macroscopic Peclet number  $Pe_L$  and hence  $D_L$  according to Eq (3.2). Obviously, the use of the CDE on the macroscopic level and the solution (3.6) for a particular set of boundary conditions are not always appropriate, which means that this method is only reliable when the assumptions for using the CDE (3.1) and its solution are met [Van Genuchten and Alves 1982].

Secondly, we may use the first and second moments of the FTD,  $\mu_t$  (ensemble average  $\langle t \rangle$ ) and  $\sigma_t^2$  (variance) respectively. Assuming that the coefficients of variation of the SPD and FTD are approximately the same, the spatial variance  $\sigma_X^2$  is determined from the temporal variance  $\sigma_t^2$  according to

$$\sigma_X^2 = \mu_X^2 \frac{\sigma_t^2}{\langle t \rangle^2}, \quad (3.7)$$

where  $\mu_X$  is the first moment of the SPD. Hence, with Eq (3.5), we obtain

$$D_L = \frac{\mu_X^2}{2t} \left( \frac{\sigma_t}{\langle t \rangle} \right)^2. \quad (3.8)$$

Because we are using temporal statistics, an estimate for  $\mu_X$  must be introduced, as well as an estimate for  $t$ . Taking  $t = \langle t \rangle$ , it is often assumed [De Arcangelis et al. 1986; Sahimi et al. 1986; Sorbie and Clifford 1991; Appelo and Postma 1993] that both  $\mu_X/\langle t \rangle = v$  and  $\mu_X = L$ . Hence, Eq (3.8) is approximated as

$$D_L = \frac{vL}{2} \left( \frac{\sigma_t}{\langle t \rangle} \right)^2. \quad (3.9)$$

However, the assumption  $\mu_X = v\langle t \rangle$  is not always valid. In particular for small  $v$ , when the macroscopic dispersion is dominated by molecular diffusion, the temporal moments  $\mu_t = \langle t \rangle$  and  $\sigma_t^2$  must become independent of  $v$ . Hence, according to the above assumption  $\mu_X$  has to vary linearly with  $v$ , which is certainly not the case, since we assume on the other hand, more correctly, that  $\mu_X = L$  is constant. Based on these considerations, it is more appropriate to approximate  $\mu_X^2$  as  $L^2$  in Eq (3.8) and use the expression

$$D_L = \frac{L^2}{2\langle t \rangle} \left( \frac{\sigma_t}{\langle t \rangle} \right)^2 \quad (3.10)$$

yielding a constant  $D_L$  for small  $v$  [Saffman 1960; Bear 1972]. In Section 3.4.2.1 we check whether indeed the temporal moments become independent of  $v$  and we evaluate this new FTD method of moments as opposed to the old method of Eq (3.9).

Sahimi et al. [Sahimi et al. 1983b] have also used an analytical solution of the CDE (3.1), from which they derived a relation between the FTD statistics and  $Pe_L$ . For small enough  $(\sigma_t/\mu_t)^2$  their expression limits to Eq (3.9) [Sorbie and Clifford 1991]. However, since this method is essentially another way of fitting the FTD statistics to a macroscopic solution, we will not discuss this any further.

For a single cylindrical pore Taylor and Aris [Taylor 1953; Aris 1956] derived a relation between the resulting (Taylor) dispersion coefficient  $D_T$ , as a function of molecular diffusion  $D_m$ , pore radius  $R$  and the average tube velocity  $u$ ,

$$D_T = D_m + k_{ax} \frac{u^2 R^2}{D_m}, \quad (3.11)$$

with  $k_{ax} = 1/48$  for a cylindrical pore. Equation (3.11) is valid for a wide range of the tube or bond Peclet number, i.e.

$$Pe_b = \frac{u\ell}{D_m}. \quad (3.12)$$

However, deviations may be expected for pore aspect ratios  $\tilde{R} = R/\ell$  close to 1, which often arise in actual porous media [Sorbie and Clifford 1991]. Obviously, dispersion in the individual pores of our model should obey Eq (3.11) in the appropriate limits.

To obtain the dispersion coefficient  $D_T$  for a single tube, Taylor [Taylor 1953] also fitted the CFTD to an analytical solution of the CDE, for a tube of infinite length,

$$\tilde{C}(\xi, \tau) = \frac{1}{2} \text{erfc} \left[ \frac{(\xi - \tau) \sqrt{Pe_T}}{\sqrt{4\tau}} \right], \quad (3.13)$$

which is often referred to as the Taylor-Aris solution [Scheidegger 1960; Bear 1972]. In Eq (3.13)  $Pe_T$  denotes the Taylor Peclet number, defined as

$$Pe_T = \frac{u\ell}{D_T} \quad (3.14)$$

and  $\xi = x/\ell$ ,  $\tau = ut/\ell$  are dimensionless distance and time for the local co-ordinates of a tube. For later use we express Eq (3.11) in terms of  $Pe_T$ ,  $Pe_b$  and  $\tilde{R}$  as

$$Pe_T = \frac{Pe_b}{1 + k_{ax} Pe_b^2 \tilde{R}^2}. \quad (3.15)$$

## 3.3 Model

### 3.3.1 Motion within a single tube

In our random walk model the movement of a particle is driven by two forces: (1) within the pore the particle experiences a series of random jumps from the origin of the spherical coordinate-system  $\mathbf{r} = (r, \varphi, \theta)$  (Brownian motion or molecular diffusion); (2) the particle

moves with the fluid velocity profile of the pore (convection) in the local cylindrical coordinate system  $(x, y)$ , where  $x$  indicates the (local) flow direction and  $y$  is the distance of the particle's position from the axis of the cylindrical tube (bond). Additionally, at nodes (intersection of pores) the particle jumps from one pore to the next, based on a probabilistic approach, which should also depend on both diffusive and convective forces, as described in Section 3.3.2. To avoid confusion with earlier Markovian models of random walkers, we prefer to call our random walk model the “Brownian directed random-walk” model, because we describe random leaps of particles in three dimensions and, additionally, track the center of a Brownian sphere along the fluid streamline.

The convective motion of the particle occurs according to the fluid velocity profile, which we assume to be either parabolic (Hagen-Poiseuille flow) or plug-like [Sahimi et al. 1986; Bruderer and Bernabé 2001], and we will study the quantitative effect on the dispersion due to either assumption. Hence, the advective velocity of the particle  $U(\lambda)$  is assigned according to

$$U(\lambda) = uf(\lambda), \text{ with } f(\lambda) = \begin{cases} 2(1 - \lambda^2) & \text{for parabolic profile} \\ 1 & \text{for uniform (plug-like) profile,} \end{cases} \quad (3.16)$$

where  $\lambda$  is the relative radial position of the particle, i.e.,  $\lambda = y/R$ .

Considering the Brownian motion, we assume that the particles describe hops in all directions around their mean position at the fluid streamlines (fluid-strand). Following Sorbie and Clifford [Sorbie and Clifford 1991] and Damion et al. [Damion et al. 2000], the lengths of these random jumps in Lagrangian space occur according to a probability function that is obtained by integrating the Green's propagator [Chandrasekhar 1943]

$$\phi(\Delta \mathbf{r}) = (4\pi D_m \Delta t)^{-3/2} \exp \left[ -\frac{\Delta \mathbf{r}^2}{4D_m \Delta t} \right] \quad (3.17)$$

over the volume of a sphere with radius vector  $\Delta \mathbf{r}$ . Hence, the probability of a leap of length  $\Delta r = |\Delta \mathbf{r}|$  over a time step  $\Delta t$  follows from the cumulative distribution function

$$P(\psi) = \text{erf}(\psi) - \frac{2\psi}{\sqrt{\pi}} e^{-\psi^2} \text{ with } \psi = \frac{\Delta r}{\sqrt{4D_m \Delta t}}. \quad (3.18)$$

The polar and azimuthal angles of the Brownian motion,  $\varphi$  and  $\theta$  respectively, are chosen from sinusoidal and uniform distributions [Damion et al. 2000], i.e.,

$$P(\varphi) = 0.5 \int_0^\varphi \sin \tilde{\varphi} d\tilde{\varphi}, \text{ where } \varphi \in [0, \pi] \quad (3.19)$$

and

$$P(\theta) = 0.5\pi^{-1} \int_0^\theta d\tilde{\theta}, \text{ where } \theta \in [0, 2\pi]. \quad (3.20)$$

In the local cylindrical coordinate system, the dimensionless displacement of a particle  $\Delta \lambda = \Delta y/R$  in the radial direction is described by

$$\Delta \lambda = \Delta \rho \sin \varphi \cos \theta, \quad (3.21)$$

where  $\Delta\rho = \Delta r/R$ . The total dimensionless displacement  $\Delta\xi = \Delta x/\ell$  in the axial direction over the dimensionless time step  $\Delta\tau = u\Delta t/\ell$  is described by

$$\Delta\xi = \Delta\tau f(\lambda) + \Delta\rho \tilde{R} \cos \varphi \quad (3.22)$$

where the two terms reflect the convective and diffusive displacements respectively. From Eq (3.18) it follows that  $\Delta\rho$  is linked to  $\psi$ , hence to the time step  $\Delta\tau$ , as  $\Delta\rho = \psi\omega/\tilde{R}$ , with  $\omega = \sqrt{4\Delta\tau/Pe_b}$ . Convergence of the numerical scheme requires a sufficiently small time step  $\Delta\tau$ , such that at least  $|\Delta\xi| < 1$  and  $|\Delta\lambda| < 1$ . The latter constraints can be rewritten into a single condition on  $\omega$ , from which  $\Delta\tau$  follows. At the pore walls reflective boundary conditions are applied [Sorbie and Clifford 1991; Damion et al. 2000].

### 3.3.2 Motion in a network of tubes: nodal jump conditions and simulation methods

We model a porous medium by a 3D cubic network with tubes of fixed length  $\ell$  and circular cross-section of varying radius  $R$ . The dimensions of the network are: length (in the main flow direction  $X$ ) ( $L \gg \ell$ ), width ( $W_Y \gg \ell$ ) and height ( $W_Z \gg \ell$ ). The pore radii  $R$ , hence the pore aspect ratios  $\tilde{R}$ , are randomly distributed from a given distribution. Furthermore, the network has (global) coordination number  $z$ , which is achieved by randomly removing pores in case  $z < 6$  [Van Dijke and Sorbie 2002]. We assume that such a network shown in Figure 3.1 will mimic a porous medium, at least hydraulically [Scheidegger 1960; Acharya et al. 2004a; Acharya et al. 2004b]. The (average) flow rate in each tube of the network is calculated from the nodal pressures, which are induced by a (global) pressure difference between inlet and outlet faces.

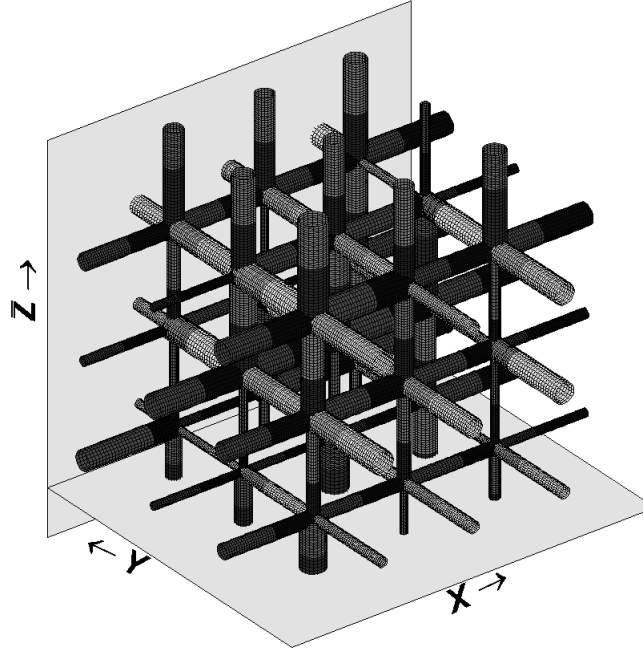


Figure 3.1: Sketch of pore network architecture with volumeless pore bodies (nodes).

The intersection of the elementary tubes is assumed to be volumeless, i.e. all pore volume is assigned to the tubes. From this assumption the problem arises of the discontinuity of the dispersion function [Park et al. 2001]. A particle that emerges at a node from one tube may enter another tube with drastically different hydraulic and diffusive regimes. This issue may be of particular interest for reproducing and understanding experiments that show long tails in breakthrough curves and which cannot be captured by classical solutions of the (continuum-scale) CDE [Sorbie and Clifford 1991; Verlaan 2001].

Sorbie and Clifford [Sorbie and Clifford 1991] proposed a general algorithm for the jump of a particle from one tube to the next at a node. In this algorithm the probability density function for the transition of a particle from node  $i$  into tube  $j$  is given by

$$p(i, j) = \frac{[(f_{i,j}(q_{i,j} + \varpi_{i,j}D_m)(1 - H)) + ((1 - f_{i,j})\varpi_{i,j}D_mH)]}{\sum_{j=1}^{z_i} [(f_{i,j}(q_{i,j} + \varpi_{i,j}D_m)(1 - H)) + ((1 - f_{i,j})\varpi_{i,j}D_mH)]}, \quad (3.23)$$

where  $H$  is the Heaviside function, defined as

$$H = \begin{cases} 0 & \text{if } q_{i,j} \geq 0 \\ 1 & \text{if } q_{i,j} < 0. \end{cases} \quad (3.24)$$

The flow rate (discharge)  $q_{i,j}$  is taken positive for fluid leaving the node.  $z_i$  is the (local) co-ordination number at node  $i$ . Equation (3.23) reflects the fact that in general the nodal transition depends not only on the flow rate, but also on molecular diffusion, represented by the term  $\varpi_{i,j}D_m$ . The term  $\varpi_{i,j}$  is a geometrical factor that is assumed to be equal to  $(a_{\times}R_j^2/\ell)$ , where  $a_{\times}$  is a shape factor (e.g. for circular pore cross-sections  $a_{\times} = \pi$ ).  $f_{i,j}$  is the fraction of particles leaving the node and entering bond  $j$  in the direction of flow. For non-zero values of  $\varpi_{i,j}$  and  $f_{i,j} < 1$ , particles may jump in a direction opposite to the flow direction. However, in the simplest assumption of ideal fully-mixed and advection dominated transport the transition occurs only downstream, i.e.  $f_{i,j} = 1$  and, additionally,  $\varpi_{i,j} = 0$ . This combination of conditions in Eq (3.23) delivers the classical transitional probability (proportional to flow rate only) [De Josselin de Jong 1958],

$$p(i, j) = \frac{q_{i,j}}{\sum_i^{z_i} q_{i,j}}, \text{ when } q_{i,j} \geq 0 \quad (3.25)$$

and  $p(i, j) = 0$  when  $q_{i,j} < 0$ . However, based on the arrival time statistics for particles in a single pore Sorbie and Clifford [Sorbie and Clifford 1991] calculated that  $f_{i,j}$  varies from a constant value of 0.5 for low flow velocities (small  $Pe_b$ ) to a constant value of 1.0 for high flow velocities. We approximate this behavior by assuming a step function,

$$f_{i,j} = \begin{cases} 0.5 & \text{if } Pe_b \leq Pe_{ref} \\ 1 & \text{if } Pe_b > Pe_{ref}, \end{cases} \quad (3.26)$$

where  $Pe_{ref} \approx 0.40$  [Sorbie and Clifford 1991].

An alternative to Eq (3.26) may be found from the Taylor-Aris solution (3.13). Although it is well established that solution (3.13) is not accurate in pores of large aspect ratio  $\tilde{R}$  and for large values of the bond Peclet number  $Pe_b$  [Taylor 1953; 1954; Sorbie and Clifford 1991], we can still use it to estimate the transition in  $f_{i,j}$  from 0.5 to 1 for small to moderate values of  $Pe_b$ . After the discharge of one pore volume of fluid (for a tube of length  $\ell$ ), i.e. for  $\tau = 1$ , the concentration at  $\xi = 0$ , i.e.  $\tilde{C}(0, 1)$ , represents the fraction of particles that has traveled in the

direction of flow, which is in effect  $f_{i,j}$ . Hence, using Eq (3.13) we approximate this fraction as

$$f_{i,j} = \frac{1}{2} \operatorname{erfc} \left( -\frac{\sqrt{Pe_T}}{2} \right). \quad (3.27)$$

From Eq (3.15) it is evident that  $Pe_T$  not only depends on  $Pe_b$  but also on  $\tilde{R}$ . However, from the plot of  $f_{i,j}$  as a function of  $Pe_b$ , shown in Figure 3.2, it is clear that for small  $Pe_b$ ,  $f_{i,j}$  is independent of  $\tilde{R}$ . This is in agreement with the findings of Sorbie and Clifford [Sorbie and Clifford 1991] and it follows from the fact that  $D_T \approx D_m$ , i.e.  $Pe_T \approx Pe_b$  for small  $Pe_b$ . Note that the transition from 0.5 to 1, following from Eq (3.27) is centered around  $Pe_b = 1$ , rather than around  $Pe_b = 0.4$  [Sorbie and Clifford 1991]. However, on the considered range of  $Pe_b$ , this is only a minor deviation. Because the Taylor-Aris solution is not valid for large  $Pe_b$ , we assume that  $f_{i,j}$  always limits to 1 for large  $Pe_b$ , again in keeping with [Sorbie and Clifford 1991]. To reflect this, we simply replace  $Pe_T$  by  $Pe_b$  in Eq (3.27), which is equivalent to taking  $\tilde{R} = 0$  in Eq (3.15), i.e. we use

$$f_{i,j} = \frac{1}{2} \operatorname{erfc} \left( -\frac{\sqrt{Pe_b}}{2} \right). \quad (3.28)$$

Hence, Eq (3.28) is a smoothed version of Eq (3.26) with  $Pe_{ref} = 1$ .

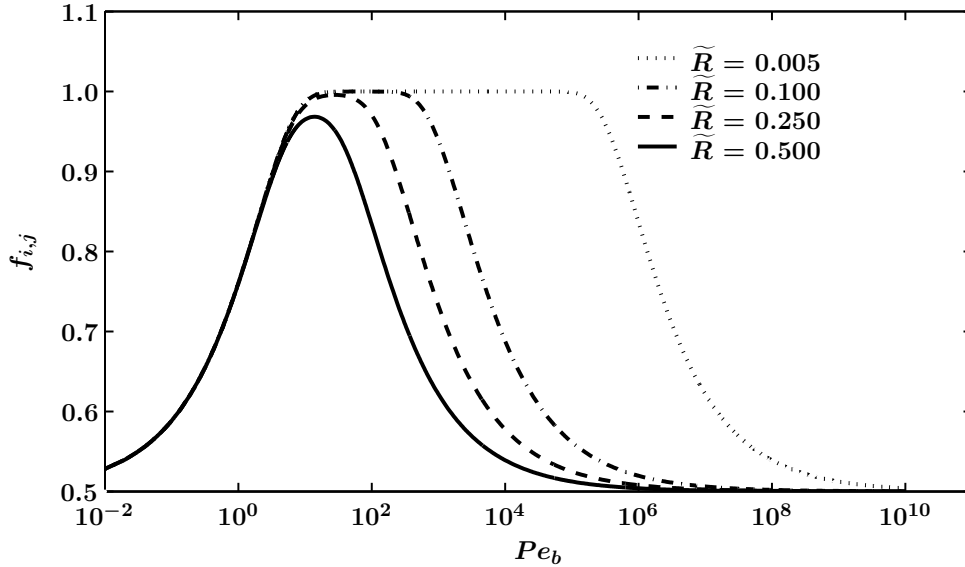


Figure 3.2: Approximation of  $f_{i,j}$  as a function of  $Pe_b$  and aspect ratio  $\tilde{R}(= R/\ell)$ , based on the Taylor-Aris solution (3.13).

After the transition of a particle from one bond to the next, we assume that the radial position of the particle is preserved. In other words, in the new bond the particle starts at the same value of the dimensionless local radial coordinate  $\lambda$  at which it left the previous bond [Sorbie and Clifford 1991; Damion et al. 2000].

Considering the global initial conditions, we distribute the particles at the inlet face proportional to the flow rate of the inlet bonds [Sorbie and Clifford 1991; Damion et al. 2000], i.e. the probability  $p(\text{inlet}, j)$  for a particle to enter the system through bond  $j$  at the inlet is given by

$$p(\text{inlet}, j) = \frac{q_{\text{inlet},j}}{Q}, \quad (3.29)$$

similar to Eq (3.25), where  $Q$  is the total discharge through the network. Similarly, the probability  $p(\lambda_0)$  for a particle to enter at radial position  $\lambda$  is proportional to the flow rate in the tube, i.e.

$$p(\lambda) = 2\lambda f(\lambda), \quad (3.30)$$

where  $f(\lambda)$  denotes the velocity profile of Eq (3.16).

## 3.4 Simulations

### 3.4.1 Single tube

We check our particle tracking algorithm by reproducing the four classical experiments of Taylor [Taylor 1953] in a single tube. Additionally, we assess how the various methods to obtain the resulting dispersion coefficient,  $D_T$  or equivalently the Taylor Peclet number  $Pe_T$  (Eq (3.14)), perform for a single tube.

The aspect ratios ( $\tilde{R} = R/\ell$ ) and the bond Peclet numbers ( $Pe_b$ ), calculated using Eq (3.12), for these experiments are given in Table 3.1. These input parameters are based on a constant tube radius  $R = 2.52 \times 10^{-4}$  m and varying tube lengths and velocities. For example, for Experiment 2,  $\ell = 0.632$  m and  $u = 2.633 \times 10^{-3}$  m/s.

For Taylor the molecular diffusion coefficient  $D_m$ , assumed the same for all four experiments, was not an input parameter, but the *result* of his experiments. Taylor determined  $D_T$  by fitting the CFTD to the Taylor-Aris solution (3.13) and then obtained  $D_m$  using (the second term of) Eq (3.11). We take the value of  $D_m = 8.0 \times 10^{-10}$  m<sup>2</sup>/s obtained by Taylor as the true “experimental” value, to calculate the indicated values of  $Pe_b$  and to recalculate the values of  $D_T$  and  $Pe_T$ , using Eqs (3.11) and (3.15) respectively, where the latter are given in Table 3.1. In the simulations we additionally assume a parabolic velocity profile in the tube from Eq (3.16) and employ 25,000 particles for the random walk calculation.

A fair comparison with Taylor’s results can only be made if we also fit our CFTD results to Eq (3.13) and compare the resulting  $Pe_T$  with the values listed in Table 3.1. This produces Taylor’s exact procedure using our particle tracking results. However, we additionally calculate  $Pe_T$  from both the secant and tangent methods for the SPD, as well as from the two methods using the FTD moments, Eqs (3.9) and (3.10) respectively, as explained in Section 3.2. Moreover, the evolution of the SPD over time and the FTD at multiples of length  $\ell$  are recorded to check whether and when the various processes limit to a constant asymptotic dispersion coefficient.

In Figure 3.3a, we present the breakthrough curve (BTC) from simulation of Taylor’s experiments at 1 unit length  $\ell$ . Observe that the BTCs for Experiments 1 and 2 are symmetric whereas the BTCs for Experiments 3 and 4 are asymmetric, indicating that, for the latter two experiments, asymptotic conditions have not yet been reached. However, as demonstrated in Figure 3.3b, after an elapse of larger times and at greater lengths the BTCs of Experiment 3 and 4 also start to approach symmetric shapes.

Also from evolution of the simulated second central moment  $\sigma_X^2$  of the SPD, presented in Figure 3.4a, it is clear that only asymptotic conditions are reached in a transition time much smaller than 0.5 for Experiments 1 and 2 [Taylor 1953; 1954; Aris 1956; Bruderer and Bernabé 2001]. Indeed, our simulation results agree with Taylor’s comments [Taylor 1953] that Experiments 3 and 4 are not suitable for obtaining  $D_T$  (hence  $D_m$ ), because of the large transition times.



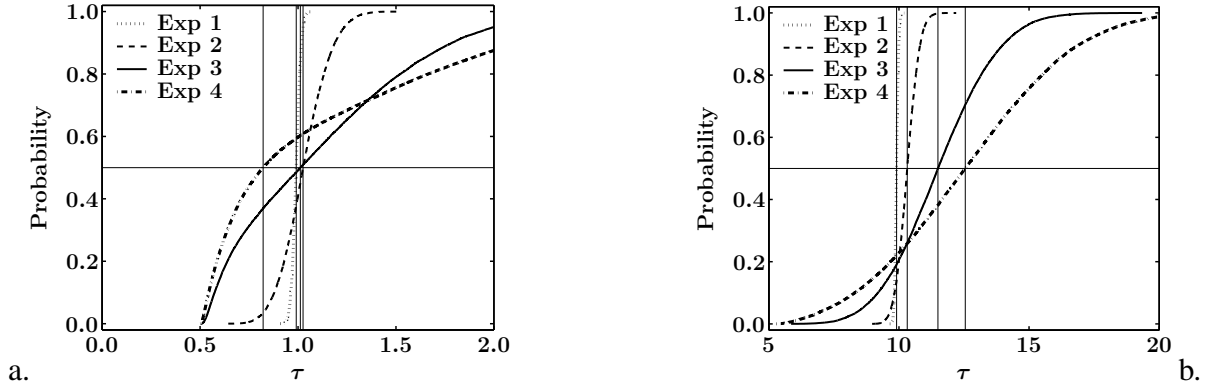


Figure 3.3: Breakthrough curves (FTD) from simulation of Taylor's experiments a. at 1 unit length and b. at 10 unit lengths.

Comparison of the analytical (experimental) and simulated  $Pe_T$  in Table 3.1, based on fitting the CFTD to Eq (3.13) shows best agreement for Experiment 2. Indeed, Taylor used Experiment 2 to obtain the indicated value of  $D_m$ . Nevertheless, this result indicates that our particle tracking method accurately reproduces the dispersion physics in a single tube. Additionally, good agreement is obtained for Experiment 1 with poorer agreement for Experiments 3 and 4, as expected.

Considering the different methods for obtaining  $Pe_T$ , Figure 3.4a visualizes the secant method, indicating that for Experiments 1 and 2, this method will accurately reproduce the experimental  $Pe_T$ . For experiments 3 and 4, results in Figure 3.4a indicate that discrepancies remain even when asymptotic conditions seem to have been reached. Similar trends are found when  $Pe_T$  is calculated using both the SPD and FTD statistics at multiples of the unit length  $\ell$  of the tube. Only for Experiments 1 and 2 does the simulated  $Pe_T$  converge immediately, although fluctuations occur for some of the methods.

As shown in Figure 3.4b, the secant method produces an average  $Pe_T$  of 150.56 with only minor fluctuations. Almost identical values are found for the new FTD method using Eq (3.10). These are structurally higher than the value found based on fitting to the CDE solution (3.13) (both experimental and simulated). The tangent method shows significant fluctuations [Bruderer and Bernabé 2001] and an even higher average value. The values for the old FTD method based on Eq (3.9) average to almost the same value as based on fitting to Eq (3.13). Notice also that the trend in the fluctuations for all methods, except the tangent method, are similar.

We conclude from these single tube simulations that our particle tracking algorithm matches the qualitative behaviour observed in the experiment. Moreover, almost identical values for the dispersion coefficient are produced, when these are obtained using the same method as in the experiment, i.e. fitting of the CFTD to Eq (3.13), and when asymptotic conditions are reached. Comparing the different methods for obtaining  $Pe_T$  shows that the tangent method is not very stable [Fadili et al. 1999; Bruderer and Bernabé 2001]. The secant method and the new FTD method produce nearly identical results, although these are different from the results obtained using the old FTD method, which in turn matches the results obtained from fitting of Eq (3.13) to the CFTD. It should be stressed that the good agreement of the latter method with the experimental result does *not* mean that this method produces a better approximation of the true dispersion coefficient. However, it is important that Eq (3.10), which is based on temporal statistics, manages to match results from the secant method, which is based on spatial statistics. Furthermore, these conclusions are based on a very limited range of  $Pe_b$  and  $\tilde{R}$  and for a single

tube only. In the next section, we investigate how these methods perform for networks of pores for a wide range of characteristic Peclet numbers, although we will no longer use the tangent method in this work.

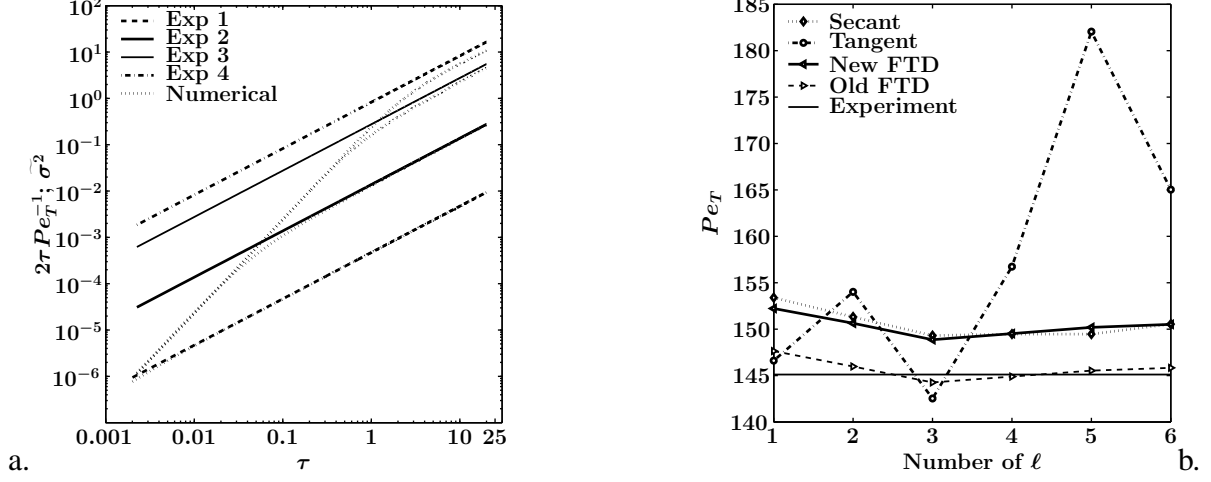


Figure 3.4: Asymptotic behaviour of dispersion for Taylor's experiments: a. evolution of simulated dimensionless second central moment (variance)  $\tilde{\sigma}^2(= (\sigma_X/\ell)^2)$  with time for the four experiments, where straight lines indicate the corresponding analytical (experimental) values  $2\tau/Pe_T$  (for Experiment 1 and 2 the numerical and analytical results exactly coincide); b.  $Pe_T$  at multiples of unit length for Experiment 2 using the various methods for calculating  $Pe_T$ .

Table 3.1: Input parameters for Taylor's single tube experiments with analytical/exp (exp) and simulated (sim) values of  $Pe_T$

Experiments	1	2	3	4
$\tilde{R} \times 10^3$	0.7900	0.3987	0.3150	0.7636
$Pe_b$	11337	2080333	66666667	34031250
$Pe_T$ (exp)	4244.50	145.11	7.26	2.42
$Pe_T$ (sim)*	4324.40	145.89	7.57	3.75

\* Simulation results processed using Eq (3.13)

### 3.4.2 Network modeling results

In Section 3.2 we have discussed various methods to determine the macroscopic dispersion coefficient  $D_L$  from pore-scale simulations. In Section 3.4.2.1 we will assess these methods based on network simulations for a very wide range of characteristic Peclet numbers  $Pe_\ell$  (Eq (3.4)), i.e.  $10^{-5} < Pe_\ell < 10^{10}$  by varying the mean velocity  $v$ . Through comparison with experimental results and on the basis of theoretical considerations, we discuss which methods are appropriate for a particular range of  $Pe_\ell$ . Based on the results from Section 3.4.2.1, we *a priori* discard the tangent method, because of its expected oscillatory behaviour, and use only the secant method for determination of  $D_L$  from the SPD approach. The network simulations are carried out for a particular choice of the nodal conditions, assuming that the effect of the

latter is small compared to the method for determining  $D_L$ . In Section 3.4.2.2 we present the sensitivity of  $D_L$  to the nodal jump conditions presented in Section 3.3.2 and the intra-tube velocity profile as described by Eq (3.16). Table 3.2 contains the parameters for the various choices of profiles and jump conditions used in our network dispersion simulations.

Table 3.2: Cases with different velocity profiles (Eq (3.16)) and nodal jump conditions

Cases	intra-tube velocity	nodal jump conditions	$Pe_{ref}$
	profile	model	
A	parabolic	Eq (3.23) with (3.26)	0.4
B	plug-like	Eq (3.23) with (3.26)	0.4
C	parabolic	Eq (3.25)	NA
D	parabolic	Eq (3.23) with (3.27)	NA
E	parabolic	Eq (3.23) with (3.26)	0.0
F	parabolic	Eq (3.23) with (3.26)	0.25

Additionally, we demonstrate the effect of increasing the network heterogeneity on the impact that the nodal jump conditions have on the longitudinal dispersion coefficient. For this purpose we have carried out simulations for two networks with different heterogeneity, labeled HW1 and HW2. Both networks have  $50 \times 25 \times 25$  nodes and coordination number  $z = 6$ . In network HW1 pore radii are distributed uniformly between  $R_{min} = 5 \times 10^{-6}$  m and  $R_{max} = 55 \times 10^{-6}$  m, and similarly, in network HW2 we take  $R_{min} = 1 \times 10^{-6}$  m and  $R_{max} = 101 \times 10^{-6}$  m.

For all simulations the diffusion coefficient is taken as being the same value as before, i.e.  $D_m = 8.0 \times 10^{-10}$  m<sup>2</sup>/s and the bond lengths are taken as constant, i.e.  $\ell = 2.5 \times 10^{-4}$  m. Hence, for example, for simulations with  $Pe_\ell = 1$ , the mean velocity is  $v = 3.2 \times 10^{-6}$  m/s. With 50 nodes in the flow direction the network length is  $L = 1.25 \times 10^{-2}$  m.

As a base case, we take the parameters of case A in Table 3.2 for the velocity profile and nodal jump conditions and network HW1. These parameters are used in Section 3.4.2.1. Furthermore, we inject 5000 particles unless stated otherwise in Section 3.4.2.1. Computation times for the base case (network HW1) range from two hours for  $Pe_\ell = 10^{10}$  to 70 hours for  $Pe_\ell = 10^{-5}$  on a computer with speed 2.6 GHz. However, simulation times vary also with heterogeneity.

In the literature dimensionless dispersivity is often plotted in two ways, i.e. either as  $D_L/D_m$  or in terms of  $v\ell/D_L$  (or the reciprocal of the latter) [Bear 1972; Sorbie and Clifford 1991], both as functions of  $Pe_\ell$ . Since on a logarithmic scale  $D_L/D_m$  distinguishes the various cases more clearly for  $Pe_\ell$  regimes where  $D_L$  is (approximately) constant, and  $v\ell/D_L$  distinguishes for  $Pe_\ell$  regimes where  $D_L$  varies (approximately) linearly with  $v$ , we use both quantities where appropriate.

### 3.4.2.1 Assessment of methods to determine macroscopic dispersion regimes

For case A of Table 3.2, we have carried out simulations in network HW1, where  $D_L$  is obtained according to the various methods described in Section 3.2. To calculate  $D_L$  based on the spatial distribution of particles (SPD), particles are injected inside the network at some distance from the inlet (9 bonds in the flow direction). This is important for low velocities, since particles

may leave the network through the inlet by diffusive action. If this happens, they are reinjected into the inlet although this may somewhat bias our results. Furthermore, when using SPD we use the secant method to determine  $D_L$ .

When using the temporal distribution of particles (FTD), we have applied the two versions of the method of moments, i.e. the old method based on Eq (3.9) and the new method based on Eq (3.10). Furthermore,  $D_L$  has been determined by fitting the CFTD to solution (3.6) of the convection-dispersion equation. For the new FTD method of moments and for fitting to the CDE, the results for both 5000 and 10000 particles are presented. In Figure 3.5 we present  $D_L/D_m$  based on the various methods as a function of  $Pe_\ell$  along with Saffman's theoretical curve [Saffman 1960]

$$\frac{D_L}{D_m} = \frac{Pe_\ell}{6} \left[ \ln\left(\frac{3}{2}Pe_\ell\right) - \frac{1}{4} \right], \quad (3.31)$$

which is shown for  $Pe_\ell \gg 1$ . In Figure 3.6 the corresponding plot of  $v\ell/D_L$  versus  $Pe_\ell$  is

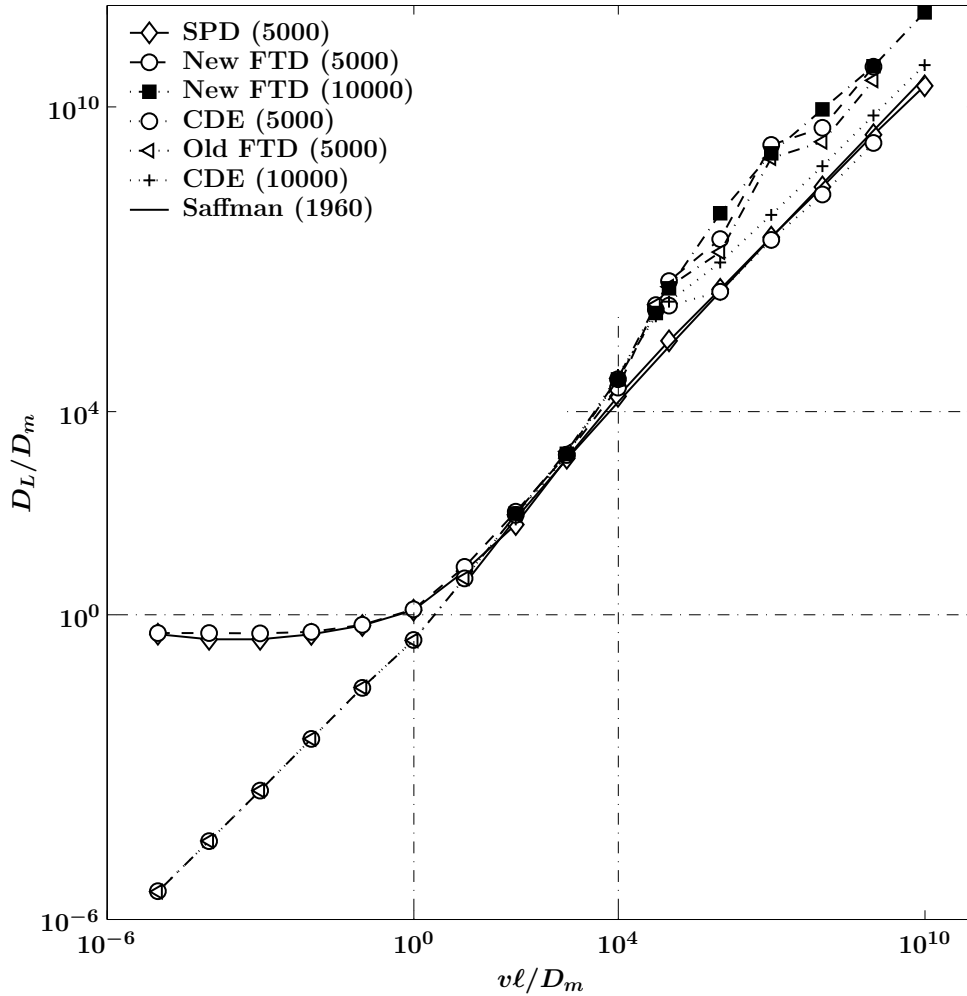


Figure 3.5:  $D_L/D_m$  as a function of  $Pe_\ell$  (for case A on network HW1) based on the following methods: the secant method for SPD (Eq (3.5)), the old FTD moment method (Eq (3.9)), the new FTD moment method (Eq (3.10)) and fitting of the CFTD to solution (3.6) of the CDE (3.1). The numbers of particles used for each method are indicated in brackets. Additionally, the Saffman (1960) theoretical relation (3.31) is shown.

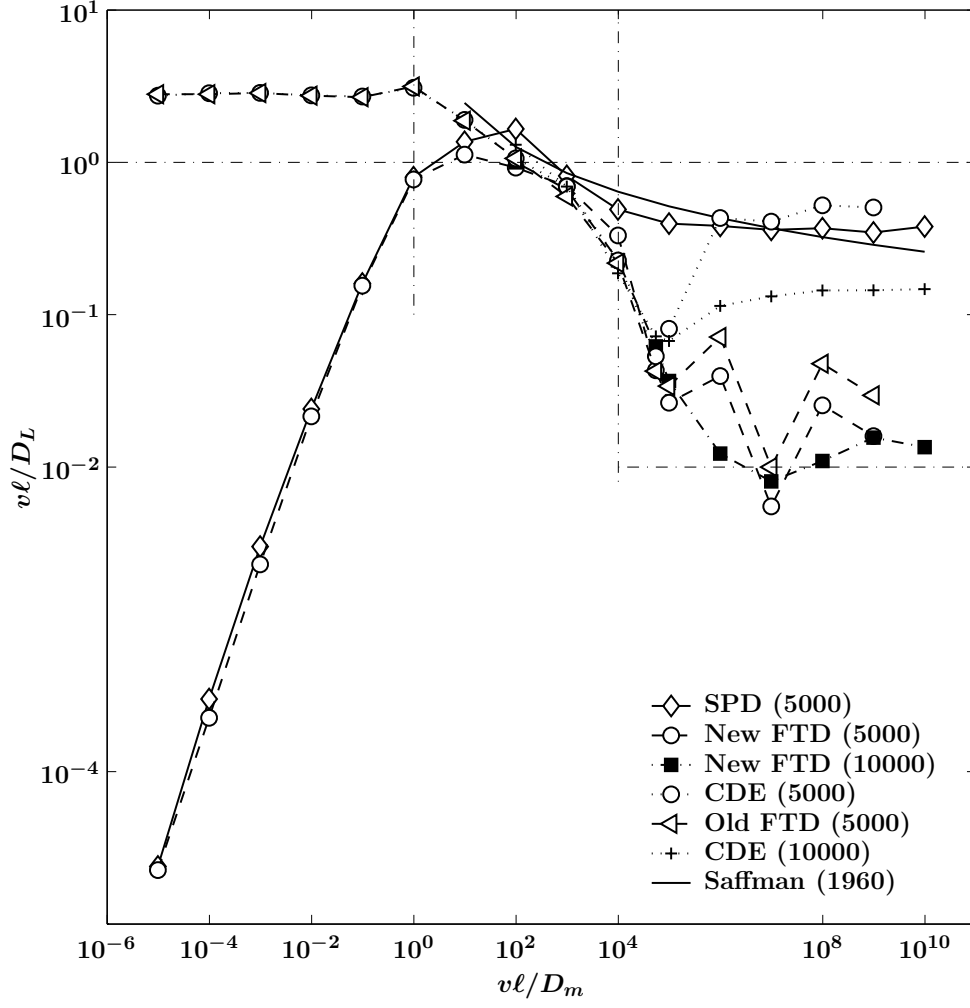


Figure 3.6:  $v\ell/D_L$  as a function of  $Pe_\ell$  (for case A on network HW1) based on the methods explained in Figure 3.5.

presented.

It is immediately clear that for small  $Pe_\ell$ , say  $Pe_\ell < 10$ , a large discrepancy arises between the SPD and the new FTD moment methods on the one hand and the remaining methods on the other hand. For the FTD we have found that both  $\langle t \rangle$  and  $\sigma_t^2$  are independent of  $v$  ( $Pe_\ell$ ), which we show explicitly in Section 3.4.2.2. As argued in Section 3.2, we believe that the SPD and the new FTD moment methods correctly produce a constant  $D_L$  in the regime  $Pe_\ell < 10^{-2}$ , where diffusion dominates [Koch and Brady 1985]. This is also in agreement with experimental results presented in the literature [Perkins and Johnston 1963; Bear 1972]. The small discrepancy between SPD and new FTD is probably caused by the above-mentioned reinjection at the inlet when using SPD. It has long been known that the SPD is most appropriate for small  $Pe_\ell$  [Sorbie and Clifford 1991], but the current results show that FTD can also be used, in agreement with the single tube results of Section 3.4.1, provided that the correct quantities are substituted for  $\mu_X$  and  $t$  in Eq (3.8).

In the approximate range  $10 < Pe_\ell < 10^4$ , all methods produce very similar results, which are in turn in agreement with Saffman's Eq (3.31). For this range, Eq (3.31) gives  $D_L/D_m \sim Pe_\ell^\beta$ , with exponent  $\beta \approx 1.19$  [Sahimi and Imdakm 1988], whereas we find  $\beta \approx$

1.29. Numerically and experimentally reported values of  $\beta$  are: 1.27 [Sahimi et al. 1983b], 1.24 [Legatski and Katz 1967], 1.2 [Brigham et al. 1961], from 0.96 to 1.51 [Carbonell 1979], from 1.0 to 2.0 [Bruderer and Bernabé 2001], hence we are well within the reported range. In this regime histograms of both SPD and FTD are close to Gaussian, hence the coefficients of variation are indeed approximately the same and, according to Eq (3.7), the results from both methods should be the same. Moreover, in this regime both convection and molecular diffusion are important, hence it is not surprising that the CDE fitting method also yields acceptable results.

For  $Pe_\ell > 10^4$ , the results for  $D_L$  from both FTD moment methods are similar, but they are different from the remaining results. The differences are more clear in the diagram of  $v\ell/D_L$  shown in Figure 3.6. The results for the FTD moment methods fluctuate, but increasing the number of particles from 5000 to 10000 (for the new FTD) suppresses the fluctuations. Anyway, in this regime the results from the SPD are known to be unreliable due to the small size of the present network. Additionally, fitting to the CDE and the FTD moment methods leads to different results. Since in this regime convection dominates over (molecular) diffusion in the longitudinal direction, the breakthrough curves are asymmetric, hence the CDE fitting results cannot be considered as being reliable [Perkins and Johnston 1963; Han et al. 1985]. The trend of the FTD results is that, approximately for  $Pe_\ell > 10^6$ ,  $v\ell/D_L$  becomes independent of  $Pe_\ell$ , i.e.  $D_L$  varies linearly with  $v$  [Brenner 1980; De Arcangelis et al. 1986; Sorbie and Clifford 1991].

In summary, we have found three distinct  $Pe_\ell$  regimes for  $D_L$  as was theoretically envisaged by Brenner [Brenner 1980]. For small  $Pe_\ell$  (roughly  $Pe_\ell < 10^{-2}$ ),  $D_L$  is independent of  $Pe_\ell$ . For intermediate  $Pe_\ell$  (roughly  $10 < Pe_\ell < 10^4$ ),  $D_L$  varies proportional to  $Pe_\ell^\beta$ , with  $\beta \approx 1.29$ . For large  $Pe_\ell$  (roughly  $Pe_\ell > 10^6$ )  $D_L$  varies linearly with  $Pe_\ell$ , with transitory behaviour in between. Considering the various methods to determine  $D_L$ , we have found that for small  $Pe_\ell$  the new FTD moment method, in agreement with the SPD, correctly yields  $D_L$  independent of  $Pe_\ell$ , contrary to the remaining FTD methods. For intermediate  $Pe_\ell$  all methods produce similar results. For large  $Pe_\ell$  both FTD moment methods produce similar results and are more appropriate than SPD, due to network size, and fitting to the CDE solution. However, an increased number of particles is required to stabilise the results obtained with the FTD moment methods.

### 3.4.2.2 Sensitivity study of nodal jump conditions and velocity profiles

In Figure 3.7, we present  $D_L/D_m$  versus  $Pe_\ell$  calculated from simulations on network HW1 using the parameters for the various choices of profiles and jump conditions of Table 3.2. In view of the results of the previous section,  $D_L$  has been calculated based on the new FTD methods of moments for all simulations, while 5000 particles have been injected.

Approximately for  $Pe_\ell < 1$  the dispersion coefficient is independent of  $Pe_\ell$  for all cases, as expected, although the close-up for low  $Pe_\ell$  in Figure 3.7a shows that this regime is more likely to be  $Pe_\ell < 10^{-2}$ , which is in close agreement with the observations made by Perkins and Johnston [Perkins and Johnston 1963]. Qualitatively, we find that cases A, D and F are almost the same, with only a small deviation around  $Pe_\ell = 0.1$ , i.e. around the value of  $Pe_{ref}$  in Eq (3.23). For example, cases A and F have different values of  $Pe_{ref}$ , but if  $Pe_\ell$  is well below these values, we may assume that also locally  $Pe_b < Pe_{ref}$ , hence no difference will be seen. Similarly, Eq (3.27) (case D) is a smoothed version of Eq (3.26) with a transition around  $Pe_\ell = 1$ . However, if diffusion at the nodes is neglected (case C) or upstream jumps are not

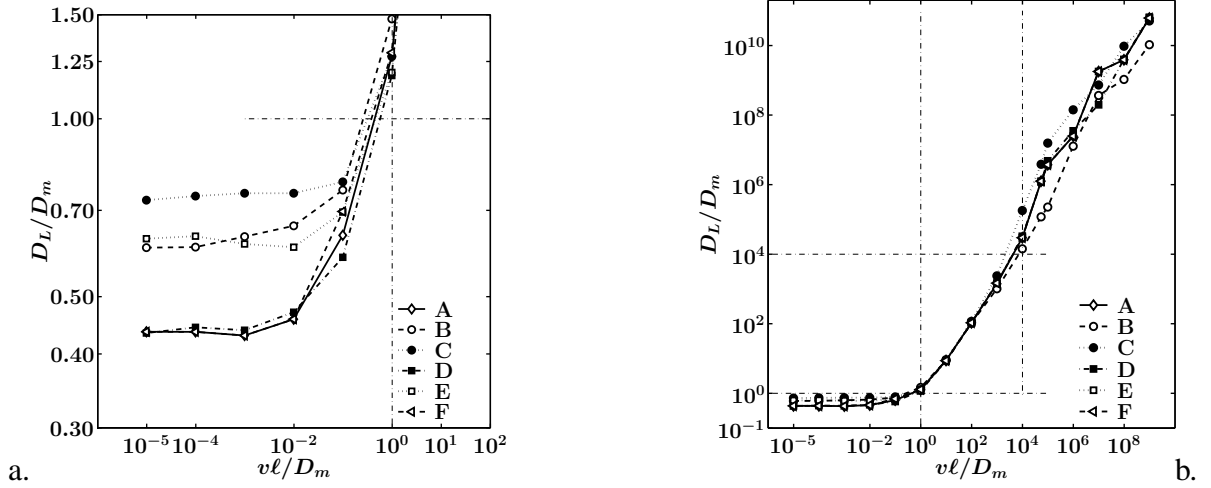


Figure 3.7:  $D_L/D_m$  versus  $Pe_\ell$  on network HW1 for the various cases indicated in Table 3.2 for a. small  $Pe_\ell$  and b. the full range of  $Pe_\ell$ .

allowed at the nodes (case E), the resulting dispersion is different. Similarly, if the velocity profile in the bonds is not parabolic (case B), an effect is found. This is slightly surprising, because in the diffusion dominated regime, we may expect that the small difference between the velocity profiles is washed out by molecular diffusion.

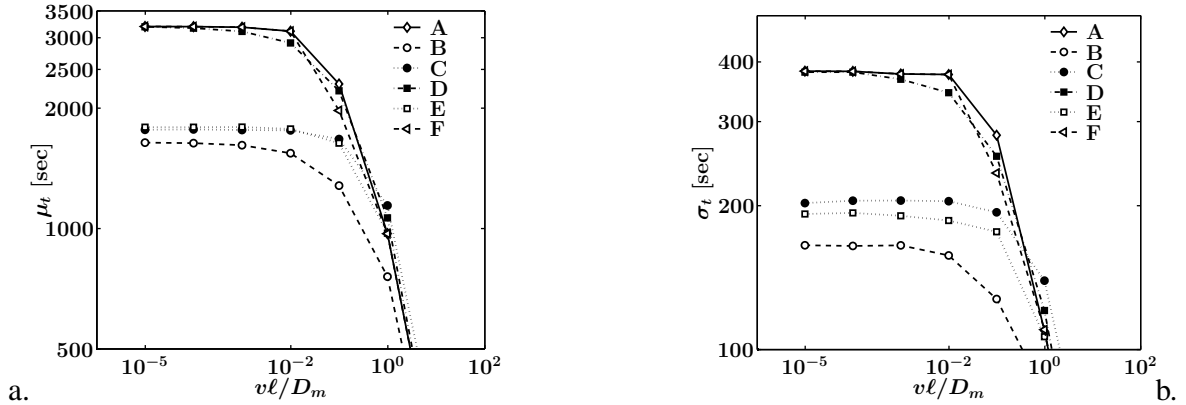


Figure 3.8: a. Mean  $\mu_t$  and b. standard deviation  $\sigma_t$  of the FTD on network HW1 for small  $Pe_\ell$  for the various cases indicated in Table 3.2.

The ordering of  $D_L$  for the various cases is slightly counterintuitive. For example, cases A, D and F with (most) diffusive action at the nodes, shows smallest  $D_L$ . To explain this, consider the raw data of the mean arrival time  $\mu_t$  and standard deviation  $\sigma_t$  as a function of  $Pe_\ell$ , presented in Figure 3.8. This shows that cases A, D and F are indeed the same with respect to both quantities for  $Pe_\ell < 10^{-2}$ . On the other hand, the remaining cases all have smaller  $\mu_t$  and  $\sigma_t$ . On balance, this leads to larger  $D_L$  when using Eq (3.10). Notice that the constant value of  $D_L/D_m$  for cases A, D and F is approximately 0.42, which falls well within the range of 0.3 to 0.707 [Bear 1972].

Approximately for  $1 < Pe_\ell < 10^3$ , all methods produce very similar  $D_L$ . In this regime, nodal jump conditions are not very important, as was envisaged by de Josselin de Jong [De Josselin de Jong 1958].

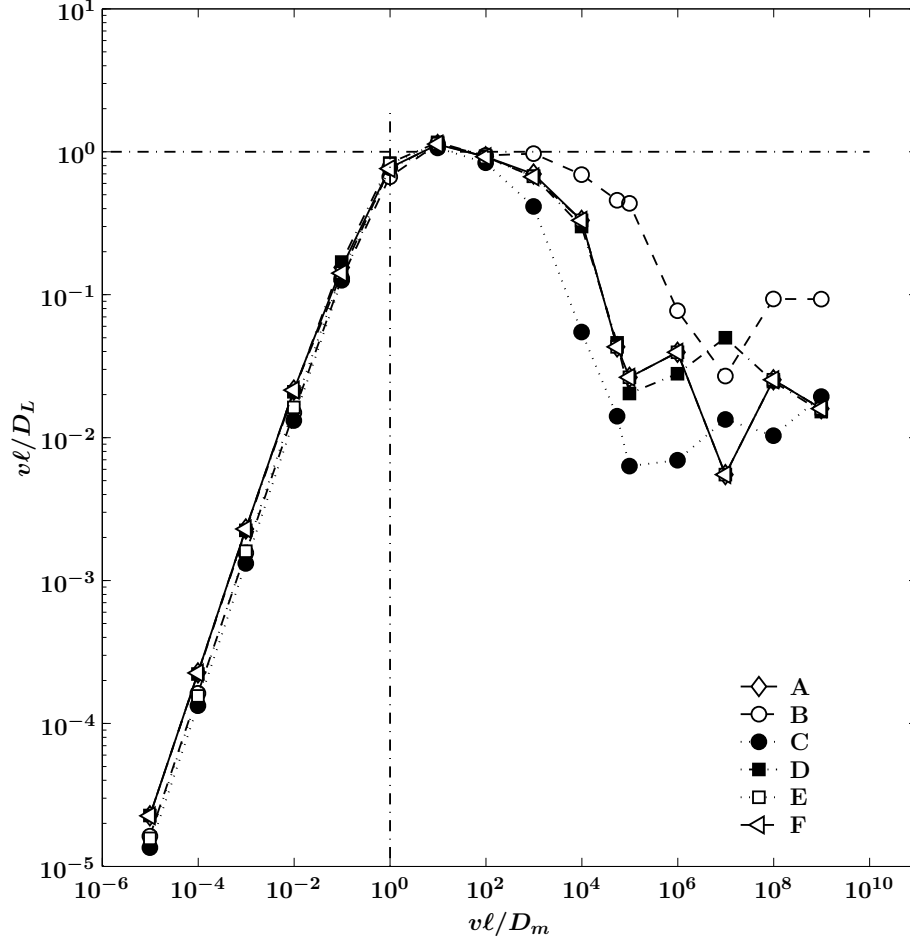


Figure 3.9:  $v\ell/D_L$  versus  $Pe_\ell$  on network HW1 for the various cases indicated in Table 3.2.

For  $Pe_\ell > 10^3$ , the plug-like velocity profile within the bonds (case B) produces significantly less dispersion than the remaining cases, where the Taylor like interaction of the parabolic intra-tube profile with molecular diffusion increases the macroscopic dispersivity [Han et al. 1985]. This becomes even more clear from the plot of  $v\ell/D_L$  versus  $Pe_\ell$  presented in Figure 3.9. Unfortunately, the oscillatory behaviour for large  $Pe_\ell$  obscures possible differences between the remaining cases. However, for the regime  $10^3 < Pe_\ell < 10^5$ , Figure 3.9 clearly demonstrates that case C, with no diffusion at the nodes, is different from cases A, D, E and F, and leads to larger macroscopic dispersion. The fact that case E ( $Pe_{ref} = 0$ ) coincides with cases A, D and F, shows that in this regime upstream jumps at the nodes do no longer occur. Notice that for  $Pe_\ell = 10^5$  the quantitative difference between the  $D_L$  for the two cases with smallest and largest dispersion (cases B and C respectively) is very significant, i.e. about 1.5 orders of magnitude. As concluded in the Section 3.4.2.1, roughly for  $Pe_\ell > 10^6$ ,  $D_L$  varies linearly with  $v$ .

In Figure 3.10 we present  $D_L/D_m$  versus  $Pe_\ell$  calculated from simulations on the more heterogeneous network HW2 (wider range of pore sizes) using the parameters for cases A to E of Table 3.2. The larger heterogeneity has increased  $D_L$  overall, although the qualitative behaviour of the profiles has hardly changed. The close-up for  $Pe_\ell < 1$  presented in Figure 3.10a shows that the effect of the intra-tube velocity profile has vanished as a result of increased heterogeneity, since the results for case B coincide with those for cases A and D. On the other



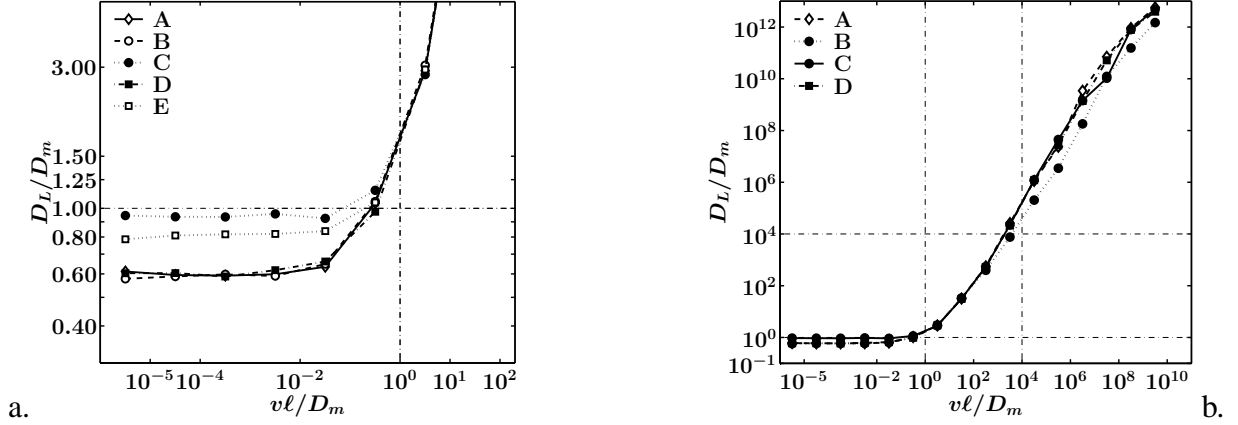


Figure 3.10:  $D_L/D_m$  versus  $Pe_\ell$  on network HW2 for a. small  $Pe_\ell$  for cases A to E indicated in Table 3.2 and b. the full range of  $Pe_\ell$  for cases A to D.

hand, absence of diffusion at the nodes, represented by case C, or suppression of upstream jumps, represented by case E, still leads to increased macroscopic dispersivity.

The constant value of  $D_L/D_m \approx 0.60$  for cases A, D and D is larger than for HW1 as the pore-size heterogeneity gives rise to more dispersion [Han et al. 1985]. The values of  $D_L/D_m \approx 0.94$  for case C and  $D_L/D_m \approx 0.80$  for case E are probably too high in view of experimental evidence [Legatski and Katz 1967; Han et al. 1985]. This means that the nodal jump conditions (3.23) must include diffusion, in both the downstream and upstream direction, as proposed by Sorbie and Clifford [Sorbie and Clifford 1991], to reproduce dispersion in porous media with substantial pore-scale heterogeneity correctly.

As in network HW1 for  $1 < Pe_\ell < 10^3$ , all methods produce very similar  $D_L$ . The exponent in the approximation  $D_L/D_m \sim Pe_\ell^\beta$  of Saffman's relation (3.31) for this regime is  $\beta \approx 1.48$  for case A, which is significantly larger than for network HW1, but still within the range of reported values, mentioned in Section 3.4.2.1. Han et al. [Han et al. 1985] showed that dispersion increases with the variance of bed-particles, i.e. pore-scale heterogeneity.

However, for  $Pe > 10^3$ ,  $D_L$  is again smaller for the plug-like flow profile (case B), as is shown more clearly in Figure 3.11 for  $v\ell/D_L$ . Contrary to the more homogeneous network, diffusion at the nodes (case C) no longer has a significant effect. Around  $Pe = 10^6$ , the largest difference in  $D_L$  between case B and the remaining cases is found, which is about 1.2 orders of magnitude. The constant value of  $v\ell/D_L$  for large  $Pe_\ell$  is smaller than for network HW1 and is reached later, i.e. roughly for  $Pe_\ell > 10^8$ .

In summary, for small  $Pe_\ell$  nodal jump conditions without diffusion (case C) and without upstream jumps (case E), as well as flow without a parabolic velocity profile (case B) lead to increased dispersivity, compared to cases including all these effects. However, for increasing network heterogeneity the effects of different profiles disappear. For intermediate  $Pe_\ell$  all nodal jump conditions produce approximately the same  $D_L$ . For large  $Pe_\ell$  some effect of neglecting nodal diffusion is observed, which disappears for increased network heterogeneity, and a significant underestimation of  $D_L$  occurs for the plug-like velocity profile compared to the remaining cases, independent of network heterogeneity. Furthermore, for increased heterogeneity  $D_L$  is larger in all regimes, the Saffman exponent  $\beta$  for the intermediate regime is larger and the regime with linear dependence on  $Pe_\ell$  is reached later.

### 3.5 Summary and conclusions

We have developed a 3D network model with particle tracking to upscale 3D Brownian motion of non-reactive tracer particles subjected to a velocity field in the network bonds, representing both molecular diffusion and convection. At the intersections of the bonds (nodes) various jump conditions have been implemented along with two different velocity profiles within the bonds. At the network scale the longitudinal dispersion of the particles is quantified through the coefficient  $D_L$ , for which we have evaluated a number of methods already known in the literature. Additionally, we have introduced a new method for deriving  $D_L$  based on the First-arrival Time Distribution (FTD), i.e. Eq (3.10). To validate our particle tracking method, we have simulated Taylor's classical experiments in a single tube [Taylor 1953; 1954]. Subsequently, we have carried out network simulations for a wide range of the characteristic Peclet number  $Pe_\ell$  to assess the various methods for obtaining  $D_L$ . Using the most suitable method, additional simulations have been carried out to evaluate the choice of nodal jump conditions and velocity profile, in combination with varying network heterogeneity.

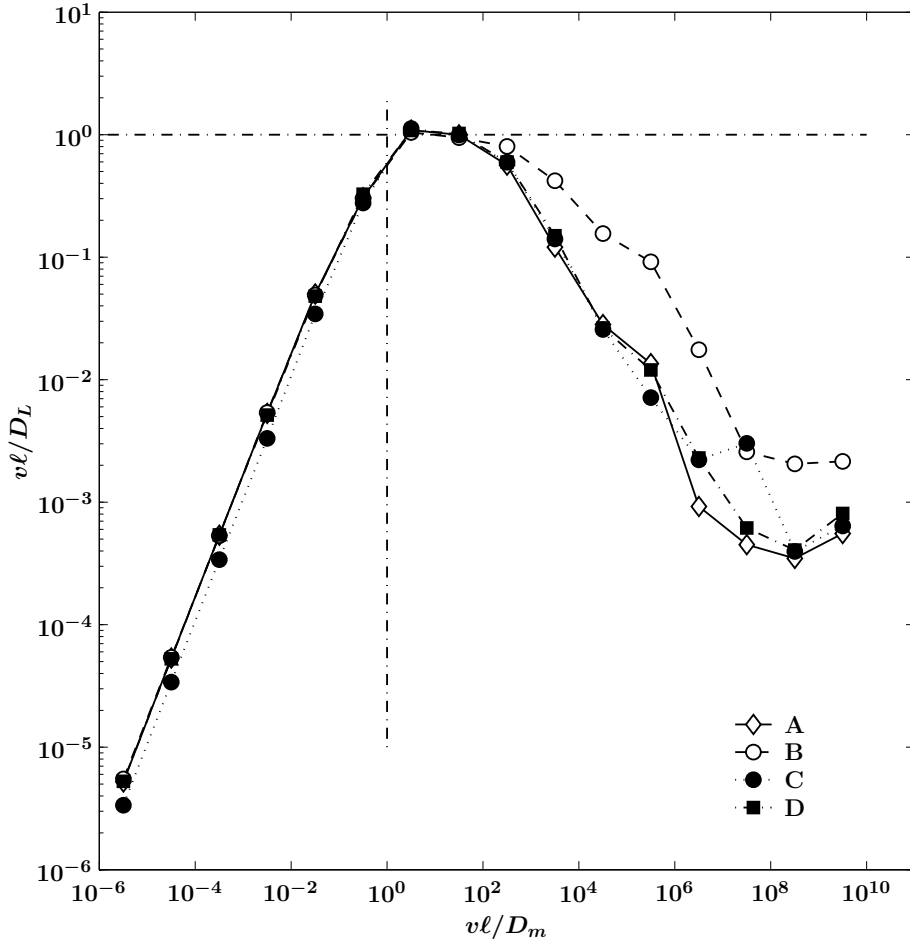


Figure 3.11:  $v\ell/D_L$  versus  $Pe_\ell$  on network HW2 for cases A to D indicated in Table 3.2.

From simulating Taylor's single tube experiments we conclude:

- (i) Our particle tracking algorithm matches the experimentally found single tube dispersion coefficient  $D_T$  very well, provided that the same method is used to obtain  $D_T$ , i.e. fitting the Cumulative FTD (CFTD) to an analytical solution of the convection-dispersion

equation. Furthermore, only in two of the four simulations the transition times to reach asymptotic conditions for  $D_T$  are short enough to produce reliable results, in agreement with the experiments. The single tube simulations show further that the tangent method to determine  $D_T$  from the Spatial Position Distribution (SPD) leads to oscillatory results and that the secant method is preferable.

From the network simulations we conclude:

- (ii) In general three distinct  $Pe_\ell$  regimes for  $D_L$  arise. For small  $Pe_\ell$ ,  $D_L$  is independent of  $Pe_\ell$  as molecular diffusion dominates. For intermediate  $Pe_\ell$ ,  $D_L$  varies proportional to  $Pe_\ell^\beta$ , with  $\beta > 1$ , in agreement with a relation by Saffman [Saffman 1960]. For large  $Pe_\ell$ ,  $D_L$  varies linearly with  $Pe_\ell$ , as convection dominates.
- (iii) Considering the various methods for determining  $D_L$ , we have found that for small  $Pe_\ell$  the new FTD moment method, in agreement with the SPD secant method, correctly yields  $D_L$  independent of  $Pe_\ell$ , contrary to the remaining FTD methods. For intermediate  $Pe_\ell$ , all methods produce similar results. For large  $Pe_\ell$ , the FTD moment methods produce similar results and are more appropriate than SPD, due to network size, and fitting of the CFTD to an analytical solution of the CDE. However, an increased number of particles is required to stabilise the results obtained with the FTD moment methods.
- (iv) For small  $Pe_\ell$ , nodal jump conditions without diffusion or without upstream jumps, as well as flow without a parabolic velocity profile lead to increased dispersivity, compared to cases including all of these effects. For intermediate  $Pe_\ell$ , all nodal jump conditions produce approximately the same  $D_L$ . For large  $Pe_\ell$ , some effect of neglecting nodal diffusion is observed and a significant underestimation of  $D_L$  occurs for the plug-like velocity profile compared to the remaining cases.
- (v) Increasing the network heterogeneity leads to larger  $D_L$  in all regimes, the Saffman exponent  $\beta$  for the intermediate regime is larger and the regime with linear dependence on  $Pe_\ell$  is reached later. Additionally, for low  $Pe_\ell$  the nodal jump conditions without diffusion, i.e. the traditional assumption of flow rate proportionality, and without upstream jumps still lead to overestimation of  $D_L$ , whereas for large  $Pe_\ell$  only the plug-like velocity profile appears to underestimate  $D_L$  quite significantly.

In general, we conclude that the presented network model with particle tracking is a robust tool for calculating the macroscopic longitudinal dispersion coefficient. We have found a new method to determine  $D_L$  from the FTD statistics, which works for the full range of characteristic Peclet numbers, provided that for large  $Pe_\ell$  a sufficiently large number of particles is used. Nodal jump conditions should include molecular diffusion and allow jumps in the upstream direction, and a parabolic velocity profile in the tubes should be implemented. Then, good agreement with experimental evidence is found for the full range of  $Pe_\ell$ , including increased  $D_L$  for increased porous medium heterogeneity.

## Acknowledgements

This study is performed under the research program ‘‘Upscaling Flow and Transport Processes in Porous Media: From Pore to Core’’ funded by the Dutch NWO/ALW project no. 809.62.010. We acknowledge the support of the European Community - Access to Research Infrastructure

action of the Improving Human Potential Programme to use the EIERO infrastructure. RCA appreciates support and cooperation from the Institute of Petroleum Engineering, Heriot-Watt University, Edinburgh, UK.

## Chapter 4

# Comparison of two approaches of pore-network modeling: Mixing cell and Brownian particle tracking<sup>\*</sup>

### Abstract

The purpose of this study is to quantify the dispersivity coefficient in the longitudinal direction by up-scaling the pore scale mixing over a network domain and verify the dispersivity with the one obtained through more rigorous upscaling such as Brownian Particle Tracking Model (BPTM). We model a porous medium with a network of pore-units that are comprised of porebodies and bonds of finite volume. Such a pore-unit is assumed to be a mixing cell with steady state flow condition of water containing a non-reactive tracer, which is allowed to penetrate. By solving the mixing cell model (MCM) for each pore-unit and averaging the concentrations for a large number of pore units as a function of time and space, the dispersivity can be obtained. A minimal size of network that ascertains an asymptotic value of dispersivity was determined and verified with large size pore networks. This numerically computed dispersivity is compared with the results from BPTM for the same porous medium and flow conditions. We have shown that the dispersivity obtained from MCM is equally reliable for the heterogeneous pore-networks and can be estimated as a function of pore size heterogeneity. For homogeneous networks with MCM, the time step for iteration plays an important role. On the other hand for networks with BPTM, the assumption of intra-bond velocity profile affects the results.

*Keywords:* mixing cell model; dispersion; transport; pore network; Brownian motion; particle tracking; nodal jump condition; method of moments; Brownian particle tracking model.

### 4.1 Introduction

Dispersion in porous media is of interest to chemical engineers who are generally concerned with reacting and adsorbing species, to petroleum engineers who are concerned with the (im)miscible displacements that occur during oil recovery [Whitaker 1967], and to civil or environmental engineers who are confronted with the problem of reactive and non-reactive transport in ground water systems. In the theory of transport, dispersion plays a central role as one of the most

---

<sup>\*</sup>by Ram C Acharya, Sjoerd EATM van der Zee and Anton Leijnse, submitted to *Adv Water Res*, 2004.

*List of symbols and notations*

$\langle . \rangle$  Ensemble average quantity

$C, \tilde{C}$  Concentration [ $\text{ML}^{-3}$ ] and dimensionless concentration

$\mathbf{D}, D_L$  Dispersion coefficients: tensor and Longitudinal [ $\text{L}^2\text{T}^{-1}$ ]

$D_m, D_h$  Molecular diffusion coefficient and mechanical dispersion [ $\text{L}^2\text{T}^{-1}$ ]

$f_{i,j}$  Advection-diffusion fraction factor of Sorbie-Clifford formulation

$f(\lambda)$  Intra-pore velocity function

$i, j$  The indices of nodes and bonds

$L, \ell$  Length of the pore-network and bond length [L]

$M_2^c$  Second central spatial moment of plume for  $X$  direction [ $\text{L}^2$ ]

$p(i, j)$  Transition probability density function

$Pe_L$  Pore-network (Column) Peclet number ( $vL/D_L$ )

$Pe_{ref}$  A reference (conditional) threshold bond Peclet number

$Pe_\ell$  Characteristic Peclet number  $v\ell/D_m$

$q_{i,j}, Q$  Discharge respectively through bonds and porenetwork [ $\text{L}^3\text{T}^{-1}$ ]

$R_{pb}, \tilde{R}_{pb}$  Radius of the porebodies respectively diemnsionful and dimensionless ( $R_{pb}/\ell$ ).

$R_b, \tilde{R}_b$  (Equivalent) radius of the bonds [L] and aspect ratio ( $R_b/\ell$ ) of bonds (Taylor's tubes)

$\alpha_L$  Longitudinal dispersivity ( $\sim D_L/v$ ) [L]

$\Delta \mathbf{r}$  Radius vector of Brownian sphere [L]

$t, \Delta t$  Time and time step of iteration [T]

$\tilde{T}$  Dimensionless time on network scale ( $vt/L$ )

$u$  Mean velocity in the Taylor's tubes [ $\text{LT}^{-1}$ ]

$v$  Mean intrinsic velocity along the principle flow direction in the pore network [ $\text{LT}^{-1}$ ]

$x, y$  Local reference system,  $x \in [0, \ell]$  along the axial direction of fluid flow [L]

$X, Y, Z$  Global (network scale) reference system [L]

$\beta$  an exponent parameter

$\phi(\Delta \mathbf{r})$  Green's probability function for Markov's processes

$\mu$  Ensemble average as specified with subscript (e.g.  $\mu_t$  and  $\mu_X$ )

$\varpi$  A factor in Sorbie-Clifford formulation  $(\pi R^2)/\ell$  [L]

$\varphi$  Polar angle of radius vector in Brownian spherical coordinate system  $[0, \pi]$

$\psi$  Deviate of the Green's function [-]

$\zeta$  tortuosity [-]

$\theta$  Azimuthal angle of radius vector in Brownian spherical coordinate system  $[0, 2\pi]$

$T, m, L, b$  Subscripts indicate Taylor, molecular, Longitudinal and bond

*Acronyms*

BPTM Brownian Particle Tracking Model

CDE Convection-Dispersion Equation

(C)FTD (Cumulative) First-arrival Times Distribution

HYPON HYdraulic POre Network model

MCM Mixing Cell Model

SPD Spatial Positions Distribution

important parameters in the Convection-Dispersion Equation (CDE) is the dispersion tensor referred to as  $\mathbf{D}$  [Bear 1972]. Hence, all solutions that have been developed from CDE need a quantification of  $\mathbf{D}$ . Dispersion is caused by two processes, namely the velocity variation of the fluid particles (that carry the miscible contaminant) and molecular diffusion, and hence, dispersion in porous media is referred to as hydrodynamic dispersion [Taylor 1953]. Velocity variation in porous medium originates from the viscous forces within the pores and from pore-scale heterogeneity. The pore-scale heterogeneity is the inherent property due to texture and structure of porous domain [Dagan 1989]. As dispersion originates from medium and fluid-flow properties, its experimental determination is resource demanding.

For a simple case of hydrodynamic dispersion in a capillary tube, Taylor [Taylor 1953] derived an analytical expression for the longitudinal component of  $\mathbf{D}$  referred to as  $D_L$  and verified it with laboratory experiments. However, the Taylor's  $D_L$  is not applicable for the whole domain of porous media [Sorbie and Clifford 1991; Bruderer and Bernabé 2001]. Using the network approach [Fatt 1956a], an upscaling step for  $D_L$  from the randomly oriented capillaries to a continuum domain of porous medium was made by Saffman [Saffman 1959; 1960], which still serves as a theoretical reference in the theory of dispersion [Bear 1972; Appelo and Postma 1993]. However, the experimental data collected so far do not completely agree with the Saffman's theoretical curve [Bear 1972; Han et al. 1985]. On a continuum scale Bear [Bear 1961b; a; 1972] modeled dispersion as a second order tensor that includes velocities, diffusion characteristics of solute and *dispersivity* ( $\sim$  (dispersion coefficient)/velocity) of the porous medium. In continuum domain, it has been established that dispersivity is due to heterogeneity [Bear 1961a; Dagan 1989]. In general, numerical models are used to derive dispersivity by rigorous upscaling. The Mixing Cell Model (MCM) is a widely used example, which employs a finite element/difference scheme to solve the CDE [Sun 1996; Suchomel et al. 1998a]. In this model, the similarity between numerical and physical dispersion is used. The numerically generated dispersion is a function of iteration time step ( $\Delta t$ ) [Sun 1996; Suchomel et al. 1998a] and hence the accuracy of such a numerical dispersion depends on the choice of  $\Delta t$ . In many applications,  $\Delta t$  is assessed by fitting the finite difference scheme into the Taylor's expansion [Sun 1996; Suchomel et al. 1998a] such that a chosen dispersion is produced. Limitation of such approach is that it assumes the concentration function continuous, which is not the case on the microscopic (pore) scale [Suchomel et al. 1998a; Bruderer and Bernabé 2001; Park et al. 2001] where pore-scale concentration function is strongly periodic and intermittent in the transversal direction (because of figuring [Valocchi 1989]). Because of such limitations, MCM has sometimes been argued as being "without foundation" [Gunn and Pryce 1969].

Statistical modeling, which is an alternative way of determining  $D_L$  originates from the Einstein's dispersion theory and the theory of Brownian motion [Chandrasekhar 1943]. In this approach, random walkers that represent the tracer particles are allowed to describe Brownian and advective displacement within the chosen porous medium [Saffman 1959; Sahimi et al. 1986; Uffink 1988; Sorbie and Clifford 1991]. By tracking the paths of these particles the Spatial Positions Distribution (SPD) for particles is found from which the dispersion tensor is derived [Chandrasekhar 1943]. Alternatively, First-arrival Times Distribution (FTD) at the outlet face of the soil-column (or network) is used to derive  $D_L$  [Sahimi et al. 1986; Sorbie and Clifford 1991]. Only a few attempts have been made to upscale Brownian motion and advective displacement from the pore scale to the network scale [Mohanty and Salter 1982; Sahimi and Imdakm 1988; Sorbie and Clifford 1991; Acharya et al. 2004b], as this method requires a huge size of the domain and needs small time steps for every Brownian jump. Hence, it requires large simulation time [Uffink 1988; Acharya et al. 2004b], which makes this approach com-

putationally unattractive. Despite being free of numerical dispersion, which makes it attractive [Uffink 1988], this approach is not easily adopted for computing more complex transport, such as non-linearly adsorbing reactive transport [Bosma and Van der Zee 1995].

As dispersion depends on micro- as well macro-scale heterogeneities, a rigorous study of dispersion at the laboratory- or at the field-scale is resource intensive. Alternatively, pore-network models have emerged as a modeling tool for upscaling physical processes from the pore-scale to the continuum scale [Celia et al. 1995] and steps have already been taken for upscaling many processes such as permeability, wettability, formation factor and dispersion [Payatakes et al. 1973; Koplik 1982; Blunt and King 1991; Bryant et al. 1993b; Ioannidis et al. 1993; Reeves 1997; Tsakiroglou and Payatakes 2000; Bruderer and Bernabé 2001; Øren and Bakke 2002; Acharya et al. 2004a]. Likewise, the representative size of pore-networks for different processes have also been established such as for permeability in 2D pore-network  $35 \times 35$  nodes are needed [Koplik 1982], whereas for a 3D pore-network  $25 \times 15 \times 15$  nodes are required [Acharya et al. 2004a]. It was also shown that the size of network for dispersion with random walk depends on the magnitude of the average velocity in the mean flow direction [Sahimi et al. 1986; Verlaan 2001; Acharya et al. 2004b]. However, the size of pore-networks to obtain an asymptotic value of dispersion through MCM has not yet been studied. Additionally, whereas dispersion depends on heterogeneity, studies to assess a systematic relation between dispersion and pore-size heterogeneity were limited to very simple cases. Furthermore, it is not yet clear how big effect in transport is produced by the numerical dispersion.

The purpose of this study is to find a representative size of the pore-network that can produce an asymptotic hydrodynamic (numerical) longitudinal-dispersivity ( $\alpha_L$ ) in a MCM, derive  $\alpha_L$ -pore-size heterogeneity relations, verify thus obtained  $\alpha_L$  with larger networks and assess whether there is an agreement between MCM and BPTM.

## 4.2 Mathematical formulation of problem

Models describing transport of non-reactive tracer on the continuum scale usually employ the convection-dispersion equation [Bear 1972; Hassanizadeh 1996]. Assuming a column of homogeneous and isotropic porous medium of length  $L$  at the macroscopic level, the 1D formulation of the CDE for the concentration  $C$

$$\frac{\partial C}{\partial t} + v \frac{\partial C}{\partial X} = D_L \frac{\partial^2 C}{\partial X^2} \quad (4.1)$$

can be used, which involves the mean flow velocity  $v$  and the longitudinal macroscopic dispersion coefficient  $D_L$ . As is seen from the equation, concentration function  $C$  can be plotted as an function of space ( $t = \text{const}$ ) that yields concentration profile (or *isochrone*) or as a function of time ( $X = \text{const}$ ) that yields a breakthrough curve (BTC).

The macroscopic intrinsic (pore water) mean velocity  $v$  is determined with the Dupuit-Forcheimer equation

$$v = \frac{QL}{V_f}, \quad (4.2)$$

where  $Q$  is the macroscopic discharge across the pore-network and  $V_f$  is its fluid volume [Acharya et al. 2004a], i.e. the subscript  $f$  denotes the fluid phase.



In dimensionless form  $D_L$  is expressed through the macroscopic Peclet number

$$Pe_L = \frac{vL}{D_L}. \quad (4.3)$$

Traditionally,  $D_L$  has been based on empirical relations such as

$$D_L = D_m/\zeta + D_h, \quad (4.4)$$

where  $\zeta$  denotes tortuosity, while  $D_m$  and  $D_h$  denote molecular diffusion and mechanical dispersion, respectively [Bear 1972]. In this paper, we aim to find the macroscopic dispersion coefficient  $D_L$  directly either by using MCM or by using BPTM (i.e. tracking the paths of particles in the flow field in a 3D pore network of length  $W_X = L$ , width  $W_Y$  and height  $W_Z$ ). Note that, although the macroscopic porous medium can be assumed homogeneous and 1D, we use a 3D network to include microscale heterogeneities by randomly distributing the pore sizes. The resulting (longitudinal) dispersion coefficient in the mean flow direction of the network is identified with the macroscopic  $D_L$  and the length of the network with  $L$ . In the case of BPTM,  $D_L$  (or  $Pe_L$ ) is determined as a function of the characteristic Peclet number  $Pe_\ell$

$$Pe_\ell = \frac{v\ell}{D_m}, \quad (4.5)$$

where  $\ell$  denotes the mean pore length (the lattice constant in pore-network), and  $\ell \ll L$ ,  $\ell \ll W_Y$  and  $\ell \ll W_Z$ .

In the case of MCM, assuming that  $D_L$  is linearly related to velocity, i.e.  $D_L \sim \alpha_L v$ , in a pore-network of  $N_X$  nodes in the mean flow direction (aligned with  $X$ ), the relation of  $Pe_L$  to dispersivity ( $\alpha_L$ ) is written as

$$\alpha_L = \frac{(N_X - 1)\ell}{Pe_L}, \quad (4.6)$$

where  $L$  is replaced with  $(N_X - 1)\ell$ . For convenience, we use dimensionless dispersivity, i.e.  $\tilde{\alpha}_L = \alpha_L/\ell$ .

By considering a non-reactive tracer through a column (pore-network) under the boundary and initial conditions given by:

$$C(X > 0, t = 0) = C_{in}; C(0, t \geq 0) = C_0; \frac{\partial C}{\partial X} \big|_{(0, t > 0)} = 0; \frac{\partial C}{\partial X} \big|_{(L, t \geq 0)} = 0, \quad (4.7)$$

and with  $C_0 > C_{in}$ , the convection-dispersion equation is solved. In Eq (4.7),  $C_0$  denotes the concentration of the continuously injected influent and  $C_{in}$  is the concentration of the solute in the fluid of the column at time  $t = 0$ . By fitting the solution of the convection-dispersion equation (4.1) [Van Genuchten and Alves 1982] to the effluent concentration in time (BTC at the outlet face of the network), i.e.

$$\tilde{C}(\tilde{X}, \tilde{T}) = \frac{1}{2} \left\{ \operatorname{erfc} \left[ \frac{\tilde{X} - \tilde{T}}{2\sqrt{\tilde{\alpha}_L \tilde{\ell} \tilde{T}}} \right] + \exp \left( \frac{\tilde{X}}{\tilde{\alpha}_L \tilde{\ell}} \right) \operatorname{erfc} \left[ \frac{\tilde{X} + \tilde{T}}{2\sqrt{\tilde{\alpha}_L \tilde{\ell} \tilde{T}}} \right] \right\} \quad (4.8)$$

$\tilde{\alpha}_L$  is determined (and  $D_L = \tilde{\alpha}_L v \ell$ ). The dimensionless quantities are:  $\tilde{C} = (C - C_{in})/(C_0 - C_{in})$ ,  $C_{in} = 0$ ,  $\tilde{\ell} = \ell/L$ ,  $\tilde{X} = X/L$  and  $\tilde{T} = vt/L$ .  $\tilde{\alpha}_L$  is found with the method of least

squares. In particle tracking methods (e.g. BPTM),  $\alpha_L$  can be obtained with the methods of moments [Sahimi et al. 1986]. As  $\tilde{C}(X, t)$  can be interpreted as a probability function, its first derivative with respect to  $X$  is used to produce the probability density function (PDF,  $f(X)$ ) [Bosma and Van der Zee 1993; Keijzer et al. 2000] according to

$$f(X) = -\frac{\partial \tilde{C}}{\partial X}. \quad (4.9)$$

Then, Eq (4.9) is used to determine the second central moment  $M_2^c$  and then  $D_L$  follows from the Einstein's relation [Chandrasekhar 1943]:

$$M_2^c = 2D_L t. \quad (4.10)$$

In Brownian particle tracking model Eq (4.10) is used for determining  $D_L$  from SPD or Eq (4.8) is used to fit the FTD of Brownian particles [Bruderer and Bernabé 2001].

### 4.3 Models

We represent a macroscopic porous medium with a cubic network of pores as shown in Figure 4.1. The dimensions of the network are: length (in the main flow direction  $X$ ,  $L \gg \ell$ ), width ( $W_Y \gg \ell$ ) and height ( $W_Z \gg \ell$ ). For the same flow conditions and the same porosity the chosen porous medium can be modeled in various ways. For example, Figure 4.1a represents the HYPON model reported earlier [Acharya et al. 2004a]. This network uses a realistic geometry with bonds of converging-diverging architecture (see Figure 4.2) and the porebodies possess volume, whereas the network shown in Figure 4.1b is a simplified traditional construct of cylindrical bonds (see Figure 4.3) without any porebodies [Van Dijke and Sorbie 2002]. The first network is more appropriate for describing a mixing cell model, whereas the second network is good for particle tracking, as the geometry of the first network makes particle tracking very cumbersome. Because both pore-networks model the same porous media and the flow conditions, the results of mixing cell model (MCM) on the first network and the particle tracking model (BPTM) on the second network are comparable. In the following we briefly describe the both models.

#### 4.3.1 Mixing cell model (MCM)

The pore-units are assumed perfectly mixed [De Josselin de Jong 1958]. We ignore the contribution of diffusion ( $D_m$ ) to transport by assuming that advection dominates the transport. Particle-tracking experiments on pore-network showed that this assumption is appropriate for characteristic Peclet numbers approximately between ten and  $10^4$  [Acharya et al. 2004b]. Hence, the equation of the mixing cell model for a pore-unit (PU) of Figure 4.2a is given by

$$V_{PU} \frac{\partial c}{\partial t} + \nabla \cdot (\mathbf{q}c) = 0, \quad (4.11)$$

where  $t$  is time,  $V_{PU}$  is the fluid volume of the pore-unit and  $c$  is the volume averaged concentration of the solute in the pore-unit. The symbol  $\mathbf{q}$  denotes the discharge vector [ $L^3 T^{-1}$ ] through bonds similar to that shown in Figure 4.2b. For each bond connected to two nodes, discharge can be computed with Hagen-Poiseuille equation

$$q_{i,j} = \frac{g}{\nu} \ell^3 G_{i,j} (h_i - h_j), \quad (4.12)$$

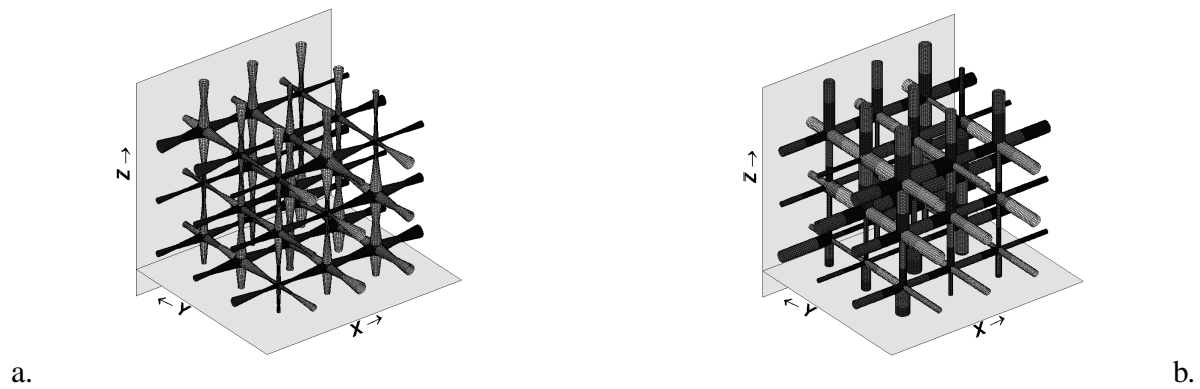


Figure 4.1: Sketches of two different versions of network architecture with similar micro/macroscale flow and porosity characteristics: a. HYPON: an assembly of converging-diverging bonds with spherical porebodies (is used for MCM) and b. Simplified pore-network version of “a” with volume less porebodies [Van Dijke and Sorbie 2002] (is used for BPTM).

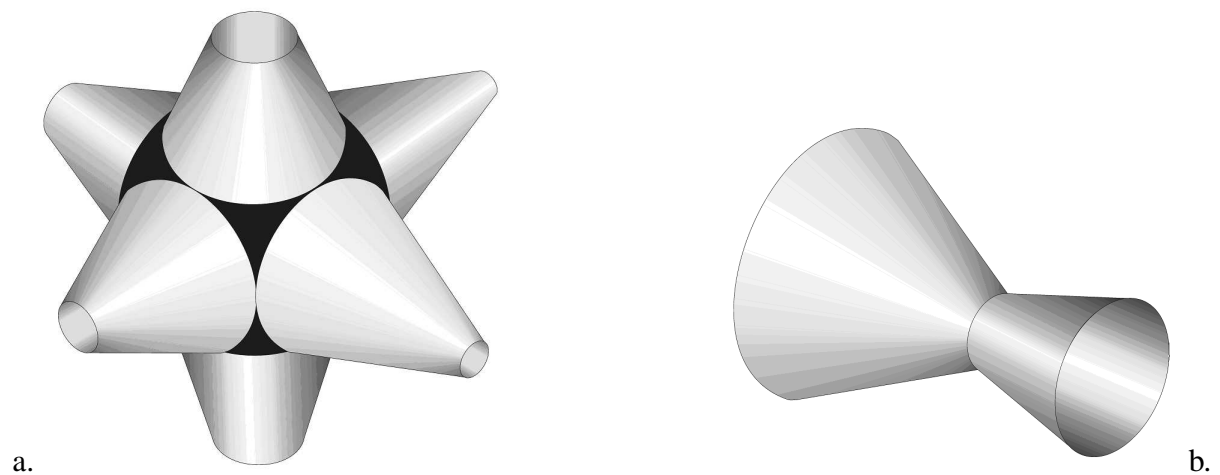


Figure 4.2: Basic elements of HYPON: a. the pore-unit (the porebody is marked with the dark color) and b. the Biconical abscissa-Asymmetric CONcentric (BACON) bond [Acharya et al. 2004a].

where subscripts  $i$  and  $j$  are the addresses of nodes (fluid flows from  $i$  to  $j$ ).  $G_{i,j}$  denotes the dimensionless bond conductance derived earlier [Acharya et al. 2004a] in which both the longitudinal as well as cross sectional shapes of bond are taken into account [Reeves and Celia 1996]. The size of the bond along  $\ell$  is derived considering the porebody radii of the adjacent porebodies and the curvature parameter  $n$ . The constant  $g$  is the magnitude of acceleration due to gravity and  $\nu$  denotes the kinematic viscosity of water. The symbols  $h_i$  and  $h_j$  are the hydraulic heads at the pore-unit centers  $i$  and  $j$ . Note that the pore geometry is expressed in terms of pore-to-pore spacing ( $\ell$ ), i.e. geometric lengths are scaled by  $\ell$ . Equation (4.12) is valid for laminar flow in a wide range of the Reynolds number and is appropriate for describing flow in the pores [Bear 1972]. For steady state flow, the divergence of discharges at nodes (pore-units) equals to zero [Acharya et al. 2004a] and that leads to a system of algebraic equations,

i.e.

$$\sum_j^{\beta} q_{i,j} = 0, j = 1, 2, \dots, \beta, \quad (4.13)$$

where  $\beta$  is the coordination number (we fix it at 6),  $j$  is the index of the adjacent pore-units. The finite difference scheme for Eq (4.11) is written as

$$c(i, t + \Delta t) = c(i, t) + \frac{\Delta t}{V_{PU}} \underbrace{\left( \sum_j c(j, t) q_{j,i} - c(i, t) (q_{PU})_i \right)}_{\Delta c(i,t)_{AD}}, \quad (4.14)$$

where the index  $j$  is chosen such that  $h_j > h_i$ . Additionally, from the boundary and initial conditions it follows that  $0 \leq \Delta c(i, t)_{AD} < (C_0 - C_{in})$ . The node discharge  $(q_{PU})_i$  is the sum of the flows entering or leaving the node  $i$ , i.e.

$$(q_{PU})_i = \sum_j |q_{j,i}|, \quad h_j > h_i, \quad j = 1, 2, 3 \dots \beta. \quad (4.15)$$

For the stability of the scheme, the minimum time step is chosen on the basis of pore-unit residence times [Sun 1996; Suchomel et al. 1998a], i.e.

$$2\Delta t \leq \min \{ [\mathbf{V}_{PU}] [\mathbf{q}_{PU}^{-1}] \} = \min \{ \mathbf{T}_{PU} \} \quad (4.16)$$

In Eq (4.16),  $\mathbf{V}_{PU}$  and  $\mathbf{q}_{PU}$  are the matrix vectors of pore-unit volumes and total (absolute) discharges from (or into) the pore-units [Acharya et al. 2004a] respectively, and  $\mathbf{T}_{PU}$  is the matrix vector of pore-unit residence times. Alternatively, we have investigated the effect of time step by fixing  $\Delta t$  according to the bond residence times, i.e.

$$2\Delta t \leq \min \{ [\mathbf{V}_b] [\mathbf{q}_b^{-1}] \} = \min \{ \mathbf{T}_b \}, \quad (4.17)$$

where subscript  $b$  denotes bond,  $\mathbf{q}_b$  is the matrix vector of discharges through the bonds given by Eq (4.12). Similarly,  $\mathbf{V}_b$  and  $\mathbf{T}_b$  denote volume and time matrices pertaining to the bonds, where  $V_b = \text{volume of bond} + \frac{1}{6} \text{ porebody volume } (i) + \frac{1}{6} \text{ porebody volume } (j)$  (see [Acharya et al. 2004a]). Average concentration for each pore-unit is updated at the end of each  $\Delta t$ . At designated time steps ( $\gg \Delta t$ ), the concentrations of pore-units that belong to a particular tier of the pore-network are averaged. The tiers are defined as the group of pore-units which possess the same  $X$ -coordinate. For averaging, the discharges from the PU (or into the PU) are used as the weighting factors of the corresponding PU concentrations. Hence, the resulting dimensionless concentration function  $\tilde{C}(X, t)$  for a 1D column (at the network scale) is written as

$$\tilde{C}(X, t) = \left[ \frac{\sum_i^{N_t} c(i, t) (|q_{PU}|)_i}{\sum_i^{N_t} (|q_{PU}|)_i} - C_{in} \right] \frac{1}{C_0 - C_{in}}, \quad i = 1, 2, 3 \dots N_t, \quad (4.18)$$

where the symbol  $N_t$  denotes the total number of pore-units that are indexed with  $i$  and that possess the same coordinate  $X$ . The subscript  $t$  denotes tier. The  $X$ -coordinate is chosen at an interval of  $\ell$ , i.e.  $X = 0, 1\ell, 2\ell, \dots L$ . Further, this concentration is plotted against space ( $X$ -coordinate) to get concentration profiles (*isochrones*) at different times. The BTC is obtained by plotting  $\tilde{C}(X = L, t)$  as a function of time. Equation (4.8) is fitted to this BTC and a value of dispersivity  $\tilde{\alpha}_L$  is obtained. In Section 4.4 we will discuss the results.

### 4.3.2 Brownian particle tracking model (BPTM)

In our random walk model, it is assumed that particles describe displacement due to diffusive and advective forces [Acharya et al. 2004b]. Within the bond of radius  $R_b$  the particle experiences a sudden jump from the origin (where it resides at that time) of the spherical coordinate-system  $\mathbf{r} = (r, \varphi, \theta)$  (Brownian motion or molecular diffusion) and the particle moves with the fluid velocity profile of the bond (convection) in the local cylindrical coordinate system  $(x, y)$ , where  $x$  indicates the (local) flow direction ( $0 \leq x \leq \ell$ ) and  $y$  is the distance of the particle's position from the axis of the cylindrical bond ( $0 \leq y \leq R_b$ ). Additionally, at nodes (intersection of bonds) the particle jumps from one bond to the next, based on a probabilistic approach, which also depends on both diffusive and convective forces, described later. In the following we briefly introduce the equations we need for upscaling the Brownian and advective displacements to the network-scale dispersion coefficient in the longitudinal direction ( $D_L$ ).

The convective motion of the particle occurs according to the fluid velocity profile, which we assume to be parabolic or plug-like described by the Hagen-Poiseuille equation [Sahimi et al. 1986; Bruderer and Bernabé 2001]. Hence, as envisaged in Figure 4.3, the displacement of a particle for a time-step  $\Delta t$  is given by

$$\Delta x = uf(\lambda)\Delta t + \Delta r \cos \varphi, \quad \Delta r \geq 0, \quad (4.19)$$

where  $u$  is the mean velocity in the bonds and  $\lambda$  is the relative radial position of the particle, i.e.,  $\lambda = y/R_b$  and  $f(\lambda) = 2(1 - \lambda^2)$  for a parabolic velocity profile and  $f(\lambda) = 1$  for a simplified plug-like velocity profile.  $\Delta r$  denotes the length of the radius vector described by the Brownian particle in the Lagrangian coordinate system and the symbol  $\varphi$  denotes polar angle [Sorbie and Clifford 1991; Damion et al. 2000].

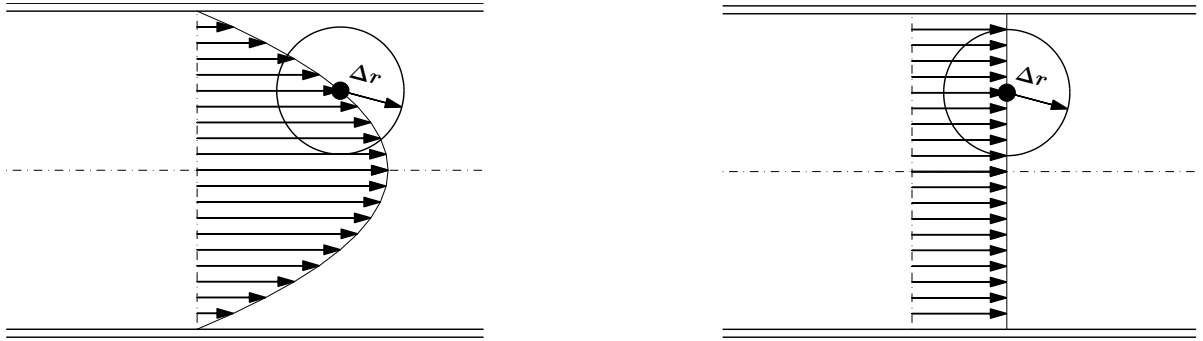


Figure 4.3: A 2D sketch of two different intra-bond velocity profiles (parabolic and plug-like) and Brownian particle displacement.  $\Delta r$  denotes the radius of Brownian jump and the solid circles denote a non-reactive tracer particle.

The omni-directional displacement  $\Delta r$  around the mean position of a particle at the fluid streamlines follows from a probability function that is obtained by integrating the Green's propagator [Chandrasekhar 1943; Sorbie and Clifford 1991; Damion et al. 2000]

$$\phi(\Delta \mathbf{r}) = (4\pi D_m \Delta t)^{-3/2} \exp \left[ -\frac{\Delta \mathbf{r}^2}{4D_m \Delta t} \right], \quad (4.20)$$

where  $\phi(\Delta \mathbf{r})$  can also be called the volumetric probability density function for 3D Brownian motion. The radial displacement  $\Delta \lambda = \Delta r \sin \varphi \cos \theta / R_b$ , where  $\theta$  denotes azimuthal angle

[Damion et al. 2000].  $D_L$  is obtained through two approaches, namely the SPD and FTD [Acharya et al. 2004b] as described in Chapter 3.

Further, we model a porous medium by a 3D cubic network (Figure 4.1b) with the bonds of fixed length  $\ell$  and circular cross-section. To have a plausible comparison of two models, we assume that the bond residence times in HYPON (Figure 4.1a) and in the simplified (Figure 4.1b) network are exactly the same. From this follows that discharges through the bonds that are calculated for MCM can be used for BPTM. Then the bond radii  $R_b$ , hence the equivalent bond aspect ratios  $\tilde{R}_b$ , are derived from the BACON bond volume  $V_b$  (i.e.  $\tilde{R}_b = \sqrt{V_b/\pi\ell^3}$ ). This also eases the computation of particle tracking in BPTM. In earlier work [Acharya et al. 2004b], the  $\tilde{R}_b$  was chosen from a random distribution.

The intersection of the elementary bonds is assumed to be volumeless, i.e. all bond volume is assigned to the bonds. From this assumption a subtle problem arises, i.e. the dispersion function becomes discontinuous [Park et al. 2001]. A particle that emerges at a node from one bond may enter another bond with drastically different hydraulic and diffusive regimes. This problem has been tackled in different ways. For example, Sorbie and Clifford [Sorbie and Clifford 1991] proposed a general algorithm for the jump of a particle from one bond to the next at a node. In this algorithm the probability density function for the transition of a particle from node  $i$  into bond  $j$  is given by Acharya et al. [2004b].

$$p(i, j) = \frac{[(f_{i,j}(q_{i,j} + \varpi_{i,j}D_m)(1 - H)) + ((1 - f_{i,j})\varpi_{i,j}D_mH)]}{\sum_{j=1}^{\beta_i} [(f_{i,j}(q_{i,j} + \varpi_{i,j}D_m)(1 - H)) + ((1 - f_{i,j})\varpi_{i,j}D_mH)]}, \quad (4.21)$$

where  $H$  is the Heaviside function, defined as

$$H = \begin{cases} 0 & \text{if } q_{i,j} \geq 0 \\ 1 & \text{if } q_{i,j} < 0. \end{cases} \quad (4.22)$$

The flow rate (discharge)  $q_{i,j}$  is taken positive for fluid leaving the node.  $\beta_i$  is the (local) coordination number at node  $i$ . Equation (4.22) reflects that in general the nodal transition depends only on the flow rate, but also on molecular diffusion, represented by the term  $\varpi_{i,j}D_m$ . The term  $\varpi_{i,j}$  is a geometrical factor that is assumed to be equal to  $(a_\times(R_b)_j^2/\ell)$ , where  $a_\times$  is a shape factor (e.g. for circular bond cross-sections  $a_\times = \pi$ ).  $f_{i,j}$  is the fraction of particles leaving the node and entering bond  $j$  in the direction of flow. For non-zero values of  $\varpi_{i,j}$  and  $f_{i,j} < 1$ , particles may jump opposite to the flow direction. However, in the simplest assumption of ideal fully-mixed and advection dominated transport the transition occurs only downstream, i.e.  $f_{i,j} = 1$  and, additionally,  $\varpi_{i,j} = 0$ . Although the assumption  $\varpi_{i,j} = 0$  and  $f_{i,j} = 1$  showed high dispersion for the low  $Pe_\ell$ , this assumption does not produce much effect for  $Pe_\ell$  considered here. Indeed the assumption in MCM that  $\varpi_{i,j} = 0$  and  $f_{i,j} = 1$  applies. We will consider plug-like and parabolic intra-velocity profiles given by  $f(\lambda)$ . For accurate description of BPTM,  $f_{i,j}$  should vary from 0.5 to 1.0 [Sorbie and Clifford 1991] according to

$$f_{i,j} = \begin{cases} 0.5 & \text{if } Pe_b \leq Pe_{ref} \\ 1 & \text{if } Pe_b > Pe_{ref}, \end{cases} \quad (4.23)$$

where  $Pe_{ref} \approx 0.40$  [Sorbie and Clifford 1991].

After the transition of a particle from one bond to the next, we assume that the radial position of the particle is preserved. In other words, in the new bond the particle starts at the same value of the dimensionless local radial coordinate  $\lambda$  at which it left the previous bond

[Sorbie and Clifford 1991; Damion et al. 2000]. Considering the global initial conditions, we distribute the particles at the inlet face proportional to the flow rate of the inlet bonds [Sorbie and Clifford 1991; Damion et al. 2000], i.e. the probability  $p(inlet, j)$  for a particle to enter the system through bond  $j$  at the inlet is given by

$$p(inlet, j) = \frac{q_{inlet, j}}{Q}, \quad (4.24)$$

where  $q_{inlet, j}$  is the bond-discharge at the inlet face. Similarly at  $t = 0$ , the probability  $p(\lambda_0)$  for a particle to enter at radial position  $\lambda$  is proportional to the flow rate in the tube, i.e.

$$p(\lambda) = 4\lambda(1 - \lambda^2). \quad (4.25)$$

Earlier work [Acharya et al. 2004b] showed that both FTD and SPD may be used for simulating the dispersion in a pore-network. Because SPD is computationally demanding and less accurate for advection dominated regimes [Acharya et al. 2004b], we use FTD. For this we inject 10000 particles from the inlet face according to Eqs (4.24) and (4.25) and produce them at the outlet face.

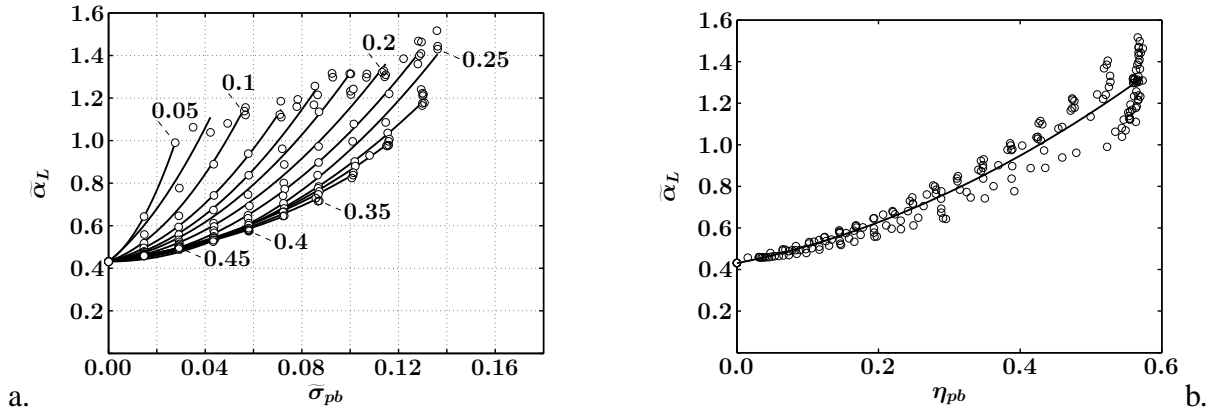


Figure 4.4: Relation of dispersivity to microscopic heterogeneity ( $\Delta t$  from Eq 4.17) a. Dispersivity as a function of standard deviation of porebody radii distribution. Each curve is associated with a particular mean porebody radius  $\langle \tilde{R}_{pb} \rangle$  as shown in the figure; b. Dispersivity as a function of coefficient of variation of porebody radii. Solid lines are the regression lines, whereas the open circles are the data obtained from numerical simulations (MCM).

## 4.4 Results

Earlier work [Acharya et al. 2004b] showed that the magnitude of  $D_L$  depends on the pore-size heterogeneity of the network. Because  $D_L$  is the most important parameter in the CDE, it is essential to define it correctly according to the pore-size heterogeneity. As the particle tracking models are computationally demanding, we chose mixing cell model to produce the relation of  $D_L$  to pore-size statistics. However, we assess our results by comparing BTCs from both MCM and BPTM results. Our preliminary simulations showed that for this purpose at least a  $33 \times 23 \times 23$  network is needed. We used the same architecture as shown in Figure 4.1a (with converging-diverging pores). We generated 209 pore networks with gradually varying  $\langle \tilde{R}_{pb} \rangle$

and  $\tilde{\sigma}_{pb}$ . By imposing a hydraulic head difference (0.07 m) across the network and assuming the no-flow boundaries on the lateral sides we obtain a 1D column, for which we solve the mixing cell model to produce BTCs for a continuously injected influent of concentration  $C_0$ , whereas  $C_{in} = 0$ . These BTCs are fitted with the solution of CDE (4.8) and the values of  $\tilde{\alpha}_L$  are computed with the method of least squares [Van Genuchten and Alves 1982]. Further we plot  $\tilde{\alpha}_L$  as a function of  $\tilde{\sigma}_{pb}$  as shown in Figure 4.4a.

From the figure it is seen that the dispersivity  $\tilde{\alpha}_L$  for each  $\langle \tilde{R}_{pb} \rangle$  is a function of  $\tilde{\sigma}_{pb}$  and therefore the simulated data can be fitted with a regression equation of type

$$\tilde{\alpha}_L(\langle \tilde{R}_{pb} \rangle) = B_1 \tilde{\sigma}_{pb}^2 + B_2 \tilde{\sigma}_{pb} + \tilde{\alpha}_0, \quad (4.26)$$

where fitting constant  $\tilde{\alpha}_0$  is the same for every  $\langle \tilde{R}_{pb} \rangle$ . However, parameters  $B_1$  and  $B_2$  differ according to  $\langle \tilde{R}_{pb} \rangle$  and are listed in Table 4.1. Eq (4.26) is valid for  $0 \leq \tilde{\sigma}_{pb} \leq \sigma_{\langle \tilde{R}_{pb} \rangle}^{max}$ .

Table 4.1: Parameters for the dispersivity function (Eq (4.26)) based on  $\Delta t$  of Eq (4.17)

$\langle \tilde{R}_{pb} \rangle$	$A_{\langle \tilde{R}_{pb} \rangle}$	$B_{\langle \tilde{R}_{pb} \rangle}$	$\tilde{\alpha}_0$	$\sigma_{\langle \tilde{R}_{pb} \rangle}^{max}$	$\mathfrak{R}^2$
0.050	455.00	7.654	0.4323	0.0276	1.0000
0.075	164.31	9.131	0.4182	0.0422	0.9641
0.100	157.25	3.985	0.4259	0.0567	0.9935
0.125	99.76	2.851	0.4314	0.0715	0.9973
0.150	85.62	2.069	0.4291	0.0865	0.9917
0.175	70.49	1.804	0.4246	0.1003	0.9857
0.200	58.92	1.334	0.4299	0.1147	0.9942
0.225	54.43	0.644	0.4402	0.1295	0.9974
0.250	52.75	-0.030	0.4523	0.1362	0.9941
0.275	39.42	0.639	0.4420	0.1307	0.9986
0.300	32.11	1.072	0.4344	0.1162	0.9994
0.325	25.25	1.479	0.4312	0.1013	0.9993
0.350	22.82	1.447	0.4316	0.0872	0.9968
0.375	19.52	1.519	0.4317	0.0727	0.9982
0.400	19.14	1.474	0.4314	0.0582	0.9979
0.425	9.15	1.887	0.4300	0.0434	0.9975
0.450	19.36	1.614	0.4307	0.0292	0.9971

Alternatively  $\tilde{\alpha}_L$  can also be plotted as a function of coefficient of variation of porebody radii ( $\eta_{pb}$ ) as shown in Figure 4.4b and fitted with another regression equation of type

$$\tilde{\alpha}_L = 1.53\eta_{pb}^2 + 0.683\eta_{pb} + \tilde{\alpha}_0, \quad \tilde{\alpha}_0 = 0.43, \quad (4.27)$$

where all parameters are uniquely defined. This relation is theoretically appealing and is equally good for low  $\eta_{pb}$ . However, for higher  $\eta_{pb}$ , Eq (4.26) gives better fitting. Note that Eq (4.27) is based on the time step criteria of Eq (4.17). However, Eq (4.17) is not only computationally demanding than criteria of Eq (4.16) but also it is known that small time-step



produces more numerical dispersion [Sun 1996; Suchomel et al. 1998b]. To verify this we used Eq (4.16) and simulated dispersion for 151 network with  $\langle \tilde{R}_{pb} \rangle \geq 0.17$ . The results are shown in Figure 4.5 and the parameters are listed in Table 4.2. In Figure 4.5a,  $\tilde{\alpha}_L$  is shown as a function of  $\tilde{\sigma}_{pb}$  whereas in Figure 4.5b dispersivity  $\tilde{\alpha}_L$  is a function of  $\eta_{pb}$ . For which another regression equation of type

$$\tilde{\alpha}_L = 0.9537\eta_{pb}^2 + 1.45\eta_{pb} + \tilde{\alpha}_0, \quad \tilde{\alpha}_0 = 0.25, \quad (4.28)$$

can be fitted. Compared to Eq (4.27) the constant  $\tilde{\alpha}_0$  differs. The figure reveals that the dispersivity for larger  $\tilde{\sigma}_{pb}$  are similar to that of Figure 4.4 but the differences are significant for small  $\tilde{\sigma}_{pb}$ . Hence, a proper assessment of time criteria is required which we will do shortly.

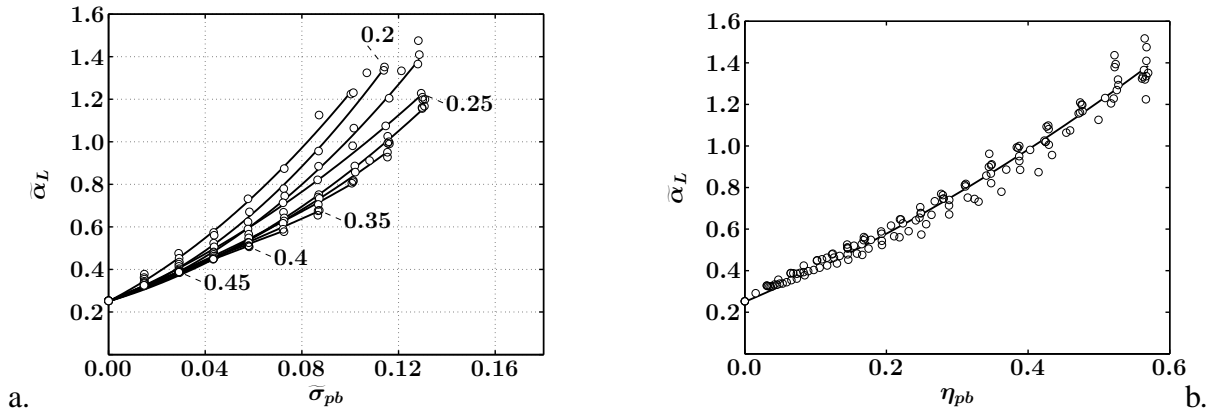


Figure 4.5: Relation of dispersivity to microscopic heterogeneity ( $\Delta t$  from Eq 4.16).

Although at the first glance Eq (4.16) seems correct, a careful analysis shows that it is less correct when a major part of the fluid in a pore-unit is immobile. For example, in a homogenous network (equal sized pores) only one third volume is mobile which means in fact in that case Eq (4.17) is more relevant which can be obtained by considering only the mobile volume in the Eq (4.16). In that case Eq (4.16) reduces to Eq (4.17). This indicates that the best reliable  $\Delta t$  should be chosen based on the bond residence times given by Eq (4.17).

To verify the reliability of dispersivity-heterogeneity relation and to assess the  $\Delta t$  criteria we use many other networks on which we apply both models MCM and BPTM. From MCM model, we produce dimensionless BTCs, whereas from Brownian particle tracking model FTDs are obtained. Although preliminary simulations of mixing cell model suggested that a  $33 \times 23 \times 23$  network is sufficient to produce a consistent (an asymptotic)  $\tilde{\alpha}_L$ , we used much larger networks of size  $301 \times 61 \times 61$  as the particle tracking model requires a larger size [Sahimi and Imdakm 1988; Verlaan 2001; Acharya et al. 2004b]. To capture the effects of microscopic heterogeneity on dispersion, five systematic cases (S000, S030, S060, S086 and S115) that are listed in Table 4.3 were considered. For the mixing cell model, the pore-units were constructed with the curvature parameter ( $n$ ) equal to one and the ensemble of dimensionless porebody radii ( $\tilde{R}_{pb}$ , i.e.  $\tilde{R}_{pb} = R_{pb}/\ell$ ) taken from a random uniform distribution [Acharya et al. 2004a]. Assuming the bond residence times ( $T_b$ ) in both models the same, for the particle tracking model (BPTM), we assign all volume to the bonds such that nodes are volumeless and the bonds are simplified cylindrical tubes with some equivalent radii ( $\sqrt{V_b/a \times \ell}$ ). Our particle tracking results for a one dimensional periodically converging-diverging tube of large length showed that this simplification does not affect the long-term second central spatial moments.

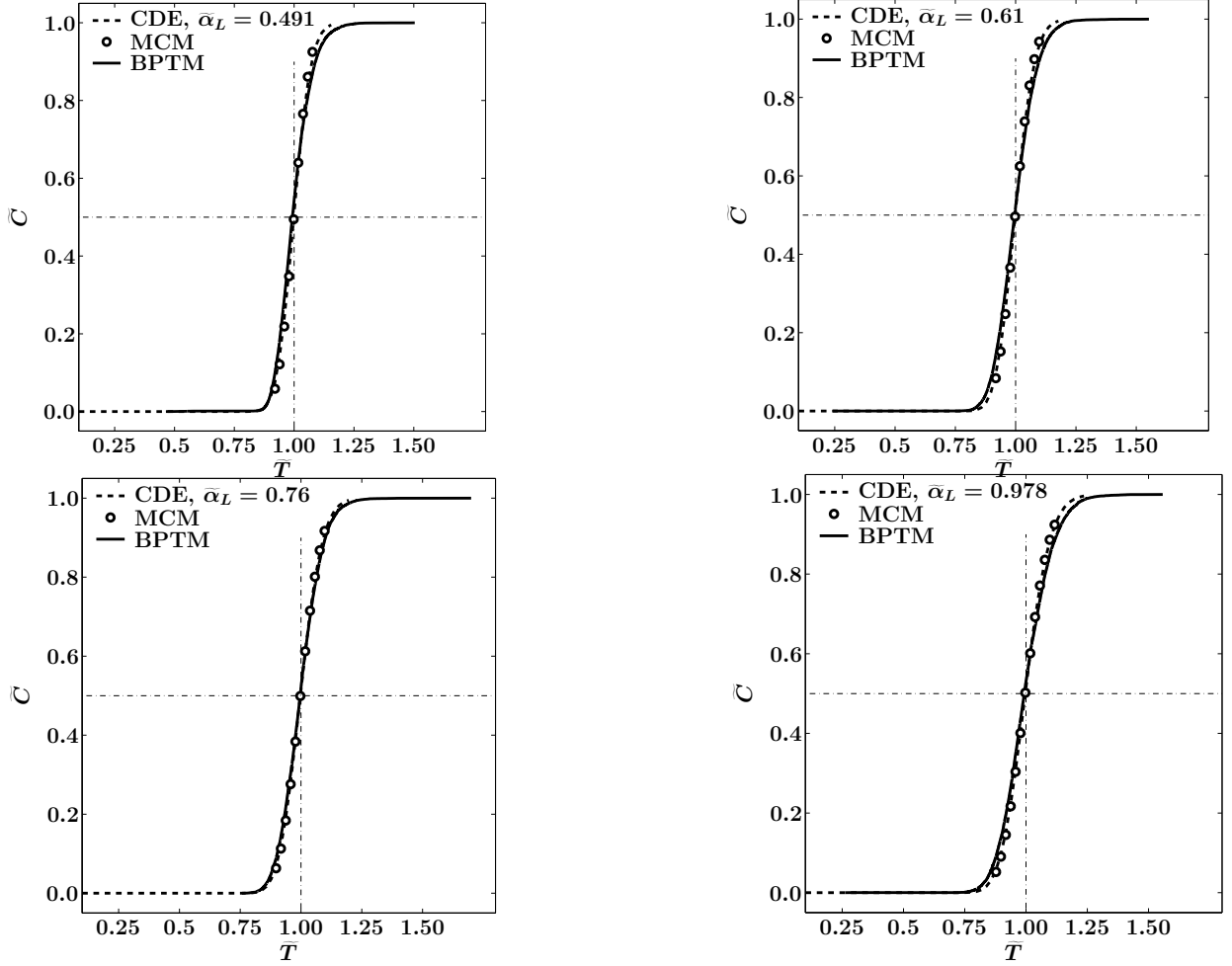


Figure 4.6: BTCs and FTDs at the outlet face of 4 networks (S030, S060, S086 and S115) of different degree of heterogeneity and uniform intra-bond velocity profile in BPTM. MCM (open circles) indicates the results from (Eq (4.18)), BPTM (solid lines) indicates the results from the BPTM model (Eq (4.19)) [Acharya et al. 2004b], CDE (dashed lines) indicates the results with  $\tilde{\alpha}_L$  in Eq (4.8) (see Table 4.3).

Additionally, the lattice constant  $\ell = 250 \times 10^{-6}$  m,  $D_m = 8 \times 10^{-10}$  m<sup>2</sup>/s [Taylor 1953], and the hydraulic head difference between inlet and outlet faces was fixed at 0.07 m. We solve both types of models on the same sized networks (note that the network for BPTM is simplified) and compare the MCM breakthrough curves of dimensionless concentration with the FTDs of BPTM. The results reveal that the BTCs and FTDs agree quite well, which can be seen from Figure 4.6.

From the figure it is seen that BTCs and FTDs at the outlet face of the network agree quite well. However, it is important to set  $f(\lambda) = 1$  for BPTM and for MCM the iteration time step  $\Delta t$  should be taken from Eq (4.17). Additionally, the pores should be variedly sized. For these conditions, the numerical dispersion produced in MCM mimics the physical dispersion and agrees with the results from BPTM. However, if equal sized pores (in our cubic network) are considered, with the same criteria of  $\Delta t$  for MCM, then MCM produces more dispersion than the BPTM model, because with  $f(\lambda) = 1$ , BPTM is able to produce only the *molecular* diffusion not the *hydrodynamic* dispersion (see Figure 4.7a) for the macroscopic domain.

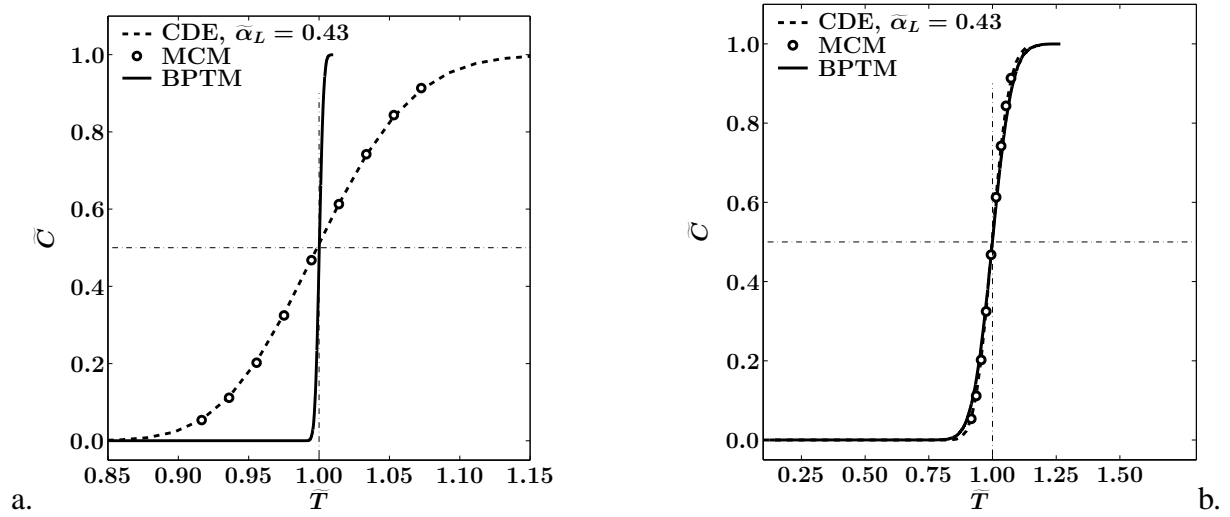


Figure 4.7: BTCs and FTDs at the outlet face of network S000 (equal-sized pores); a. uniform intra-bond velocity profile; b. parabolic intra-bond velocity profile in BPTM. For legends see 4.6.

However, with the same conditions but  $f(\lambda) = 2(1 - \lambda^2)$  the results from the both models agree (see Figure 4.7b). If parabolic intra-bond velocity profile is used in heterogeneous pore-networks, then the FTDs become much flatter than the BTCs of MCM for the same  $\Delta t$  criteria of Eq (4.17). The FTDs shown in Figure 4.8 with intra-bond parabolic profile for two different networks: S086 and S115, systematically deviate from the BTCs. From this we can conclude that  $\Delta t$  criteria proposed here (i.e. Eq (4.17)) is just sufficient to produce *hydrodynamic* dispersion in microscopically heterogeneous medium with an assumption that velocity is plug-like which is less than the actual dispersion because the actual lamellar velocity profile in the bonds is parabolic.

Table 4.2: Parameters for the dispersivity function (Eq (4.26)) based on  $\Delta t$  of Eq (4.16)

$\langle \tilde{R}_{pb} \rangle$	$A_{\langle \tilde{R}_{pb} \rangle}$	$B_{\langle \tilde{R}_{pb} \rangle}$	$\tilde{\alpha}_0$	$\sigma_{\langle \tilde{R}_{pb} \rangle}^{max}$	$\mathfrak{R}^2$
0.1750	39.1597	5.8855	0.2500	0.1003	0.9972
0.2000	49.2539	3.9843	0.2500	0.1142	0.9965
0.2250	40.6840	3.6135	0.2500	0.1286	0.9979
0.2500	21.3078	4.7342	0.2500	0.1294	0.9994
0.2750	27.4419	3.3769	0.2500	0.1309	0.9987
0.3000	19.7721	3.8083	0.2500	0.1162	0.9978
0.3250	10.0178	4.4823	0.2500	0.1013	0.9997
0.3500	2.2837	4.6758	0.2500	0.0872	0.9968
0.3750	-5.5367	4.9701	0.2500	0.0726	0.9994
0.4000	-4.3661	4.7532	0.2500	0.0582	0.9983
0.4250	-10.0605	4.9588	0.2500	0.0434	0.9999
0.4500	-22.6439	5.3028	0.2500	0.0292	1.0000

## 4.5 Summary and discussion

In the theory of transport, two types of models are commonly used: mixing-cell models (e.g. the MCM considered here) and random walk models (e.g. the BPTM considered here). The first are argued to be subjected to numerical dispersion and dispersion in general depends on the choice of time step for iteration. The time step is usually derived by fitting the finite difference scheme into the Taylor's expansion. The limitation of such approach is that it is correct when concentration function is both locally and globally continuous. However, in a pore network model it is not the case because the pore-scale concentration function is strongly periodic in the transversal directions and may locally be periodic even in the mean flow direction due to transversal mass-transfer. This leads to the discontinuity (change of sign) of the first or higher-order derivatives of the pore scale concentration function ( $c$ ). In such cases the best way for assessing a  $\Delta t$  of iteration is particle tracking. Also, particle tracking models cannot provide a unique solution as the dispersion in these models depends on the assumption of intra-bond velocity profiles. In earlier work [Acharya et al. 2004b] it was shown that the parabolic intra-bond velocity profile systematically produces higher dispersion than the plug-like profile.

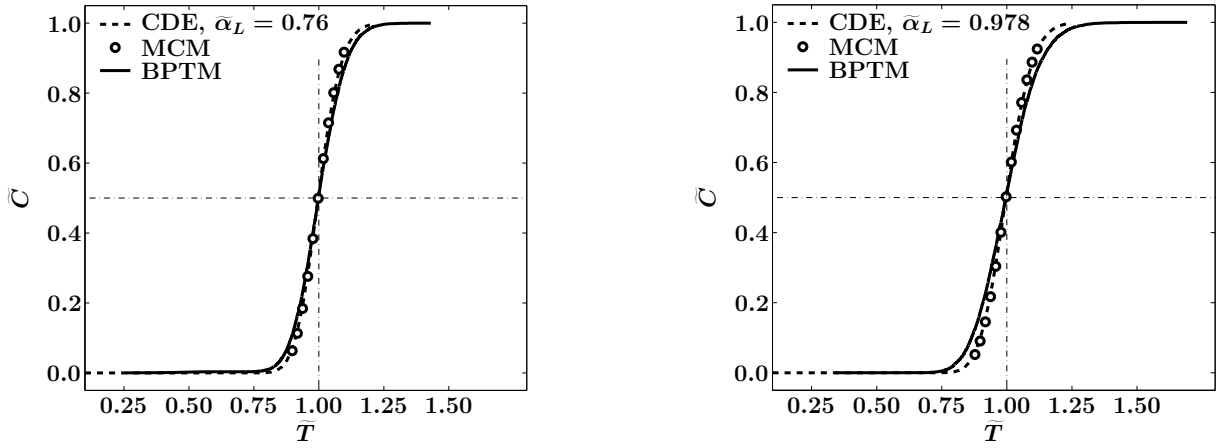


Figure 4.8: BTCs and FTDs at the outlet face of two-different heterogeneous pore-networks: S086 (left) and S115 (right) with parabolic intra-bond velocity profile in BPTM (compare with Figure 4.6).

Table 4.3: Microscopic and macroscopic input parameters for the numerical experiments

Networks	S000	S030	S060	S086	S115
$\min \{\tilde{R}_{pb}\}$	0.300	0.248	0.204	0.152	0.100
$\max \{\tilde{R}_{pb}\}$	0.300	0.352	0.412	0.450	0.500
$\tilde{\sigma}_{pb}$	0.000	0.030	0.060	0.086	0.115
$\tilde{\sigma}_b$	0.00	0.011	0.022	0.033	0.043
Porosity	0.240	0.243	0.265	0.267	0.285
$\min \{\tilde{R}_b\}$	0.159	0.133	0.111	0.082	0.054
$\max \{\tilde{R}_b\}$	0.159	0.186	0.215	0.233	0.255
$Pe_\ell$	384	386	430	405	420

$\tilde{\sigma}_b$  is the standard deviation of aspect ratios ( $\tilde{R}_b$ ).

Theoretically dispersion in MCM is a function of  $\Delta t$  and therefore may be adjusted at any desired value, but what a plausible criteria for  $\Delta t$  is, was the point of departure of this work. We proposed two distinct criteria for the choice of  $\Delta t$  (i.e. Eqs (4.16) and (4.17)), and pursued preliminary simulations for finding a minimal size of the pore-network that can produce an asymptotic value of dispersivity  $\tilde{\alpha}_L$ , which delivered a size of  $33 \times 23 \times 23$  pore-units. Then we made extensive simulations for  $\tilde{\alpha}_L$  on that size and covered a wide range of ensemble averages and variances of porebody radii. Thus based on that data we could derive dispersivity-heterogeneity relations for MCM. With large networks of size  $301 \times 61 \times 61$  pore-units we verified whether newly derived relations are asymptotic. These simulations conformed that  $\tilde{\alpha}_L$  obtained from  $33 \times 23 \times 23$  network is indeed asymptotic. Further, we verified  $\Delta t$  criteria for MCM with the help of BPTM model with two different assumptions of intra-tube velocity profile. BPTM simulations revealed that time step criteria given by Eq (4.17) is indeed the best criteria to produce a comparable dispersion in a MCM. However, it appeared that MCM with these criteria produces the same dispersion as the one produced by BPTM with plug-like intra-bond velocity profile on networks with  $\tilde{\sigma}_{pb} > 0$  and with parabolic intra-bond velocity profile on networks with  $\tilde{\sigma}_{pb} = 0$ .

From this study we can conclude that for deriving an asymptotic numerical dispersion at least a  $33 \times 23 \times 23$  network is required. The numerical dispersivity in MCM is systematic and can be related to the porebody size variance. A family of such relations (i.e. Eq (4.25)) is found through regression and we recommend  $\Delta t$  from Eq (4.17) for which fitting parameters are recommended from Table 4.1. Hence, while considering a reactive transport analytically, there is no need of routing a non-reactive tracer just for determining the hydrodynamic (numerical) dispersion. The numerical dispersion for the proposed  $\Delta t$  of MCM can mimic the dispersion produced by a BPTM with plug-like intra-tube velocity profile. However, for the case of  $\tilde{\sigma}_{pb} = 0$  the numerical dispersion of MCM mimics the dispersion of BPTM with parabolic intra-tube velocity profile. For  $\tilde{\sigma}_{pb} > 0$  the dispersion produced by BPTM is larger than the numerical dispersion of MCM with the  $\Delta t$  proposed here. Hence, although MCM was assessed as a “without foundation” model [Gunn and Pryce 1969], this study revealed that MCM is a flexible model and numerical dispersion can be well controlled by  $\Delta t$ . Because of this ability, MCM can be used for upscaling reactive and non-reactive transport in porous media. Additionally, MCM is more appealing than the BPTM because MCM consumes much less computation time than the BPTM. For example, for the simulations reported here MCM on network S060 takes 6:10 CPU hrs, whereas for the same case BPTM takes 21:65 CPU hrs on 2.6 GHz machine with 500 MB RAM. Linearly and non-linearly reactive transport can easily be modeled with MCM, whereas BPTM has not yet been able to reveal any convincing results. However, so far MCM is applied only on HYPON [Acharya et al. 2004a] which has more realistic pore-unit architecture, but no studies is made whether MCM can produce the similar results if some other simplified networks are used is a question for further research.

## Acknowledgements

This study is performed under the research program “Upscaling Flow and Transport Processes in Porous Media: From Pore to Core” funded by the Dutch NWO/ALW project no. 809.62.010 and the project “Integrated Soil and Water Protection (SOWA)” funded by the European Commission (EVK1-CT-2002-80022). We appreciate useful discussions with Professor Ken Sorbie and Dr. Rink van Dijke, Heriot-Watt University, UK.



## Chapter 5

# Transport modeling of nonlinearly adsorbing solutes in physically heterogeneous pore-networks\*

### Abstract

The purpose of this study is to up-scale non-linearly reactive transport from the pore scale to a heterogeneous porous medium with the aid of an adequately large 3D pore-network model. We consider a porous medium that is physically heterogeneous, i.e. with spatially variable pore size. Our numerical experiments are aimed at the assessment whether traveling wave (TW) behavior develops, which also requires getting an impression how large the network should be to allow our conclusions. This study revealed that for this purpose network should include more than a million pore-units and this size can vary with the degree of heterogeneity. This assessment is based on changes of the moments of a migrating plume of non-linearly adsorbing solutes. In networks of equal sized pores, TW behavior occurs, and wave concentration distributions can be predicted by an available analytical solution. It is shown that with the increase of physical heterogeneity, the balance between the dispersive and adsorptive forces remains absent because the second central moment continues to grow as a function of time, whereas the moment growth rate appeared to be a function of pore-scale heterogeneity. To capture an asymptotic moment-growth rate a sufficiently large network is required.

**KEYWORDS:** reactive transport; dispersion; pore-network; non-linear adsorption; groundwater; upscaling; scale; traveling wave.

### 5.1 Introduction

Both from the need to understand natural (subsoil) systems and because of contamination problems of soil and groundwater, the transport of solutes in porous media has become an important issue. Solute transport is affected by intrinsic structure and texture of the porous medium. Additionally, solutes generally are not inert, but react with each other, with the solid phase, and with biota present in the porous medium. Such reactions may have a large effect on transport, and for this reason, much effort is being addressed to understanding and quantification of this

---

\*by Ram C Acharya, Sjoerd EATM van der Zee and Anton Leijnse, *Water Resour Res*, 2004, **in press**.

*List of symbols and notations* $\langle . \rangle$  Ensemble average $c, C$  Microscopic and macroscopic concentration [ $\text{ML}^{-3}$ ]

BPTM Brownian Particle Tracking Model

CDE Convection Dispersion Equation

BACON Biconical abscissa-Asymmetric CONcentric

 $\Delta c_{AD}$  Microscopic concentration increment [ $\text{ML}^{-3}$ ] $C_0, C_{in}$  Influent and initial effluent concentrations [ $\text{ML}^{-3}$ ] $D_m, D_L$  Molecular diffusion and longitudinal dispersion coefficients [ $\text{L}^2\text{T}^{-1}$ ] $G_{i,j}$  Dimensionless conductance [-]

HYPON HYdraulic POre Network

 $h_i, h_j$  hydraulic heads [L] $k$  Microscopic sorption coefficient [ $(\text{ML}^{-3})/(\text{ML}^{-3})^p$ ] $K_F$  Macroscopic sorption coefficient [ $(\text{MM}^{-1})/(\text{ML}^{-3})^p$ ] $\ell, L$  Node-to-node (bond) and the network lengths [L] $\tilde{\ell}$  Scaling factor ( $\ell/L$ ) [-] $M_1, M_n$  First [L] and nth spatial moments [ $\text{L}^n$ ] $M_2^c, b, \hat{b}$  Second-central moment  $\hat{b} = M_2^c(t = t_{tr})$  and  $b \sim \hat{b}$  [ $\text{L}^n$ ]

min, max minimum and maximum

 $N_t$  Total number of pore-units included in the inner core of the chosen tier $N_X, N_{XY}$  Number of nodes along  $X$  and  $XY$  plane

PDF Probability Density Function

 $Pe_\ell, \alpha_L$  Characteristic Peclet number ( $v\ell/D_m$ ) and dispersivity ( $D_L/v$ ) [-]

PU Pore Unit

 $\mathbf{q}, q_{i,j}, Q$  Discharges: vector, through bond  $i, j$  and through porenetwork [ $\text{L}^3\text{T}^{-1}$ ] $R$  Retardation factor [-] $R_{pb}, \tilde{R}_{pb}$  Dimensionfull [L] and dimensionless [-] porebody radius ( $\tilde{R}_{pb} = R_{pb}/\ell$ ) $s$  Microscopic sorption, mass absorbed per unit volume of flume [ $\text{ML}^{-3}$ ] $S$  Macroscopic sorption (mass of solute absorbed/mass of solid phase) [ $\text{MM}^{-1}$ ] $t, t_{tr}, \Delta t$  Time, transition time and time step of iteration [T] $\mathbf{T}$  Residence time vector [T]

TW Traveling Wave

 $v$  Mean intrinsic velocity along the principle flow direction in the pore network [ $\text{LT}^{-1}$ ] $V_{PU}, V_f$  Pore-unit and total fluid phase volumes [ $\text{L}^3$ ] $x, X$  Local (along bond  $0 \leq x \leq \ell$ ) and global (along network  $0 \leq X \leq L$ ) axis $\alpha_{res}, \hat{\alpha}_{res}$   $M_2^c$  growth rates with respect to  $M_1$  after transition times [L] $\gamma, \kappa$  Coefficients of skewness and kurtosis [-] $\varepsilon$  Porosity [-] $\mu_k$  Mean adsorption coefficient $\nu$  Coefficient of kinematic viscosity [ $\text{L}^2\text{T}^{-1}$ ] $\tilde{\sigma}_{pb}^2$  Variance of dimensionless porebody radii  $\tilde{R}_{pb}$  [-] $(i, j), L, m, pb, PU, n, tr, t$  Subscripts indicate the indices of nodes, Longitudinal, molecular, porebody, Pore Unit, nth, transition and tier (respectively). $c$  Superscript indicates central



effect. Because of the limitations with respect to scale and frequency of observations, experiments alone cannot provide this qualitative and quantitative understanding of transport, and mathematical modeling is needed.

Modeling is a scale dependent process, where smaller scale properties result in larger scale mass balance equations that contain effective coefficients [Bear 1972]. The convection-dispersion equation (CDE) [Whitaker 1969; Bear 1972] is an example of this kind. Basically such coefficients require explicit up-scaling [Whitaker 1969; Hassanizadeh and Gray 1979a], i.e. deriving upper scale definitions based on the lower scale quantities through mathematical operations. For porous media, up-scaling starts at the pore scale, where pore-scale geometry and other properties affect the macroscopic description of transport, i.e. both types of equations and their parameters. For this reason, pore-network models may be regarded as elementary tools for up-scaling studies [Fatt 1956a], because of their ability to develop understanding of the quantitative and qualitative effects of pore-scale heterogeneity [Celia et al. 1995].

It has been established that CDE is valid for porous media and analytical solutions have been provided for simplified cases such as mono-component, non-reactive or linearly adsorbing solutes transport in one or more-dimensional domains [Van Genuchten and Wierenga 1976; Van Genuchten and Alves 1982; Chrysikopoulos et al. 1990]. In agreement with the complexity of biogeochemical reactions [Bolt 1982], non-linear adsorbing solute transport in porous media has been considered [Van der Zee 1990; 1991]. To our best knowledge, the upscaling step from individual and networks of pores to the continuum scale of a porous medium has not yet been studied for nonlinearly reactive solute transport. Hence, it is not yet justified that the extension of the CDE with (non-linear) reaction terms is appropriate. Such a step has been made for multiphase transport [Mohanty and Salter 1982; Reeves and Celia 1996; Dahle and Celia 1999; Held and Celia 2001; Blunt et al. 2002]. Because of the flexibility for up-scaling [De Josselin de Jong 1958], pore-network models have already been applied for up-scaling a number of phenomena [Van Brakel 1975] such as multiphase flow dynamics [Celia et al. 1995; Reeves and Celia 1996; Gielen et al. 2002; Hassanizadeh et al. 2002], porosimetry, hysteresis, diffusion, dispersion, and (relative) permeability [Mohanty and Salter 1982; Sahimi et al. 1986; Dullien 1991; Ioannidis and Chatzis 1993; Tsakiroglou and Payatakes 2000; Blunt et al. 2002; Acharya et al. 2004b]. Although (non)-reactive transport in fractures and capillaries has been studied for quite a long time [Taylor 1953; Aris 1956; Berkowitz and Zhou 1996], little attention is paid to explicitly address the non-linearly adsorbing miscible transport in more complex pore geometry such as that of a 3D pore-network model [Reeves and Celia 1996; Acharya et al. 2004a; Acharya et al. 2004b]. The biofilm growth study in a simplified 2D pore-network [Suchomel et al. 1998a] and 2D pore-network analysis of non-ideal breakthrough curve (BTC) [Sugita and Gillham 1995b] are examples that have been considered. Suchomel et al. [Suchomel et al. 1998a] clearly showed that biofilms can have an considerable impact on permeability, without quantifying this impact. We expect that only the 3D pore-network geometry may allow us to integrate the three dimensional micro-structural effects and more-complex biogeochemical reactions into a transport model [Celia et al. 1995]. However, such networks have not yet been used for up-scaling the transport of non-linearly reactive solutes in heterogeneous porous media.

One of the most important issues in upscaling is the length-scale of the small process-scale ( $\ell$ ) and that of the large system-scale (i.e. representative volume) ( $L$ ), as the theory on volume averaging requires that  $\ell \ll L$  [Whitaker 1969; Bear 1972; Hassanizadeh and Gray 1979a]. Only for proper scaling factors ( $\tilde{\ell}$ , i.e.  $\tilde{\ell} = \ell/L$ ) statistically stable and stationary effective parameters result. The appropriate scaling factor ( $\tilde{\ell}$ ) depends not only on the discretization of

space but also on the type of process (or effective parameters) under consideration. For example, Koplik [Koplik 1982] showed that a 2D pore-network should comprise at least  $35 \times 35$  nodes in order to produce an asymptotically effective hydraulic permeability (*conductivity*), whereas for a 3D pore-network it can be as small as  $25 \times 15 \times 15$  nodes [Acharya et al. 2004a]. However, if the attention is turned to a different process like dispersion, these size constraints may not apply any more [Verlaan 2001]. Particle tracking studies that take diffusion ( $D_m$ ) into account showed that a consistent size for dispersion coefficient depends on the characteristic Peclet number ( $v\ell/D_m$ , with  $v$ , the average velocity across the network) [Sahimi et al. 1986; Acharya et al. 2004b]. Also at the capillary scale, Taylor-Aris theory suggests that the hydrodynamic dispersion depends on aspect-ratio and the capillary-Peclet number [Taylor 1953; Aris 1956]. Hence, the minimum scaling factor ( $\tilde{\ell}$ ) and the minimal ergodic size of the pore-network needed for studying non-linearly reactive transport is an important issue to investigate.

The purpose of this paper is to apply a 3D pore-network model for up-scaling non-linear reactive transport from the pore scale to a physically heterogeneous porous medium. Our numerical experiments are aimed at the assessment of whether the Traveling Wave (TW) behavior actually develops that is expected for non-linearly adsorbing reactive transport if the CDE is extended with a nonlinear reaction term. For this aim we quantify the development of the spatial moments of the migrating plume of non-linearly adsorbing solutes. We also investigate the minimal ergodic size of the pore-network such that we can draw quantitative and qualitative conclusions.

## 5.2 Mathematical formulation

We consider two scales, i.e. the microscopic or pore-scale, and the macroscopic or the continuum-scale, e.g. many thousand pores. Our pore-network is a cubic lattice with a coordination number  $\beta$  equal to six, and is comprised of pore-units (PUs). The centers of these pore-units are placed at a regular grid length, i.e. the lattice constant  $\ell$  and  $\ell \ll L$ . The symbol  $L$  denotes the length of the network. Each pore-unit is composed of a porebody (large void) of radius  $R_{pb}$  (i.e.  $R_{pb} = \tilde{R}_{pb}\ell$  and  $0 < \tilde{R}_{pb} \leq 0.5$ , where  $\tilde{R}_{pb}$  is the dimensionless porebody radius) and six converging cones (small voids) of different lengths (measured from the pore-unit center). The cones from each two adjacent porebodies form a converging-diverging Biconical abscissa-Asymmetric CONcentric bond (BACON bond). Hence, the size of the BACON bond along  $\ell$  is varying and follows from the simple power functions ( $f(R_{pb})$ ) given in our earlier work [Acharya et al. 2004a]. Depending on the wall curvature ( $n$ ), the BACON bonds are the union of two hyperbolic, parabolic or straight cones and hence possess a narrowest section (i.e. *the throat*), which is fixed by the intersection of two power functions that originate from the centers of the adjacent porebodies. For illustration a typical pore-unit is shown in Figure 5.1a, a typical BACON bond is shown in Figure 5.1b and a typical network is shown in Figure 5.2. Such a network mimics a porous medium, at least hydraulically [Van Brakel 1975; Acharya et al. 2004a]. The construction of such a pore-network is discussed by Acharya et al. [Acharya et al. 2004a] and therefore, would not be repeated here. In the following we introduce the equations of transport both in a pore and in a pore-network.

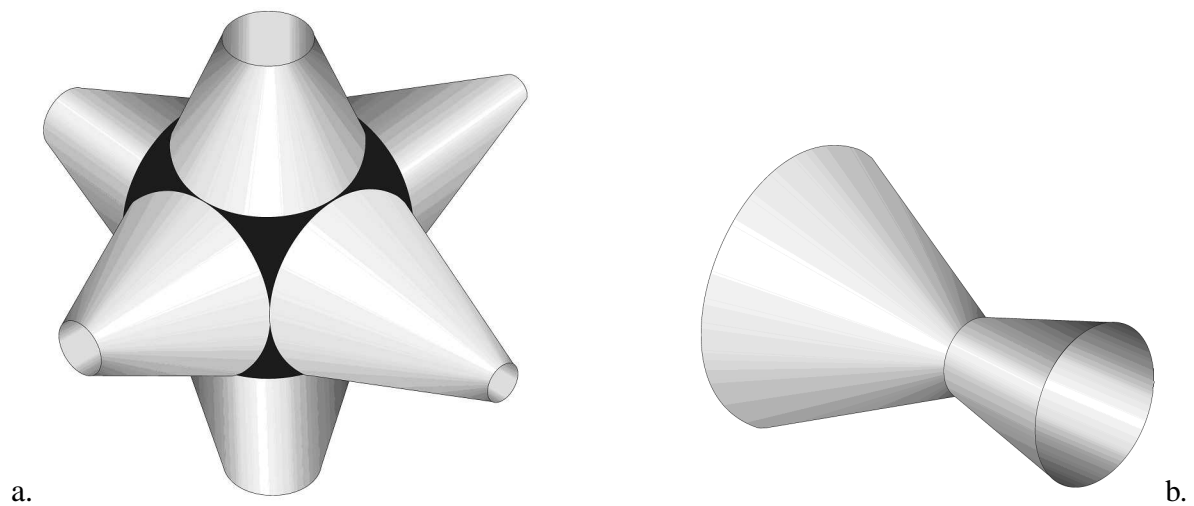


Figure 5.1: Basic elements of HYdraulic Pore Network (HYPON): a. the pore-unit (the pore-body is marked with the dark color) and b. the Biconical abscissa Asymmetric CONcentric (BACON) bond [Acharya et al. 2004a].

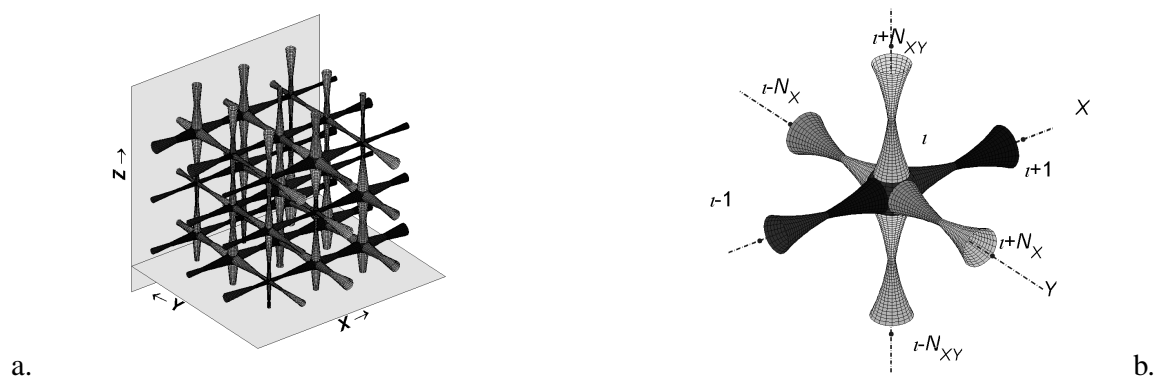


Figure 5.2: 3D Pore-network construction: a. Pore-network as an aggregate of pore-units b. A typical connectivity scheme for a cubic lattice with pores of circular cross section shape [Acharya et al. 2004a]. The symbols  $X$ ,  $Y$ , and  $Z$  denote coordinate axes, whereas  $N$  is the number of pore-units as specified by the subscripts:  $N_X$  along  $X$ ,  $N_{XY}$  in the  $XY$  plane and  $l$  is the index of the pore-unit.

### 5.2.1 Flow and transport equations at pore-scale

We represent a macroscopic porous medium with a cubic network of elementary pore-units as shown in Figure 5.1a. Such units may be assumed to be perfectly mixed [De Josselin de Jong 1958]. We ignore the contribution of diffusion ( $D_m$ ) to transport by assuming that advection dominates the transport. Particle-tracking experiments on pore-network showed that this assumption is appropriate for characteristic Peclet numbers ( $Pe_\ell = v\ell/D_m$ ) approximately between ten and  $10^4$  [Acharya et al. 2004b]. Hence, the equation of transport in a PU of HYPON is given by

$$V_{PU} \left( \frac{\partial c}{\partial t} + \frac{\partial s}{\partial t} \right) + \nabla \cdot (\mathbf{q}c) = 0, \quad (5.1)$$

where  $V_{PU}$  (see *the list of symbols and notations*) is the fluid volume of the pore-unit. We assume that sorption  $s$  (mass per fluid phase volume) is given by the Freundlich isotherm

$$s = kC^p, \quad (5.2)$$

where  $k$  is the Freundlich coefficient of adsorption and  $p$  is a parameter ( $0 < p < 1$ ).

The symbol  $\mathbf{q}$  denotes the discharge vector [ $L^3T^{-1}$ ] through bonds similar to that shown in Figure 5.1b. For each bond connected to two nodes, discharge can be computed with Hagen-Poiseuille equation

$$q_{i,j} = \frac{g}{\nu} \ell^3 G_{i,j} (h_i - h_j), \quad (5.3)$$

where subscripts  $i$  and  $j$  are the addresses of nodes (fluid flows from  $i$  to  $j$ ).  $G_{i,j}$  denotes the dimensionless bond conductance derived by Acharya et al. [Acharya et al. 2004a] in which both the longitudinal as well as cross sectional shapes of bond are taken into account [Reeves and Celia 1996]. The size of the BACON bond along  $\ell$  is derived considering the porebody radii of the adjacent porebodies and the curvature parameter  $n$ . The constant  $g$  is the magnitude of acceleration due to gravity and  $\nu$  is the kinematic viscosity of water. The symbols  $h_i$  and  $h_j$  are the hydraulic heads at the pore-unit centers  $i$  and  $j$ . Note that the pore geometry is expressed in terms of pore-to-pore spacing ( $\ell$ ), i.e. geometric lengths are scaled by  $\ell$ . Equation (5.3) is valid for laminar flow in a wide range of the Reynolds number and is appropriate for describing flow in the pores [Bear 1972]. For steady state flow, the divergence of discharges at nodes (pore-units) equals to zero [Acharya et al. 2004a] and that leads to a system of algebraic equations, i.e.

$$\sum_j^{\beta} q_{i,j} = 0, \quad j = 1, 2, \dots, \beta, \quad (5.4)$$

where  $j$  is the index of the adjacent pore-units.

### 5.2.2 Transport equations on macroscopic scale

Assuming no-flow boundaries at the lateral sides of the pore-network and introducing a flow from the left to the right macroscopically, a 1D-column is obtained. For such a column the mass balance equation is given by the CDE,

$$\varepsilon \frac{\partial C}{\partial t} + (1 - \varepsilon) \rho_s \frac{\partial S}{\partial t} + \varepsilon v \frac{\partial C}{\partial X} = \varepsilon D_L \frac{\partial^2 C}{\partial X^2}, \quad (5.5)$$

where  $S$  is the adsorbed mass per unit mass of the solid phase [ $MM^{-1}$ ], usually expressed in moles of adsorbate per kilogram of dry soil (with a density of  $\rho_s$ ). The adsorption equation is given by the Freundlich isotherm,

$$S = K_F C^p, \quad (5.6)$$

where  $K_F$  is the Freundlich adsorption coefficient and  $C$  is the concentration [ $ML^{-3}$ ] expressed in terms of mass per unit volume of fluid. After replacing the expression of  $S$  in Eq (5.5) and

dividing both sides of Eq (5.5) by porosity ( $\varepsilon$ ), an average adsorption coefficient for the fluid-phase can be expressed as

$$\mu_k = K_F(1 - \varepsilon)\rho_s/\varepsilon. \quad (5.7)$$

For a chosen value of  $K_F$ , the average coefficient  $\mu_k$  is computed on the basis of  $\rho_s$  and  $\varepsilon$  or vice versa. As a simplest choice, we take  $k$  of Eq (5.2) to equal  $\mu_k$  and  $k$  is the same in every pore unit. The longitudinal dispersion coefficient ( $D_L$ ) follows from upscaling pore-scale non-reactive transport [Acharya et al. 2004b]. Based on our numerical experiments, it was found that  $D_L$  can be estimated on the basis of pore size statistics and therefore, there is no need of routing non-reactive solute for the purpose of only determining  $\alpha_L$  [Van der Zee et al. 2004a]. The dimensionless dispersivity (i.e.  $\tilde{\alpha}_L = \alpha_L/\ell$ ) can be estimated as a function of standard deviation ( $\tilde{\sigma}_{pb}$ ) of the dimensionless porebody radii ( $\tilde{R}_{pb} = R_{pb}/\ell$ ) according to

$$\tilde{\alpha}_L(\langle \tilde{R}_{pb} \rangle) = B_1 \tilde{\sigma}_{pb}^2 + B_2 \tilde{\sigma}_{pb} + \tilde{\alpha}_0, \quad (5.8)$$

where  $\tilde{\alpha}_L$  is valid for a chosen ensemble average porebody radius ( $\langle \tilde{R}_{pb} \rangle$ ), because  $B_1$  and  $B_2$  are the fitting coefficients for the chosen  $\langle \tilde{R}_{pb} \rangle$ . Symbol  $\tilde{\alpha}_0$  is a constant (intercept) (see Table 5.1). Numerical study of Eq (5.8) is described in Chapter 4.

We use the fitted coefficients of Eq (5.8) and not a simpler relation of  $\tilde{\alpha}_L$  that can also be derived as a function of coefficient of variation,

$$\tilde{\alpha}_L = 1.53\eta_{pb}^2 + 0.683\eta_{pb} + \tilde{\alpha}_0, \quad (5.9)$$

where  $\eta_{pb}$  is the coefficient of variation of porebody radii (i.e.  $\eta_{pb} = \langle \tilde{R}_{pb} \rangle / \tilde{\sigma}_{pb}$ ). Compared to Eq (5.8) this equation has a less accurate fitting variance for which reason we ignore it in this paper. Since Eq (5.9) holds for different mean porebody radii (which is not the case for  $B_1$  and  $B_2$  values), Eq (5.9) is theoretically more appealing. It was shown that the values estimated by the above two equations are in good agreement [Van der Zee et al. 2004a] with the results obtained from particle tracking [Acharya et al. 2004b], which is a more robust method for determining the dispersion coefficient. In Section 5.4, we will also check the results of particle tracking with the results obtained through the mixing cell model (Eq (5.1)).

The macroscopic intrinsic (pore water) velocity  $v$  is determined with the Dupuit-Forcheimer equation

$$v = \frac{QL}{V_f}, \quad (5.10)$$

where  $Q$  is the macroscopic discharge across the pore-network and  $V_f$  is its fluid volume [Acharya et al. 2004a], i.e. the subscript  $f$  denotes the fluid phase.

We prescribe the initial and boundary conditions given by:

$$C(X > 0, t = 0) = C_{in}; C(0, t \geq 0) = C_0; \frac{\partial C}{\partial X} \big|_{(0, t > 0)} = 0; \frac{\partial C}{\partial X} \big|_{(L, t \geq 0)} = 0, \quad (5.11)$$

with  $C_0 > C_{in}$ . Under these boundary and initial conditions for times  $t \rightarrow \infty$ , Eq (5.5) and Eq (5.6) with  $0 < p < 1$  lead to the following relations to hold [Van Duijn and Knabner 1990]:

$$S' > 0, \quad S'' < 0, \quad (5.12)$$

where  $S' = dS(C)/dC$  and  $S'' = d^2S(C)/dC^2$  are the first and second derivatives of sorption with respect to concentration.

### 5.2.3 Analytical solutions

In a homogeneous porous medium, Eq (5.5) and Eq (5.6) subject to the boundary and initial conditions Eq (5.11) lead to a traveling wave [Van der Zee 1990; 1991; Knabner and Van Duijn 1992; Bosma and Van der Zee 1993]. The non-linearity of adsorption causes lower concentrations to experience a larger retardation than the higher concentrations, which opposes the Fickian spreading of front. Consequently, the concentration distribution  $C(X, t)$  approaches a limiting TW front, i.e. the  $C$ -front approaches a time-invariant shape and a constant travel velocity. Assuming that the Local Equilibrium Assumption (LEA) is valid and performing a Lagrangian transformation given by

$$\eta = X - vt/R \quad (5.13)$$

with corresponding boundary and initial conditions for the new coordinate system an analytical solution can be obtained [Van der Zee 1990; 1991; Bosma and Van der Zee 1993], that is given by

$$\tilde{C}(\eta) = \begin{cases} \left\{ 1 - \exp \left[ v(\eta - \eta^*)(1 - p)(R - 1)(RD_L)^{-1} \right] \right\}^m & \text{if } (\eta - \eta^*) \leq 0 \\ 0 & \text{otherwise,} \end{cases} \quad (5.14)$$

where the dimensionless concentration  $\tilde{C}(\eta) = (C(\eta) - C_{in})/(C_0 - C_{in})$ , the parameter  $m$  equals to  $1/(1 - p)$  and the retardation factor ( $R$ ) is given by

$$R = 1 + \frac{\rho_s(1 - \varepsilon)}{\varepsilon} \frac{\Delta S(C)}{\Delta C}. \quad (5.15)$$

In Eq (5.15),  $\Delta C = C_0 - C_{in}$  and  $\Delta S(C)$  is the corresponding change in the adsorbed amount. The reference value  $\eta^*$  is a constant [Van der Zee 1990; Bosma and Van der Zee 1993]. Note that  $C_0$  and  $C_{in}$  are respectively the concentration of the injected influent and initial (background) concentration of the solute in the considered system,  $C$  is the time-space concentration function [ $\text{ML}^{-3}$ ]. As was mentioned earlier,  $D_L$  is obtained by routing the non-reactive tracer through a column (pore-network) under the same boundary and initial conditions (given by Eq (5.11)). In that case,  $D_L$  is obtained by fitting the well known error function (i.e. the solution of CDE with  $k = 0$ ), given by [Van Genuchten and Alves 1982],

$$\tilde{C}(\tilde{X}, \tilde{T}) = \frac{1}{2} \left\{ \text{erfc} \left[ \frac{\tilde{X} - \tilde{T}}{2\sqrt{\tilde{\alpha}_L \tilde{\ell} \tilde{T}}} \right] + \exp \left( \frac{\tilde{X}}{\tilde{\alpha}_L \tilde{\ell}} \right) \text{erfc} \left[ \frac{\tilde{X} + \tilde{T}}{2\sqrt{\tilde{\alpha}_L \tilde{\ell} \tilde{T}}} \right] \right\}. \quad (5.16)$$

In Eq (5.16) it is assumed that  $D_L \sim \alpha_L v$ , which is a plausible assumption for the characteristic Peclet numbers considered in our simulations [Acharya et al. 2004b]. The dimensionless quantities are:  $\tilde{\ell} = \ell/L$ ,  $\tilde{X} = X/L$  and  $\tilde{T} = vt/L$ . While fitting this equation to a BTC at the outlet face of the pore-network,  $\tilde{X}$  is fixed at 1.0, then  $\tilde{\alpha}_L$  is found with the method of least squares. In particle tracking methods  $\alpha_L$  can be obtained with the methods of moments [Sahimi et al. 1986]. As  $\tilde{C}(X, t)$  can be interpreted as a probability function, its first derivative with respect to  $X$  is used to produce the probability density function (PDF,  $f(X)$ ) [Bosma and Van der Zee 1993; Keijzer et al. 2000] according to

$$f(X) = -\frac{\partial \tilde{C}}{\partial X}. \quad (5.17)$$

### 5.2.4 Spatial moments for non-linear adsorption and transport

Since it has been shown that the validity of Eq (5.14) can be evaluated more accurately with the second central spatial moment ( $M_2^c$ ) than by comparing front shapes of  $C(X, t)$ , we use the expression for  $M_2^c$  derived by Bosma and Van der Zee [Bosma and Van der Zee 1993]. Assuming  $D_L = v\alpha_L$  and introducing

$$\tilde{\eta} = (\eta - \eta^*) \leq 0, P = \frac{R-1}{mR\alpha_L} \text{ with } m > 1, \quad (5.18)$$

the dimensionless concentration profile can be written as

$$\tilde{C}(\tilde{\eta}) = \frac{C(\tilde{\eta}) - C_{in}}{C_0 - C_{in}} = 1 + \sum_{i=1}^m \chi_i \exp(Pi\tilde{\eta}), \chi_i = (-1)^i \frac{m!}{(m-i)!i!}, \quad (5.19)$$

for  $i = 0, 1, 2, 3, \dots, m$  and  $m$  is an integer.  $\tilde{C}(\tilde{\eta})$  for non-integer values of  $m$  are obtained graphically through interpolation.

As is seen from Eq (5.19),  $\tilde{C}$  varies from zero to one and has the properties of a probability function. Using first derivative of  $\tilde{C}(X, t)$  (i.e. Eq (5.17)) spatial moments of all orders are computed:

$$M_n^c(t) = \frac{\int_{-\infty}^{\infty} [X - M_1(t)]^n f(X) dX}{\int_{-\infty}^{\infty} f(X) dX}, M_1(t) = \frac{\int_{-\infty}^{\infty} X f(X) dX}{\int_{-\infty}^{\infty} f(X) dX}, n = 2, 3, \dots \quad (5.20)$$

$$\gamma = \frac{M_3^c}{\sqrt{(M_2^c)^3}}, \kappa = \frac{M_4^c}{(M_2^c)^2}, \quad (5.21)$$

where subscript  $n$  denotes the order of spatial moments and the superscript  $c$  indicates “central”, e.g.  $M_1(t)$  is the first spatial moment at time  $t$ . Symbol  $\gamma$  denotes the coefficient of skewness or the measure of symmetry, whereas  $\kappa$  is the coefficient of kurtosis or the measure of peakedness or flatness. For a normal distribution  $\gamma = 0$  and  $\kappa = 3.0$ . The distribution with  $\gamma < 0$  not equal to zero is called skewed distribution. The distribution having a  $\kappa > 3$  is called leptokurtic, whereas the one with a  $\kappa$  less than three is called platykurtic. For the case of non-reactive tracer transport, by assuming  $D_L \sim \alpha_L v$ , the dispersivity ( $\alpha_L$ ) can be expressed in terms of the Einstein's relation [Chandrasekhar 1943], i.e.

$$\alpha_L = 0.5 \frac{M_2^c(t_2) - M_2^c(t_1)}{M_1(t_2) - M_1(t_1)}, \quad (5.22)$$

where  $t_1$  and  $t_2$  are the times. Equation (5.22) shows that  $\alpha_L$  is the half-slope of the second central spatial moment to the first spatial moment ( $M_1$ ). For a TW, the second central moment ( $M_2^c$ ), i.e. the spatial variance of the front, approaches a fixed value asymptotically given by

$$M_2^c = -\frac{1}{P^2} \left[ 2 \sum_{i=1}^m \frac{\chi_i}{i^2} + \left( \sum_{i=1}^m \frac{\chi_i}{i} \right)^2 \right], i \geq 1 \quad (5.23)$$

and so do the higher order spatial moments [Bosma and Van der Zee 1993; Keijzer et al. 2000]. Rearranging Eq (5.23) yields

$$\frac{M_2^c}{\alpha_L^2} = -\left( \frac{mR}{R-1} \right)^2 \left[ 2 \sum_{i=1}^m \frac{\chi_i}{i^2} + \left( \sum_{i=1}^m \frac{\chi_i}{i} \right)^2 \right]. \quad (5.24)$$

Equation (5.24) is shown graphically in Figure 5.3. The figure reveals that second central moment of TW explicitly depends on retardation factor, non-linearity of adsorption and dispersion. Figure 5.3 shows that second central moment of the traveling front is not sensitive to  $R$  for large retardation factors, but is influenced mainly by the degree of non-linearity ( $p$ ) of adsorption (i.e. parameter  $m$  and  $m > 1$ ).

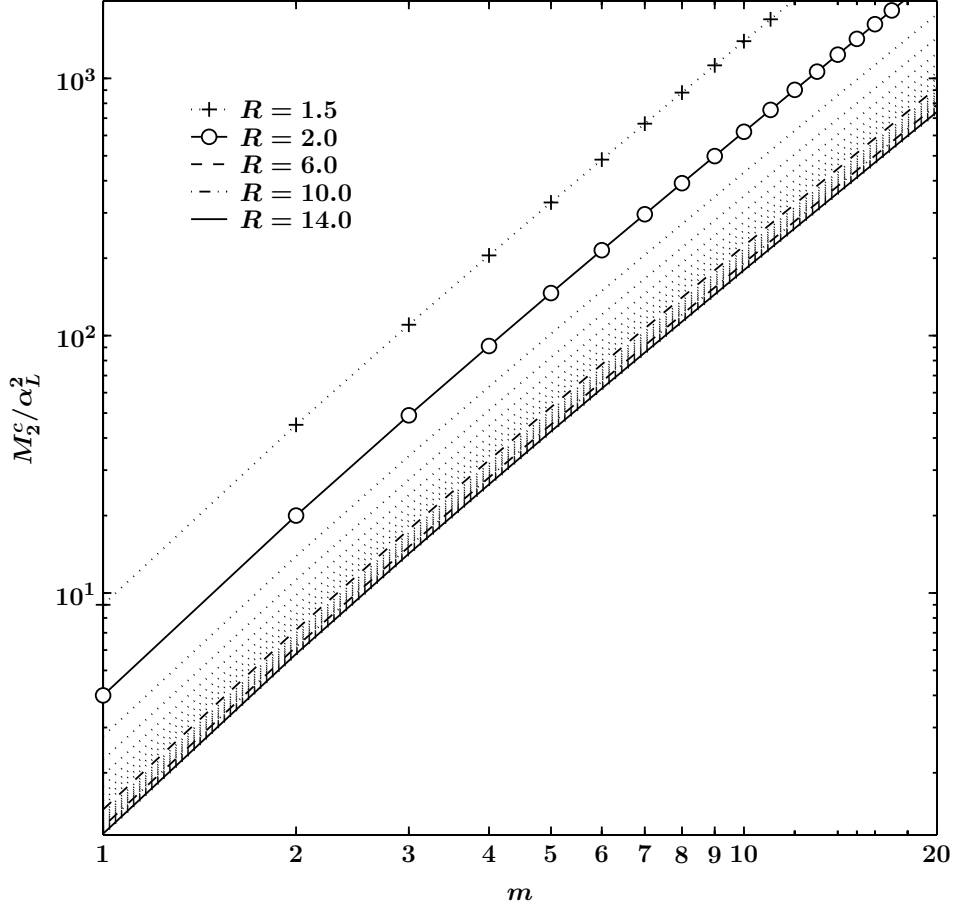


Figure 5.3: Asymptotic non-dimensionalized second central moment of the TW front (Eq (5.19)) as a function of parameter ( $m$ ) and retardation factor ( $R$ ) [Bosma et al.].

### 5.3 Numerical procedure

Imposing a hydraulic head difference across the pore-network in the  $X$ -direction, Eq (5.4) is solved for hydraulic heads and subsequently the discharges through the bonds (i.e. Eq (5.3)) are calculated. The computation of transport in pore-units, i.e. Eq (5.1) depends on these discharges. At the network scale, we can use the analytical solution (Eq (5.14)) to predict the concentration profiles along the mean flow direction, because  $v$ ,  $D_L$  and  $R$  are known [Bosma and Van der Zee 1992].



### 5.3.1 Numerical scheme for microscopic approximation

Under initial and boundary conditions given by Eq (5.11) the numerical scheme for the computation of transport in a pore-unit can be written as

$$c(i, t + \Delta t) - c(i, t) + k[c(i, t + \Delta t)]^p - k[c(i, t)]^p = \underbrace{\frac{\Delta t}{V_{PU}} \left[ \sum_j c(j, t) q_{j,i} - c(i, t) (q_{PU})_i \right]}_{\Delta c(i, t)_{AD}}, \quad (5.25)$$

where the index  $j$  is chosen such that  $h_j > h_i$ . The node discharge  $(q_{PU})_i$  is the sum of the flows entering or leaving the node  $i$ , i.e.

$$(q_{PU})_i = \sum_j |q_{j,i}|, \quad h_j > h_i, \quad j = 1, 2, 3 \dots \beta. \quad (5.26)$$

Rewriting Eq (5.25) as

$$c(i, t + \Delta t) + k[c(i, t + \Delta t)]^p = \Delta c(i, t)_{AD} + k[c(i, t)]^p + c(i, t) = B(i, t + \Delta t), \quad (5.27)$$

the resulting Eq (5.27) can be solved using an optimization technique, such as Newton-Raphson [Sun 1996]. For the stability of the scheme, the minimum time step is chosen on the basis of bond residence times, i.e.

$$2\Delta t \leq \min \{ [\mathbf{V}_b][\mathbf{q}_b^{-1}] \} = \min \{ \mathbf{T}_b \}, \quad (5.28)$$

where subscript  $b$  denotes bond,  $\mathbf{q}_b$  is the matrix vector of discharges through the bonds given by Eq (5.3). Similarly,  $\mathbf{V}_b$  and  $\mathbf{T}_b$  denote volume and time matrices pertaining to the bonds, where  $V_b = \text{volume of bond} + \frac{1}{6} \text{ porebody volume } (i) + \frac{1}{6} \text{ porebody volume } (j)$  (see [Acharya et al. 2004a]). Average concentration for each pore-unit is updated at the end of each  $\Delta t$ .

### 5.3.2 Numerical scheme for macroscopic approximation: Averaging

At designated time steps ( $\gg \Delta t$ ), the concentrations of pore-units that belong to a particular tier of the pore-network are averaged. The tiers are defined as the group of pore-units which possess the same  $X$ -coordinate. To avoid boundary effects, we consider the pore-units of the inner core only [Reeves and Celia 1996; Held and Celia 2001], i.e. the network volume left after the exclusion of a chosen volume at the no-flow boundaries. The excluded volume at each no-flow boundary is chosen to be  $5\ell$  thick. For averaging, the discharges from the PU (or into the PU) are used as the weighting factors of the corresponding PU concentrations. Hence, the resulting dimensionless concentration function  $\tilde{C}(X, t)$  for a 1D column (at the network scale) is written as

$$\tilde{C}(X, t) = \left[ \frac{\sum_i^{N_t} c(i, t) (|q_{PU}|)_i}{\sum_i^{N_t} (|q_{PU}|)_i} - C_{in} \right] \frac{1}{C_0 - C_{in}}, \quad i = 1, 2, 3 \dots N_t, \quad (5.29)$$

where the symbol  $N_t$  denotes the total number of pore-units that are indexed with  $i$  and that possess the same coordinate  $X$ . The subscript  $t$  denotes tier. The  $X$ -coordinate is chosen

at an interval of  $\ell$ , i.e.  $X = 0, 1\ell, 2\ell, \dots L$ . Further, this concentration is plotted against space ( $X$ -coordinate) to get concentration profiles (*isochrones*) at different times. The BTC is obtained by plotting  $\tilde{C}(X = L, t)$  as a function of time. The PDF (5.17) is discretized by choosing  $\partial X \approx \ell$ , i.e

$$f(X + \frac{1}{2}\ell, t) = -\frac{\tilde{C}(X + \ell, t) - \tilde{C}(X, t)}{\ell}. \quad (5.30)$$

## 5.4 Simulation cases

Preliminary simulations suggested that at least a million ( $10^6$ ) pore-units are required to achieve the asymptotic growth rates of second central moments of non-linearly adsorbing solute migration in a microscopically heterogeneous medium. Hence, we use a cubic pore-network of size  $301 \times 61 \times 61$  pores for the reported simulations. To capture effects of microscopic heterogeneity on transport, five systematic cases (S000, S030, S060, S086 and S115) that are listed in Table 5.1 were considered. The pore-units are constructed with the curvature parameter ( $n$ ) equal to one and the ensemble of dimensionless porebody radii ( $\tilde{R}_{pb}$ , i.e.  $\tilde{R}_{pb} = R_{pb}/\ell$ ) taken from a uniform distribution [Acharya et al. 2004a].

Table 5.1 reveals that Case S000 represents a homogeneous medium, whereas the other cases represent physically heterogeneous media. In all cases, we fixed the mean ( $\langle \tilde{R}_{pb} \rangle$ ) of the porebody radii at 0.30, and for each case we generated a pore-network with a chosen standard deviation ( $\tilde{\sigma}_{pb}$ ) of  $\tilde{R}_{pb}$  that varies from zero (Case S000) to 0.115 (Case S115). In all cases the macroscopic hydraulic head drop across the network was fixed at 0.07 m. Additionally,  $\ell = 0.25 \times 10^{-3}$  m and  $D_m = 8.0 \times 10^{-10}$  m<sup>2</sup>/sec (Taylor's data, [Taylor 1953]) are used for the Brownian particle tracking model [Acharya et al. 2004b]). As Table 5.1 reveals, each

Table 5.1: Microscopic and macroscopic input parameters for the numerical experiments

Cases	S000	S030	S060	S086	S115
$\min \tilde{R}_{pb}$	0.300	0.248	0.204	0.152	0.100
$\max \tilde{R}_{pb}$	0.300	0.352	0.412	0.450	0.500
$\tilde{\sigma}_{pb}$	0.000	0.030	0.060	0.086	0.115
$\varepsilon$	0.240	0.243	0.265	0.267	0.285
$\mu_k$	8.11	7.96	7.09	6.88	6.39
$R$	9.11	8.96	8.09	7.88	7.39
$\tilde{\alpha}_L$	0.434	0.496	0.614	0.764	0.982
$Pe_\ell$	384	386	430	405	420

Coefficient  $\mu_k$  is computed based on fixed  $K_F$ , the density of the solid phase ( $\rho_s$ ) and the porosity ( $\varepsilon$ ) of modeled porous medium.  $\tilde{\alpha}_L|_{\langle \tilde{R}_{pb} \rangle = 0.30} = 32.11\tilde{\sigma}_{pb}^2 + 1.072\tilde{\sigma}_{pb} + 0.4344$  (see Eq (5.8)).

case has a different porosity ( $\varepsilon$ ) of the network. Consequently, although we choose the same influent of unit concentration ( $C_0 = 1$  g/m<sup>3</sup>) for injection and same value of  $K_F$ , the value of adsorption coefficient  $\mu_k$  (and also  $k = \mu_k$ ) differs from case to case. The reason of such difference follows from Eq (5.7), as it depends on density of the solid phase and the porosity of porous medium. The values of  $\mu_k$  presented in the table are calculated on the basis of  $\rho_s = 2.6$

$\text{Mg/m}^3$ ,  $K_F = 0.982 \times 10^{-3} (\text{Mg/Mg})/(\text{g/m}^3)^p$  and the corresponding porosity ( $\varepsilon$ ). The parameter  $p$  is fixed at 0.667 and  $C_{in} = 0$ . Further we assume  $k$  to be constant over the whole network, i.e.  $k$  in each pore-unit is constant in space and time. The retardation factor  $R$  is calculated with Eq (5.15).

In Table 5.1,  $\tilde{\alpha}_L$  was calculated with Eq (5.8). A cross-check was made for Cases S086 and S115 by routing a non-reactive tracer (i.e.  $K_F = 0$ ) with two methods: mixing cell model (MCM) and Brownian particle tracking model (BPTM) [Acharya et al. 2004b]. The BTCs at the outlet face of the networks from both methods are displayed in Figure 5.4. Also the BTC computed with Eq (5.16) by using  $\tilde{\alpha}_L$  is shown in the same figure. The slight difference between BPTM and MCM results because in MCM (see Eq (5.1))  $D_m$  is not included whereas in BPTM  $D_m$  is included. The small differences indicate that contribution of  $D_m$  is not important. Figure 5.4 reveals that the BTC from BPTM is more dispersed than the one from MCM, which is theoretically correct. However, it is worth to note that in Case S115 slightly larger deviation is evident than in Case S086. That can be the effect of large aspect ratios (bond radius to  $\ell$  ratio), where particle tracking models are quite sensitive [Sorbie and Clifford 1991]. Furthermore, we expect that the non-linearity of adsorption decreases the diffusion within individual pores (see Section 5.2.4). Hence, the results obtained with MCM are expected to be valid and the values of  $\tilde{\alpha}_L$  given in Table 5.1 are reasonable approximations.

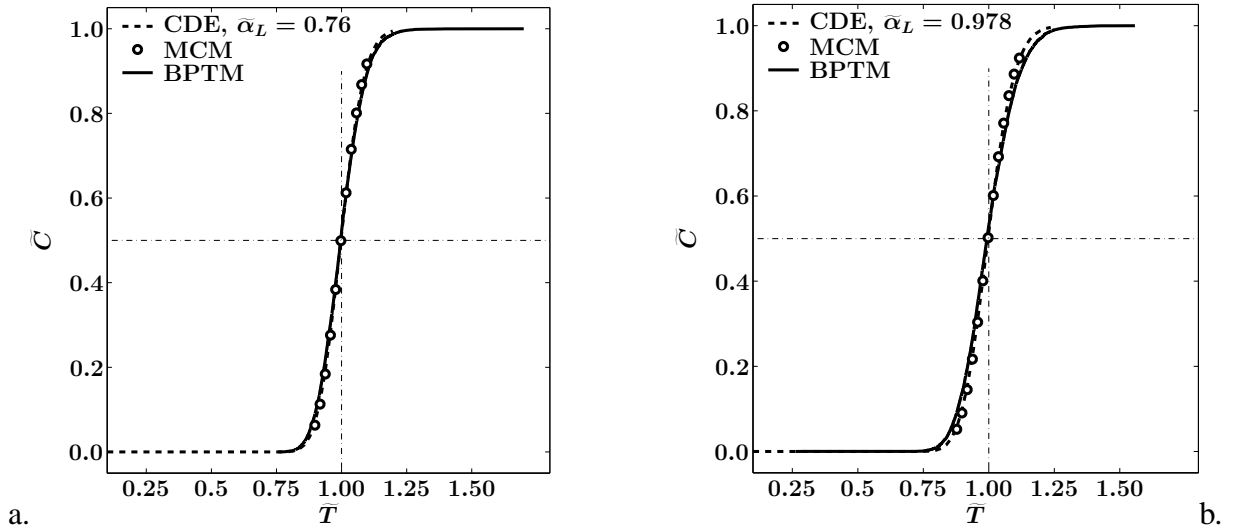


Figure 5.4: BTCs at the outlet face of the network a. Case S086 b. Case S115. MCM (open circles) indicates the results of numerical simulations from pore-network model HYPON (Eq (5.29)), BPTM (solid lines) indicates the results from the simplified network in which Brownian particle tracking procedure is applied [Acharya et al. 2004b], CDE (dashed lines) indicates the results from Eq (5.16) with  $\tilde{\alpha}_L$  of Table 5.1 (and as displayed in the figure).

In addition, one control Case S086\* (a separate realization with the same statistics as of S086) was proposed for the consistency test, i.e. to assess whether the used size is ergodic. A second verifying Case S086\*\* is proposed for verifying the moment-growth rate and pore radii statistics relations. This case is distinguished with  $\langle \tilde{R}_{pb} \rangle = 0.25$ ,  $\tilde{\sigma}_{pb} = 0.086$ ,  $\varepsilon = 0.194$  and  $\mu_k = 10.57 (\text{g/m}^3)^{(1-p)}$ . Discussion on these additional cases is deferred in the latter sections.

## 5.5 Results

The primary output of the numerical simulations are the concentration profiles at different times (see Eq (5.29)).

### 5.5.1 Concentration profiles

In Figure 5.5a, the dimensionless (numerical) concentration profiles for Case S000 are shown. On the network scale, TW solution (i.e. Eq (5.14)) is used with upscaled adsorption coefficient (Eq (5.7)) to predict the concentration profiles analytically. These predicted dimensionless profiles are also shown in the same figure.

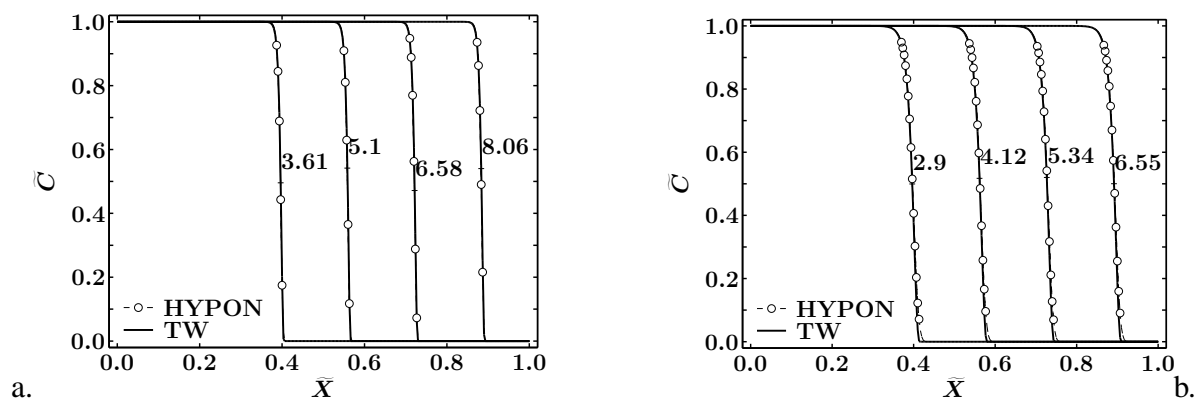


Figure 5.5: Dimensionless concentration profiles at different times as a function of fraction of column length ( $\tilde{X} = X/L$ ) a. Case S000 b. Case S115. HYPON (dashed lines with open circles) indicates the results of numerical simulations from pore-network model HYPON (Eq (5.29)), TW (solid lines) indicates the analytical TW solution (Eq (5.14)) with the same adsorption coefficient (see also Table 5.1). The labels of curves indicate the times, i.e. the pore volumes of effluent discharged from the network.

Figure 5.5 shows that numerical and analytical profiles agree excellently at larger times. Such an agreement is an indicator that in a microscopically homogeneous medium TW occurs, i.e. numerical front shape and front velocity become invariant in time. A similar comparison is shown in Figure 5.5b for Case S115, which case represents a microscopically heterogeneous medium. Unlike in the previous case, a perfect agreement does not develop in this case. Slight differences are found particularly for small concentrations.

### 5.5.2 Second central moment

For better comparison of analytical and numerical results, spatial moments [Bosma and Van der Zee 1993; Keijzer et al. 2000] are computed. For such a computation a PDF is required which is obtained with Eq (5.30). Figure 5.6a gives an impression of the PDF produced by Case S000, whereas Figure 5.6b represents the PDF of Case S115.

Figure 5.6 reveals that for these two cases the behavior of the fronts is not the same. In the first case the front is more sharper than in Case S115. Common in both is that both  $M_1$  of both PDFs are skewed indicating to a non-Fickian behavior. To gain a better insight, the second central moments for all cases for different times are plotted against the first spatial moment as shown in Figure 5.7.

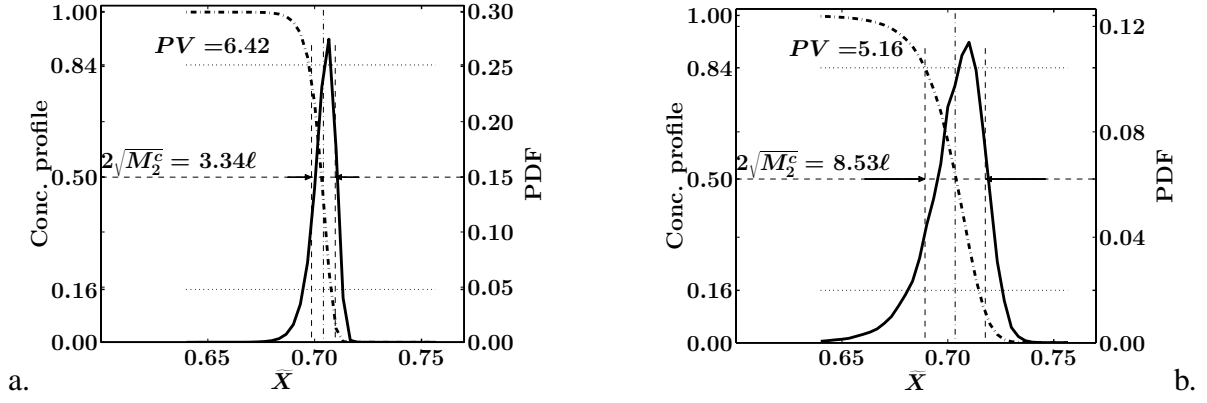


Figure 5.6: Typical PDFs ( $f(X)\ell$ ) of concentration profiles in a pore-network. a. Case S000. b. Case S115. Shown are the PDFs (solid lines) and concentration profile (dash-dotted lines) at the chosen times ( $PV$ ) as shown in the figure, i.e. number of pore volumes ( $PV$ ) discharged from the network. The values of  $2\sqrt{M_2^c}$  at times  $\tilde{T} = PV$  are shown.

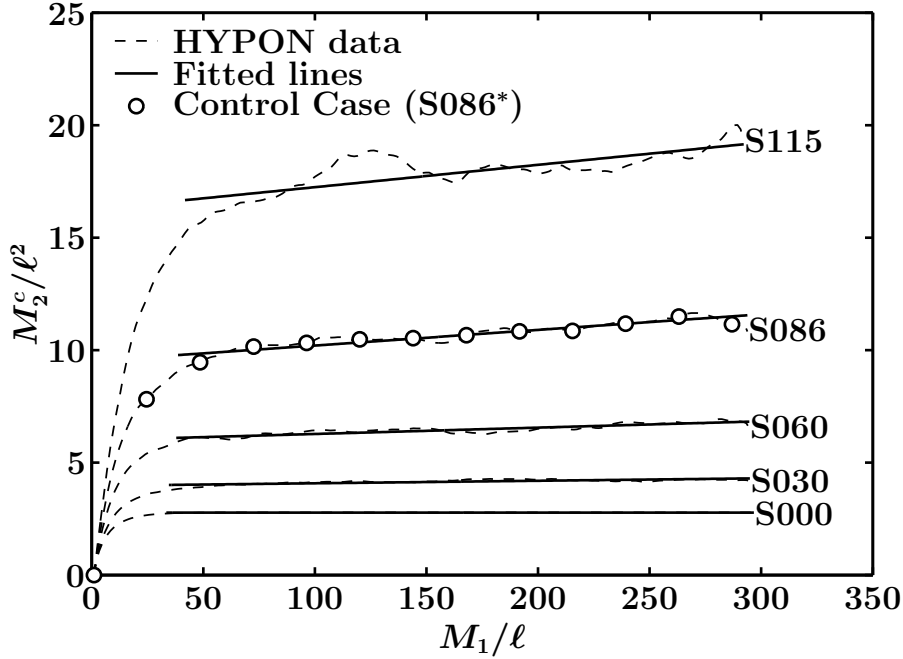


Figure 5.7: Dimensionless second central moments ( $M_2^c/\ell^2$ ) and fitted lines. Second central moments (dashed lines) as a function of  $M_1/\ell$  and the fitted lines (solid lines,  $\widehat{M}_2^c/\ell^2$ , Eq (5.31)) for cases as identified at the lines. With open circles  $M_2^c$  of the control Case S086\* are indicated.

Figure 5.7 reveals that for Case S000 convergence occurs to the TW, because after some transition length  $M_2^c$  acquires an asymptotic value [Van der Zee 1990; 1991; Bosma and Van der Zee 1993]. Because of the asymptotic behavior after a transition time,  $M_2^c$  has no slope ( $\alpha_{res} = 0$ ) as a function of time, i.e. a time-invariant spreading and self-sharpening of the front. Similar plots for the other cases show a gradual increase of slopes of the fitted lines ( $\widehat{M}_2^c$ ) which increases with an increase of heterogeneity (see Table 5.1). Also the intercept ( $b$ ) increases as

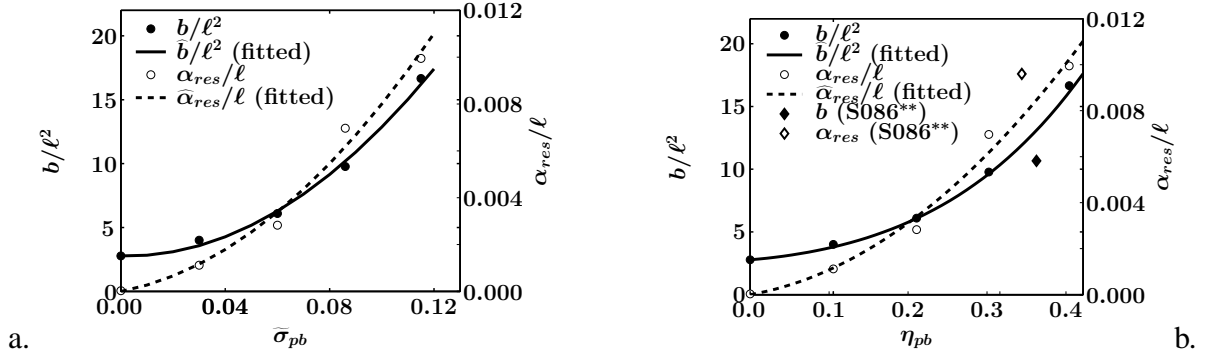


Figure 5.8: Slopes and intercepts a. Slopes ( $\alpha_{res}$ ) and intercepts ( $b$ ) of  $\widehat{M}_2^c$  as a function of standard deviation ( $\tilde{\sigma}_{pb}$ ) of porebody radii. The solid line (fitted,  $\widehat{b}$ ) and the solid circles ( $b$ ) indicate intercepts; the dashed line (fitted,  $\widehat{\alpha}_{res}$ ) and the open circles ( $\alpha_{res}$ ) indicate the slopes (see Table 5.2, Eq (5.33) and Eq (5.34)). b. Slopes ( $\alpha_{res}$ ) and intercepts ( $b$ ) of  $\widehat{M}_2^c$  as a function of coefficient of variation of porebody radii ( $\eta_{pb} = \tilde{\sigma}_{pb}/\langle \tilde{R}_{pb} \rangle$ ). The solid line (fitted,  $\widehat{b}$ ) and the solid circles ( $b$ ) indicate intercepts; the dashed line (fitted,  $\widehat{\alpha}_{res}$ ) and the open circles ( $\alpha_{res}$ ) indicate the slopes. The solid diamond indicates the intercept and the open diamond indicates the slope  $\alpha_{res}$  of the verifying Case S086\*\* (see Table 5.2, Eq (5.33) and Eq (5.34)).

heterogeneity increases. The fitted lines follow the regression equation for  $\widehat{M}_2^c$  given by

$$\widehat{M}_2^c(t) = \alpha_{res}[M_1(t) - M_1(t_{tr})] + b, t > t_{tr}, \quad (5.31)$$

where  $\alpha_{res}$  is the slope which is valid for the long run after the transition time ( $t_{tr}$ ). At time  $t = t_{tr}$  second central moment reaches a value  $b$ , which we call intercept of fitting. In analogy with Eq (5.22),  $\frac{1}{2}\alpha_{res}$  can be seen as the reduced dispersivity of non-linearly adsorbing transport. Both  $\alpha_{res}$  and  $b$  are presented in Table 5.2. The coefficients of correlation ( $\mathcal{R}^2$ ) of  $M_2^c$  and  $\widehat{M}_2^c$  are also listed in the same table.

Table 5.2: Parameters of linear-equation fitting to the numerical second central moments

Cases	S000	S030	S060	S086	S115
$\alpha_{res}/\ell$ [-]	0.0000	0.0011	0.0028	0.0070	0.0099
$b/\ell^2$ [-]	2.7760	4.0046	6.0957	9.7764	16.6647
$\mathcal{R}^2$ [-]	0.9999	0.7739	0.9021	0.9312	0.7695

See Figure 5.7.

Figure 5.7 clearly shows that the goodness of fitting of the regression equations also varies. The Case S000 shows a perfect agreement with the numerical data. Cases S030 and S060 also show a good agreement. In Case S086 individual deviations are noticeable. However, the statistical stability of the used size cannot be questioned, because the control Case S086\* perfectly match the base Case S086. That affirms the sufficiency and ergodicity of the pore-network of size  $301 \times 61 \times 61$  (at least for the chosen data set). That indicates that Monte Carlo simulations are not necessary to reach robust conclusions. Unfortunately, in Case S115, the deviations are the largest. That indicates that the chosen network might still be small to accommodate the chosen pore size statistics of this case. For ergodic reasons, larger than the

size  $301 \times 61 \times 61$  could not be simulated. Nevertheless, considering the fitness (which is fair) into account, it can be argued that Monte Carlo simulations are not needed in this case either but larger network size would be recommendable. As we can see, in sufficiently large networks, the first derivative of second central moment with respect to the first spatial moment becomes positive and the second derivative approaches to zero, i.e.

$$\frac{dM_2^c}{dM_1} \geq 0, \quad \frac{d^2 M_2^c}{dM_1^2} \rightarrow 0. \quad (5.32)$$

In Figure 5.8a, the slopes ( $\alpha_{res}$ ) and intercepts ( $b$ ) of  $\widehat{M}_2^c$  (see Table 5.2) are plotted as a function of standard deviation of porebody radii (see Table 5.1). Subsequently, the data pertaining to  $\alpha_{res}$  are regressed with  $\widehat{\alpha}_{res}$  whereas the intercepts are fitted with  $\widehat{b}$ . Both for the slope  $\widehat{\alpha}_{res}$  and for the intercept  $\widehat{b}$ , quadratic regression equations of the standard deviation of porebody radii were fitted to the numerical results. In terms of standard deviation of porebody radii, the equation of  $\widehat{\alpha}_{res}$  for the slope is given by

$$\widehat{\alpha}_{res} = (0.588\widetilde{\sigma}_{pb}^2 + 0.0212\widetilde{\sigma}_{pb})\ell \quad (5.33)$$

and  $\widehat{b}$  for the intercept is described with

$$\widehat{b} = (1057.3\widetilde{\sigma}_{pb}^2 - 4.8965\widetilde{\sigma}_{pb} + 2.7760)\ell^2, \quad (5.34)$$

These relations demonstrate the functional link between the pore size heterogeneity and the plume spreading. Note that these relations are valid for a particular mean porebody radii ( $\langle \widetilde{R}_{pb} \rangle = 0.30$ ). For other mean radii, more simulations have to be pursued and empirical relations need to be deduced. Unfortunately, the simulations are quite excessive with respect to the CPU times and memory requirements for which reason we did not pursue this in the present paper. Alternatively, the equation of  $\widehat{\alpha}_{res}$  for the slope can also be expressed in terms of coefficient of variation of the porebody radii, i.e.

$$\widehat{\alpha}_{res} = (0.532\eta_{pb}^2 + 0.0063\eta_{pb})\ell \quad (5.35)$$

and  $\widehat{b}$  for the intercept is given according to

$$\widehat{b} = \left( 11.66\eta_{pb}^2 + 1.67\eta_{pb} + \sqrt{2.776} \right)^2 \ell^2. \quad (5.36)$$

In Figure 5.8b  $\alpha_{res}$  and  $b$  are plotted as a function of  $\eta_{pb}$ . Also the fitted functions  $\widehat{\alpha}_{res}$  and  $\widehat{b}$  are shown in the same figure. Figure 5.8b reveals a good agreement of the fitted functions with the numerical data. To verify the validity of Eqs (5.35) and (5.36) for other ensemble averages ( $\langle \widetilde{R}_{pb} \rangle$ ), the values of  $\alpha_{res}$  and  $b$  of the verifying Case S086\*\* are also shown in the same figure but with different symbols (see figure). Figure 5.8b reveals that although the values of Case S086\*\* do not fall on the regression line, the relations of  $\widehat{\alpha}_{res}$  and  $\widehat{b}$  as a function of  $\eta_{pb}$  are theoretically appealing.

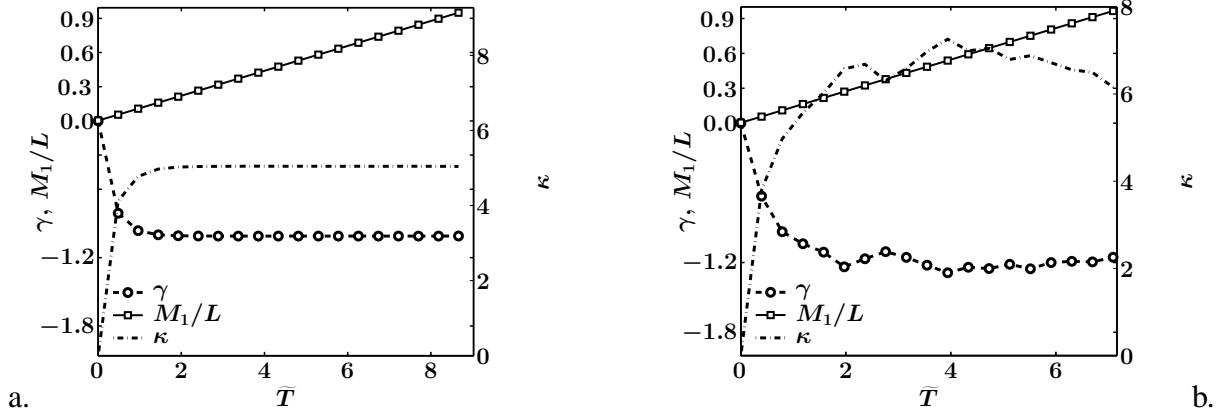


Figure 5.9: Macroscopic spatial first moment, skewness ( $\gamma$ ) and kurtosis ( $\kappa$ ) of plume (Table 5.1) as a function of pore volume of the effluent: a. Case S000; b. Case S115. The legends are shown in the figure.

### 5.5.3 First and higher-order spatial moments

The higher-order spatial central moments are the quantitative measure of spread ( $M_2^c$ ), symmetry ( $\gamma$ ) and peakedness ( $\kappa$ ) of concentration distribution function (see section 5.2.4), whereas the first spatial moment shows the location of front in space. In Figure 5.9a first spatial moment ( $M_1$ ) and other higher order spatial moments, namely skewness ( $\gamma$ ) and kurtosis ( $\kappa$ ) for Case S000 are shown.

Figure 5.9 shows that the growth of  $M_1$  is constant as a function of time, which is necessary as the transport velocity is based directly on the mass balance (the injection rate of solute is constant). After a transition time  $t_{tr}$ , both skewness ( $\gamma$ ) and kurtosis ( $\kappa$ ) become asymptotic and stable for S000. The value of  $\gamma$  indicates that the wave shape is skewed negatively, and note  $\gamma = 0$  as for normal distribution. The kurtosis shows a relative measure in relation to the normal distribution function, for which its value is 3. The normal Gaussian function is characteristic of Fickian transport. The higher value means that the front shape is more peaked (leptokurtic) and narrower than the normal distribution function. Both  $\gamma$  and  $\kappa$  indicate that the transport is non-Fickian. Although similar characteristics are seen also in Case S115 (see Figure 5.9a), the higher order moments for this case are not stable along the column length. The decrease of stability of higher order moments is known to be a first indication of the need to increase the domain size. However, at this stage it is not possible to check whether this instability is only caused by the restricted size of the pore-network, as the larger pore-networks are costly with respect to the simulation times and the memory requirements. For example, the CPU time for the used size of Case S115 is 147 CPU hours on a Pentium 4 (2.6 GHz) machine with a RAM of 1 GB. The most important fact of this analysis is that  $\gamma \neq 0$  and  $\kappa > 3$  indicates that the error equation of type

$$\tilde{C} = \frac{1}{2} \operatorname{erfc} \left[ \frac{X - vt}{2\sqrt{D_L t}} \right] \quad (5.37)$$

may hardly represent the macroscopic front in physically heterogeneous media, with sorption given by Eq (5.2) at the pore level.



## 5.6 Conclusions

We modeled five cases of macroscopically homogeneous and isotropic medium with the aid of a pore-network. Each of these cases was constructed with different variances of porebody radii but the mean size was the same. Thus, pore-networks were obtained ranging from microscopically homogeneous ( $\tilde{\sigma}_{pb} = 0$ ) to microscopically heterogeneous ( $\tilde{\sigma}_{pb} > 0$ ). It was found that to capture an asymptotic growth rate of second central moments a large size of pore-network is required for which no recommendation was found in the literature. Considering the computational costs and the current CPU capacity, a trial and error approach was used to determine an ergodic size of the 3D pore-network. Therefore, for the simulations reported here a size of  $301 \times 61 \times 61$  nodes was accepted as a minimum size for the study of non-linearly adsorbing solute transport. This size was checked for an average case by using two different realization of pore-networks (i.e. Case S086 and Case S086\*) with the same statistics of the porebody radii. As the agreement between the two cases was perfect, the size was accepted. Hence, it can be argued that the statistics of the moments does not vary from realization to realization of a specific pore-network. However, a larger size might be required for a smaller values of  $\mu_k$  and/or smaller values of excess concentration (i.e.  $C_0 - C_{in}$ ), as Figure 5.3 suggests that for higher values of retardation factor ( $R$ ) second central spatial moments are dictated by the non-linearity of adsorption ( $p$ ), at least in physically homogeneous medium. This may not apply to all cases of heterogeneity but it may apply to the magnitude of the intercepts ( $b$ ) we computed in the previous section and of course it may apply to the size of the transition time and transient length.

Further, concentration profiles along the mean flow direction of the network were obtained through averaging the concentrations of the pore-units. Our numerical experiments were interpreted with the TW solution that describes the non-linearly adsorbing transport in a porous medium. Hence, analytical equations were compared with the network results at the macroscopic level. For the microscopically homogeneous case, the results show that the numerical concentration profiles perfectly match the TW profiles predicted by the TW equation [Van der Zee 1990; 1991; Bosma and Van der Zee 1993]. The TW front for a homogeneous domain is shown in the 2D-snapshot of Figure 5.10a.

With the growth of heterogeneity the disagreement between the predicted and numerical concentration distributions grows. Analysis with the method of moments showed that in such conditions the reactive transport is non-Fickian [Van der Zee 1990]. Numerically up scaled results suggested that an asymptotic value for second-order central moments does not occur in a heterogeneous medium. Because in such media hydrodynamic dispersion is not adequately counterbalanced by adsorption (i.e. no or little *self-sharpening* of the front), this results in steady growth of second central moments as a function of time. It was found that the growth rate of moment is constant at least after the transition times ( $t \rightarrow \infty$ ). A distinct inflexion of  $M_2^c$  at the end of transition time is characteristic in all cases. After the transition time  $M_2^c$  grows with a rate equal to  $\alpha_{res}$ , which is determined by the pore size statistics (e.g. Eq (5.33)). Thus, the steady growth of second central moments can be accurately quantified with the help of pore size statistics. Equations (5.33)-(5.36) are the examples of the functional relation of pore size statistics to the growth rates of second central moments. However, to extrapolate these relations to wider range of pore size statistics and wider range of retardation factors more simulations are required. It is indeed computationally costly work, as one such simulation on Pentium 4 (2.6 GHz) processor takes 147 CPU hours.

The steady growth of second central moments is attributed to the fact that the lateral pores

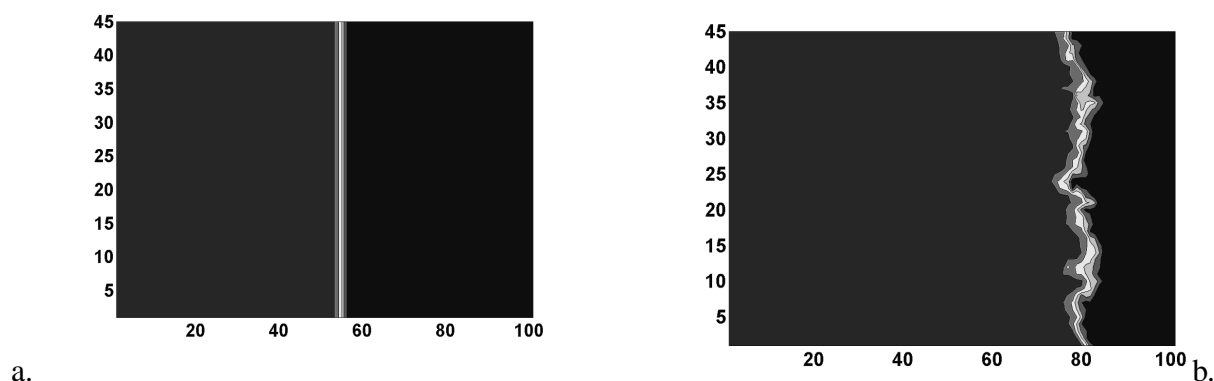


Figure 5.10: 2D-snapshots of non-linearly adsorbing plume-migration in chemically homogeneous porous media. a. in physically homogeneous pore-network; b. in physically heterogeneous pore-network. The front is progressing from the left to the right.

( $\perp$  to the mean flow direction) experience local gradient of concentration, which creates a suitable environment for the lateral mass-transfer. The laterally transported mass may increase the concentration, as a result the incoming mass may move forward with less retardation. As a result along the front concentration distribution may not be homogeneous. Because during non-linear adsorption the lower concentrations are retarded more than the higher ones, the solute-molecules from higher concentration regions move faster and from the lower concentration-regions creep slower to the longitudinal direction. This would lead to a favourable condition for fingering. That causes an unequal displacement (and wider spread) of the front in the longitudinal direction. Subsequently, the fingering process leads to the spreading of front as a function of time. The 2D-snapshot displayed in Figure 5.10b suggests the same. The snapshot gives only a preliminary impression, because the size of pore-network for this visualization is just  $101 \times 47 \times 47$  nodes, which is not enough for quantitative analyses.

In quantitative terms  $\frac{1}{2}\alpha_{res}$  can be seen as the reduced dispersivity during non-linearly adsorbing transport and fairly compared with  $\alpha_L$ . It was found that  $\frac{1}{2}\alpha_{res} \ll \alpha_L$ . Although  $\frac{1}{2}\alpha_{res}$  can be estimated quite accurately based on the statistics of pore sizes and the properties of adsorbing solutes, the challenge for analytically solving the transport problem arises, because the numerical computation of transport, although transparent, is cumbersome and costly. As is seen from the statistics of the front of non-linearly adsorbing solutes that  $\gamma \neq 0$  and  $\kappa > 0$  indicating that Fickian solution may not represent the front and efforts are needed for alternative solutions [Keijzer et al. 2000].

## Acknowledgements

This study is performed under the research program “Upscaling Flow and Transport Processes in Porous Media: From Pore to Core” funded by the Dutch NWO/ALW project no. 809.62.010 and the project “Integrated Soil and Water Protection (SOWA)” funded by the European Commission (EVK1-CT-2002-80022).

# Chapter 6

## Transport modeling of nonlinearly adsorbing solutes in physically and chemically heterogeneous pore-networks\*

### Abstract

The purpose of this study is to up-scale non-linearly reactive transport from the pore scale to a physically and chemically heterogeneous porous domain with the aid of an adequately large (more than a million pore-units) 3D pore-network model. We study the development of spatial moments in physically and chemically heterogeneous networks. It is shown that with the increase of either physical or chemical heterogeneity, the counterbalance between the dispersive and adsorptive forces weakens and hence the second central moment continues to grow as a function of time. The growth rates of second-order spatial moments are derived and related to the heterogeneity-parameters.

**KEYWORDS:** reactive transport; dispersion; mass transfer; non-linear adsorption; groundwater; upscaling; scale.

### 6.1 Introduction

The front behavior of reactive solute transport has become a prime concern in the recent years. Experimental evidence suggests that transport of such solutes in natural formations is dominated by the spatial variations of physical and chemical properties [Bolt 1982; De Haan et al. 1987; Bellin et al. 1993; Bosma et al. 1993; Rusch et al. 1997] such as the hydraulic conductivity and sorption coefficients [Dagan 1989]. Moreover, ubiquitous kinetics of biogeochemical reactions adds to the complexity. The sorption process is site-specific and therefore may vary in every pore of a porous domain. In other words, sorption and reactive solute transport are affected by intrinsic structure, texture and pore-scale chemical properties of porous medium. These processes are mainly governed by site-specific sorption rates and retardation factors that differ from pore to pore [Sugita and Gillham 1995a; Serrano 2003].

---

\*by Ram C Acharya, Sjoerd EATM van der Zee and Anton Leijnse, submission in preparation.

*List of symbols and notations* $\langle . \rangle$  Ensemble average $c, C$  Microscopic and macroscopic concentration [ $\text{ML}^{-3}$ ]

BPTM Brownian Particle Tracking Model

CDE Convection Dispersion Equation

BACON Biconical abscissa-Asymmetric CONcentric

 $\Delta c_{AD}$  Microscopic concentration increment [ $\text{ML}^{-3}$ ] $C_0, C_{in}$  Influent and initial effluent concentrations [ $\text{ML}^{-3}$ ] $D_m, D_L$  Molecular diffusion and longitudinal dispersion coefficients [ $\text{L}^2\text{T}^{-1}$ ] $G_{i,j}$  Dimensionless conductance [-]

HYPON HYdraulic POre Network

 $h_i, h_j$  hydraulic heads [L] $k$  Microscopic sorption coefficient [ $(\text{ML}^{-3})/(\text{ML}^{-3})^p$ ] $K_F$  Macroscopic sorption coefficient [ $(\text{MM}^{-1})/(\text{ML}^{-3})^p$ ] $\ell, L$  Node-to-node (bond) and the network lengths [L] $\tilde{\ell}$  Scaling factor ( $\ell/L$ ) [-] $M_1, M_n$  First [L] and nth spatial moments [ $\text{L}^n$ ] $M_2^c, b, \hat{b}$  Second-central moment  $\hat{b} = M_2^c(t = t_{tr})$  and  $b \sim \hat{b}$  [ $\text{L}^n$ ]

min, max minimum and maximum

 $N_t$  Total number of pore-units included in the inner core of the chosen tier $N_X, N_{XY}$  Number of nodes along  $X$  and  $XY$  plane

PDF Probability Density Function

 $Pe_\ell, \alpha_L$  Characteristic Peclet number ( $v\ell/D_m$ ) and dispersivity ( $D_L/v$ ) [-]

PU Pore Unit

 $\mathbf{q}, q_{i,j}, Q$  Discharges: vector, through bond  $i, j$  and through porenetwork [ $\text{L}^3\text{T}^{-1}$ ] $R$  Retardation factor [-] $R_{pb}, \tilde{R}_{pb}$  Dimensionfull [L] and dimensionless [-] porebody radius ( $\tilde{R}_{pb} = R_{pb}/\ell$ ) $s$  Microscopic sorption, mass absorbed per unit volume of flume [ $\text{ML}^{-3}$ ] $S$  Macroscopic sorption (mass of solute absorbed/mass of solid phase) [ $\text{MM}^{-1}$ ] $t, t_{tr}, \Delta t$  Time, transition time and time step of iteration [T] $\mathbf{T}$  Residence time vector [T]

TW Traveling Wave

 $v$  Mean intrinsic velocity along the principle flow direction in the pore network [ $\text{LT}^{-1}$ ] $V_{PU}, V_f$  Pore-unit and total fluid phase volumes [ $\text{L}^3$ ] $x, X$  Local (along bond  $0 \leq x \leq \ell$ ) and global (along network  $0 \leq X \leq L$ ) axis $\alpha_{res}, \hat{\alpha}_{res}$   $M_2^c$  growth rates with respect to  $M_1$  after transition times [L] $\gamma, \kappa$  Coefficients of skewness and kurtosis [-] $\varepsilon$  Porosity [-] $\mu_k$  Mean adsorption coefficient $\nu$  Coefficient of kinematic viscosity [ $\text{L}^2\text{T}^{-1}$ ] $\tilde{\sigma}_{pb}^2$  Variance of dimensionless porebody radii  $\tilde{R}_{pb}$  [-] $(i, j), L, m, pb, PU, n, tr, t$  Subscripts indicate the indices of nodes, Longitudinal, molecular, porebody, Pore Unit, nth, transition and tier (respectively). $c$  Superscript indicates central

A useful tool for studying upscaling is the network of pores, i.e. an aggregate of elementary pore-units (PUs) [Fatt 1956a; Acharya et al. 2004a]. The behavior of reactive and non-reactive transport in elementary pore-units such as fractures and capillaries (hereafter called bonds) has been studied for quite a long time [Taylor 1953; Aris 1956; Berkowitz and Zhou 1996; Park and Lee 1999; Tsang and Doughty 2003]. Although multi-dimensional pore-networks have been applied for studying and upscaling quite a number of phenomena [Van Brakel 1975], e.g. multiphase flow dynamics [Celia et al. 1995; Reeves and Celia 1996; Gielen et al. 2002; Hassanizadeh et al. 2002], porosimetry, hysteresis, diffusion, dispersion, and (relative) permeability [Mohanty and Salter 1982; Sahimi et al. 1986; Dullien 1991; Ioannidis and Chatzis 1993; Reeves and Celia 1996; Suchomel et al. 1998a; Dahle and Celia 1999; Tsakiroglou and Payatakes 2000; Held and Celia 2001; Verlaan 2001; Blunt et al. 2002; Acharya et al. 2004b], little attention is paid to explicitly address the non-linearly adsorbing miscible transport. We are aware of only a few examples where pore-networks were used to study reactive transport, such as the impact of bacterial growth on the response of the porosity-permeability functions [Suchomel et al. 1998b], how pore-scale retardation factors affect breakthrough curves (BTCs) [Sugita and Gillham 1995a] and the effect of non-linear adsorption on transport in a pore-network model [Van der Zee et al. 2004a]. The latter revealed that pore-scale physical heterogeneity causes a steady growth of second-order central spatial moment ( $M_2^c$ ) confirming that the counterbalance between adsorptive and dispersive forces weakens during reactive transport of non-linearly adsorbing solutes. However, transport of non-linearly adsorbing solutes in both chemically and physically heterogeneous pore-networks has not yet been studied.

It has been established that the convection-dispersion equation (CDE) is valid to describe transport for porous media and analytical solutions have been provided for simplified cases such as mono-component, non-reactive or linearly adsorbing solutes transport in one or more-dimensional domains [Van Genuchten and Wierenga 1976; Van Genuchten and Alves 1982; Chrysikopoulos et al. 1990]. In agreement with the complexity of biogeochemical reactions [Bolt 1982], non-linearly adsorbing solute transport in porous media has been considered [Van der Zee 1990; 1991]. To our best knowledge, the upscaling step from individual and networks of pores to the continuum scale of a porous medium has not yet been studied for nonlinearly reactive solute transport. Hence, it is not yet justified that the extension of the CDE with (non-linear) reaction terms is appropriate for tackling the reactive transport problems of non-linearly adsorbing solutes in physically and chemically heterogeneous porous medium.

The purpose of this paper is to use a 3D pore-network model for up-scaling non-linearly reactive transport from the pore scale to a physically and chemically heterogeneous porous medium. Using the minimal ergodic size ( $> 10^6$  pore-units), we focus our numerical experiments on the assessment of how the growth rates of spatial moments of a migrating plume of non-linearly adsorbing solutes can be related to the chemical and physical heterogeneity of pore-networks. We also aim at assessing whether the Traveling Wave (TW) that occurs in physically homogeneous network still develops in case of chemical heterogeneity.

## 6.2 The model

We consider two scales, i.e. the microscopic or pore-scale, and the macroscopic or the continuum-scale, e.g. many thousand pores. Our pore-network is a cubic lattice with a coordination number  $\beta$  equal to six, and is comprised of pore-units with pore-to-pore varying chemical properties. The centers of these pore-units are placed at a regular grid length, i.e. the lattice constant  $\ell$ ,

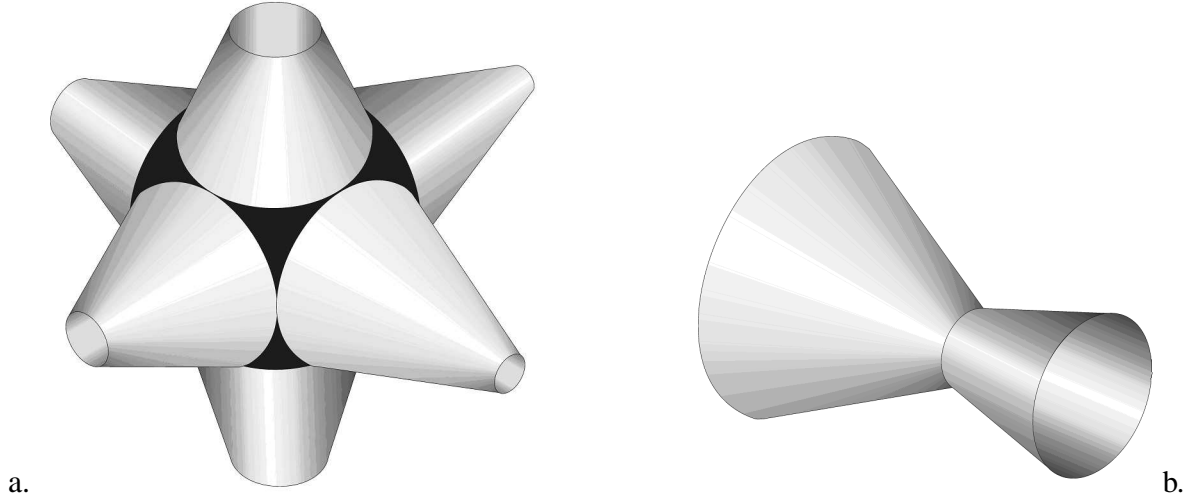


Figure 6.1: Basic elements of HYdraulic Pore Network (HYPON): a. the pore-unit (the porebody is marked with the dark color) and b. the Biconical abscissa-Asymmetric CONcentric (BACON) bond [Acharya et al. 2004a].

where  $\ell \ll L$ ,  $\ell \ll W_b$  and  $\ell \ll W_h$ . The symbols  $L$ ,  $W_b$  and  $W_h$  denote the length, width and the height of the Euclidian space occupied by the pore-network. Each pore-unit is composed of a porebody (large void) of radius  $R_{pb}$  (i.e.  $R_{pb} = \tilde{R}_{pb}\ell$  and  $0 < \tilde{R}_{pb} \leq 0.5$ ,  $\tilde{R}_{pb}$  - is the dimensionless radius) and six converging cones (small voids) of different lengths (measured from the pore-unit center). The cones from each two adjacent porebodies form a converging-diverging Biconical abscissa-Asymmetric CONcentric bond (BACON bond). Hence, the size of the BACON bond along  $\ell$  is varying and follows from the simple power functions of porebody radii ( $f(R_{pb})$ ) developed earlier [Acharya et al. 2004a]. Depending on the wall curvature ( $n$ ), the BACON bonds are the union of two hyperbolic, parabolic or straight cones and hence possess a narrowest section (i.e. *the throat*), which is fixed by the intersection of two power functions that originate from the centers of the adjacent porebodies. For illustration a typical pore-unit is shown in Figure 6.1a, a typical BACON bond is shown in Figure 6.1b and a typical network is shown in Figure 6.2. Such a network mimics a porous medium, at least hydraulically [Scheidegger 1960; Van Brakel 1975; Acharya et al. 2004a]. For the construction of such a pore-network an ensemble of  $\tilde{R}_{pb}$  is required which has a mean  $\langle \tilde{R}_{pb} \rangle$  and a variance  $\tilde{\sigma}_{pb}^2$  [Acharya et al. 2004a]. In the following we introduce the equations of transport both in a pore-unit and in a pore-network.

### 6.2.1 Pore-unit scale flow and transport equations

We represent a macroscopic porous medium by a cubic network of elementary pore-units as shown in Figure 6.1a. Such units may be assumed to be perfectly mixed [De Josselin de Jong 1958]. We ignore the contribution of diffusion ( $D_m$ ) to transport by assuming that advection dominates the transport [Van Genuchten and Alves 1982]. Particle-tracking experiments on pore-network confirmed the validity of this assumption for characteristic Peclet numbers ( $Pe_\ell = v\ell/D_m$ ) approximately between 10 and  $10^4$  [Acharya et al. 2004b]. Hence, the equation for a pore-unit of HYPON is given by

$$V_{PU} \left( \frac{\partial c}{\partial t} + \frac{\partial s}{\partial t} \right) + \nabla \cdot (\mathbf{q}c) = 0, \quad (6.1)$$

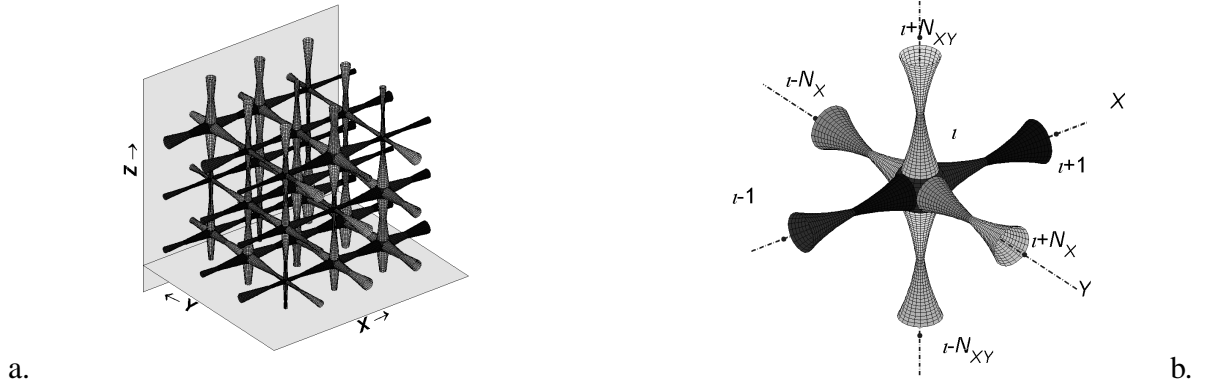


Figure 6.2: A 3D Pore-network (a) and a typical connectivity scheme for a cubic lattice with pores of circular cross section shape (b). The symbols  $X$ ,  $Y$ , and  $Z$  denote coordinate axes, whereas  $N$  is the number of pore-units as specified by the subscripts:  $N_X$  along  $X$ ,  $N_{XY}$  in the  $XY$  plane and  $\iota$  is the index of the pore-unit (from [Acharya et al. 2004a]).

where  $V_{PU}$  (see *the list of symbols and notations*) is the fluid volume of the pore-unit and  $c$  is the concentration. We assume that sorption  $s$  (mass of solute per fluid phase volume) is given by the Freundlich isotherm

$$s = kc^p, \quad (6.2)$$

where  $k$  is the Freundlich coefficient (a space function) of adsorption that varies from pore-unit to pore-unit, i.e.  $k = k(X, Y, Z)$ . The values of  $k$  are sampled from a random distribution that has a mean  $\mu_k$  and variance  $\sigma_k^2$  [Rusch et al. 1997]. The exponent  $p$  is a parameter ( $0 < p < 1$ ). A dimensionless indicator of chemical heterogeneity is given by

$$\eta_k = \frac{\sigma_k}{\mu_k}, \quad (6.3)$$

where  $\eta_k$  is the coefficient of variation of  $k$ . In Eq (6.1), the symbol  $\mathbf{q}$  denotes the discharge vector [ $\text{L}^3\text{T}^{-1}$ ] through bonds similar to that shown in Figure 6.1b. For each bond connected to two nodes, discharge can be computed with the Hagen-Poiseuille equation

$$q_{i,j} = \frac{g}{\nu} \ell^3 G_{i,j} (h_i - h_j), \quad (6.4)$$

where subscripts  $i$  and  $j$  denote the addresses of nodes (fluid flows from  $i$  to  $j$ ).  $G_{i,j}$  denotes the dimensionless bond conductance derived earlier [Acharya et al. 2004a] in which both the longitudinal as well as cross sectional shapes of bond are taken into account. The size of the BACON bond along  $\ell$  is derived considering the porebody radii of the adjacent porebodies and the curvature parameter  $n$ . The constant  $g$  is the magnitude of acceleration due to gravity and  $\nu$  denotes the kinematic viscosity of water. The symbols  $h_i$  and  $h_j$  denote the hydraulic heads at the pore-unit centers  $i$  and  $j$ . Note that the pore geometry is expressed in terms of pore-to-pore spacing ( $\ell$ ), i.e. geometric lengths are scaled by  $\ell$ . Equation (6.4) is valid for laminar flow in a wide range of the Reynolds number and is appropriate for describing flow in the pores [Bear 1972]. For steady state flow, the divergence of discharges at nodes (pore-units) is zero [Acharya et al. 2004a], which leads to a system of algebraic equations, i.e.

$$\sum_j^{\beta} q_{i,j} = 0, \quad j = 1, 2, \dots, \beta, \quad (6.5)$$

where  $j$  is the index of the adjacent pore-units.

### 6.2.2 Network scale transport equations

A pore-network with no-flow lateral boundaries under a constant pressure difference between inlet and outlet faces yields a 1D-column macroscopically. For such a column the mass balance equation is given by the CDE,

$$\varepsilon \frac{\partial C}{\partial t} + (1 - \varepsilon) \rho_s \frac{\partial S}{\partial t} + \varepsilon v \frac{\partial C}{\partial X} = \varepsilon D_L \frac{\partial^2 C}{\partial X^2}, \quad (6.6)$$

where  $C$  is the concentration [ $\text{ML}^{-3}$ ] expressed in terms of mass of solute per unit volume of fluid.  $D_L$  and  $\varepsilon$  respectively denote the coefficient of longitudinal dispersion and porosity. The symbol  $S$  denotes the adsorbed mass of solute per unit mass of the solid phase [ $\text{MM}^{-1}$ ], usually expressed in moles of adsorbate per kilogram of dry soil (with a density of  $\rho_s$ ).  $S$  is obtained by integrating  $s$  (Eq (6.2)) over fluid phase volume ( $V_f$ ) of the network and dividing by the solid phase mass, i.e.

$$S = \frac{\int_{V_f} s dV_f}{V_s \rho_s}, \quad (6.7)$$

where  $V_s$  denotes the solid phase volume, i.e.  $V_s = (1 - \varepsilon)V$ . The symbol  $V$  denotes the total volume of the Euclidian space occupied by the network. The subscripts  $s$  and  $f$  denote solid and fluid phases respectively. The adsorption equation is given by the Freundlich isotherm

$$S = K_F C^p, \quad (6.8)$$

where  $K_F$  is the Freundlich adsorption coefficient. After replacing the expression of  $S$  in Eq (6.6) and dividing both sides of Eq (6.6) by porosity ( $\varepsilon$ ), an average adsorption coefficient for the fluid-phase can be expressed as

$$\mu_k = K_F (1 - \varepsilon) \rho_s / \varepsilon. \quad (6.9)$$

For a chosen value of  $K_F$ , the coefficient  $\mu_k$  is computed on the basis of  $\rho_s$  and  $\varepsilon$  or vice versa. For simulations, we generate random distribution of  $k$  (i.e.  $k_1, k_2, k_3 \dots k_N$ ) that has a mean  $\mu_k$  and variance  $\sigma_k^2$ . Further we assign a  $k_i$  to the  $i$ th pore-unit and thus we use Eq (6.2) to calculate sorption in each pore-unit.

The longitudinal dispersion coefficient ( $D_L$ ) follows from pore-scale modeling of non-reactive transport [Acharya et al. 2004b]. It was found that the dispersivity ( $\alpha_L \sim D_L/v$ ) can be estimated based on the pore size statistics and therefore, there is no need to consider non-reactive solute for the purpose of determining  $\alpha_L$  [Legatski and Katz 1967; Detwiler et al. 2000]. For a network used here, the dimensionless dispersivity (i.e.  $\tilde{\alpha}_L = \alpha_L/\ell$ ) for a particular  $\langle \tilde{R}_{pb} \rangle$  can be estimated as a function of  $\tilde{\sigma}_{pb}$  according to

$$\tilde{\alpha}_L(\langle \tilde{R}_{pb} \rangle) = B_1 \tilde{\sigma}_{pb}^2 + B_2 \tilde{\sigma}_{pb} + \tilde{\alpha}_0, \quad (6.10)$$

where  $\tilde{\alpha}_L$  is valid for a chosen  $\langle \tilde{R}_{pb} \rangle$  for which the fitting parameters ( $B_1$  and  $B_2$ ) are obtained. Symbol  $\tilde{\alpha}_0$  denotes a constant (see Table 6.1). However, the value obtained from Eq (6.10) was checked by considering a non-reactive transport (i.e.  $K_F = 0$ ) case and thus  $\tilde{\alpha}_L$  was verified numerically. In addition, these values were further compared with  $\tilde{\alpha}_L$  obtained from particle tracking results [Acharya et al. 2004b] and therefore, the reliability of Eq (6.10) was affirmed.



The macroscopic intrinsic (pore water) velocity  $v$  is determined with the Dupuit-Forcheimer equation

$$v = \frac{QL}{V_f}, \quad (6.11)$$

where  $Q$  is the macroscopic discharge across the pore-network [Acharya et al. 2004a].

We prescribe the initial and boundary conditions given by:

$$C(X > 0, t = 0) = C_{in}; C(0, t \geq 0) = C_0; \frac{\partial C}{\partial X} \big|_{(0, t > 0)} = 0; \frac{\partial C}{\partial X} \big|_{(L, t \geq 0)} = 0, \quad (6.12)$$

with  $C_0 > C_{in}$ . Under these boundary and initial conditions for times  $t \rightarrow \infty$ , Eq (6.6) and Eq (6.8) with  $0 < p < 1$  lead to the following relations to hold [Van Duijn and Knabner 1990]:

$$\frac{dS(C)}{dC} > 0, \quad \frac{d^2 S(C)}{dC^2} < 0. \quad (6.13)$$

### 6.2.3 Analytical solution

In a physically homogeneous porous medium, Eq (6.6) and Eq (6.8) subject to the boundary and initial conditions Eq (6.12) lead to a TW [Van der Zee 1990; 1991; Knabner and Van Duijn 1992; Bosma and Van der Zee 1993; Oya and Valocchi 1997]. The non-linearity of adsorption causes lower concentrations to experience a larger retardation than the higher concentrations, which opposes the Fickian spreading of front. Consequently, the concentration distribution  $C(X, t)$  approaches a limiting TW front, i.e. the  $C$ -front approaches a time-invariant shape and a constant travel velocity. The TW equation is obtained by assuming that the Local Equilibrium Assumption (LEA) is valid and performing a Lagrangian transformation given by

$$\eta = X - vt/R, \quad (6.14)$$

where the retardation factor ( $R$ ) is

$$R = 1 + \frac{\rho_s(1 - \varepsilon)}{\varepsilon} \frac{\Delta S(C)}{\Delta C}. \quad (6.15)$$

In Eq (6.15),  $\Delta C = C_0 - C_{in}$  and  $\Delta S(C)$  is the corresponding change in the adsorbed amount. The dimensionless concentration function in the Lagrangian coordinate system  $\tilde{C}(\eta)$  was obtained analytically [Van der Zee 1990; 1991; Bosma and Van der Zee 1993] and reads

$$\tilde{C}(\eta) = \begin{cases} \left\{ 1 - \exp \left[ v(\eta - \eta^*)(1 - p)(R - 1)(RD_L)^{-1} \right] \right\}^m & \text{if } (\eta - \eta^*) \leq 0 \\ 0 & \text{otherwise,} \end{cases} \quad (6.16)$$

where  $\tilde{C} = (C - C_{in})/(C_0 - C_{in})$  and the parameter  $m$  equals to  $1/(1 - p)$ . The reference value  $\eta^*$  is a constant [Van der Zee 1990; Bosma and Van der Zee 1993].

For non-reactive tracer,  $D_L$  is obtained by fitting the solution of CDE with  $K_F = 0$ , given by [Van Genuchten and Alves 1982],

$$\tilde{C}(\tilde{X}, \tilde{T}) = \frac{1}{2} \left\{ \operatorname{erfc} \left[ \frac{\tilde{X} - \tilde{T}}{2\sqrt{\tilde{\alpha}_L \tilde{\ell} \tilde{T}}} \right] + \exp \left( \frac{\tilde{X}}{\tilde{\alpha}_L \tilde{\ell}} \right) \operatorname{erfc} \left[ \frac{\tilde{X} + \tilde{T}}{2\sqrt{\tilde{\alpha}_L \tilde{\ell} \tilde{T}}} \right] \right\}. \quad (6.17)$$

In Eq (6.17) it is assumed that  $D_L \sim \alpha_L v$  and this assumption is valid for the characteristic Peclet numbers considered in our simulations [Acharya et al. 2004b]. Further,  $\tilde{\ell} = \ell/L$ ,  $\tilde{X} = X/L$  and  $\tilde{T} = vt/L$ . Fitting Eq (6.17) to a breakthrough curve at the outlet face of the pore-network ( $\tilde{X} = 1$ ) is done by minimizing the least square differences. In random-walk particle tracking methods  $\alpha_L$  can be obtained with the methods of moments [Sahimi et al. 1986]. The first derivative of  $\tilde{C}(X, t)$  with respect to  $X$  gives the probability density function (PDF,  $f(X)$ ) [Bosma and Van der Zee 1993; Keijzer et al. 2000], i.e.

$$f(X) = -\frac{\partial \tilde{C}}{\partial X}. \quad (6.18)$$

### 6.2.4 Equations for spatial moments

Since it has been shown that the validity of Eq (6.16) can be evaluated more accurately with the method of moments than by comparing front shapes of  $\tilde{C}$ , we compute central spatial moments ( $M_n^c$ ) with the procedure given by Bosma and Van der Zee [Bosma and Van der Zee 1993; Keijzer et al. 2000]:

$$M_n^c(t) = \frac{\int_{-\infty}^{\infty} [X - M_1(t)]^n f(X) dX}{\int_{-\infty}^{\infty} f(X) dX}, \quad M_1(t) = \frac{\int_{-\infty}^{\infty} X f(X) dX}{\int_{-\infty}^{\infty} f(X) dX}, \quad n = 2, 3 \dots \quad (6.19)$$

$$\gamma = \frac{M_3^c}{\sqrt{(M_2^c)^3}}, \quad \kappa = \frac{M_4^c}{(M_2^c)^2}, \quad (6.20)$$

where  $M_1(t)$  is the first spatial moment at time  $t$ , subscript  $n$  denotes the order of moment, superscript  $c$  denotes “central”,  $\gamma$  is the coefficient of skewness or the measure of symmetry, whereas  $\kappa$  is the coefficient of kurtosis or the measure of peakedness or flatness. For a normal distribution and Fickian-type displacement  $\gamma$  is zero and  $\kappa$  is three. Non-Fickian type plumes produce  $\gamma$  and  $\kappa$  other than respectively zero and three. For the case of non-reactive tracer transport ( $D_L \sim \alpha_L v$ ), the moments and the dispersivity ( $\alpha_L$ ) are related according to the Einstein’s relation [Chandrasekhar 1943], i.e.

$$\alpha_L = 0.5 \frac{M_2^c(t_2) - M_2^c(t_1)}{M_1(t_2) - M_1(t_1)}, \quad (6.21)$$

where  $t_1$  and  $t_2$  are the times. For a TW, the second central moment ( $M_2^c$ ), i.e. the spatial variance of the front, approaches a fixed value asymptotically [Van der Zee 1990; Van Duijn and Knabner 1990; Van der Zee 1991; Bosma and Van der Zee 1992; Van Duijn et al. 1996; Oya and Valocchi 1997], which depends on retardation factor, non-linearity of adsorption and dispersivity.

## 6.3 Numerical experiments

Imposing a hydraulic head difference across the pore-network in the  $X$ -direction, Eq (6.5) is solved for hydraulic heads and subsequently the discharges through the bonds (i.e. Eq (6.4)) are calculated. The computation of transport in pore-units, i.e. Eq (6.1) depends on these discharges. At the network scale, we can use (wherever applicable) the analytical solution (i.e. Eq (6.16)) to predict the concentration profiles along the mean flow direction, because  $v$ ,  $D_L$  and  $R$  are known [Bosma and Van der Zee 1992].

### 6.3.1 Numerical scheme for transport in pore-units

Under initial and boundary conditions given by Eq (6.12) the numerical scheme for the computation of transport in a pore-unit can be written as

$$c(i, t + \Delta t) - c(i, t) + k[c(i, t + \Delta t)]^p - k[c(i, t)]^p = \underbrace{\frac{\Delta t}{V_{PU}} \left[ \sum_j c(j, t) q_{j,i} - c(i, t) (q_{PU})_i \right]}_{\Delta c(i, t)_{AD}}, \quad (6.22)$$

where the index  $j$  is chosen such that  $h_j > h_i$ . Note that  $k = k(i)$  and  $k$  is specific to pore-unit  $i$ . The concentration increment  $\Delta c(i, t)_{AD}$  should be zero or more. The node discharge  $(q_{PU})_i$  is the sum of the flows entering or leaving the node  $i$ , i.e.

$$(q_{PU})_i = \sum_j |q_{j,i}|, \quad h_j > h_i, \quad j = 1, 2, 3 \dots \beta. \quad (6.23)$$

Rewriting Eq (6.22) as

$$c(i, t + \Delta t) + k[c(i, t + \Delta t)]^p = \Delta c(i, t)_{AD} + k[c(i, t)]^p + c(i, t) = B(i, t + \Delta t), \quad (6.24)$$

the resulting Eq (6.24) is solved with an optimization technique, such as Newton-Raphson [Sun 1996]. For the stability of the scheme, the minimum time step is chosen on the basis of bond residence times, i.e.

$$2\Delta t \leq \min \left\{ [\mathbf{V}_b][\mathbf{q}_b^{-1}] \right\} = \min \{ \mathbf{T}_b \}, \quad (6.25)$$

where subscript  $b$  denotes bond,  $\mathbf{q}_b$  is the matrix vector of discharges through the bonds given by Eq (6.4). Similarly,  $\mathbf{V}_b$  and  $\mathbf{T}_b$  denote volume and time matrices pertaining to the bonds, where  $V_b$  = volume of bond +  $\frac{1}{6}$  porebody volume ( $i$ ) +  $\frac{1}{6}$  porebody volume ( $j$ ) (see [Acharya et al. 2004a]). Average concentration for each pore-unit is updated at the end of each  $\Delta t$ .

### 6.3.2 Average concentration function

At designated time steps ( $\gg \Delta t$ ), the concentrations of pore-units that belong to a particular tier (at  $X$ ) of the pore-network are averaged to obtain a flux-averaged dimensionless macroscopic concentration  $\tilde{C}(X, t)$ . The tiers are defined as the group of pore-units which possess equal  $X$ -coordinates. To avoid boundary effects, we consider the pore-units of the inner core only [Reeves and Celia 1996; Held and Celia 2001], i.e. we exclude a  $5\ell$  thick layer at the no-flow boundaries. Hence,  $\tilde{C}(X, t)$  is given by

$$\tilde{C}(X, t) = \left[ \frac{\sum_i^{N_t} c(i, t) (|q_{PU}|)_i}{\sum_i^{N_t} (|q_{PU}|)_i} - C_{in} \right] \frac{1}{C_0 - C_{in}}, \quad i = 1, 2, 3 \dots N_t, \quad (6.26)$$

where  $N_t$  denotes the total number of pore-units at the same  $X$ -coordinates. These PUs are indexed with  $i$ . The subscript  $t$  denotes tier. The  $X$ -coordinate is chosen at an interval of  $\ell$ , i.e.  $X = 0, 1\ell, 2\ell, \dots L$ . The Eq (6.18) is discretized by choosing  $\partial X \approx \ell$ , i.e.

$$f(X + \frac{1}{2}\ell, t) = -\frac{\tilde{C}(X + \ell, t) - \tilde{C}(X, t)}{\ell}. \quad (6.27)$$

## 6.4 Simulation cases

We used the same cubic pore-network of size  $301 \times 61 \times 61$  pores that was used earlier to study the effect of physical heterogeneity on reactive transport of non-linearly adsorbing solutes [Van der Zee et al. 2004a; Van der Zee et al. 2004b]. With an aim of capturing effects of microscopic heterogeneity on transport, 15 systematic cases with five different pore-network realizations (as identified in Table 6.1) of gradually varying physical heterogeneity (S000, S030, S060, S086 and S115) with three different loads of chemical heterogeneity ( $\eta_k = 0$ ,  $\eta_k = 0.29$  and  $\eta_k = 0.43$ ) were considered. The pore-units were constructed with the curvature parameter ( $n$ ) equal to one and the ensemble of dimensionless porebody radii ( $\tilde{R}_{pb}$ , i.e.  $\tilde{R}_{pb} = R_{pb}/\ell$  [Acharya et al. 2004a]) taken from a random uniform distribution. We introduced a spatially variable  $k$  over the network domain and  $k$  is also sampled from a random uniform distribution. Note that  $R_{pb}$  and  $k$  are uncorrelated.

Table 6.1 reveals that network S000 represents a physically homogeneous medium, whereas the other networks represent physically heterogeneous media. In all networks,  $\langle \tilde{R}_{pb} \rangle$  is 0.30, whereas the standard deviation ( $\tilde{\sigma}_{pb}$ ) varies from zero (network S000) to 0.115 (network S115). We compute the coefficient of variation  $\eta_{pb}$  as the ratio of  $\tilde{\sigma}_{pb}$  to  $\langle \tilde{R}_{pb} \rangle$  (i.e.  $\eta_{pb} = \tilde{\sigma}_{pb}/\langle \tilde{R}_{pb} \rangle$ ). In all cases the macroscopic hydraulic head drop across the network was fixed at 0.07 m. Additionally,  $\ell = 0.25 \times 10^{-3}$  m and  $D_m = 8.0 \times 10^{-10}$  m<sup>2</sup>/sec (Taylor's data, [Taylor 1953]) were used for Brownian particle tracking model [Acharya et al. 2004b].

Table 6.1: Microscopic and macroscopic input parameters for the numerical experiments

Networks	S000	S030	S060	S086	S115
$\min \tilde{R}_{pb}$	0.300	0.248	0.204	0.152	0.100
$\max \tilde{R}_{pb}$	0.300	0.352	0.412	0.450	0.500
$\tilde{\sigma}_{pb}$	0.000	0.030	0.060	0.086	0.115
$\eta_{pb}$	0.000	0.100	0.200	0.287	0.383
$\varepsilon$	0.240	0.243	0.265	0.267	0.285
$\tilde{\alpha}_L$	0.434	0.496	0.614	0.764	0.982
$\mu_k$	8.11	7.96	7.09	6.88	6.39
$R$	9.11	8.96	8.09	7.88	7.39
$Pe_\ell$	384	386	430	405	420

Coefficient  $\mu_k$  is computed based on fixed  $K_F$ , the density of the solid phase ( $\rho_s$ ) and the porosity ( $\varepsilon$ ) of the modeled porous medium.  $\tilde{\alpha}_L|_{\langle \tilde{R}_{pb} \rangle=0.30} = 32.11\tilde{\sigma}_{pb}^2 + 1.072\tilde{\sigma}_{pb} + 0.4344$  (see Eq (6.10)).

As Table 6.1 reveals, each network has a different porosity ( $\varepsilon$ ). Consequently, although we choose the same influent of unit concentration ( $C_0 = 1$  g/m<sup>3</sup>) for injection and same value of  $K_F$ , the value of adsorption coefficient  $\mu_k$  differs from case to case (Eq (6.9)). The values of  $\mu_k$  presented in the table are calculated on the basis of  $\rho_s = 2.6$  Mg/m<sup>3</sup>,  $K_F = 0.982 \times 10^{-3}$  (Mg/Mg)/(1 g/m<sup>3</sup>) <sup>$p$</sup>  and the corresponding porosity ( $\varepsilon$ ). The parameter  $p$  is fixed at 0.667. Further we assume  $k(X, Y, Z)$  to be varying over the network, i.e.  $k$  differs from pore-unit to pore-unit but is constant in time. At the network scale, the retardation factor  $R$  is calculated with Eq (6.15). In Table 6.1,  $\tilde{\alpha}_L$  was calculated with Eq (6.10). We also made a cross-check for two networks (S060 and S086) by routing a non-reactive tracer (i.e.  $k = \mu_k = 0$ ) with

two methods: mixing cell model (MCM) and the Brownian particle tracking model (BPTM) [Acharya et al. 2004b]. Only a slight difference between BPTM and MCM resulted. Hence, the results obtained with MCM are expected to be valid and the values of  $\tilde{\alpha}_L$  given in Table 6.1 are plausible approximations. Additional four networks (S001 ( $\tilde{\sigma}_{pb} = 0.001$ ), S002 ( $\tilde{\sigma}_{pb} = 0.002$ ), S003 ( $\tilde{\sigma}_{pb} = 0.003$ ) and S011 ( $\tilde{\sigma}_{pb} = 0.011$ )) were considered with  $\eta_k = 0.43$  to obtain a smooth growth rate to porebody heterogeneity relation.

## 6.5 Results

The primary output of the numerical simulations are the concentration profiles at different times (see Eq (6.26)). From the concentration profiles we derive PDFs and subsequently compute the spatial moments of the plume.

### 6.5.1 Concentration profiles

For illustration we show the dimensionless (numerical) concentration profiles for networks S000 ( $\eta_{pb} = 0$ ) and S115 ( $\eta_{pb} = 0.383$ ) with different chemical heterogeneity (see Figure 6.3). For predicting concentration profiles for the network, the TW solution (6.16) is used with upscaled adsorption coefficient given by Eq (6.9). These analytically predicted dimensionless profiles are also shown in the same figure.

The homogeneous case ( $\eta_k = 0$  and  $\eta_{pb} = 0$ ) of Figure 6.3a shows that the numerical and analytical profiles agree excellently at larger times, which implies that a TW occurs, i.e. the numerical front shape and the front velocity become invariant in time. A similar comparison is shown in Figure 6.3b for  $\eta_k = 0$  and  $\eta_{pb} = 0.383$ , i.e., a physically heterogeneous medium with homogeneous chemical properties. Unlike in the previous case, slight differences are observed particularly for small concentrations.

If  $\eta_k$  is fixed at 0.29 for both networks, the figures reveal that the introduced heterogeneity has more impact on network S000 than that on network S115. This indicates that the presence of chemical heterogeneity in a physically homogeneous network leads to less favorable conditions for the development of TWs. By further increasing the heterogeneity to  $\eta_k = 0.43$ , we observe a distinct disagreement between the TW equation predictions and the numerical fronts. The chemical heterogeneity sorts remarkably small effects in a physically heterogeneous network.

### 6.5.2 Second central moments

For a robust comparison of analytical and numerical results, spatial moments of the migrating plume are computed [Bosma and Van der Zee 1993; Oya and Valocchi 1997; Keijzer et al. 2000]. For such a computation PDFs are required which are obtained with Eq (6.27). For illustration, PDFs for two networks (S000 and S115) are shown in Figure 6.4. Figure 6.4 reveals that the introduction of chemical heterogeneity increases the front width in a physically homogeneous pore-network, whereas the effect of chemical heterogeneity does not produce significant changes in the results of network S115. Compared to the front spread ( $2\sqrt{M_2^c}$ ) for  $\eta_k = 0$ , the increase in  $2\sqrt{M_2^c}$  for network S115 (with  $\eta_k = 0.43$ ) is only 12%, whereas  $2\sqrt{M_2^c}$  is more than a four fold larger in the network S000 for the same chemical heterogeneity. Figure 6.4 not only indicates that chemical heterogeneity has most effect on a homogeneous network

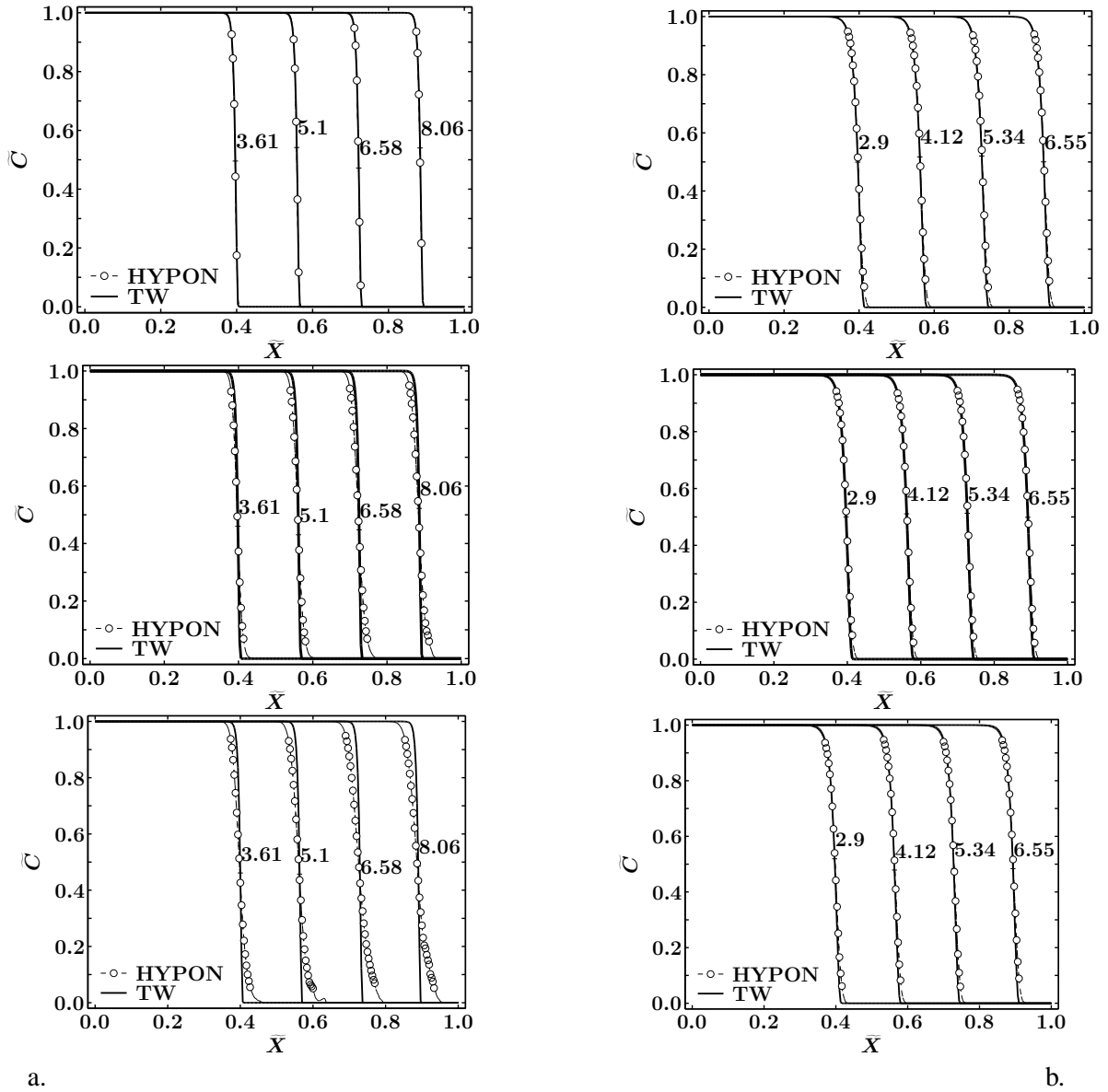


Figure 6.3: Dimensionless concentration profiles at different times as a function of fraction of column length ( $\bar{X} = X/L$ ) of a pore-network with three different chemical heterogeneity:  $\eta_k = 0$  (top row),  $\eta_k = 0.29$  (middle row) and  $\eta_k = 0.43$  (bottom row) a. network S000 ( $\eta_{pb} = 0$ ) b. network S115 ( $\eta_{pb} = 0.383$ ). HYPON (dashed lines with open circles) indicates the results of numerical simulations from pore-network model HYPON (Eq (6.26)), TW (solid lines) indicates the analytical TW solution (6.16) with the same  $K_F$  (see also Table 6.1). The labels of curves indicate the times, i.e. the pore volumes of effluent discharged from the network.

but also shows more symmetry of the PDF for this case. Furthermore the fluctuations for S000 and  $\eta_k = 0.43$  reveal that the network may be of too small size for adequately representing the PDF.

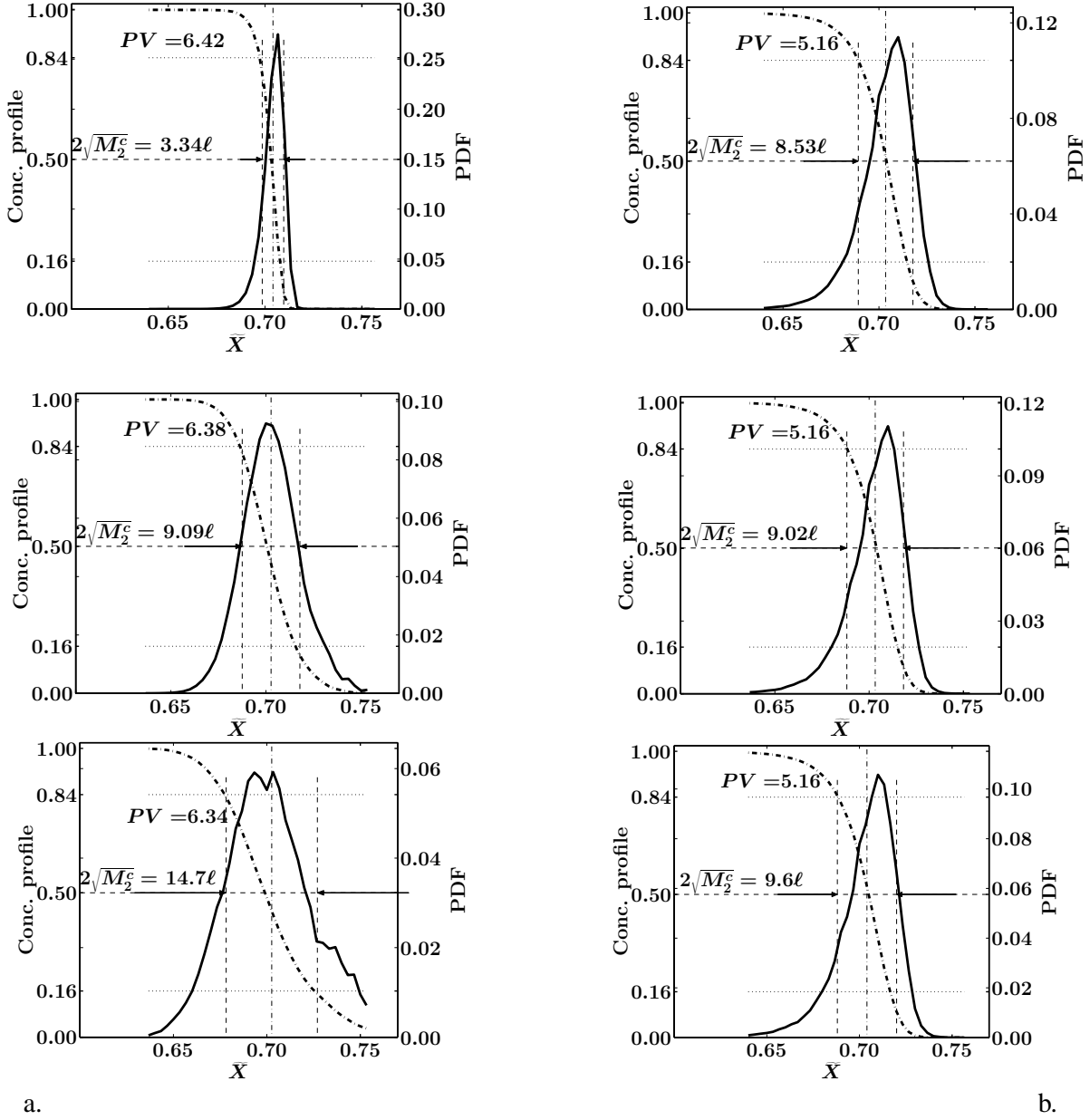


Figure 6.4: Typical PDFs ( $f(X) \cdot \ell$ ) of concentration profiles in a pore-network with three different chemical heterogeneities:  $\eta_k = 0$  (top),  $\eta_k = 0.29$  (middle) and  $\eta_k = 0.43$  (bottom). a. network S000. b. network S115. Shown are the PDFs (solid lines) and concentration profiles (dash-dotted lines) at the chosen times ( $PV$ ) as shown in the subplots, i.e. the number of pore volumes ( $PV$ ) discharged from the network. The values of  $2\sqrt{M_2^c}$  at time  $\tilde{T} = PV$  are indicated in the figure.

For a better insight, the second central moments for all cases for different times are shown as a function of first spatial moment in Figure 6.5. Figure 6.5a reveals that for network S000 with  $\eta_k = 0$  convergence occurs to the TW, because after some transition length  $M_2^c$  acquires

an asymptotic value ( $b$ , see Eq (6.28)) [Van der Zee 1990; 1991; Bosma and Van der Zee 1993]. Similar plots for the other networks show a fast increase of  $M_2^c$  which after a transition time ( $t_{tr}$ ) is followed by a linear increase. Hence, for larger times the numerically obtained front variance can be fitted with

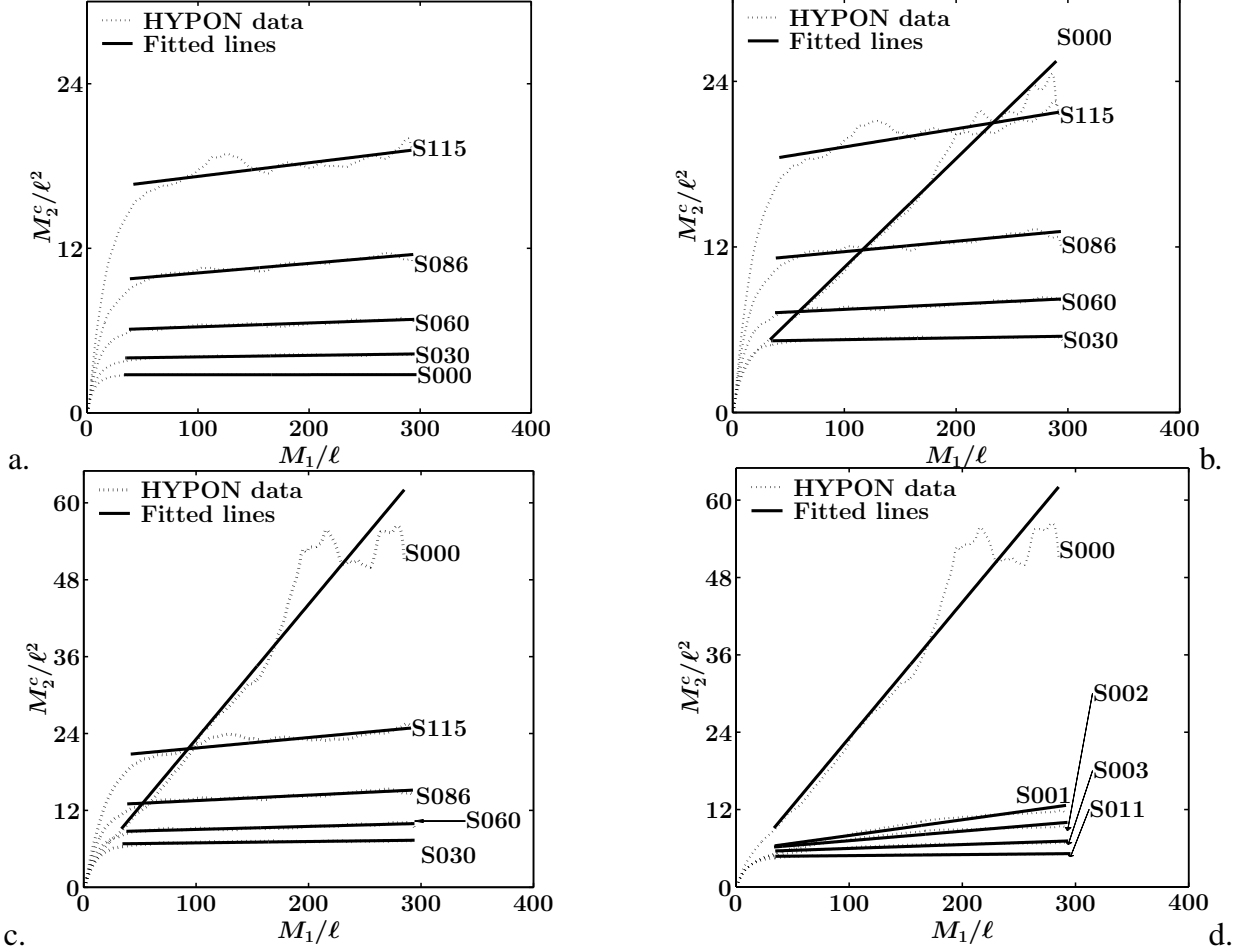


Figure 6.5: Dimensionless second central moments ( $M_2^c/\ell^2$ ) and fitted lines. Second central moments (dotted lines) and the fitted lines (solid lines,  $\widehat{M}_2^c/\ell^2$ , Eq (6.28)) as a function of  $M_1/\ell$  for three different chemical variation coefficients: a.  $\eta_k = 0$ , b.  $\eta_k = 0.29$ , c. (and d).  $\eta_k = 0.43$ . The networks are identified with symbols that correspond to Table 6.1. The networks S001, S002, S003 and S011 have  $\eta_k = 0.43$  (see Section 6.4).

$$\widehat{M}_2^c(t) = \alpha_{res}[M_1(t) - M_1(t_{tr})] + b, t > t_{tr}, \quad (6.28)$$

where  $\widehat{M}_2^c(t)$  is the fitted second central spatial moment at time  $t$  that is larger than transition time ( $t_{tr}$ ) and  $\alpha_{res}$  is the slope. In analogy with Eq (6.21),  $\frac{1}{2}\alpha_{res}$  can be seen as the reduced dispersivity of non-linearly adsorbing transport,  $b$  is the magnitude of  $M_2^c$  at the end of the transition time ( $t_{tr}$ ) which we call transition variance or intercept.  $M_1(t_{tr})$  is the magnitude of the first moment at the end of the transition time. Table 6.2 gives  $\alpha_{res}$ ,  $b$  and the coefficients of correlation ( $\mathcal{R}^2$ ) of  $M_2^c$  and  $\widehat{M}_2^c$ . The table shows that an increase of  $\alpha_{res}$  and  $b$  of the fitted lines  $\widehat{M}_2^c$  corresponds to the increase of physical heterogeneity (at constant  $\eta_k$ ) or chemical heterogeneity (at constant  $\eta_{pb}$  with some exceptions for small  $\eta_k$ ).



Table 6.2: Parameters of linear-equation fitting to the numerical second central moments

Cases	S000	S030	S060	S086	S115
$\eta_k = 0.00$					
$\alpha_{res}/\ell$ [-]	0.0000	0.0011	0.0028	0.0070	0.0099
$b/\ell^2$ [-]	2.7760	4.0046	6.0957	9.7764	16.6647
$\mathfrak{R}^2$ [-]	0.9999	0.7739	0.9021	0.9312	0.7695
$\eta_k = 0.29$					
$\alpha_{res}/\ell$ [-]	0.0788	0.0013	0.0039	0.0076	0.0131
$b/\ell^2$ [-]	5.2786	5.1949	7.2323	11.1934	18.4815
$\mathfrak{R}^2$ [-]	0.9919	0.7578	0.9384	0.9211	0.8138
$\eta_k = 0.43$					
$\alpha_{res}/\ell$ [-]	0.2103	0.0021	0.0047	0.0085	0.0163
$b/\ell^2$ [-]	9.1493	6.7939	8.7416	13.0132	20.7906
$\mathfrak{R}^2$ [-]	0.9717	0.8141	0.9327	0.9178	0.8348

Table 6.3: Parameters of linear-equation fitting for additional networks with chemical variation coefficient  $\eta_k = 0.43$ 

Cases	S000	S001	S002	S003	S011
$\alpha_{res}/\ell$ [-]	0.2103	0.0244	0.0148	0.0060	0.0016
$b/\ell^2$ [-]	9.1493	6.3760	6.1934	5.5854	4.7538
$\mathfrak{R}^2$ [-]	0.9717	0.9635	0.9314	0.8846	0.8367

See Figure 6.5d.

Additionally, the fitting parameters for S001, S002, S003, and S011 are listed in Table 6.3.

Figure 6.5a shows that the goodness of fitting of the regression equations is acceptable. In sufficiently large networks, the first derivative of second central moment with respect to the first spatial moment becomes positive and the second derivative approaches to zero, i.e.

$$\frac{dM_2^c}{dM_1} \geq 0, \quad \frac{d^2 M_2^c}{dM_1^2} \longrightarrow 0. \quad (6.29)$$

The results for  $\eta_k = 0.29$  in Figure 6.5b, show a large effect of chemical heterogeneity for the physically homogeneous network. The cases for  $\eta_k = 0.29$  reveal two striking features. For network S000,  $M_2^c$  increases linearly for  $t > t_{tr}$  and in view of the symmetry of the PDF, behavior is Fickian. Furthermore, chemical heterogeneity only slightly affects the trend of  $M_2^c$  for the physically heterogeneous networks. The same observations are made for  $\eta_k = 0.43$ . In addition we observe significant fluctuations for S000 (with increased  $\eta_k$ ) and also for increasing  $\eta_{pb}$ . We attribute these fluctuations to an inadequate network size. For the S000-case, this was also apparent from Figure 6.4. The remarkable dissimilarity between S000 and the other cases was the motivation for closer consideration of the effect of decreasing  $\eta_{pb}$ -values (cases of Table 6.3). In Figure 6.5d and Table 6.3 we observe that  $\alpha_{res}$  and  $b$  systematically decrease as the physical heterogeneity increases, until physical heterogeneity prevails. That means a slight perturbation in physical homogeneity induces a major change in the behavior

of displacement, i.e. growth rate of  $M_2^c$  decreases immensely. The reason for such a reduction can be the transversal advection. The parameters  $\alpha_{res}$  and  $b$  of  $\widehat{M}_2^c$  with corresponding  $\mathfrak{R}^2$  for all three chemical heterogeneities are listed in Table 6.2 and 6.3. From the values of  $\mathfrak{R}^2$  we can conclude that the results of fitting are quite good.

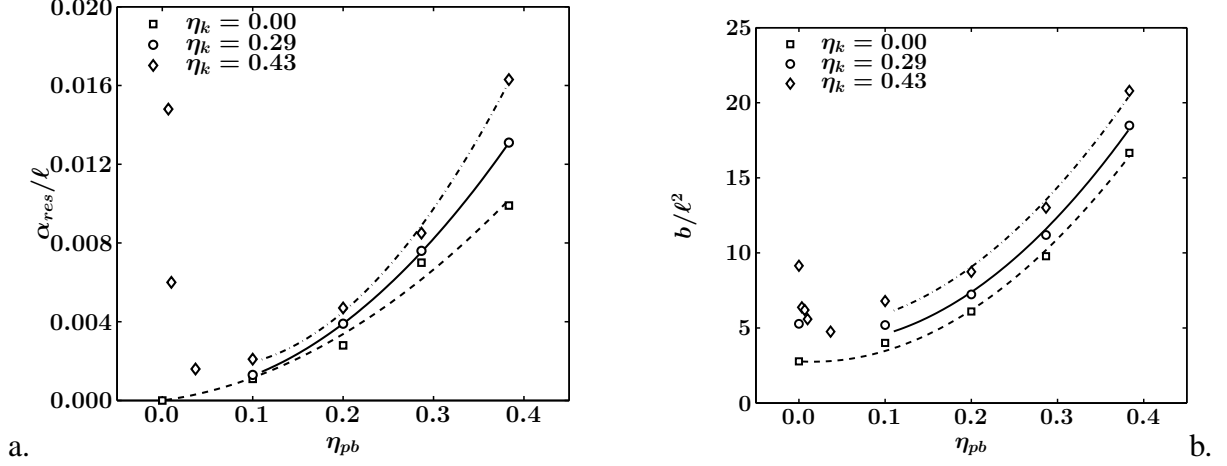


Figure 6.6: Slopes ( $\alpha_{res}/\ell$ ) and intercepts (transition spatial variance,  $b/\ell^2$ ) as a function of the coefficient of variation ( $\eta_{pb}$ ) of porebody radii. Dashed lines for  $\eta_k = 0$  solid lines for  $\eta_k = 0.29$ , and dash-dotted lines for  $\eta_k = 0.43$  according to Eq (6.30) and Tables 6.4 - 6.5

In Figure 6.6 we show  $\alpha_{res}$  and  $b$  as a function of physical heterogeneity. A completely different behavior for small and large  $\eta_{pb}$  is apparent. Also shown in Figure 6.6 are the regression lines (as a quadratic function of  $\eta_{pb}$ ) according to

$$\widehat{y} = B_1\eta_{pb}^2 + B_2\eta_{pb} + B_3, \quad (6.30)$$

where parameters of fitting ( $B_1$ ,  $B_2$  and  $B_3$ ) and coefficient of correlation ( $\mathfrak{R}^2$ ) for both  $\widehat{y} = \widehat{\alpha}_{res}/\ell$  and  $\widehat{y} = \widehat{b}/\ell^2$  are given in Tables 6.4 and 6.5 respectively.

Table 6.4: Fitting parameters for the growth rate function  $\widehat{y} = \widehat{\alpha}_{res}/\ell$  in Equation (6.30)

$\eta_k$	$B_1$	$B_2$	$B_3$	$\mathfrak{R}^2$
0.00	0.0529	0.0063	0.0000	0.9937
0.29	0.0836	0.0013	0.0003	1.0000
0.43	0.1349	-0.0150	0.0021	0.9983

See Figure 6.6a.

Equation (6.30) reveals functional relationships between pore size heterogeneity, chemical heterogeneity and the macroscopic front spreading. Note that these relations are valid for a particular mean porebody radii ( $\langle \widehat{R}_{pb} \rangle = 0.3$ ) and particular chemical heterogeneities ( $\eta_k = 0$ ,  $\eta_k = 0.29$  and  $\eta_k = 0.43$  with a constant  $K_F$ ). For the extrapolation of these results more simulations are needed to firmly base the relations. Unfortunately, the simulations are quite excessive with respect to the CPU times and memory requirements for which reason we did not pursue this in the present paper.

Table 6.5: Fitting parameters for the interception function  $\hat{y} = \hat{b}/\ell^2$  in Equation (6.30)

$\eta_k$	$B_1$	$B_2$	$B_3$	$\mathcal{R}^2$
0.00	101.2500	-3.1602	2.776	0.9959
0.29	101.3200	-5.1128	4.000	0.9838
0.43	109.1000	-1.4842	5.000	0.9719

See Figure 6.6b.

### 6.5.3 Higher-order spatial moments

The higher-order spatial central moments are the quantitative measure of spread ( $M_2^c$ ), symmetry ( $\gamma$ ) and peakedness ( $\kappa$ ) of concentration distribution function (see section 6.2.4), whereas the first spatial moment shows the location of front in space. In Figure 6.7 shown are the third- and fourth-order central moments (i.e. skewness ( $\gamma$ ) and kurtosis ( $\kappa$ )) as a function of dimensionless time, which are commonly used to evaluate the behavior of a migrating plume.

For  $\eta_k = 0$  with S000, the occurrence of a TW is confirmed with the asymptotic and stable skewness ( $\gamma < 0$ ) and kurtosis ( $\kappa > 3$ ) that deviate from Fickian values. As we increase the chemical heterogeneity (i.e.  $\eta_k > 0$ ) with the same network,  $\gamma$  and  $\kappa$  change indicating to the deviation of  $\tilde{C}$  front from the TW. Thus,  $\gamma$  changes from a negative value to positive values close to zero and  $\kappa$  fluctuates at values close to three. Because of these fluctuations, it is difficult to ascertain whether Fickian displacement develops. The fluctuations indicate that the network size should be increased which, however, was not pursued as a single simulation takes more than 197 CPU hours on a Pentium 4 (2.6 GHz) machine with 1 GB RAM.

We notice that the influence of chemical heterogeneity has negligible effects on skewness and kurtosis of the fronts that migrate in physically heterogeneous pore-networks. The concentration front responds with only slight changes to the increase of chemical heterogeneity. The major conclusion for the physically heterogeneous media ( $\eta_{pb} > 0$ ) is that transport remains non-Fickian. Hence, we question whether the error equation of type

$$\tilde{C} = \frac{1}{2} \operatorname{erfc} \left( \frac{X - vt}{2\sqrt{D_L t}} \right) \quad (6.31)$$

is still valid for cases  $\gamma \neq 0$  and  $\kappa \neq 3$  with sorption given by Eq (6.2) at the pore level and we question whether the attempts to extend this equation to describe biogeochemical reactions are in the right direction or should any other formalization be sought.

## 6.6 Discussion and conclusions

With the aid of a simple cubic pore-network, we designed 15 cases of transport of non-linearly adsorbing solutes in porous media. We considered five networks with different physical heterogeneity ( $0 \leq \eta_{pb} \leq 0.383$ ). For each network, we used three different levels of chemical heterogeneity ( $0 \leq \eta_k \leq 0.430$ ). We fixed parameters such as  $\langle \tilde{R}_{pb} \rangle$ ,  $p$ ,  $\rho_s$ ,  $K_F$  and the hydraulic head difference between the outlet and inlet faces of the network. Thus we had a variety of cases ranging from the chemically and physically homogeneous ( $\eta_k = 0$  and  $\eta_{pb} = 0$ ) to coupled uncorrelated heterogeneous ( $\eta_k > 0$  and  $\eta_{pb} > 0$ ). For a non-linearly adsorbing solute, the concentration profiles along the mean flow direction of the network were obtained through

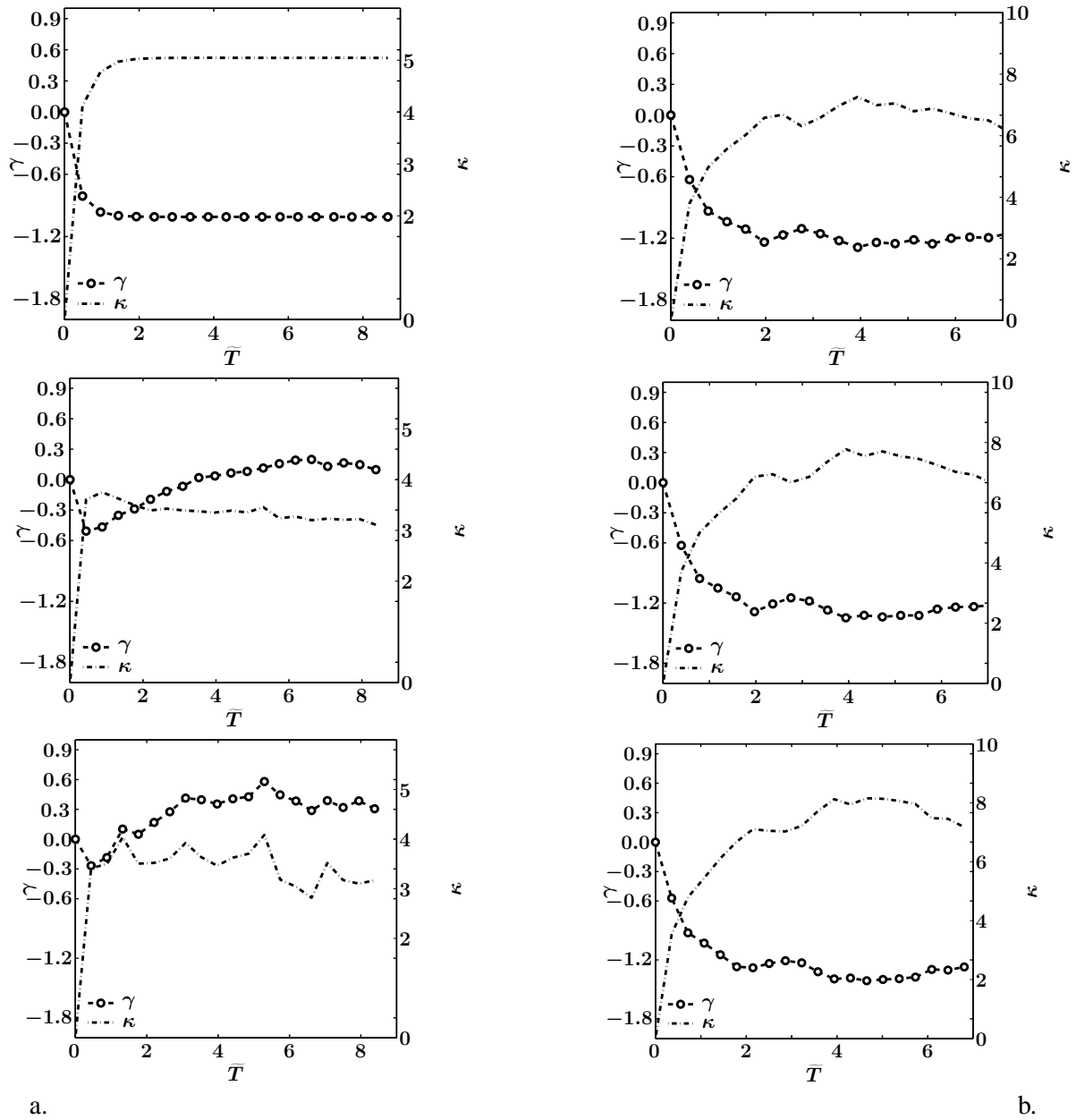


Figure 6.7: Skewness ( $\gamma$ ) and kurtosis ( $\kappa$ ) of plume as a function of pore volume of the effluent: a. network S000 (left column); b. network S115 (right column);  $\eta_k = 0$  (top row),  $\eta_k = 0.29$  (middle row) and  $\eta_k = 0.43$  (bottom row)

averaging the concentrations of the pore-units. Our numerical experiments were interpreted with the TW solution that describes the non-linearly adsorbing transport in porous media, by comparison with the network results at the macroscopic level. For the homogeneous case (i.e.  $\eta_{pb} = 0$  and  $\eta_k = 0$ ), the results show that the numerical concentration profiles perfectly match the profiles predicted by the TW equation [Van der Zee 1990; 1991; Bosma and Van der Zee 1993].

With the growth of either physical or chemical heterogeneity the disagreement between TW-behavior and numerical concentration distributions becomes distinct. The effect of chemical heterogeneity on a physically homogeneous medium appeared to be more dramatic than that on the physically heterogeneous medium. With the increase of chemical heterogeneity in a physically homogeneous medium the difference compared with the TW increases. The continuous growth of the second central moment and the fluctuations of  $\gamma$  close to zero and  $\kappa$  close to three may imply that the transport is Fickian.

The case of coupled heterogeneity ( $\eta_{pb} > 0$  and  $\eta_k > 0$ ) also causes that the TW-behavior does not develop as in this case  $M_2^c$  grows as a function of time with a rate that increases as  $\eta_{pb}$  increases. This case has stable higher-order moments, i.e.  $\gamma < 0$  and  $\kappa > 3$  and  $\gamma$  that are not much affected by  $\eta_k$ . That means that the transport in a physically heterogeneous medium is always non-Fickian.

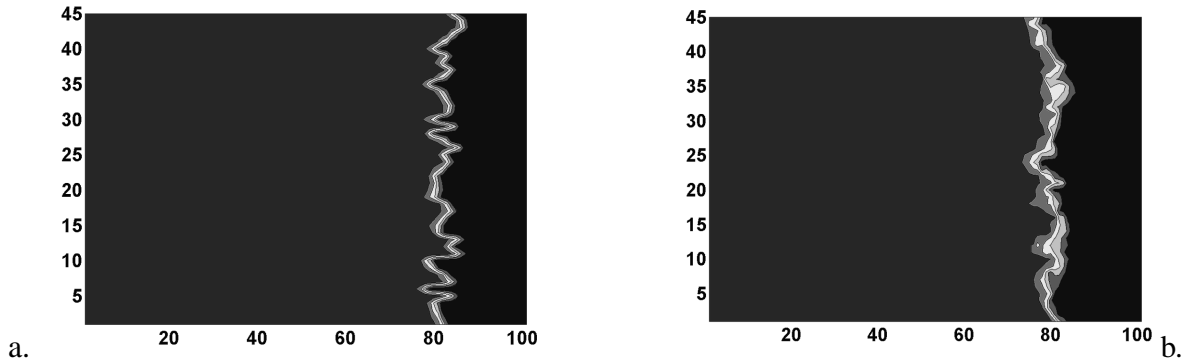


Figure 6.8: 2D-snapshots of non-linearly adsorbing plume-migration in chemically heterogeneous porous media. a. in physically homogeneous pore-network; b. in physically heterogeneous pore-network. The front is progressing from the left to the right.

With the introduction of heterogeneity, transversal mass transfer occurs. This leads to the reduction of displacement velocities in the longitudinal direction [Sahimi and Imdakm 1988]. Due to transversal mass loss, fast moving fingers become slower as sorption is non-linear whereas at slower figures, transversal gain of mass will make them faster. Also in the case when  $\eta_k > 0$  and  $\eta_{pb} = 0$  and  $D_m = 0$  we observe fingering (see the 2D-snapshot in Figure 6.8a) and the growth rate ( $\alpha_{res}$ ) of  $M_2^c$  is large.

Obviously, fingering developed here is due to the “clutch and release” effect, i.e. the pore-units along the flow axis impose randomly high or low retardation depending on the value of  $k$ . In the pore-units with low  $k$  the dispersion prevails whereas in the pore-units with high  $k$  front gets acutely retarded. Because of this each row of pore-units along the flow axis shows a different position of the first spatial moment in the 2D plane. Hence, although the front is locally narrow the macroscopic  $M_2^c$  is large because of large variations in the first spatial moments of individual rows of pore-units in the mean flow direction. Now question arises whether this phenomenon is realistic in porous media. For that purpose we used our additional experiments

on networks: S001 ( $\tilde{\sigma} = 0.001$ ), S002 ( $\tilde{\sigma} = 0.002$ ), S003 ( $\tilde{\sigma} = 0.003$ ) and S011 ( $\tilde{\sigma} = 0.011$ ) with  $\eta_k = 0.43$ . With a slight perturbation (say  $\tilde{\sigma} = 0.001$ ) the slope  $\alpha_{res}$  was reduced ten fold from  $0.2103\ell$  to  $0.0244\ell$  (see Table 6.3). The reason of such a change is that by introducing heterogeneity we enhance the transversal mass transfer that causes a reduction in the growth of  $M_2^c$ . From this we can understand that transversal dispersion is crucial. A pore-network of equal sized pore-units acts as a bundle of hydraulically non-interacting parallel tubes with periodically (randomly along the flow axis) chemical properties (i.e.  $k$ ) where a “clutch and release” effect is produced because of which the  $M_2^c$  manifests large growth. This manifestation is the price we pay for our assumption that  $D_m$  is zero and the porous medium is composed of same sized pores. From this it is clear that without considering transversal dispersion a realistic impression of the spread of the front spreading in a homogeneous idealization of porous media is impossible. Fortunately, real porous media including bed of uniform beads are made of differently sized pores [Yanuka et al. 1986] and the pore-networks are the model of such beds. Ignoring  $D_m$  in such pore networks, the transversal advection is compensated, as the physicochemical heterogeneity ( $\eta_{pb} > 0$  and  $\eta_k > 0$ ) does not produce essential different effects compared to those of  $\eta_{pb} > 0$  and  $\eta_k = 0$ . The combination of physical and chemical heterogeneity has little effects as is seen in the snapshot shown in Figure 6.8b. This snapshot is very similar to a case of physically heterogeneous medium with  $\eta_k = 0$  shown in Figure 5.10b. A quantitative analysis cannot be done based on this snapshot as it was produced for a pore-network of size  $101 \times 47 \times 47$  which is too small.

We conclude that fingering process is an unavoidable process and this process enhances the migration of solutes both in transversal and longitudinal directions. Hence, transversal dispersion cannot be ignored [Van der Zee et al. 2004a; Van der Zee et al. 2004b]. In combination with non-linear sorption, an essential new displacement behavior develops. The transport behavior of non-linearly adsorbing solutes in heterogeneous media, reveals a linear growth of  $M_2^c$  as a function of time after a short transition period. Typical of this behavior is that it is neither according to a TW nor is it Fickian. Consequently, no analytical solutions are yet available, whereas at the same time it is questionable to describe non-linear transport using a CDE with a non-linear sorption term.

## Acknowledgements

This study is performed under the research program “Upscaling Flow and Transport Processes in Porous Media: From Pore to Core” funded by the Dutch NWO/ALW project no. 809.62.010 and the project “Integrated Soil and Water Protection (SOWA)” funded by the European Commission (EVK1-CT-2002-80022).

# Chapter 7

## General conclusions

### 7.1 Upscaling permeability

In Chapter 2, we developed a new technique for discretization of continuum space into a hydraulic pore-network (HYPON). This technique revealed that regardless of the type of porebody size distribution the throat size of the bonds obeys a Gamma-type distribution, which indeed was an experimentally observed pore-size distribution. Also other morphological properties of HYPON are similar to those of the physically based network models. The study of *diagenesis* with HYPON revealed non-unique porosity-permeability relations, which are affected by the location of filling or scouring in the pore space. It provided insight how the simulated flow field should be handled if biogeochemical interactions affect the pore size (due to dissolution or clogging). For example, if interactions affect the porebody sizes then the sensitivity of permeability is secondary to porosity. The practical implication is that there is no need of updating the pressure field frequently in case of e.g. a gradually dissolving solid matrix. On the other hand, in case of clogging in the bonds, the sensitivity of porosity is secondary to permeability. In this case it is necessary to update the pressure field frequently. Additionally, the representative size of the pore-network that produces an asymptotic permeability is also determined. For the systems considered here, the network should comprise of at least  $25 \times 15 \times 15$  pore-units.

### 7.2 Upscaling dispersion

Modeling with the Brownian Particle Tracking Model (BPTM) revealed that our particle tracking algorithm matches the experimentally found single tube dispersion coefficient, provided that the same method is used to process First-arrival Times Distribution (FTD) data (Chapter 3). The study also revealed the limitations of different methods for temporal and spatial data processing. In general, we conclude that the presented network model with particle tracking is a robust tool for calculating the macroscopic longitudinal dispersion coefficient. We have introduced a new method to determine longitudinal dispersion coefficient from FTDs. The new method works for the full range of characteristic Peclet numbers ( $Pe_\ell$ ), provided that for large Peclet number a sufficiently large number of particles is used. Nodal jump conditions should include molecular diffusion and allow jumps in the upstream direction, and a parabolic velocity profile in the tubes should be implemented. Then, good agreement with experimental evidence is found for the full range of  $Pe_\ell$ , including increased  $D_L$  for increased porous medium heterogeneity. However, BPTM is computationally not attractive.

Alternatively modeling with the Mixing Cell Model (MCM) revealed that for numerically deriving an asymptotic dispersivity ( $\sim$  (dispersion coefficient)/velocity) at least a  $33 \times 23 \times 23$  network is required. The dispersivity in MCM is systematic and can be related to the porebody size heterogeneity. A family of such relations is found through regression and we recommend choose the iteration time step as described in Chapter 4. Hence, while considering to reactive transport analytically, there is no need of routing a non-reactive tracer just for determining the hydrodynamic (numerical) dispersion. The numerical dispersion with an iteration time step used here, MCM can mimic the dispersion produced by a BPTM with the plug-like intra-pore velocity profile, which is still smaller than the actual dispersion with parabolic intra-pore velocity profile. In BPTM the “so-called” microscopically homogeneous medium cannot be treated with plug-like intra-tube velocity profile as it leads to only *diffusion* not to *hydrodynamic dispersion*. In general, MCM proves to be a flexible model and numerical dispersion can be well controlled with iteration time step. Additionally, MCM is much more attractive with respect to simulation times and can take linearly or non-linearly reactive solutes transport into account.

### 7.3 Upscaling reactive transport

The network modeling of non-linearly adsorbing solutes transport revealed that to capture an asymptotic growth rate of second central moment at least a million pore units are required. Hence, our numerical experiments that base on  $301 \times 61 \times 61$  sized network reveal that non-linearly adsorbing transport fronts in homogeneous media approach traveling waves, which indeed is theoretically expected. With the growth of heterogeneity the disagreement between the traveling waves and numerical concentration distributions becomes noticeable and can be better quantified with the method of moments. Although, a steady growth of second central moments was observed in response to the increase of pore-size heterogeneity, the higher-order moments indicate that the front is non-Fickian/non-Gaussian. The growth rate of second central moments is a quadratic function of the standard deviation of pore-sizes and therefore, it can be systematically estimated. A few relations have been derived in Chapter 5.

The results of modeling of non-linearly adsorbing solutes transport in both physically and chemically (uncorrelated) heterogeneous media (Chapter 6) revealed that with the growth of either physical or chemical heterogeneity the disagreement between traveling wave behavior and numerical concentration distributions becomes distinct. The effect of chemical heterogeneity on a physically homogeneous medium appears more dramatic than that on the physically heterogeneous medium. With the increase of chemical heterogeneity in a physically homogeneous medium the difference compared with the traveling wave increases. The continuous growth of the second central moment and the fluctuations of skewness coefficient close to zero and kurtosis-coefficient close to three may imply that the transport is Fickian. Also for the case with physically and chemically heterogeneous media, traveling wave behavior does not develop as in this case the second central moment grows as a function of time with a rate that increases as pore-size heterogeneity increases. This case seems to obey the non-Fickian/non-Gaussian regime. Hence, in both cases fingering occurs but the impact of the fingering differs. For example, with a heterogeneous chemistry in a physically homogenous medium the front is locally narrow and sharp, whereas in comparison in the physically heterogeneous medium it is wider. That indicates that transversal dispersion is crucial. A pore-network of equal sized pore-units acts as a bundle of hydraulically non-interacting parallel tubes with periodically



(randomly along the flow axis) chemical properties where a “clutch and release” effect is produced because of which the second central moment manifests large growth. This manifestation is the price we pay for our assumption that molecular diffusion is zero and the porous medium is composed of equal sized pores. From this it is clear that without considering transversal dispersion a realistic impression of the size of the front spreading in a homogeneous idealization of porous media is impossible.

For a non-linearly adsorbing solute transport, we can conclude that the combination of *uncorrelated* physical and chemical heterogeneity has little effects compared with the effects of a single heterogeneity. Fingering of plumes originates from heterogeneity and is therefore an unavoidable process that enhances the migration of solutes both in transversal and longitudinal directions. Hence, transversal dispersion should not be ignored while simulating transport. In combination with non-linear sorption, an essential new displacement behavior develops. The transport behavior of non-linearly adsorbing solutes in heterogeneous medium reveals a linear growth of second central moment as a function of time after a short transition period. Typical of this behavior is that it is neither according to a traveling wave nor is it Fickian. Consequently, no analytical solutions are yet available, whereas at the same time it is questionable to describe non-linear transport using a convection-dispersion equation with a non-linear sorption term.



## References

- Acharya RC, SEATM Van der Zee and A Leijnse (2004a), Porosity-permeability properties generated with a new 2-parameter 3D Hydraulic Pore Network Model for consolidated and unconsolidated porous media, *Adv Water Res* 27(7), 707-723.
- Acharya RC, MIJ Van Dijke, A Leijnse, SEATM Van der Zee and KS Sorbie (2004b), Upscaling of tracer transport including convection and Brownian motion using a 3D network model, in Miller CT, MW Farthing, WG Gray and GF Pinder, *Proceedings of Computational Methods in Water Resources June, 2004, Chapel Hill, NC*; 1: pp 115-125, Elsevier.
- Appelo CAJ and D Postma (1993), *Geochemistry, groundwater and pollution*, 535 pp, A. A. Balkema, Rotterdam.
- Aris R (1956), On the dispersion of a solute in a fluid flowing through a tube, *Proc R Soc Lond A* 235, 67-77.
- Bakke S and PE Øren (1996), 3-D pore scale modelling of heterogeneous sandstone reservoir rocks and quantitative analysis of the architecture, geometry and spatial continuity of the pore network, *SPE paper* 35479.
- Bear J (1961a), On the tensor form of dispersion in porous media, *J Geophys Res* 66(4), 1185-1197.
- Bear J (1961b), Some experiments in dispersion, *J Geophys Res* 66(8), 2455-2467.
- Bear J (1972), *Dynamics of fluids in porous media*, 764 pp, Dover Publications, Inc., New York.
- Bear J and Y Bachmat (1990), *Introduction to modeling of transport phenomena in porous media*, 4, 554 pp, Kluwer Academic Publishers, Dordrecht / Boston / London.
- Bellin A, A Rinaldo, WJP Bosma, SEATM Van der Zee and Y Rubin (1993), Linear equilibrium adsorbing solute transport in physically and chemically heterogeneous porous formations 1. Analytical solutions, *Water Resour Res* 29(12), 4019-4030.
- Berkowitz B and JY Zhou (1996), Reactive solute transport in a single fracture, *Water Resour Res* 32(4), 901-913.
- Blunt M and P King (1991), Relative permeabilities from 2-dimensional and 3-dimensional pore-scale network modeling, *Transp Porous Med* 6(4), 407-433.
- Blunt MJ (2001), Flow in porous media-pore-network models and multiphase flow, *Curr Opinion Colloid Interf Sci* 6(3), 197-207.
- Blunt MJ, MD Jackson, M Piri and PH Valvatne (2002), Detailed physics, predictive capabilities and macroscopic consequences for network models of multiphase flow, *Adv Water Res* 25(8-12), 1069-1089.
- Bolt GH (1982), Movement of solutes in soil: principles of adsorption/exchange chromatography, in *Soil chemistry B: Physico chemical models*, edited by Bolt GH, pp 285-348, Elsevier, Amsterdam.
- Bosma WJP, A Bellin, SEATM Van der Zee and A Rinaldo (1993), Linear equilibrium adsorbing solute transport in physically and chemically heterogeneous porous formations 2. Numerical results, *Water Resour Res* 29(12), 4031-4043.
- Bosma WJP and SEATM Van der Zee (1992), Analytical approximation for nonlinear adsorbing solute transport and first order degradation, *Transp Porous Med* 11, 33-43.
- Bosma WJP and SEATM Van der Zee (1993), Transport of reactive solute in a one-dimensional, chemically heterogeneous porous medium, *Water Resour Res* 29(1), 117-131.
- Bosma WJP and SEATM Van der Zee (1995), Dispersion of a continuously injected, nonlinearly adsorbing solute in chemically or physically heterogeneous porous formations, *J Contam Hydrol* 18(3), 181-198.

- Brenner H (1980), A general theory of Taylor dispersion phenomena, *Phys Chem Hydrodynamics* 6, 91-123.
- Brigham WE, PW Reed and JN Dew (1961), Experiments on mixing during miscible displacement in porous media, *Trans SPE* 222(1), 1-8.
- Brinkman HC (1947), A calculation of the viscous force exerted by a flowing fluid on a dense swarm of particles, *Appl Sci Res A* 1, 27-34.
- Bruderer C and Y Bernabé (2001), Network modeling of dispersion: Transition from Taylor dispersion in homogeneous ones to mechanical dispersion in very heterogeneous ones, *Water Resour Res* 37(4), 897-908.
- Bryant SL, PR King and DW Mellor (1993a), Network model evaluation of permeability and spatial correlation in a real random sphere packing, *Transp Porous Med* 11, 53-70.
- Bryant SL, DW Mellor and CA Cade (1993b), Physically Representative Network Models of Transport in Porous-Media, *AIChE J* 39(3), 387-396.
- Carbonell RG (1979), Effect of pore distribution and flow segregation on dispersion in porous-media, *Chem Eng Sci* 34(8), 1031-1039.
- Celia M, PC Reeves and LA Ferrand (1995), Recent advances in pore scale models for multiphase flow in porous media, *Rev. Geophys. Suppl., U.S. National Report to International Union of Geodesy and Geophysics 1991-1994*, pp 1049-1057.
- Chandrasekhar S (1943), Stochastic problems in physics and astronomy, *Rev Mod Phys* 15, 1-89.
- Chatzis I and FAL Dullien (1977), Modelling pore structure by 2-D and 3-D networks with applications to sandstones, *J Canad Petrol Technol* 16(1), 97-108.
- Choy TC (1999), *Effective medium theory*, 182 pp, Clarendon Press, Oxford.
- Chrysikopoulos CV, PK Kitanidis and PV Roberts (1990), Analysis of one dimensional solute transport through porous media with spatially variable retardation factor, *Water Resour Res* 26, 437-446.
- Dagan G (1988), Time-dependent macrodispersion for solute transport in anisotropic heterogeneous aquifers, *Water Resour Res* 24, 1491-1500.
- Dagan G (1989), *Flow and Transport in porous formations*, 465 pp, Springer-Verlag, Berlin.
- Dahle HK and MA Celia (1999), A dynamic network model for two-phase immiscible flow, *Computat Geosci* 3, 1-22.
- Damion RA, KJ Packer, KS Sorbie and SR McDougall (2000), Pore-scale network modelling of flow propagators derived from pulsed magnetic field gradient spin echo NMR measurements in porous media, *Chem Eng Sci* 55, 5981-5998.
- David C, Y Gueguen and G Pampoukis (1990), Effective medium theory and network theory applied to the transport properties of rock, *J Geophys Res* 95(B5), 6993-7005.
- De Arcangelis L, J Koplik, S Redner and D Wilkinson (1986), Hydrodynamic dispersion in network models of porous media, *Phys Rev Lett* 57(8), 996-999.
- De Haan FAM, SEATM Van der Zee and WH Riemsdijk (1987), The role of soil chemistry and soil physics in protecting soil quality: Variability of sorption and transport of cadmium as an example, *Neth J Agric Sci* 35, 347-359.
- De Josselin de Jong G (1958), Longitudinal and transverse diffusion in granular deposits, *Trans Am Geophys Union* 39, 67-74.
- Detwiler RL, H Rajaram and RJ Glass (2000), Solute transport in variable-aperture fractures: An investigation of the relative importance of Taylor dispersion and macrodispersion, *Water Resour Res* 36(7), 1611-1625.

- Dias MM and AC Payatakes (1986), Network models for two-phase flow in porous media Part I: Immiscible microdisplacement of non-wetting fluids, *J Fluid Mech* 164, 305-336.
- Du Plessis JP (1999), Introducing a percolation threshold in pore-scale modelling, *Phys Chem Earth A* 24(7), 617-620.
- Dullien FAL (1991), Characterization of porous media—pore level, *Transp Porous Med* 6, 581-606.
- Dullien FAL (1992), *Porous media: Fluid transport and pore structure*, 574 pp, Academic Press, San Diego.
- Fadili A, R Ababou and R Lenormand (1999), Dispersive particle transport: Identification of macroscale behavior in heterogeneous stratified subsurface flows, *Math Geol* 31(7), 793-840.
- Fatt I (1956a), The network model of porous media, Part I: Capillary characteristics, *Petrol Trans AIME*, 144-159.
- Fatt I (1956b), The network model of porous media, Part II: Dynamic properties of single size tube network, *Petrol Trans AIME*, 160-163.
- Fatt I (1956c), The network model of porous media, Part III: Dynamic properties of networks with tube radius distribution, *Petrol Trans AIME*, 164-181.
- Finney JL (1968), Random packings and the structure of liquid state, *PhD Thesis*, University of London.
- Finney JL (1970), Random packings and the structure of simple liquids I. The geometry of random close packing, *Proc R Soc Lond A* 319, 479-494.
- Freeze RA and JA Cherry (1979), *Groundwater*, 604 pp, Prentice-Hall, Englewood Cliffs, New Jersey.
- French SE (1995), *Fundamentals of structural analysis*, 737 pp, West Publishing company, Minneapolis.
- Freyberg DL (1986), A natural gradient experiment on solute transport in sand aquifer: 2. Spatial moments and the advection and dispersion of none-reactive tracers, *Water Resour Res* 22(13), 2031-2046.
- Gelhar LW, C Welty and KR Rehfeldt (1992), A critical review of data on field-scale dispersion in aquifers, *Water Resour Res* 28(7), 1955-1974.
- Gielen T, SM Hassanizadeh, MA Celia and HK Dahle (2002), Study of Pc-Sw relationship using a dynamic pore-scale network model, in Hassanizadeh SM, RJ Schotting, WM Gray and GF Pinder, *Proceedings of Computational Methods in Water Resources, Delft, the Netherlands*; 2: pp 1099-1106, Elsevier.
- Gunn DJ and C Pryce (1969), Dispersion in packed beds, *Trans Inst Chem Eng* 47, T341-T350.
- Han NW, J Bhakta and RG Carbonell (1985), Longitudinal and lateral dispersion in packed-beds - effect of column length and particle-size distribution, *AIChE J* 31(2), 277-288.
- Happel J and H Brenner (1965), *Low Reynolds number hydrodynamics with special applications to particulate media*, 553 pp, Prentice-Hall, Inc., Englewood Cliffs, N.J.
- Harding E and D Kendall, Eds. (1974), Stochastic Geometry, in Series *Stochastic Geometry*, Wiley, London.
- Hashin Z (1983), Analysis of composite-materials - a survey, *J Appl Mech* 50, 481-505.
- Hassanizadeh SM (1996), On the transient non-Fickian dispersion theory, *Transp Porous Med* 23(1), 107-124.
- Hassanizadeh SM, MA Celia and HK Dahle (2002), Dynamic Effect in the Capillary Pressure-Saturation Relationship and their Impacts on Unsaturated Flow, *Vadose Zone Hydrol* 1, 38-57.

- Hassanizadeh SM and WG Gray (1979a), General conservation equations for multiphase systems, 1: Averaging procedures, *Adv Water Res* 2, 131-144.
- Hassanizadeh SM and WG Gray (1979b), General conservation equations for multiphase systems, 2: Mass, momenta, energy and entropy equations, *Adv Water Res* 2, 191-203.
- Held RJ and MA Celia (2001), Pore-scale modeling extension of constitutive relationships in the range of residual saturations, *Water Resour Res* 37(1), 165-170.
- Hestenes MR (1980), *Conjugate direction methods in optimization*, 325 pp, Springer-Verlag, New York.
- Hidajat I, HA Rastogi, M Singh and KK Mohanty (2002), Transport properties of porous media reconstruction from thin sections, *SPE J*(March), 40-48.
- Hilfer R (1996), Transport and relaxation phenomena in porous media, *Adv Chem Phys XCII*, 299-424.
- Hilfer R (2002), Review on scale dependent characterization of the microstructure of porous media, *Transp Porous Med* 46, 373-390.
- Hoffmann MR (2003), Macroscopic equations for flow in unsaturated porous media, *PhD Thesis*, 123 pp, Wageningen University, Wageningen.
- Ioannidis MA, I Chatzis and EA Sudicky (1993), The effect of spatial correlations on the accessibility characteristics of three-dimensional cubic networks as related to drainage displacements in porous media, *Water Resour Res* 29(6), 1777-1785.
- Ioannidis MA and J Chatzis (1993), Network modelling of pore structure and transport properties of porous media, *Chem Eng Sci* 48(5), 951-972.
- Ives KJ (1975), *The scientific basis of filtration*, pp 218-219, Noordhoff International Publishing, Leiden, The Netherlands.
- Jerauld GR and S Salter (1990), The effect of pore structure on hysteresis in relative permeability and capillary pressure: Pore level modeling, *Transp Porous Med* 5, 103-151.
- Jiao C (2001), Miscible displacements in porous media with variation of fluid density and viscosity, *PhD Thesis*, 167 pp, University of Karlsruhe, Karlsruhe.
- Katz AJ and AH Thompson (1986), Quantitative prediction of permeability in porous rock, *Phys Rev B* 34(11), 8179-8181.
- Katz AJ and AH Thompson (1987), Prediction of rock electrical conductivity from mercury injection measurements, *J Geophys Res* 92, 599-607.
- Keijzer H, RJ Schotting and SEATM Van der Zee (2000), Semi-analytical traveling wave solution of one-dimensional aquifer bioremediation, *Commun Appl Nonlin Analys* 7;1-20.
- Keijzer H, MIJ Van Dijke and SEATM Van der Zee (1999), Analytical approximation to characterize the performance of in situ aquifer bioremediation, *Adv Water Res* 23(3), 217-228.
- Keller AA (1997), High resolution CAT imaging of fractures in consolidated materials, *J Rock Mech Min Sci* 34(3/4), 358.
- Knabner P and CJ Van Duijn (1992), Travelling waves in the transport of reactive solutes through porous media: Adsorption and ion exchange - Part 1, *Transp Porous Med* 8, 167-194.
- Koch DL and JF Brady (1985), Dispersion in fixed beds, *J Fluid Mech* 154, 399-427.
- Koplik J (1982), Creeping flow in two-dimensional networks, *J Fluid Mech* 119, 219-247.
- LaBolle EM, J Quastel and GE Fogg (1998), Diffusion theory for transport in porous media: Transition probability densities of diffusion processes corresponding to advection-dispersion equations, *Water Resour Res* 34(7), 1685-1693.
- Legatski MW and DL Katz (1966), Dispersion coefficients for gases flowing in consolidated porous media, *J Petrol Technol* 18(9), 1106-1116.

- Legatski MW and DL Katz (1967), Dispersion coefficients for gases flowing in consolidated porous media, *SPE J*(March), 43-53.
- Lernormand R, C Zarcone and A Sarr (1983), Mechanisms of the displacement of one fluid by another in a network of capillary ducts, *J Fluid Mech* 135(Oct), 337-353.
- Liang Z, MA Ioannidis and I Chatzis (2000), Geometric and topological analysis of three dimensional porous media: pore space partitioning based on morphological skeletonization, *J Colloid Interf Sci* 221, 13-24.
- Lindquist WB, S-M Lee, DA Coker, KW Jones and P Spanne (1996), Medial axis analysis of void structure in three-dimensional tomographic images of porous media, *J Geophys Res* 101(B4), 8297-8310.
- Lindquist WB and A Venkatarangan (1999), Investigating 3D geometry of porous media from high resolution images, *Phys Chem Earth A* 25(7), 593-599.
- Mason GA (1971), A model of pore space in a random packing of equal spheres, *J Colloid Interf Sci* 35(2), 279-287.
- Mayer RP and RA Stowe (1966), Mercury porosimetry: Filling of toroidal void volume following breakthrough between packed spheres, *J Phys Chem* 70(12), 3867-3873.
- Mogensen K and EH Stenby (1998), A dynamic two-phase pore-scale model of imbibition, *Transp Porous Med* 32(3), 299-327.
- Mohanty K and S Salter (1982), Multiphase flow in porous media: II. Pore-level modeling, *SPE paper 11018*.
- Mualem Y (1976), A new model for predicting the hydraulic conductivity of unsaturated porous media, *Water Resour Res* 12(3), 513-522.
- Mualem Y (1992), Modeling the hydraulic conductivity of unsaturated porous media, in Van Genuchten MT, FJ Leij and LJ Lund, *Proceedings of In indirect methods for estimating the hydraulic properties of unsaturated soils*, Riverside, CA; pp 15-36, U.S. Salinity Laboratory.
- Nowicki SC, HT Davis and LE Scriven (1992), Microscopic determination of transport parameters in drying porous media, *Drying Technol* 10(4), 925-946.
- Øren PE and S Bakke (2002), Process based reconstruction of sandstones and prediction of transport properties, *Transp Porous Med* 46(2-3), 311-343.
- Øren PE, S Bakke and OJ Arntzen (1998), Extending predictive capabilities to network models, *SPE J* 3(4), 324-336.
- Okabe A, B Boots and K Sugihara (1992), *Spatial tessellation: Concepts and applications of Voronoi diagrams*, Wiley and Sons, Inc., New York.
- Or D and M Tuller (1999), Liquid retention and interfacial area in variably saturated porous media: Upscaling from single-pore to sample-scale model, *Water Resour Res* 35(12), 3591-3605.
- Oya S and AJ Valocchi (1997), Characterization of traveling waves and analytical estimation of pollutant removal in one-dimensional subsurface bioremediation modeling, *Water Resour Res* 33(1117-1127).
- Panda MN and LW Lake (1994), Estimation of single-phase permeability from parameters of particle-size distribution, *AAPG Bull* 78(7), 1028-1039.
- Park YJ, JR De Dreuzy and KK Lee (2001), Transport and intersection mixing in random fracture networks with power law length distribution, *Water Resour Res* 37(10), 2493-2501.
- Park YJ and KK Lee (1999), Analytical solutions for solute transfer characteristics at continuous fracture junctions, *Water Resour Res* 35(5), 1531-1537.

- Payatakes AC, C Tien and RM Turian (1973), A new model for granular porous media - Part I: Model formulation, *AIChE J* 19, 67-76.
- Perkins TK and OC Johnston (1963), A review of diffusion and dispersion in porous media, *SPE J* 3, 70-84.
- Press F and R Siever (1986), *Earth*, 656 pp, Freeman, New York.
- Quiblier J (1984), A new three dimensional modeling technique for studying porous media, *J Colloid Interf Sci* 98, 84.
- Rajaram H, LA Ferrand and MA Celia (1997), Prediction of relative permeabilities for unconsolidated soils using pore-scale network models, *Water Resour Res* 33(1), 43-52.
- Reeves PC (1997), The development of pore-scale network models for the simulation of capillary pressure - saturation - interfacial area - relative permeability relationships in multi-fluid porous media, *PhD Thesis*, 347 pp, Princeton University, Princeton.
- Reeves PC and MA Celia (1996), A functional relationship between capillary pressure, saturation, and interfacial area as revealed by a pore-scale network model, *Water Resour Res* 32(8), 2345-2358.
- Roychoudhury AN (2001), Dispersion in unconsolidated aquatic sediments, *Estuar Coast Shelf Sci* 53, 745-757.
- Rubinstein J and S Torquato (1989), Bounds on Various Electrostatic and Hydrodynamic Capacities, in *Random Media and Composites*, 60, edited by Kohn RV and GW Milton, Society of Industrial and Applied Mathematics.
- Rusch U, M Borkovec, J Daicic and WH Van Riemsdijk (1997), Interpretation of competitive adsorption isotherms in terms of affinity distributions, *J Colloid Interf Sci* 191, 247-255.
- Saffman PG (1959), A theory of dispersion in a porous medium, *J Fluid Mech* 6(3), 321-349.
- Saffman PG (1960), Dispersion due to molecular diffusion and macroscopic mixing in flow through a network of capillaries, *J Fluid Mech* 7, 194-208.
- Sahimi M (1993), Flow phenomena in rocks: From continuum models to fractals, percolation, cellular automata and simulated annealing, *Rev Mod Phys* 65, 1393.
- Sahimi M, DH Barry, LE Scriven and HT Davis (1983a), Stochastic transport in disordered systems, *J Chem Phys* 78(11), 6849-6864.
- Sahimi M, HT Davis and LE Scriven (1983b), Dispersion in disordered porous media, *Chem Eng Sci Commun* 23, 329-341.
- Sahimi M, A Heiba, H Davis and L Scriven (1986), Dispersion in flow through porous media - I One phase flow, *Chem Eng Sci* 41(8), 2103-2122.
- Sahimi M and AO Imdakm (1988), The effect of morphological disorder on hydrodynamic dispersion in flow through porous media, *J Phys A Math Gen* 21(19), 3833-3870.
- Scheidegger A, M Borkovec and H Sticher (1993), Coating of silica sand with goethite: preparation and analytical identification, *Geoderma* 58(1-2), 43-65.
- Scheidegger AE (1960), *The physics of flow through porous media*, 313 pp, University of Toronto Press, Toronto.
- Serrano SE (2003), Propagation of nonlinear reactive contaminants in porous media, *Water Resour Res* 39(8), 1228.
- Shames IH (1992), *Mechanics of fluids*, 858 pp, McGraw-Hill, Inc., New York.
- Sok RM, MA Knackstedt, AP Sheppard, WV Pinczewski, WB Lindquist, A Venkatarangan and L Paterson (2002), Direct and stochastic generation of network models from tomographic images; Effect of topology on residual saturation, *Transp Porous Med* 46, 345-372.
- Sorbie KS and PJ Clifford (1991), The inclusion of molecular diffusion effects in the network



- modelling of hydrodynamic dispersion in porous media, *Chem Eng Sci* 46(10), 2525-2542.
- Steele DD and JL Nieber (1994a), Network modeling of diffusion coefficients for porous media. I. Theory and model development, *Soil Sci Soc Am J* 58(5), 1337-1345.
- Steele DD and JL Nieber (1994b), Network modeling of diffusion coefficients for porous media. II. Simulations, *Soil Sci Soc Am J* 58(5), 1346-1354.
- Stoyan D, W Kendall and J Mecke (1995), *Stochastic geometry and its applications*, Akademie-Verlag/Wiley, Berlin/Chichester.
- Suchomel BJ, BM Chen and MB Allen (1998a), Macroscale properties of porous media from a network model of biofilm processes, *Transp Porous Med* 31(1), 39-66.
- Suchomel BJ, BM Chen and MB Allen (1998b), Network model of flow, transport and biofilm effects in porous media, *Transp Porous Med* 30(1), 1-23.
- Sugita F and RW Gillham (1995a), Pore Scale Variation in Retardation Factor as a Cause of Nonideal Reactive Breakthrough Curves, 1: Conceptual-Model and Its Evaluation, *Water Resour Res* 31(1), 103-112.
- Sugita F and RW Gillham (1995b), Pore Scale Variation in Retardation Factor as a Cause of Nonideal Reactive Breakthrough Curves, 3: Column Investigations, *Water Resour Res* 31(1), 121-128.
- Sun N-Z (1996), *Mathematical modeling of groundwater pollution*, 377 pp, Springer-Verlag, New York.
- Taylor G (1953), Dispersion of solute matter in solvent flowing slowly through a tube, *Proc R Soc Lond A* 219, 186-203.
- Taylor G (1954), The dispersion of matter in turbulent flow through a pipe, *Proc R Soc Lond A* 223, 446-468.
- Thompson KE and HS Fogler (1997), Modeling flow in disordered packed beds from pore-scale fluid mechanics, *AIChE J* 43(6), 1377-1389.
- Tien C and AC Payatakes (1979), Advances in deep bed filtration (Journal Review), *AIChE J* 25(5), 737-759.
- Toledo PG, LE Scriven and HT Davis (1994), Equilibrium and stability of static interfaces in biconical pore segments, *SPE Form Eval* 9(1), 61-65.
- Torquato S and S Hyun (2001), Effective-medium approximation for composite media: Realizable single-scale dispersion, *J Appl Phys* 89(3), 1725-1729.
- Tsakiroglou CD and AC Payatakes (1991), Effects of pore-size correlations on mercury porosimetry curves, *J Colloid Interf Sci* 146(2), 479-494.
- Tsakiroglou CD and AC Payatakes (2000), Characterization of the pore structure of reservoir rocks with the aid of serial sectioning analysis, mercury porosimetry and network simulation, *Adv Water Res* 23(7), 773-789.
- Tsang CF and C Doughty (2003), A particle-tracking approach to simulating transport in a complex fracture, *Water Resour Res* 39(7), 1174-1181.
- Tuller M, D. OR and LM Dudley (1999), Adsorption and capillary condensation in porous media -liquid retention and interfacial configurations in angular pores, *Water Resour Res* 35(7), 1949-1964.
- Turian RM (1973), A new model for granular porous media - Part I: Model formulation, *AIChE J* 19, 67-76.
- Uffink GJM (1988), *Modeling of solute transport with the random walk method*, Reidel Publishing Company, Holland.

- Valocchi AJ (1989), Spatial moment analysis of transport of kinetically absorbing solutes through stratified aquifers, *Water Resour Res* 25, 273-279.
- Valvatne PH (2002), Predictive pore scale modelling: A report submitted to the Department of Earth Science and Engineering of Imperial College, *Predictive pore scale modelling: A report submitted to the Department of Earth Science and Engineering of Imperial College*, pp 7-63, Department of Earth Science and Engineering of Imperial College, London.
- Van Brakel J (1975), Pore space models for transport phenomena in porous media review and evaluation with special emphasis on capillary liquid transport, *Powder Technol* 11, 205-236.
- Van de Weerd H, A Leijnse and WH Van Riemsdijk (1998), Transport of reactive colloids and contaminants in groundwater: Effect of nonlinear kinetic interactions, *J Contam Hydrol* 32(3-4), 313-331.
- Van der Zee SEATM (1990), Analytical travelling wave solutions for transport with nonlinear and nonequilibrium adsorption, *Water Resour Res* 26(10), 2563-2578.
- Van der Zee SEATM (1991), Correction to Analytical travelling wave solutions for transport with nonlinear and nonequilibrium adsorption, *Water Resour Res* 27(5), 983.
- Van der Zee SEATM, RC Acharya and GMCM Janssen (2004a), Upscaling biogeochemically reactive chemical transport, in Aagaard P, E Bedbur, G Bidoglio, L Candela, G Nuetzmann, M Trevisan, M Vanclooster and P Viotti, *Proceedings of International Workshop Saturated and Unsaturated Zone - Integration of process knowledge into effective models, May 5-7, Rome, Italy*; pp 355-362, La Goliardica Pavese, Pavia, It.
- Van der Zee SEATM, GMCM Janssen and RC Acharya (2004b), Upscaling biogeochemically reactive chemical transport in natural porous media, in Halm D and P Grathwohl, *Proceedings of 2nd International Workshop on Integrated Soil and Water Protection: Risks from Diffuse Pollution (SOWA), Prague, Czech Republic, June 28-29*; pp 62-66, Tuebingen Wissenschaftlicher Arbeiten (TGA), Tuebingen.
- Van Dijke MIJ and KS Sorbie (2002), Pore-scale network model for three-phase flow in mixed-wet porous media, *Phys Rev E* 66(4), 046302.
- Van Duijn CJ, RE Grundy and CN Dawson (1996), Limiting profiles in reactive solute transport, *Limiting profiles in reactive solute transport AM-R9604*, pp 1-28, CWI, Amsterdam.
- Van Duijn CJ and P Knabner (1990), Travelling waves in the transport of reactive solute through porous media: Adsorption and binary exchange, Part 2, *Report 205*, Schwerpunktprogramm der Deutsche Forschungsgemeinschaft, Univ. Augsburg, Inst. Mathematik.
- Van Genuchten MT and WJ Alves (1982), Analytical solutions of the one dimensional convective-dispersive solute transport equation, *Analytical solutions of the one dimensional convective-dispersive solute transport equation USDA ARS Technical Bulletin Number 1661*, U.S. Salinity Laboratory, 4500 Glenwood Drive, Riverside, CA 92501.
- Van Genuchten MT and PJ Wierenga (1976), Mass transfer studies in sorbing porous media. I. Analytical solutions, *J Soil Sci Soc Am* 40(4), 473-480.
- Verlaan M (2001), Dispersion in heterogeneous media: Fundamental issues inspired by underground gas storage, *PhD Thesis*, 145 pp, TUDelft, Delft.
- Whitaker S (1967), Diffusion and dispersion in porous media, *AIChE J* 13(3), 420-427.
- Whitaker S (1969), Advances in the theory of fluid flow in porous media, *Ind Eng Chem* 12, 14-28.
- Whitaker S (1972), Forced convection heat transfer correlations for flow in pipes, past flat plates, single cylinders, single spheres and for flow in packed beds and tube bundles,

- AIChE J* 18(2), 361-371.
- Whitaker S (1986), Flow in porous media. II. The governing equations of immiscible, two-phase flow, *Transp Porous Med* 1, 105-125.
- Wise WR (1992), A new insight on pore structure and permeability, *Water Resour Res* 28(1), 189-198.
- Woodside W and JH Messmer (1961), Thermal conductivity of porous media, *J Appl Phys* 32, 1688-99.
- Yanuka M, F Dullien and D Enick (1986), Percolation processes and porous media, *J Colloid Interf Sci* 112, 24-41.
- Zhuang J, K Nakayama, GR Yu and T Miyazaki (2000), Scaling of saturated hydraulic conductivity: A comparison of models, *Soil Sci* 165(9), 718-727.



## Summary

The problem of contaminants in the sub-soils (porous media) has been a widely spoken issue in the recent years. The *biogeochemical* reactions that take place in porous media and the transport of solutes are very complex processes that we wish to understand. This thesis makes a contribution to the understanding of the complexities of these processes. The thesis describes a rigorous numerical technique for upscaling the flow and transport from individual pores to the core scale. In this thesis, geometric properties of pores are emphasized, the physics and chemistry in the pore are described by exact equations and a suitable averaging procedure is applied to upscale the pore-scale processes to the core-scale. Hydraulic pore-network model HYPON is used as an elementary tool for *upscaling*. Through *upscaling* the key macroscopic parameters of the flow and the convection-dispersion equations are deduced and functional relations of these parameters to the pore-size heterogeneity are explored. The study of concentration front-behavior is emphasized. This thesis contains seven chapters. The first chapter introduces the problem, objective and the approach of the research, whereas the last one summarizes the major findings and the conclusions of the research. The remaining chapters, namely from Chapter 2 through Chapter 6, describe different themes of the research but share a common thread, the *upscaling*. Some overlaps between these five chapters are caused due to the fact that each chapter is an independently-readable already-published or partially-published article. In the following the procedure of research is outlined followed by the conclusions.

In Chapter 2, we develop a new technique for the construction of a comparatively realistic pore-network model. According to this technique, the continuum domain is discretized into a network of pore-units with converging-diverging architecture. The morphological characteristics of such a network are compared with those of physically based pore-networks. Further, the porosity-permeability relations of this network are upscaled. Steady-state conditions are imposed on the network and the Kirchoff problem is solved numerically by using preconditioned conjugate gradients. The solution provides an intrinsic permeability of the network. For an asymptotic value of intrinsic permeability a representative size of pore network is deduced by using the Monte Carlo technique and this size is verified with the effective medium theory. Additionally, the results are verified also with the Carman-Kozeny theory. With several realizations of pore sizes we derive permeability for realistic porosity ranges reported in the literature. The non-unique porosity-permeability relations are explored assuming diagenesis either in the large voids (porebodies) or in the converging-diverging capillary space (bonds). We expect that that will provide an insight whether it is necessary to periodically update the pressure field while simulating certain cases of reactive solutes transport.

Chapter 3 and 4 deal with the quantification of local displacements due to Brownian motion caused by molecular diffusion ( $D_m$ ) and advection of non-reactive tracer particles and focus on upscaling such pore-scale displacements to a macroscopic parameter known as the longitudinal dispersion coefficient ( $D_L$ ) for a core. For this purpose we develop two models: the Brownian Particle Tracking Model (BPTM) and the Mixing Cell Model (MCM). Chapter 3 describes the procedure of BPTM development and extensively elucidates the results from this model. We start with developing BPTM for a Taylor's capillary tube and verify it by reproducing the Taylor's laboratory experiments. Then the model is extended to the network scale. The results obtained from BPTM for the network are compared with the theoretical model of Saffman (1960) and with the experimental data compiled by earlier researchers. Different intra-pore velocity profiles are considered. Different types of jump conditions at the intersections of pores and different regimes with respect to characteristic Peclet number ( $Pe_\ell = v\ell/D_m$ , where

$\ell$  denotes lattice constant (the *mean pore length*), and  $v$  denotes the intrinsic velocity in the mean flow direction) are considered. Also the impact of physical heterogeneity of the pore sizes on longitudinal dispersion is analyzed numerically. The data are generated with two approaches: at designated time intervals the positions of the particles are scanned to obtain a Spatial Positions Distribution (SPD) or alternatively the particles are injected from the inlet of the network and produced at the outlet to obtain a First-arrival Times Distribution (FTD). The method of moments is used for processing the BPTM data. A new method for FTD data processing is introduced to achieve an agreement between the results originated from FTDs and SPDs.

In Chapter 4, we develop a MCM and use it to obtain  $D_L$  for HYPON. The starting point is the determination of the representative size of the pore-network that can produce an asymptotic magnitude of *dispersivity* ( $\alpha_L \sim D_L/v$ ). Then the functional relationship of  $\alpha_L$  and the pore-size heterogeneity is explored. Also, attention is paid on how these relations respond to the value of the iteration time  $\Delta t$ . Finally, these relations are verified in big pore-networks and thus, asymptotic magnitudes of  $\alpha_L$  are validated. In the next-step we verify whether MCM is plausible for quantifying dispersivity. For that purpose five large networks of gradually varying pore-size heterogeneity are considered and the dispersivity with BPTM model was computed, to compare with MCM results.

The upscaling problem of non-linearly reactive transport is dealt in Chapters 5 and 6. In Chapter 5, numerical simulations are aimed at whether in physically heterogeneous porous media (differently sized pores) traveling wave behavior develops. For this purpose, the starting point is again the determination of a representative size of pore-network. Then several cases with different pore-size variance are designed and the transport of solutes that obey Freundlich isotherm is simulated. The network of equal sized pores with homogeneous chemical properties is a special case of interest because in such a network theoretically a traveling wave behavior should develop. Additionally, the size of the front spreading for this case can be graphically determined according to the simplified moment equation of traveling wave developed by Bosma and Van der Zee (1993). This case is also a reference bench mark for other cases. In addition to the direct comparison of numerical and theoretical (analytical) fronts, the (dis) agreement of the two is judged with the method of moments (up to fourth order). Then the functional relations of the moment growth rates to pore-size statistics are derived.

Chapter 6 elucidates on non-linearly adsorbing solutes transport in porous media of combined heterogeneities: physical (pore size variance  $\geq 0$ ) as well as chemical (chemical property of each pore different). We examine how the growth rates of second central spatial moments respond to the chemical and physical heterogeneities. Efforts are aimed at understanding the competition of chemical and physical heterogeneities. Attention is paid on exploring when one or the other heterogeneity prevails in determining the fate of the plume. Additionally, the reasons of fingering development during non-linearly reactive transport are touched upon.

In Chapter 7 we summarize and generalize the conclusions of the above five chapters. A short summary of conclusions follows:

The new technique (Chapter 2) for discretization of continuum space into a hydraulic pore-network (HYPON) revealed that regardless of the type of porebody size distribution the throat size of the bonds obeys a Gamma-type distribution, which in indeed was an experimentally observed throat-size distribution. Also other morphological properties of HYPON are similar to those of the physically based network models. The study of *diagenesis* with HYPON showed that non-unique porosity-permeability relations are inevitable and are greatly influenced by the location of filling or scouring in the pore space. For example, if a solute precipitates in

large voids (porebodies) then the permeability is less sensitive than the porosity. The practical implication is that in this case there is no need of updating the flow field frequently. On the other hand, if the contaminant becomes adsorbed in the capillary space (bonds) then the permeability is more sensitive than porosity and as a consequence, during transport simulation the flow field needs to be updated periodically. Additionally, the representative size of the pore-network that produces an asymptotic permeability is also determined, which, for the system considered here, needs to comprise of at least  $25 \times 15 \times 15$  pore-units.

We conclude that the presented network model with particle tracking is a robust tool for calculating the macroscopic longitudinal dispersion coefficient (Chapter 3). We have found a new method to determine longitudinal dispersion coefficient from FTDs. The new method works for the full range of characteristic Peclet numbers ( $Pe_\ell$ ), provided that for large Peclet numbers a sufficiently large number of particles is used. Nodal jump conditions should include molecular diffusion and allow jumps in the upstream direction, and a parabolic velocity profile in the tubes should be implemented. Then, good agreement with experimental evidence is found for the full range of  $Pe_\ell$ , including increased  $D_L$  for increased porous medium heterogeneity. Also BPTM results match the experimentally found single tube dispersion coefficient, provided that the same method is used to process FTD data. The limitations of different methods for temporal and spatial data processing are also explored. However, BPTM is computationally not attractive.

The alternative modeling with the MCM revealed that for deriving an asymptotic dispersivity ( $\sim$  (dispersion coefficient)/(magnitude of velocity)) at least a  $33 \times 23 \times 23$  network is required (Chapter 4). The dispersivity in MCM is systematic and can be related to the pore-body size statistics. A family of such relations is found through regression. Hence, while considering a reactive transport analytically, there is no need of routing a non-reactive tracer just for determining the hydrodynamic dispersion. The dispersion with an iteration time step used here, mimics the physical dispersion produced by a BPTM with the plug-like intra-pore velocity profile, which is still smaller than the actual dispersion with parabolic intra-pore velocity profile. In BPTM the “so-called” microscopically homogeneous medium cannot be treated with the plug-like intra-tube velocity profile as it leads to only *diffusion* not to *hydrodynamic dispersion*. In general, MCM proves to be a flexible model and numerical dispersion can be well controlled with iteration time step. Additionally, MCM is more attractive with respect to simulation times and can take linearly or non-linearly reactive solutes transport into account.

The network modeling of non-linearly adsorbing solutes transport revealed that to capture an asymptotic growth rate of second central moment at least a million pore units are required (Chapter 5). Hence, our numerical experiments based on  $301 \times 61 \times 61$  sized network reveal that fronts of the non-linearly adsorbing solute transport in homogeneous media approach traveling waves, which indeed is theoretically expected. With the growth of heterogeneity the disagreement between the traveling wave predictions and numerical concentration distributions becomes noticeable and can be better assessed with the method of moments. Although a steady growth of second central moments was observed in response to the increase of pore-size heterogeneity, the higher-order moments indicate that the front is non-Fickian/non-Gaussian. The growth rate of second central moments is a quadratic function of the standard deviation of pore-sizes and therefore, it can be systematically estimated. A few relations have been derived.

The results of modeling of non-linearly adsorbing solutes transport in physically and chemically coupled but uncorrelated heterogeneous media (Chapter 6) revealed that with the growth of either physical or chemical heterogeneity the disagreement between traveling wave behavior and numerical concentration distributions becomes distinct. More importantly, the competi-

tion between the physical and chemical heterogeneities is apparent. With the decrease of one heterogeneity, another starts to prevail. The effect of chemical heterogeneity on a physically homogeneous medium appears more dramatic than for a physically heterogeneous medium. With the increase of chemical heterogeneity in a physically homogeneous medium the difference compared with the traveling wave increases. Also for the case with physically and chemically heterogeneous media, traveling wave behavior does not develop as in this case second central moment grows as a function of time with a rate that increases as pore-size heterogeneity increases. This case seems to obey non-Fickian/non-Gaussian regime. Hence, in both cases fingering appears but impact of the fingering on plume spreading differs. For example, with a heterogeneous chemistry in a physically homogeneous medium the front is locally narrow and sharp, whereas in the physically heterogeneous medium it is in comparison broader. That indicates that transversal dispersion is crucial. A pore-network of equal sized pore-units acts as a bundle of hydraulically non-interacting parallel tubes with periodically (randomly along the flow axis) distributed chemical properties where a “clutch and release” effect is produced because of which the second central moment manifests large growth, whereas the front is locally sharp and narrow. From this it is clear that without considering transversal dispersion a realistic impression of the size and the behavior of the plume-spreading in a homogeneous idealization of porous media is impossible.

In general, we conclude that in comparison with that of a single heterogeneity, the combination of *uncorrelated* physical and chemical heterogeneity has little effects. Fingering of plumes originates from heterogeneity and is therefore an unavoidable process that enhances the migration of solutes both in transversal and longitudinal directions. Hence, transversal dispersion should not be ignored while simulating transport. In combination with non-linear sorption, an essential new displacement behavior develops. The transport behavior of non-linearly adsorbing solutes in heterogeneous medium reveals a linear growth of second central moment as a function of time after a short transition period. Typical of this behavior is that it is neither according to a traveling wave nor is it Fickian. Consequently, no analytical solutions are yet available, whereas at the same time it is disputable to describe non-linear transport using a convection-dispersion equation with a non-linear sorption term.



## Samenvatting

Het probleem van verontreinigingen in de ondergrond (poreuze media) heeft de afgelopen jaren veel aandacht gekregen. De *biogeochemische* reacties die in poreuze media plaatsvinden en het transport van opgeloste stoffen zijn zeer complexe processen, die wij graag wensen te doorgronden. Dit proefschrift draagt bij aan het begrijpen van de complexiteit van deze processen. In het proefschrift wordt een nauwkeurige numerieke methode beschreven voor het opschalen van de stroming en transport in individuele poriën naar de *core scale* (letterlijk: de schaal van boorkernen). In dit proefschrift worden de geometrische eigenschappen van poriën benadrukt, de fysische en chemische eigenschappen in de porie worden door exacte wiskundige formules beschreven en wordt een geschikte procedure toegepast voor het uitmiddelen, over de *core scale*, van de processen op porieschaal, om zo tot een correcte opschalingsmethode te komen. Het hydraulische porienetwerkmodel HYPON wordt gebruikt als basisinstrument voor de *opschaling*. Door middel van *opschaling* worden de essentiële macroscopische parameters van de stroming en de convectie-dispersievergelijkingen afgeleid en worden wiskundige relaties tussen deze parameters en de heterogeniteit in de poriegrootte onderzocht. Extra nadruk wordt gelegd op het gedrag van de concentratiefronten. Dit proefschrift bevat zeven hoofdstukken. Het eerste hoofdstuk beschrijft het probleem, het doel en de aanpak van het onderzoek, terwijl het laatste hoofdstuk de belangrijkste bevindingen en conclusies van het onderzoek samenvat. In de andere hoofdstukken, met name Hoofdstuk 2 tot en met 6, worden verschillende thema's van het onderzoek beschreven, maar hebben als rode draad het *opschalingsproces*. Enig overlap tussen deze vijf hoofdstukken wordt veroorzaakt door het feit dat elk hoofdstuk een onafhankelijk te lezen artikel is dat of in zijn geheel of gedeeltelijk al gepubliceerd is. Hieronder wordt de gebruikte onderzoeksmethode in grote lijnen aangegeven gevolgd door de conclusies.

In Hoofdstuk 2 ontwikkelen we een nieuwe methode voor de constructie van een relatief realistisch porienetwerkmodel. Volgens deze methode wordt het continue domein verdeeld in een netwerk van porie-eenheden met een convergerende-divergerende opbouw. De morfologische eigenschappen van zo'n netwerk worden vergeleken met die van zogenaamde *physically based pore-networks*. Verder worden de porositeit-doorlatendheid relaties van dit netwerk opgeschaald. Steady-state condities worden aan het netwerk opgelegd en het Kirchhoff probleem wordt numeriek opgelost door methode van *preconditioned conjugate gradients*. De uitkomst verschaft een intrinsieke doorlatendheid van het netwerk. Voor een asymptotische waarde van de intrinsieke doorlatendheid is een representatieve grootte van het porienetwerk afgeleid met behulp van Monte Carlo methoden, waarbij deze grootte wordt geverifieerd met de theorie van effectieve media. Bovendien worden de resultaten geverifieerd met de Carman-Kozeny theorie. Met behulp van verschillende poriegrootterealisaties leiden wij doorlatendheid af voor een realistische range in porositeit, als vermeld in de literatuur. De niet-unieke porositeit-doorlatendheid relaties worden onderzocht waarbij is aangenomen dat *diagenesis* ofwel plaatsvindt in de grote leegtes (porielichamen) of in de convergerende-divergerende capillaire ruimtes (bindingen). Wij verwachten dat dat inzicht zal geven in de relevantie van het periodiek bijwerken van het drukveld tijdens de simulatie van bepaalde gevallen van reactief transport van opgeloste stoffen. Hoofdstuk 3 en 4 behandelen de kwantificering van locale verplaatsingen als gevolg van *Brownian motion* veroorzaakt door moleculaire diffusie ( $D_m$ ) en advectie van nonreactieve tracerdeeltjes en richten zich op het opschalen van zulke verplaatsingen op de porieschaal naar een macroscopische parameter, bekend als de longitudinale dispersiecoëfficiënt ( $D_L$ ) voor een boorkern. Voor dit doel hebben wij twee modellen ontwikkeld: het *Brownian Particle Tracking Model* (BPTM) en het *Mixing Cell Model* (MCM). Hoofdstuk 3 beschrijft de procedure van

de ontwikkeling van BPTM en de resultaten van dit model worden uitgebreid toegelicht. We beginnen met de ontwikkeling van BPTM voor Taylors capillaire buis en de validatie ervan door Taylors laboratoriumexperimenten te reproduceren. Vervolgens wordt het model uitgebreid naar de netwerkschaal. De met BPTM verkregen resultaten voor het netwerk worden vergeleken met het theoretische model van Saffman (1960) en met de experimentele data bijeengebracht door eerdere onderzoekers. Verschillende intra-porie snelheidsprofielen worden beschouwd. Verschillende typen *jump conditions* worden beschouwd bij het snijpunt van poriën en verschillende regimes met betrekking tot het karakteristieke pecllet getal ( $Pe_\ell = v\ell/Dm$ , waarin  $\ell$  de roosterconstante (*lattice constant*) is (de *gemiddelde porie lengte*), en  $v$  de intrinsieke snelheid in de gemiddelde stromingsrichting). Ook wordt de impact van fysieke heterogeniteit in de poriegrootte op de longitudinale dispersie numeriek geanalyseerd.

De data worden door twee verschillende aanpakken gegenereerd: in de eerste aanpak worden op gezette tijdsintervallen de posities van de deeltjes gescanned om een *Spatial Positions Distribution* (SPD) te verkrijgen. In de tweede methode worden de deeltjes geïnjecteerd in de ingang van het netwerk en opgevangen aan de uitgang om een *First-arrival Times Distribution* (FTD) te verkrijgen. De methode van momenten wordt gebruikt om de BPTM data te verwerken. Een nieuwe methode wordt geïntroduceerd om de FTD data te verwerken om overeenstemming te bereiken tussen de resultaten van FTD en SPD. In Hoofdstuk 4 ontwikkelen we een MCM en gebruiken dit voor de bepaling van  $D_L$  voor HYPON. Het startpunt is de bepaling van de representatieve grootte van het porienetwerk welke een asymptische waarde van de dispersiviteit ( $\alpha_L \sim D_L/v$ ) oplevert. Daarna wordt de functionele relatie tussen  $\alpha_L$  en de heterogeniteit van de poriegrootte onderzocht. Ook wordt aandacht besteed aan hoe deze relaties afhangen van de discretisatie in de tijd  $\Delta t$ . Teslotte worden deze relaties geverifieerd in grote porienetwerken en op die manier worden de asymptotische waarden van  $\alpha_L$  gevalideerd. In een volgende stap controleren we of MCM bruikbaar is voor de kwantificering van de dispersiviteit. Voor dit doel worden vijf grote netwerken beschouwd, variërend in de mate van heterogeniteit in de poriegrootte, en wordt de dispersiviteit met een BPTM model berekend, ter vergelijking met resultaten verkregen met MCM.

Het probleem van het opschalen van niet-lineair reactief transport wordt behandeld in Hoofdstukken 5 en 6. In Hoofdstuk 5 worden numerieke berekeningen uitgevoerd om te zien of in poreuze media met fysische heterogeniteit (variërende poriegrootte) lopende golven worden gevormd. Weer wordt begonnen met de bepaling van een representatieve grootte van het porienetwerk. Vervolgens worden een aantal realisaties met verschillende varianties van de poriegrootte gegenereerd en wordt transport gesimuleerd van verbindingen welke zich gedragen volgens de Freundlich isotherm. Het netwerk met constante poriegrootte en homogene chemische eigenschappen is van speciaal belang omdat in een dergelijk netwerk theoretisch gezien lopende golven zouden moeten ontstaan. Ook kan voor dit geval de mate van frontspreiding grafisch worden bepaald volgens de vereenvoudigde momentenvergelijking ontwikkeld door Bosma en Van der Zee (1993). Bovendien is het homogene geval een referentiepunt voor de andere gevallen. Naast de directe vergelijking van de numerieke en de theoretische (analytische) fronten, wordt de mate van overeenstemming tussen de twee beoordeeld met behulp van de momentenmethode (tot en met de vierde orde). Daarna worden de functionele relaties tussen de groeisnelheden van de momenten en de statistieken van de poriegrootte afgeleid.

Hoofdstuk 6 gaat in op niet-lineair transport van sorberende verbindingen in poreuze media met gecombineerde heterogeniteit: zowel fysisch (variantie van de poriegrootte  $\geq 0$ ) als chemisch (de chemische eigenschappen van iedere porie verschilt). We onderzoeken hoe de groeisnelheden van de tweede centrale ruimtelijke momenten afhangen van de fysische en

chemische heterogeniteiten. Ons onderzoek is gericht op het begrijpen van de competitie tussen de fysische en chemische heterogeniteiten. Aandacht wordt besteed aan wanneer welke vorm van heterogeniteit van de pluim domineert. Ook worden de oorzaken van de vorming van “fingers” tijdens niet-lineair transport besproken.

In Hoofdstuk 7 worden de conclusies van de voorgaande vijf hoofdstukken samengevat en gegeneraliseerd. Een korte samenvatting van de conclusies is als volgt:

De nieuwe techniek (Hoofdstuk 2) voor discretisatie van de continue ruimte tot een hydraulisch porienetwerk (HYPON) heeft getoond dat onafhankelijk van het type verdeling van de grootte van de poriëlichamen, de halsgrootte van de bindingen een Gamma-type distributie volgt, wat inderdaad ook een experimenteel waargenomen halsgrootteverdeling is. Ook andere morfologische eigenschappen van HYPON komen overeen met die van op fysica gebaseerde netwerkmodellen. Het onderzoek naar *diagenesis* met HYPON liet zien dat het onvermijdelijk is dat porositeit-doorlatendheid relaties niet uniek zijn en dat ze in grote mate worden beïnvloed door de locatie van het vullen en leeglopen van de porieruimte. Bijvoorbeeld, als een oplossing neerslaat in grote lege ruimtes (*porebodies*), dan is de doorlatendheid minder gevoelig dan de porositeit. De praktische consequentie is dat in dat geval er geen noodzaak is om het stromingsveld frequent opnieuw te berekenen. In het andere geval, als de vervuiling geadsorbeerd wordt in de capillaire ruimte (bindingen) dan is de doorlatendheid gevoeliger dan de porositeit, met als gevolg dat gedurende de transportsimulatie het stromingsveld regelmatig opnieuw moet worden berekend. Daarbij wordt ook de representatieve grootte van het porienetwerk dat een asymptotische doorlatendheid produceert bepaald, wat, voor het systeem dat we hier beschouwen, ten minste  $25 \times 15 \times 15$  porie-eenheden moet bevatten.

We concluderen dat het gepresenteerde netwerkmodel met “particle tracking” een robuuste methode is om de macroscopische longitudinale dispersiecoëfficiënt te berekenen (Hoofdstuk 3). Wij hebben een nieuwe methode gevonden om longitudinale dispersiecoëfficiënten van FTDs te bepalen. De nieuwe methode kan toegepast worden voor de volledige range van karakteristieke Pecletgetallen ( $Pe_\ell$ ), onder voorwaarde dat voor de grote Pecletgetallen een voldoende groot aantal particles wordt gebruikt. “Nodal jump conditions” moeten moleculaire diffusie bevatten en sprongen in de stroomopwaartse richting toelaten, en in de buizen moet een parabolisch snelheidsprofiel geïmplementeerd worden. In dat geval is er een goede overeenstemming met de experimentele uitkomsten voor de volledige range van ( $Pe$ ), waaronder een verhoogde  $D_L$  voor een verhoogde heterogeniteit van het poreuze medium. Ook de BPTM resultaten komen overeen met de experimenteel gevonden dispersiecoëfficiënt voor een enkelvoudige buis, onder voorwaarde dat dezelfde methode wordt gebruikt om de FTD data te verwerken. De beperkingen van de verschillende methodes voor het verwerken van temporele en ruimtelijke gegevens worden ook uiteengezet. Echter, BPTM is vanuit rekenkundig oogpunt niet aantrekkelijk.

Het modelleren met de MCM als alternatief liet zien dat om een asymptotische dispersiviteit af te leiden ( $\sim$  (dispersie coëfficiënt)/(grootte van de snelheid)) tenminste een  $33 \times 23 \times 23$  netwerk vereist is (Hoofdstuk 4). De dispersiviteit in MCM is systematisch en kan gerelateerd worden aan de statistieken van de grootte van de poriëlichamen. Een groep van zodanige relaties wordt gevonden door regressie. Daarom, wanneer reactief transport analytisch wordt beschouwd, is het niet nodig om een niet-reactieve tracer te *tracken*, enkel om de hydrodynamische dispersie te bepalen. De dispersie met een herhalende tijdstap die hier gebruikt wordt, bootst de fysische dispersie na die geproduceerd wordt door een BPTM met het “plug-like” intra-porie snelheidsprofiel, dat nog steeds kleiner is dan de actuele dispersie met een parabolisch intra-porie snelheidsprofiel. In BPTM kan het zogenaamde microscopisch homo-

gene medium niet behandeld worden met het “plug-like” intra-buis snelheidsprofiel, omdat het alleen leidt tot dispersie en niet tot hydrodynamische dispersie. Over het algemeen blijkt MCM een flexibel model te zijn en numerieke dispersie kan goed beheersd worden met de tijdsdiscretisatie. Verder is MCM aantrekkelijker met betrekking tot de simulatietijd en kan het gebruikt worden voor zowel lineair als niet-lineair reactieve oplossingen.

Het modelleren van het transport van niet lineair adsorberende (opgeloste) stoffen met behulp van de netwerken wijst uit dat, om een asymptotische groeisnelheid van het tweede centrale moment te verkrijgen, tenminste een miljoen porie-eenheden vereist zijn (Hoofdstuk 5). Vandaar dat ons numeriek experiment, gebaseerd op een netwerk ter grootte van  $301 \times 61 \times 61$ , uitwijst dat fronten van het transport van niet lineair adsorberende (opgeloste) stoffen in homogene media lopende golven benaderen. Dit wordt volgens de theorie ook verwacht. Met de toename van de heterogeniteit wordt het verschil zichtbaar tussen de voorspellingen van de lopende golf en de numerieke concentratieverdelingen en kan deze beter worden bepaald met de methode van momenten. Hoewel een gestage toename van tweede centrale momenten is waargenomen in antwoord op de toename van de heterogeniteit in de poriegrootte, duiden de hogere orde momenten op het feit dat het front “non-Fickian/non-Gaussian” is. De groeisnelheid van tweede centrale momenten is een kwadratische functie van de standaarddeviatie van de poriegrootte en daarom kan het systematisch worden geschat. Enkele relaties zijn afgeleid.

De resultaten van het modelleren van het transport van niet-lineair adsorberende (opgeloste) stoffen in fysisch en chemisch gekoppelde maar niet gecorreleerde heterogene media (Hoofdstuk 6) wijst uit dat met de toename van of de fysische of chemische heterogeniteit het verschil tussen het lopende golf gedrag en de numerieke concentratieverdeling duidelijk wordt. Belangrijker is dat de competitie tussen fysische en chemische heterogeniteit duidelijk is. Bij een afname van een van de heterogeniteiten krijgt de ander de overhand. Het effect van chemische heterogeniteit op een fysische homogeen medium blijkt meer dramatisch dan op een fysisch heterogeen medium. Bij een toename van de chemische heterogeniteit in een fysisch homogeen medium neemt het verschil in vergelijking met de lopende golven toe. Ook in het geval van fysisch en chemisch heterogene media ontwikkelt het lopende golf gedrag niet omdat in dat geval het tweede centrale moment groeit als functie van de tijd met een snelheid die toeneemt wanneer de porie-grootte toeneemt. Dit geval lijkt een “non-Fickian/non-Gaussian” regime te volgen. Vandaar dat in beide gevallen “fingering” ontstaat, maar de impact hiervan op de spreiding van de pluim kan verschillen. Bijvoorbeeld bij een heterogene chemie in een fysisch homogeen medium is het front lokaal smal en scherp, terwijl het front in een fysisch heterogeen medium breder is. Dit geeft aan dat transversale dispersie cruciaal is. Een porienetwerk met porie-eenheden van gelijke grootte gedraagt zich als een bundel van hydraulische, niet op elkaar inwerkende, parallelle buizen met periodieke (willekeurig langs de stromingsas) verdeelde chemische eigenschappen, waar een “clutch and release” effect wordt geproduceerd, waardoor het tweede centrale moment grote groei vertoont terwijl het front lokaal scherp en smal is. Uit dit blijkt dat zonder transversale dispersie te beschouwen een realistische weergave van de grootte en het gedrag van de spreiding van de pluim in een homogene idealisering van poreuze media niet mogelijk is.

In het algemeen kunnen we concluderen dat in vergelijking met een enkele heterogeniteit, de combinatie van niet-gecorrleerde fysische en chemische heterogeniteit weinig effect heeft. “Fingering” van de pluimen komt voort uit heterogeniteit en is daardoor een onvermijdelijk proces dat de migratie van opgeloste stoffen in zowel transversale als longitudinale richting versterkt. Vandaar dat transversale dispersie niet genegeerd kan worden bij simulatie van transport. In combinatie met niet-lineaire sorptie ontstaat er een geheel nieuw verplaatsingsgedrag.

Het transport van niet-lineair adsorberende (opgeloste) stoffen in een heterogeen medium vertoont een lineaire groei van het tweede centrale moment als een functie van de tijd na een korte omschakelingsperiode. Typisch voor dit gedrag is dat het niet volgens een lopende golf is noch “Fickian” is. Derhalve zijn er op tot op heden geen analytische oplossingen beschikbaar, terwijl het tegelijkertijd betwistbaar is of niet-lineair transport beschreven kan worden met een convectie-dispersie vergelijking met een niet-lineaire sorptie term.



## Biography

Ram Chandra Acharya was born on July 30, 1962 in Nepal. After his SLC examinations in 1978 he joined the Faculty of Science and Technology of PN Campus, Pokhara. Due to the unstable political situations in the country, it took him almost 4 years to get his diploma of ISc. Finally, in 1982 with a dream of being a water-resource engineer, he left for the former Soviet Union to study civil engineering. He took his preparatory course at the Yerevan State University in Armenia. In September 1983 he went to Moscow and joined the Faculty of Hydraulic Structures of Moscow State University of Environmental Engineering (MSUEE) (formerly Moscow Institute of Hydrotechnical Engineering and Land Reclamation) and started his mission for mastering water. As a part of his Masters thesis he with Prof. Grigory Kaganov developed a new technique for the design of double-curved cantilever of arch-dam. In 1988 he returned to Nepal with a degree of engineer, water constructor. Upon his return in Nepal, he joined the Department of Irrigation where he was responsible for the construction of an irrigation canal. In 1990 he moved to the Department of Hydrology and Meteorology and hence, a new journey for hydrologist was started. First three months of 1992 he spent at the National Institute of Hydrology, Roorkie (India), learning low-flow modeling. In October, 1992, Ram arrived in Delft for his Masters degree in Hydrology. His course work with Dr. Pieter de Laat and Dr. Piet Warmerdam was on hydrological modeling of Hupselse Beek. After his first year at IHE, he was sent to the Center of Mathematical Methods of RIVM for his internship (*stage*) to work with Dr. Peter Heuberger and Dr. Arnold Dekkers on ammonia transport modeling project. From IHE Prof. Mike Hall supervised his thesis. Eventually, on May 26, 1994 IHE conferred on him the MSc degree of Hydrology. In Nepal many projects were waiting for him. Since 1994-1999 Ram carried out a number of hydrological studies and hydraulic design for irrigation, roads, bridges and hydropower projects. In 1996-1997 he spent three months at the University of Delaware (USA) and at TERI (India) learning sustainable energy and environment policy course. In the mean time his fascination for structural engineering brought him with some construction and consulting groups, where he served as a structural designer and executer of steel structures such as bridges, communication towers and large-span roofing structures of sports halls and industrial sheds. He was very pleased with the success of his turn-key project of high communication towers for the first GSM project in Nepal. In 2000 the Soil Quality Section of the Department of Environmental Sciences at Wageningen University appointed Ram for a PhD position with Prof. Sjoerd van der Zee and Prof. Toon Leijnse. The position was assigned for a *NWO* project “Upscaling of flow and transport: From pore to core”. In the course of research Ram spent the first three months of 2002 at the Heriot-Watt University working with Prof. Ken Sorbie and Dr. Rink van Dijke. This thesis is the compilation of results of the research he carried out from January 10, 2000 to August 10, 2004. From January 2005 Ram has a Postdoc position at the University of Illinois at Urbana-Champaign (USA) to work with Prof. Al Valocchi and Prof. Charles Werth.



Netherlands Organisation for Scientific Research

This study was performed under the research program “Upscaling Flow and Transport Processes in Porous Media: From Pore to Core” funded by the Dutch NWO/ALW project no. 809.62.010.

The research was partly supported by the project “Integrated Soil and Water Protection (SOWA)” funded by the European Commission (EVK1-CT-2002-80022).

European Community - Access to Research Infrastructure action of the Improving Human Potential Programme to use the EIERO infrastructure - supported the three-month long visit of the researcher to the Heriot-Watt University, Edinburgh, UK.

The Institute of Petroleum Engineering provided hospitality and logistics to the researcher during his stay in Edinburgh.

---

Cover design and art work: Thomas Schröder

Printed and bound in The Netherlands by Grafisch bedrijf Ponsen & Looijen BV, Postbus 68, 6700 AB Wageningen.



# Stellingen

1. The type of distribution of pore throats is independent of the type of distribution of pore-body sizes, although each throat size is derived from the adjacent porebody sizes.

(Chapter 2 of this thesis)

2. The typical behavior of the front for non-linearly adsorbing transport in heterogeneous pore networks is neither according to the traveling wave nor is it Fickian.

(Chapters 5 and 6 of this thesis)

3. Happiness is something that has to be learnt and practiced by the human himself.

4. For the sustainable management of groundwater, dams for storage of surface water are needed.

5. Before starting a Ph. D. research, graduate students should undergo an intensive training on preventive measures against RSI (Repetitive Strain Injury).

6. Environmental problems are nothing but the result of human behavior.

7. Happiness is something that has to be learnt and practiced by the human himself.

Stellingen behorende bij het proefschrift van R. C. Acharya: "Upscaling of Nonlinear Reactive Transport: from Pore to Core", 21 december 2004.